Engineered Zircaloy Cladding Modifications for Improved Accident Tolerance of LWR Nuclear Fuel

Fuel Cycle
Integrated Research Project

Brent Heuser
University of Illinois, Urbana Champaign

In collaboration with:
University of Florida
University of Michigan

Frank Goldner, Federal POC
Jon Carmack, Technical POC

NEUP | Nuclear Energy University Programs
U.S. Department of Energy

Final Report

CFP: NEUP-002-12 Integrated Research Projects

Title: IPR—Engineered Zircaloy Cladding Modifications for Improved Accident Tolerance of LWR Fuel

Project Director: Brent J. Heuser/University of Illinois

Partner Institutions:

University of Illinois: Brent J. Heuser, Thomasz Kozlowski, Rizwan Uddin, James F. Stubbins, Dallas R. Trinkle, Robert. S. Averback

University of Michigan: Thomas J. Downar, Gary S. Was

University of Florida: Yong Yang, Simon R. Phillpot

Idaho National Laboratory: Piyush Sabharwall, Michael V. Glazoff, Jason D. Hales

ATI Wah Chang: Melissa Martinez, Greg Vignoul

The DOE NEUP sponsored IRP on accident tolerant fuel (ATF) entitled *Engineered Zircaloy Cladding Modifications for Improved Accident Tolerance of LWR Nuclear Fuel* involved three academic institutions, Idaho National Laboratory (INL), and ATI Materials (ATI). Detailed descriptions of the work at the University of Illinois (UIUC, prime), the University of Florida (UF), the University of Michigan (UMich), and INL are included in this document as separate sections. This summary provides a synopsis of the work performed across the IRP team.

Two ATF solution pathways were initially proposed, coatings on monolithic Zr-based LWR cladding material and self-healing modifications of Zr-based alloys. The coating pathway was extensively investigated, both experimentally and in computations. Experimental activities related to *ATF coatings* were centered at UIUC, UF, and UMich and involved coating development and testing, and ion irradiation. Neutronic and thermal hydraulic aspects of *ATF coatings* were the focus of computational work at UIUC and UMich, while materials science aspects were the focus of computational work at UF and INL. ATI provided monolithic Zircaloy 2 and 4 material and a binary Zr-Y alloy material. The *self-healing* pathway was investigated with advanced computations only. Beryllium was identified as a valid self-healing additive early in this work. However, all attempts to fabricate a Zr-Be alloy failed. Several avenues of fabrication were explored. ATI ultimately declined our fabrication request over health concerns associated with Be (we note that Be was not part of the original work scope and the ATI SOW). Likewise, Ames Laboratory declined our fabrication request, citing known litigation dating to the 1980s and 1990s involving the U.S. Federal government and U.S. National Laboratory employees involving the use of Be. Materion (formerly, Brush Wellman) also declined our fabrication request, citing the difficulty in working with a highly reactive Zr and Be. International fabrication options were explored in Europe and Asia, but this proved to be impractical, if not impossible. Consequently, experimental investigation of the Zr-Be binary system was dropped and exploration binary Zr-Y binary system was initiated. The motivation behind the Zr-Y system is the known thermodynamic stability of yttria over zirconia.

Experimental findings

The ability of FeCrAl, CrAl, and pure Cr coatings to prevent oxidation of underlying Zircaloy was investigated in high-temperature steam (HTS). These coatings were applied using magnetron sputtering physical vapor deposition. Some coatings were investigated in simulated LWR immersion experiments using autoclaves at the University of Michigan. In addition, selected coatings were irradiated with energetic proton and Fe ions to simulate fast neutron displacement cascade damage with some of these subsequently exposed to either HTS and/or simulated LWR environments. All ion irradiation tests were performed at the University of Michigan. Aluminum coatings were also investigated by the IRP team. These coating were applied to Zircaloy material using a packed cementation diffusion coating (PCDC) process. The following conclusions are drawn from this work.

1. FeCrAl performed very well as an oxidation inhibitor in 700-°C HTS. This coating system favors alumina formation over both chromia and zirconia formation, with the alumina serving as a protective oxide during HTS exposure. However, the Fe-Zr eutectic at approximately 950 °C leads to a loss of the coating via melting at above this temperature. This invalidates the FeCrAl system for ATF use since design-based accident scenarios require protection up to and including 1200 °C. It is possible that thick (20-50 microns) FeCrAl coatings (our work investigated <10 micron coatings) may alleviate the Fe-Zr eutectic effect on coating integrity with respect to melting. However, magnetron sputtering is not a practical avenue for the deposition of thick overlayers.

2. The FeCrAl system performed well in simulated recirculating LWR immersion environments and was not adversely affected by displacement cascade damage.

3. CrAl and pure Cr also performed well in 700-°C HTS, but not at higher steam exposure temperatures. For example, we could not duplicate the 1200 °C HTS results obtained by the French for pure Cr. We suspect

our thinner coatings (<10 microns) may not be sufficiently thick to provide an adequate source of Cr for chromia formation.

4. The behavior of the Zr-Y binary system to 700 °C HTS exposure lead to initially more rapid weight gain relative to Zircaloy, but much lower weight gain at long times. However, the overall conclusion is that Y is detrimental to the performance in HTS with respect to oxidation.

5. PCDC aluminized Zr-4 exhibits a larger weight gain in normal LWR operating conditions compared to Zircaloy. This is attributed to the highly porous coating morphology promoting aluminum hydroxide (Boehmite) formation. On the other hand, the aluminization has shown an improved oxidation resistance over the uncoated Zircaloy-4 claddings under off-normal 800 °C HTS exposure conditions. Of course, one important criterion for ATF solutions is not to worsen the performance under normal LWR conditions. The PCDC pathway fails this criterion. However, the PCDC aluminization could be a valid solution pathway if the process was refined to minimize coating porosity.

6. Self-healing of Zircaloy was investigated with advanced computations. The segregation of elemental Be to the free surface was demonstrated. The driving force for Be segregation was a low energy configuration in near surface sites within hexagonal Zr. The proximity of Be to the free surface is anticipated to promote BeO formation. BeO is a brittle oxide and cracking of such an oxide scale would be likely. However, continuous migration of Be to newly exposed surfaces would occur, resulting in continuous BeO formation. Thus, our conclusion was that Be is a possible self-healing additive worthy of experimental investigation.

7. Thermodynamic properties and phase equilibria was described for Zirconium, Zr-2, and Zr-4. Hydrogen uptake facilitates oxidation of Zr. In the equilibrium state, hydrogen solubility is same for all three alloys, but Zr-4 is better than Zr-2 (less hydrogen uptake), so hydrogen uptake is not a thermodynamic controlled phenomenon but driven by kinetics. Zr is thermodynamically unstable to oxidation even at room temperature and the process of oxidation and hydrogen pick-up is controlled kinetically, which increases with increase in temperature.

8. Sputtering temperature for coatings should be either below 500 C or above 700 C. The optimal composition of Fe-Cr-Al protective coating should be in the range from 80-18-2 to 80-14-6, preferably 80-15-5 weight percent Fe-Cr-Al. The chemical composition of YSZ-doped ZRO_2 should be established based on matching thermo-physical properties of Zr-2 and Zr-4 and desired temperature of oxygen transport activation to get self-healing mechanism started. Beryllium additions (~1ppm to 5ppm Be) should be explored during Zr alloy ingot casting. Thermal stability of clad with Be ancillary additions still needs further investigation.

Neutronics and thermal hydraulics findings

Neutronics, thermal-hydraulics, and fuel performance analysis were performed for enhanced accident tolerance fuel. The VTT's reactor physics code Serpent and NRC's neutron diffusion code PARCS were used for neutronics analysis; INL's BISON code was used for fuel performance analysis; NRC's RELAP5 and TRACE were used for thermal-hydraulics analysis. Neutronics analysis was used to narrow down the cladding material to two of the most promising candidate materials, FeCrAl and SiC, for further analysis.

1. Application of either FeCrAl or SiC could improve performance from the fuel performance standpoint. The axial temperature profile is flattened for operating conditions and the gap closure time is significantly increased, which means the pellet-cladding mechanical interaction is greatly delayed. From the fuel performance point of view, the disadvantages for the SiC and FeCrAl application are that the fission gas release is increased; and fuel temperature is ~50K higher at low to medium burnup.

2. The thermal-hydraulics analysis showed no appreciable differences in operating and design basis accidents relative to Zircaloy cladding. Beyond design basis, the FeCrAl cladding would delay oxidation and hydrogen release, SiC cladding would practically eliminate oxidation and hydrogen.

3. A neutron penalty was identified when FeCrAl is used as monolithic cladding for current oxide fuel. To compensate for the drop in reactivity, it will be required to do one or more of the following: (1) increasing the oxide fuel enrichment; (2) minimizing the cladding thickness to reduce the neutron penalty; (3) reduce cycle length.

Each of these approaches would substantially increase the fuel and electricity costs. Therefore, from the reactor physics standpoint, application of the FeCrAl alloy as a coating layer on surface of Zircaloy cladding is a more practical. Meanwhile, SiC increases reactivity, and the neutron penalty is of no concern.

The main remaining issues to be resolved for FeCrAl cladding, are the creep behavior, coating spallation, and inter-diffusion with zirconium. For SiC, its high thermal conductivity, excellent creep resistance, low neutron absorption cross-section, and irradiation stability (negligible swelling) make it an excellent candidate material for future nuclear fuel/cladding research.

DOE NEUP-002-12 Integrated Research Projects
Engineered Zircaloy Cladding Modifications for Improved Accident Tolerance of LWR Fuel
Final Report

1.   Introduction

This document serves as the final report for Project 12-4728 annual report (M2NU-12-IL-UIUC-0201-0629-Final Report - (Project 12-4728) Engineered Zircaloy Cladding Modifications for Improved Accident Tolerance of LWR Nuclear Fuel). The report contains separate sections from each of the primary PIs as follows:

Brent Heuser/UIUC and Gary Was/UMich
James Stubbins/UIUC
Tomasz Kozlowski/UIUC and Thomas Downar/UMich
Rizwan Uddin/UIUC
Dallas Trinkle/UIUC
Yong Yang/UF
Simon Phillpot/UF
Piyush Sabharwall and Michael Glazoff/INL

Each section is self-contained and includes a bibliography.

2.   Heuser, Stubbins, and Was

2.1   FeCrAl/CrAl/Cr coated Zircaloy

Coatings with different compositions have been deposited on Zircaloy-2 by magnetron sputtering to study their oxidation behavior at high temperature steam environment [1]. These coatings include ternary Iron-Chromium-Aluminum alloy (FeCrAl), binary Chromium-Aluminum alloy (CrAl) and metallic Chromium coating. Coated Zircaloy-2 have been exposed to 700 ℃ and 1200 ℃ steam environment, and the weight gain of coated specimens was measuring during the exposure. Specimens included in this report are listed in Table 1, which provides the thickness and compositions of different coatings, and the exposure temperature. Auger Electron Spectroscopy (AES) has been applied to quantify the oxidation kinetics and chemical depth profile. X-ray diffraction (XRD) and (Scanning) Transmission Electron Microscope (STEM) with the capability of Energy dispersive spectroscopy (EDS) have been performed to analyze the microstructure of as-grown and post-exposure coated Zircaloy-2.

Table 1. Steam exposure sample matrix showing coating compositions and thickness, and the exposure condition.

coating	Sample ID	Composition[Fe/Cr/Al] Atomic percentage	Thickness[um]	Exposure temperature[°C]
FeCrAl	62/4/34 FeCrAl	62/4/34	0.6/0.9/1.1	700
	71/7/22 FeCrAl	71/7/22	0.6	700
	53/29/18 FeCrAl	53/29/18	0.3	700
	86/10/4 FeCrAl	86/10/4	0.3	700
CrAl	42/58 CrAl	0/42/58	1	700
	57/43 CrAl	0/57/43	1	700
	67/33 CrAl	0/67/33	1	700
	81/19 CrAl	0/81/19	1	700
	42/58 CrAl_1200 °C	0/42/58	5	1200
	85/15 CrAl_1200 °C	0/85/15	6.5	1200
Cr	Cr	0/0/100	1	700
	Cr_1200 °C	0/0/100	3.5	1200

Oxidation kinetics

Weight gain measurement was performed on different coating systems exposed to 700 °C steam environment. All samples were coated on both sides with the edge receiving partial coatings, and the normalized weight gain have been corrected for the effect of incomplete coverage of the edges. This correction was made by subtracting the measured uncoated Zy2 response multiplied by the (estimated) fractional area of the coated sample edges. The weight gain for FeCrAl coatings with four different compositions are shown in Figure 1A. Three compositions (Fe/Cr/Al in atomic percent, 53/29/18, 62/4/34, and 71/7/22) results in much lower weight gain than the uncoated Zircaloy-2, and the fourth composition (88/10/2) has a poor oxidation response, consistent with the low Al and Cr concentration. Figure 1B shows the normalized weight gain of CrAl and Cr coatings up to 20 hours under 700 °C steam environment. Same as the Figure 1A, the normalized weight gain was calculated by subtracting the weight gain from the four edges

assuming the edges performed similar to the uncoated Zircaloy. CrAl coatings and Cr coating have similar normalized weight gain from the steam exposure. Weight gain under the steam environment comes from both oxidation and hydriding. As the oxidation kinetics in the coated surface are slow, most hydrogen were generated from the zirconium-steam reaction at the edges of the specimens. Results of synchrotron X-ray diffraction and cross sectional optical microscope demonstrated the delta-zirconium formation from the steam exposure [not shown]. To understand the oxidation performance of the coating, weight gain from the oxide of the coating was quantified, and the result is shown in the subset of Figure 1B. A thick layer of Cr_2O_3 was developed on the 81/19 CrAl coating, and the coating has the highest weight gain from the oxide. CrAl coatings with the composition of 42/58 and 57/43 have same alumina thickness, and the weight gain from the oxide are the same for these two coatings. Calculation of the weight gain from the oxide was based on the cross section STEM analysis, which will be presented in the microstructure session.
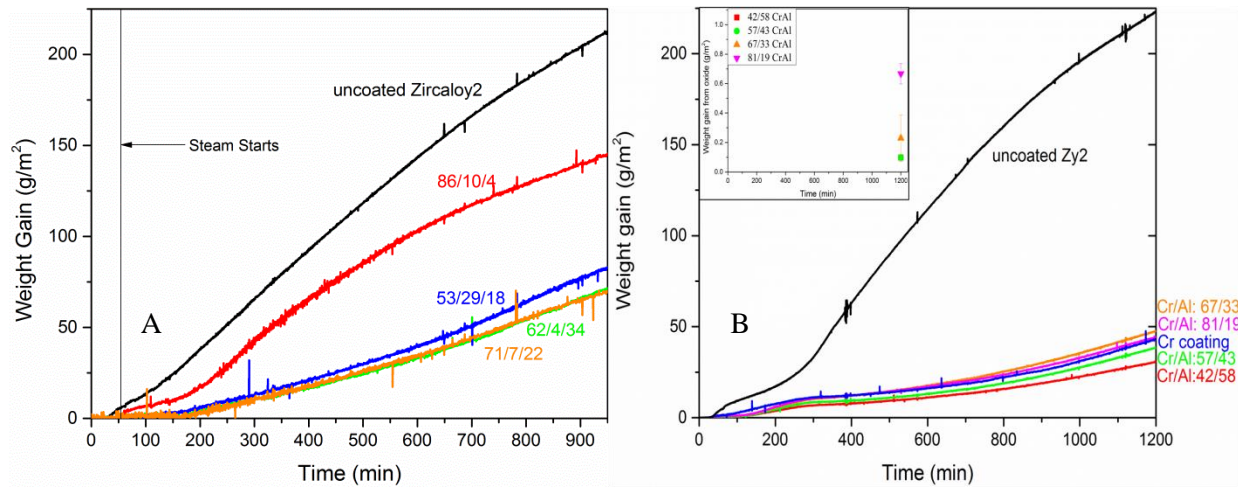
Figure 1. Weight gain normalized to total sample surface area versus time during 700 ℃ steam exposure for FeCrAl/CrAl/Cr coated Zircaloy with different compositions. (A) Weight gain of FeCrAl coatings with the composition of 86/10/4, 53/29/18, 62/4/34, and 71/7/22. (B) Weight gain of Cr coating and CrAl coating with the composition of 81/19, 67/33, 57/43, and 42/58. The subset figure in (B) are the weight gain from the surface oxide that was calculated from the cross sectional STEM images shown in Figure 10 – 13.

To compare the weight gain of different coating systems under 700 ℃ steam environment, Figure 2A shows the ternary plot of weight gain for different coatings at 425 minutes, and Figure 2B shows the ternary plot of weight gain slope at 425 minutes. The coatings at the zero Iron concentration line represent CrAl or Cr coatings. For reference, uncoated Zircaloy has a weight gain of 50 g/m^2 and a weight gain slope of 26 g/m^2/hr at 425 minutes.
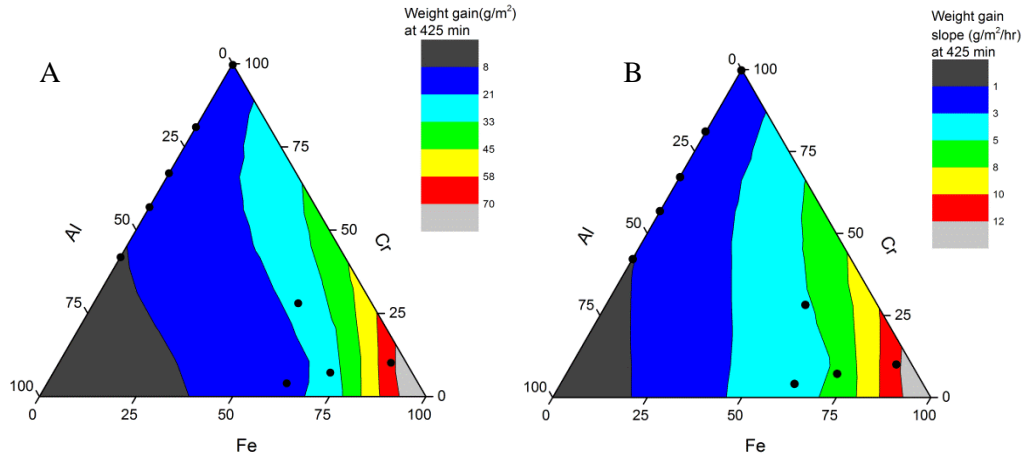
Figure 2. (A) Ternary plot of weight gain at 425 minutes for FeCrAl/CrAl/Cr coating systems. (B) Ternary plot of weight gain slope at 425 minutes for FeCrAl/CrAl/Cr coating systems. For reference, uncoated Zircaloy has a weight gain of 50 g/m^2 and a weight gain slope of 26 g/m^2/hr at 425 minute.

As 62/4/34 FeCrAl coating has the best performance among the four compositions FeCrAl coatings, it was selected for extensive study. FeCrAl coatings with the thickness of 0.9um and 1.1um have been exposed to 700 ℃ steam for up to 20 hours. Depth profiles have been measured for specimens exposed to 0.5, 2, 3.7, 6, 10, 15, and 20 hours by Auger Electron microscopy along with the as-grown coated Zircaloy-2. The depth profiles are shown in the Figure 3. The depth profiles up to 3.7 hours were performed on the 0.9um thick FeCrAl coatings assuming that the oxidation kinetics are same for the 1.1um thick FeCrAl coatings as no zirconia formation was observed before 15 hours. The AES depth scale in the Figure 3 was determined from the sputter time scale by assuming the constant sputter rate throughout the measurement, and by setting the half Zr depth as the coating/substrate interface assuming the interface does not move. Although the thickness of the coating is not necessary invariant, all AES depth scales were determined by the same way, acknowledging the potential sources of the systematic error with respect to the depth scale. Aluminum oxide was developed on the surface at 700 ℃ steam environment, and it grew as exposure time. Iron and Aluminum inward diffusion into the substrate was observed, while Chromium accumulated within the coating. It is noted that the FeCrAl coating prevents Zr oxide formation up to 15 hours, when a layer of ZrO_2 with the thickness of 80um was expected to form on an uncoated Zircaloy-2[2].
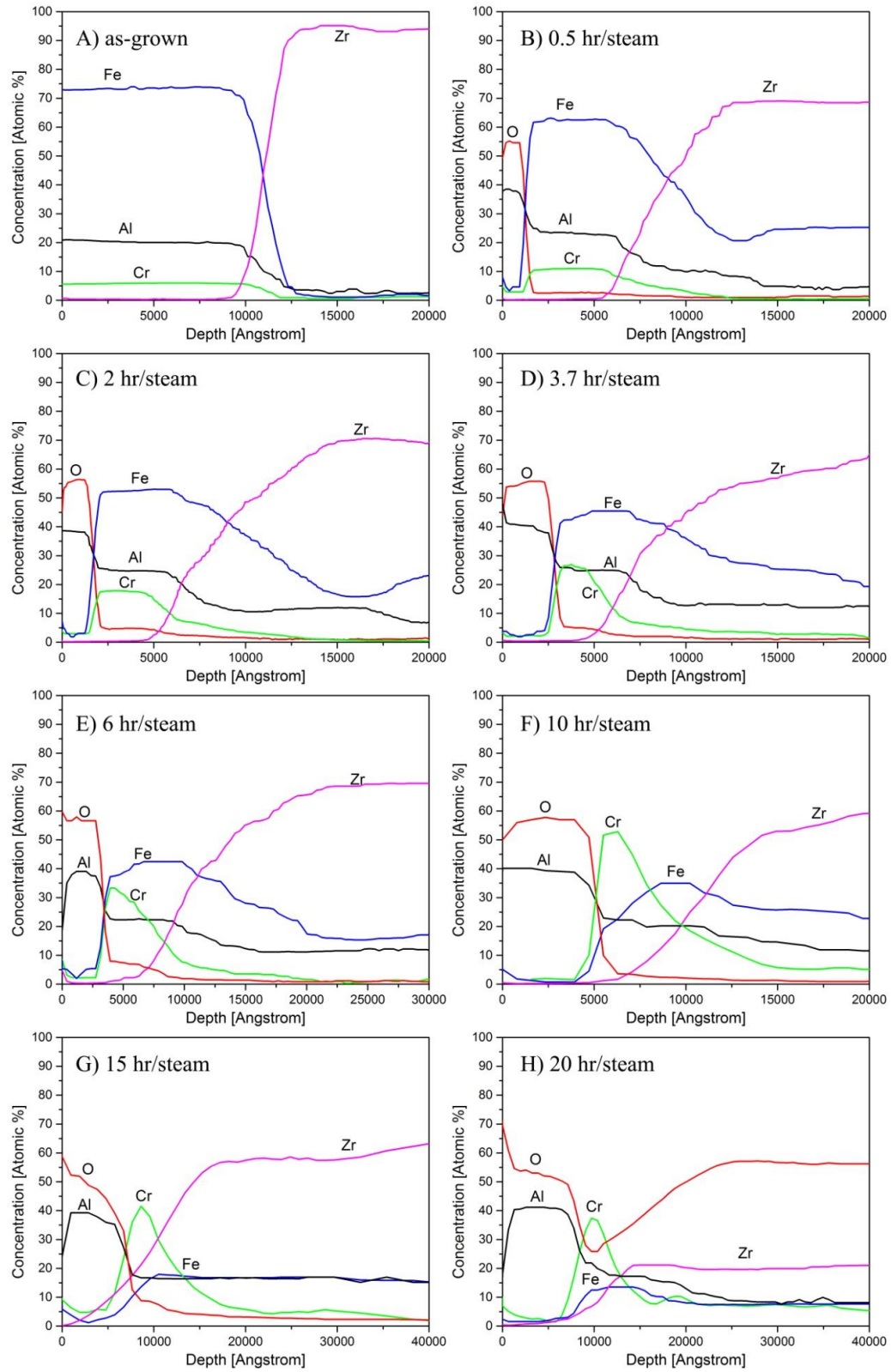
Figure 3. AES depth profiles for 62/4/34 FeCrAl coatings. A) As-grown coating; B)-H) 700°C steam exposure for sequentially longer times as indicated.
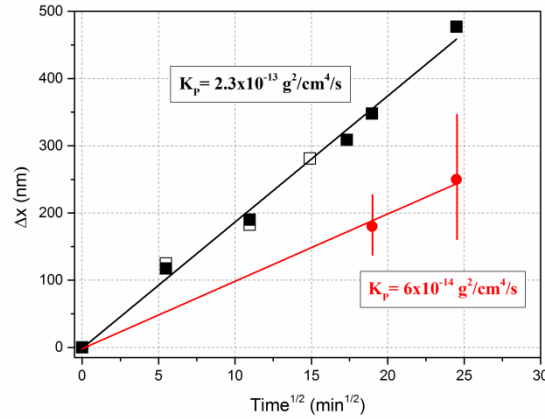
Figure 4. Time dependence of alumina oxide layer growth during 700 ºC steam exposure obtained for AES depth profiles; open boxes (0.9um thick FeCrAl coatings), solid boxes (1.1um thick FeCrAl coatings). Additional solid red circles symbols correspond to profilometer measurements of a AES craters terminated at the alumina/coating interface depth, as discussed in the text. The best-fit lines are proportional to the square root of the parabolic rate constants shown in the insets.

Aluminum oxide growth kinetics was determined from the AES depth profiles. Figure 4 shows the aluminum oxide thickness versus square root of the exposure time. The filled boxes are the AES Al_2O_3 thickness of 1.1um thick FeCrAl, and the open boxes are the AES Al_2O_3 thicknesses of 0.9um thick FeCrAl. A linear function of alumina thickness versus the square root of time was observed with the rate constant of $2.3 \times 10^{-13} g^2/cm^4/s$. However, as mentioned above, it is difficult to calibrate the depth scale from the sputter time in the AES measurement, and there are potential sources of systematic error. Therefore, to calibrate the alumina thickness, profilometer measurements were performed on the AES craters terminated at the Al_2O_3/FeCrAl interface of 6 hours and 10 hours exposed FeCrAl coatings. 6 hours and 10 hours were two of the longest exposed time, and thicker alumina layers were expected. Therefore, they were selected on purpose for better profilometer result. However, rougher topography was observed for these prolonged exposed FeCrAl coatings, and associated errors were expected in the measurement. The profilometer measured Al_2O_3 thicknesses are shown as circles in the Figure 4. The profilometer parabolic rate constant is quantified to be $6 \times 10^{-14} g^2/cm^4/s$, a factor of four lower than the AES result, and it is in a better agreement with the monolithic FeCrAl of others' works [3].

Extended depth profiles of FeCrAl coatings with the composition of 62/4/34 and 88/10/2 are shown in Figure 5. 0.6um thick 62/4/34 FeCrAl coating and 0.3um thick 88/10/2 FeCrAl coating were exposed to 700 ºC steam for 15 hours. Fe_2O_3 formation was observed on the 88/10/2 FeCrAl coating. The lack of alumina formation on this sample and significant zirconia growth is consistent with the poor oxidation protection and associated weight gain observed for this composition in Figure 1A. Oxygen-Zr stoichiometry consistent with zirconia persists to depths of microns, followed by stoichiometry consistent with the α-Zr-O solid solution phase. It is also noted the tendency for greater Fe segregation in the thinner coatings, as opposed to Cr

6

segregation in the thicker coatings (compare Figs. 3G and 5A). This is attributed to lower total Cr inventory in thinner coatings and the lack of significant diffusivity of cation impurities (Fe, Cr, and Al) into ionic ZrO_2.
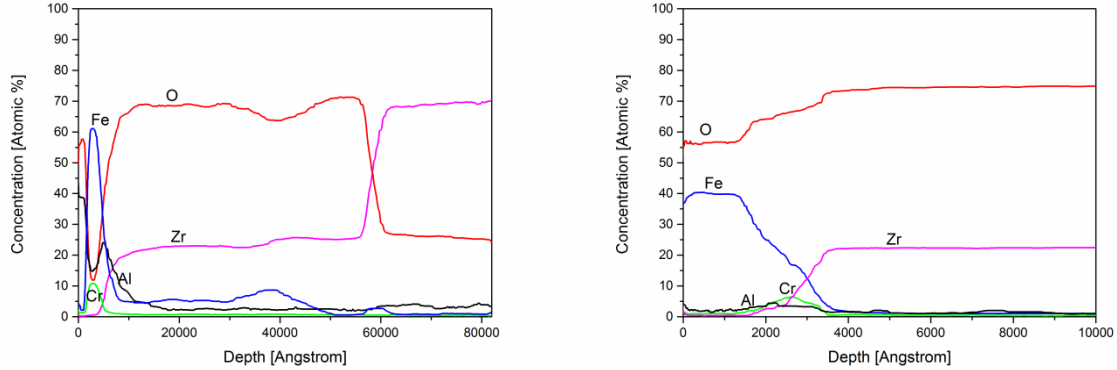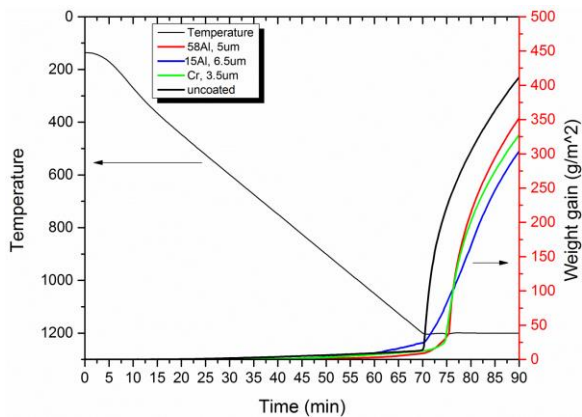

Figure 5. AES depth profiles for FeCrAl coatings for two different compositions for 15 hours under 700 ℃ steam environment. A) 62/4/34 FeCrAl with the thickness of 0.6um. B) 88/10/2 FeCrAl coating with the thickness of 0.3um.

Oxidation behavior was also studied under 1200 ℃ steam environment. However, eutectic reaction of Fe-Zr at around 900 ℃ leads to a complete film lost at higher temperature, and the film does not provide protection. To overcome the eutectic issue, a buffer layer of Cr or Cr_2O_3 has been proposed to deposited between the substrate and FeCrAl coating, or replacing FeCrAl coating with CrAl or Cr coatings. In this report, the latter method was applied, and the weight gain of coated Zircaloy-2 at 1200 ℃ steam environment is shown in Figure 6. Oxidation kinetics is expected to be much faster in higher temperature, therefore, thicker coatings were deposited to study its oxidation behavior. Significantly oxidation was observed when steam was introduced into the chamber. However, for coated zircaloy, the significant oxidation was delayed by five minutes approximately. Nevertheless, the kinetics was comparable to uncoated zircaloy after that.

Figure 6. Weight gain of CrAl coatings and Cr coating at 1200 ℃ steam environment. Delayed oxidation was observed for the Cr coating and 42/58 CrAl coating.

X-ray diffraction

X-ray diffraction pattern of as-grown and post exposed 62/4/34 FeCrAl coatings on Zircaloy-2 were performed and they are shown in Figure 7. Ω-2θ scans on the as-grown FeCrAl coating shows a primitive cubic (Pm-3m) structure with reflections indexed to FeAl, an intermetallic compound with extended solid solution solubility. The difference between this lattice structure and the Fe_3Al BCC (Im-3m) structure is the presence of the forbidden (100) reflection. In addition, glancing incident X-ray diffraction (GIXRD) was performed on the exposed FeCrAl-zircaloy system. Reflections from the 0.5 hour exposed sample can be indexed to the primitive cubic FeAl or α-alumina; Zr-matrix intensity has been completely eliminated by the glancing-angle geometry. Prolonged, 10 h exposure has resulted in consumption of FeCrAl and the formation of α-alumina and a $Fe_2(CrAl)$ intermetallic phase (Fd-3m) that was observed with AES. The alumina is indexed as α-alumina. However, many different Al oxides phases exist with significant overlap of diffraction intensity and this indexing should not be considered conclusive.
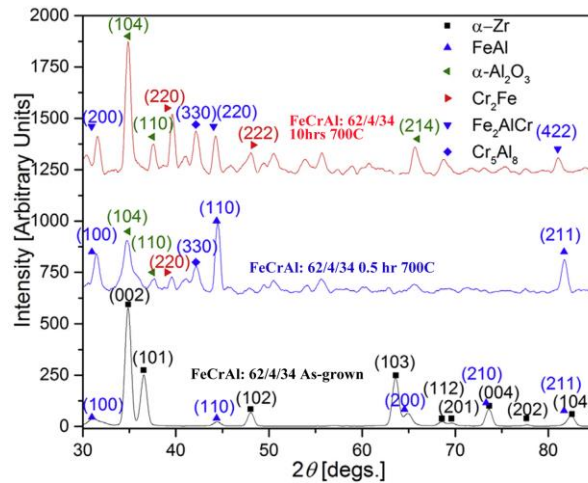
Figure 7. XRD scans of as-grown and post-exposure at 700 °C steam for 62/4/34 FeCrAl coating on Zircaloy-2. The FeCrAl coatings at this atomic composition grow as primitive cubic (Pm-3m). All peaks can be indexed as Zr matrix or primitive cubic FeAl film reflections. Additional diffraction intensity indexed to α-alumina and a $Fe_2(CrAl)$ (Fd-3m) intermetallic phase is observed from the post-exposed samples. The unindexed diffraction intensity (for example, at $2\theta \sim 32°$ in 0.5 hour exposure pattern, and at $2\theta \sim 41°$ - $43°$ and $47°$ in 10 hours exposure pattern) is likely due to intermetallic phase formation involving a combination of Fe, Al, Cr, and Zr.

X-ray diffraction has been applied on both as-grown and post-exposed CrAl/Cr coated Zircaloy systems at 700 °C steam environment for 20 hours. The XRD scans on the as-grown coatings were performed at a glancing angle of 2°, and the scans on the post-exposed samples were performed at a glancing angle of 3° to maximize the diffraction from the coatings

Figure 8A shows the as-grown CrAl and Cr coatings. Three Cr-Al phases were indexed, cubic Cr with a space group of Im-3m for the Cr coating and the 81/19 CrAl coating; tetragonal $AlCr_2$ with a space group of P4/mmm for the 67/33 CrAl and 57/43 CrAl coatings; and rhombohedral Al_8Cr_5 with a space group of R3m for the 42/58 CrAl coating. It is noted that CrAl coating with

the composition of 81/19 does not have the stoichiometry of either pure Cr or $AlCr_2$, and the diffraction intensity lies between the cubic Cr pattern and tetragonal $AlCr_2$ pattern. Although Cr and $AlCr_2$ do not have the same structure, their major peaks are neighboring. Therefore the index of the as-grown 81/19 CrAl phase as cubic Cr phase is not conclusive.
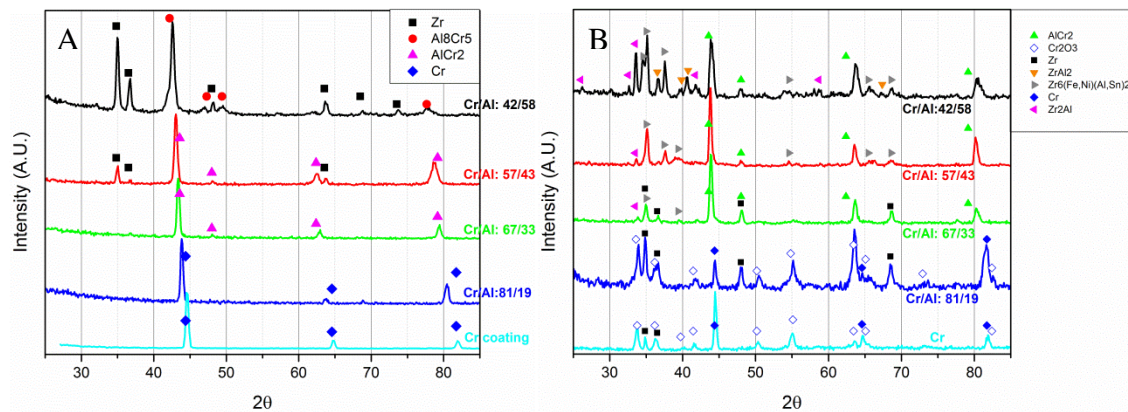

Figure 8. X-ray diffraction for CrAl and Cr coatings. A) As-grown coatings. B) After 20 hours exposure at 700 ℃ steam environment. Chromia, coatings and intermetallic phase's structure were indexed. The layer of Al_2O_3 was too thin to be indexed from the XRD. However, its structure was identified in SAD in Figure 11B.

The glancing incident XRD (GIXRD) for CrAl coatings after 20 hours exposure at 700 ℃ steam environment are shown in Figure 8B. Strong Cr_2O_3 peaks were observed on both the Cr and the 81/19 CrAl coatings. Unreacted Chromium peaks were also observed from the post-exposure diffraction scan, which indicates that the coatings would provide longer protection over 20 hours. There are some minor diffraction intensity that were not indexed, which could be attributed to the intermetallic phases involving the coating and the substrate.

Strong peaks intensity of intermetallic phases were observed for CrAl coatings with high Aluminum composition. Hexagonal $Zr_6(Fe,Ni)(Al,Sn)_2$ structure with the space group of P-62m and hexagonal Zr_2Al structure with the space group of P63/mmc were indexed on the post-exposed CrAl coatings with the composition of 67/33, 57/43 and 42/58. The peaks intensity are stronger for the coatings with higher Al composition, which indicates that the intermetallic phases are thicker in the higher Al composition coatings. In addition, hexagonal $ZrAl_2$ structure with the space group of P63/mmc was indexed on the 42/58 CrAl coating. This high Al composition structure was only observed on the highest Al composition coating (42/58 CrAl) in this report.

$AlCr_2$ peaks intensity was indexed for the post-exposure coated samples and the diffracted intensity are slightly shifted to the higher angle. The shift in d-spacing indicates the compressive strain in the coating, which results from either off - stoichiometry or oxygen solution in the coatings. Although Al_2O_3 formation was observed on all CrAl coatings in this report, which will be demonstrate later, the peaks intensity do not appear on the diffraction pattern. This is attribute to the thin layer of the oxide.

Microstructure

(S)TEM/EDS analysis was performed on the cross section of the as-grown and post-exposure of the CrAl coatings at 700 ℃ steam. Two types of second phase intermetallic particles were usually observed in Zircaloy-2, laves phase hexagonal $Zr(Fe,Cr)_2$ with the space group of P63/mmc, and body-centered tetragonal $Zr_2(Fe,Ni)$ with the space group of I4/mcm[4]. Figure 9 shows the TEM cross sectional image of the as-grown 42/58 CrAl coating on Zircaloy-2. Columnar structure of the coating was observed on the coating with the thickness of 1um. CrAl grains are smaller at the coating/substrate interface, and they grow as the film thickens. The average grain size is 100nm approximately at the surface of the coating, which is in an agreement with the SEM plan view image [not shown]. The columnar structure was also observed on the CrAl coatings with different compositions. Three second phase particles are demonstrated in the image. Two of them are attached to each other with one of the being $Zr_2(Fe,Ni)$, and the other being $Zr(Fe,Cr)_2$. The chemical compositions of the particles were measured by STEM/EDS.
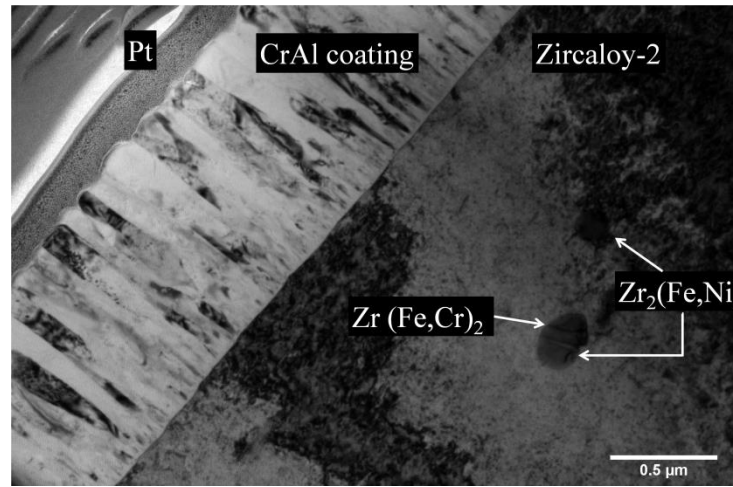
Figure 9. TEM image of as-grown 42/58 CrAl coating on Zircaloy-2. Columnar structure of as-grown CrAl coating is observed. Three second phase particles are observed in the Zircaloy-2 matrix.

Cross sectional STEM analysis on the post-exposed CrAl coated Zircaloy at 700 ℃ steam is shown as following. Figure 10 is the cross sectional image of 42/58 CrAl coating after exposed to 700 ℃ steam for 10 hours. The vertical strips in the images are the artifacts of milling during the sample preparation using Focused Ion Beam. Two layers of Pt were deposited on the surface, ion-Pt layer and electron-Pt layer (e-Pt). The e-Pt layer was deposited to protect the surface oxide of the specimens. Alumina formation was promoted at the surface. Intermetallic layers were developed underneath the coating, and the chemical compositions were measured by EDS. The first intermetallic layer under the coating has the stoichiometry of $Zr(Al,Cr,Fe,Ni)_2$, where Al concentration dominates. This is consistent with the $ZrAl_2$ peak intensity observation in GIXRD in Figure 8B. In addition, this layer was only observed on the cross sectional STEM image of 42/58 CrAl coating, which is in an agreement with the XRD results. The layer below it has a

stoichiometry of Zr_2Al, and no concentration of other elements was observed. And a layer of intermetallic phase with the stoichiometry of $Zr_2(Al,Sn,Fe,Ni)$ was observed between the layer of Zr_2Al and Zircaloy substrate. The total concentration of Al and Sn takes up 21 at%, and the total concentration of Fe and Ni takes up 13 at%, which are approximately equivelant to 2/9 and 1/9 respectively. This corresponds to the $Zr_6(Fe,Ni)(Al,Sn)_2$ formation observed in GIXRD in Figure 8B. What's more, the thickness of the intermetallic phases $Zr_6(Fe,Ni)(Al,Sn)_2$ is the thickest among the three layers of intermetallic phases, which is in a good agreement with its strongest peak intensity observed in the GIXRD.

The total thickness for the layers of intermetallic phases is over 2um. As the coating does not have Iron, Nickel, or Tin, these elements must come from the Zircaloy matrix. Iron and Nickel has limited solubility in Zircaloy, and they exist as the second phase particles $Zr_2(Fe,Ni)$ as mentioned earlier. The intermetallic layers developed after the steam exposure might indicate the decomposition of the secondary phase particles. The intermetallic phase formation was also observed on the CrAl coatings with different compositions, which will be presented below.
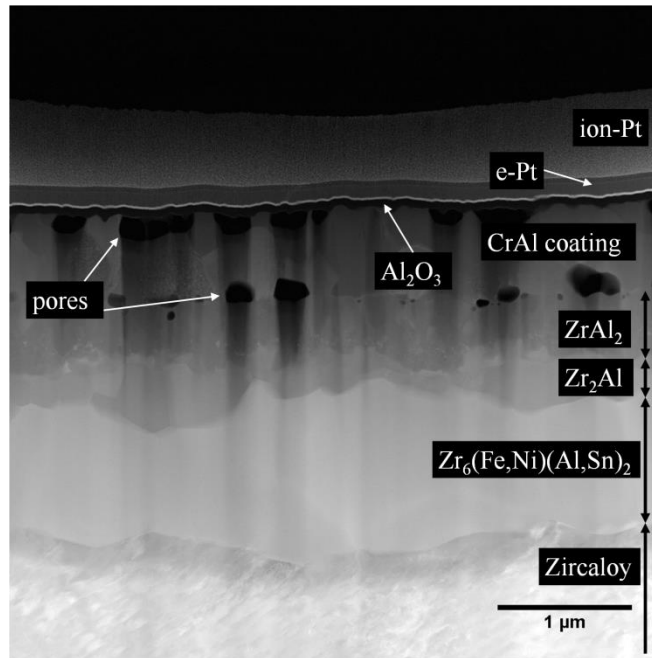
Figure 10. STEM image of 42/58 CrAl after 10 hours exposure under 700 °C steam environment. Layers of intermetallic phases were developed between the CrAl coating and the Zircaloy matrix. Porosity was developed and confined in the coating. Alumina formation was observed on the surface.

Porosity was observed within the coatings, and they are either at the alumina/coating interface or at the coating/intermetallic interface. The porosity at the alumina/coating interface is attributed to the outward growth of the alumina layer. The outward diffusion of Aluminum must be accompanied by a counter flow of vacancies across the alumina/coating interface into the CrAl coating according to the kirkendall effects. The vacancies accumulate at the interface and form pores. This also explains the pores formation at the coatings/intermetallic layer, where Al

diffusion to substrate to form intermetallic phases. It is also noted that the columnar structure in the as-grown coating in Figure 9 transformed into equiaxed grains, and the thickness of the coating reduced to 700nm after the exposure.
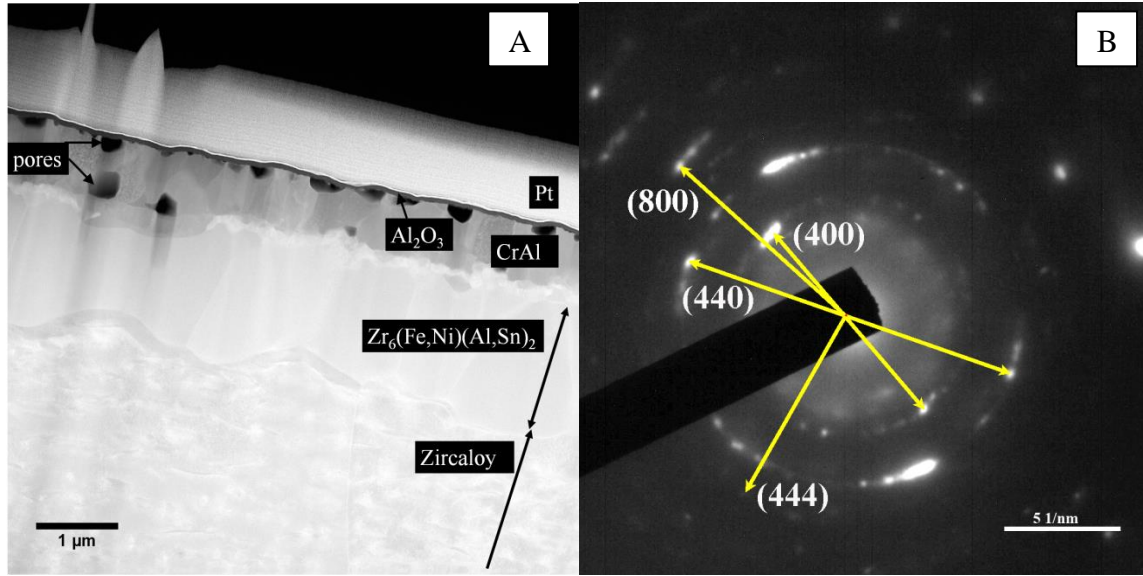

Figure 11. STEM cross sectional image of 57/43 CrAl coating after 20 hours exposure under 700 ºC steam environment, Porosity was developed and confined in the coating. A layer of intermetallic phases with the stoichiometry of $Zr_2(Al,Sn,Fe,Ni)$ was developed under the coatings. Alumina was developed, and it is indexed as γ-Al_2O_3. The SAD pattern is shown in B).

Intermetallic phases were also observed in the CrAl coatings with different compositions. Figure 11A shows the cross sectional STEM image of the 57/43 CrAl coating after 20 hours exposure under 700 ºC steam environment. An 1.5um intermetallic layer with the stoichiometry of $Zr_2(Al,Sn,Fe,Ni)$ was observed. This is corresponding to the $Zr_6(Fe,Ni)(Al,Sn)_2$ peaks intensity in the Figure 8B. There is a layer of the thickness of 100nm between the coating and the layer of $Zr_6(Fe,Ni)(Al,Sn)_2$, which might be attributed to the formation of Zr_2Al from the XRD result in Figure 8B. Similar porosity distribution was also observed within the coating.

The thickness of the alumina developed on 57/43 CrAl coating is 60nm approximately. To identify the structure of the alumina layer, select area diffraction (SAD) was performed on the alumina layer. Although the smallest aperture, 200nm, is larger than the alumina thickness, the selected area was confined to the alumina layer neighboring a pore so that only the diffraction of the alumina phase was shown on the diffraction pattern, without the interference of the CrAl coating. The diffraction pattern is shown in Figure 11B, and it is indexed as cubic structure γ-Al_2O_3 with a space group of Fd-3m. The diffraction rings (instead of diffraction spots) shown in the pattern indicate that the grain size of the alumina is small, probably in the order of 10ns. Although SAD on alumina was only performed for the 57/43 CrAl coating, it is speculated that alumina phase developed on the coatings with other compositions are also γ-Al_2O_3, as similar

oxidation weight gain response was observed under 700 ℃ steam environment. The small grains and the thin layer of γ-Al_2O_3 render it difficult to index in the XRD in Figure 8B.

CrAl coatings with the compositions of 67/33 and 81/19 are the coatings with two lowest Al concentrations in this report, and the cross sectional STEM images are shown in the Figure 12 and Figure 13. Layer of intermetallic phase were also observed on the coatings, although these layers are much thinner, compared to the layers developed in the high Aluminum coating in Figure 10 and Figure 11. In addition to the formation of $Zr_6(Fe,Ni)(Al,Sn)_2$ layer, a layer of the stoichiometry of $Zr(Cr,Fe,Al,Ni)_2$ with Cr dominance was observed between the coating and the $Zr_6(Fe,Ni)(Al,Sn)_2$ layer. Although Zircaloy-2 contain Cr, it is believed that Cr in the intermetallic phase $Zr(Cr,Fe,Al,Ni)_2$ comes at least partially from the coating rather than totally from the second phase particles $Zr(Fe,Cr)_2$ due to the two reasons. First, Cr concentration in $Zr(Cr,Fe,Al,Ni)_2$ is more than twice of Iron concentration, while in the second phase particles $Zr(Fe,Cr)_2$ in an untreated Zircaloy, Chromium concentration is comparable to Iron[4]. Second, the lave phase $Zr(Cr,Fe,Al,Ni)_2$ only develops at the coatings with Cr concentration over 67%. Its preferential formation at high Cr coatings indicates that Cr in the coatings contributes to the formation of $Zr(Cr,Fe,Al,Ni)_2$. The formation of $Zr(Cr,Fe,Al,Ni)_2$ is in agreement with other's observation of $Zr(Fe,Cr)_2$ formation in the FeCrAl/Zr system[5]. However, the layer of $Zr(Cr,Fe,Al,Ni)_2$ is approximately 100nm or less, which renders it difficult to index in XRD pattern in Figure 8B. It is noted that the thickness of the intermetallic phase layers are thicker for the higher Al composition coatings in Figure 10 to Figure 13, this is in an agreement with stronger peaks intensity from the intermetallic phase for high Al composition coating in Figure 8B.

In addition, both Al_2O_3 and Cr_2O_3 formation were observed on 67/33 CrAl and 81/19 CrAl coatings in Figure 12 and Figure 13, with Cr_2O_3 at the top of Al_2O_3. An STEM/EDS analysis was also performed on 81/19 CrAl coating after 1 hour exposure at 700 ℃ steam environment[not shown], and only Cr_2O_3 formation was observed. This indicates that chromia formed initially at 700 ℃ steam environment, and it is likely that when Cr concentration decreased in the coating, alumina started to develop. In addition, alumina formation under the layer of chromia indicates alumina inward growth by oxygen anion diffusing across the layer of Cr_2O_3. Although Cr_2O_3 formation was observed on the 67/33 CrAl coating from the cross sectional STEM image, it is too thin to show up in the XRD pattern in Figure 8B. In contrast, a layer of Cr_2O_3 with the thickness of over 300nm was observed on STEM/EDS image of the 81/19 CrAl coating in Figure 13, and strong peaks intensity of Cr_2O_3 was observed in the XRD measurement in Figure 8B

More importantly, there is no Zirconium oxide formation after 20 hours exposure in 700 ℃ steam environment for CrAl coatings with all tested compositions and for Cr coating, which indicates CrAl and Cr coatings have a better oxidation response in 700 ℃ steam environment than FeCrAl coatings tested in this report, which exhibits ZrO_2 formation at 20 hours in Figure 3H.

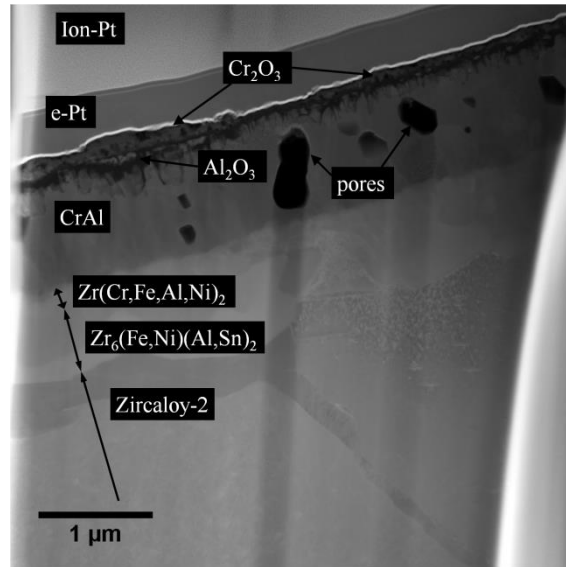Figure 12. STEM cross sectional image of 67/33 CrAl coating after 20 hours exposure under 700 ℃ steam environment. Both Cr_2O_3 and Al_2O_3 were developed. Layers of intermetallic phase $Zr(Cr,Fe,Al,Ni)_2$ and $Zr_2(Al,Sn,Fe,Ni)$ formation were observed.
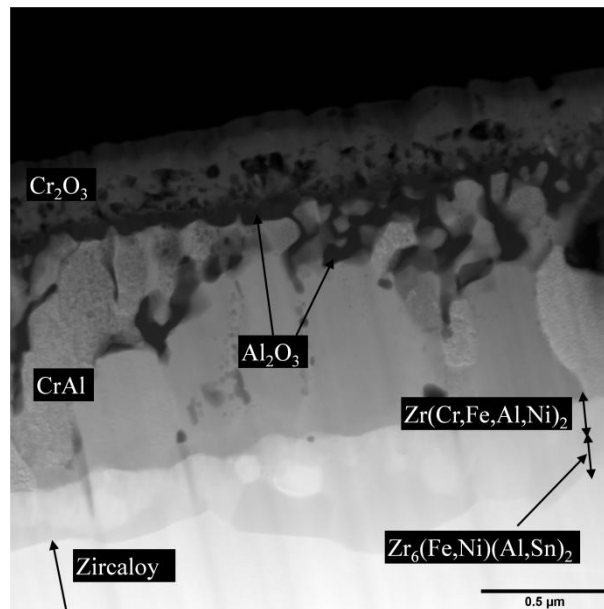

Figure 13. STEM cross sectional image of 81/19 CrAl coating after 20 hours exposure under 700 ℃ steam environment. Al_2O_3 and thick layer of Cr_2O_3 were observed. Layers of intermetallic phase $Zr(Cr,Fe,Al,Ni)_2$ and $Zr_2(Al,Sn,Fe,Ni)$ were observed. The intermetallic layers are thinner than the one formed in the coatings with higher Al composition.

Conclusion

FeCrAl, CrAl and Cr coatings with varying compositions deposited on Zircaloy-2 have been investigated with respect to oxidation weight gain in 700 ℃ steam with the goal of impeding or eliminating rapid oxidation of the base metal. FeCrAl film compositions that promoted alumina formation (Al concentration of 18 atomic percent or higher in this study) significantly reduced oxidation during high-temperature steam exposure. The growth of a near-surface alumina layer was quantified in AES depth profiles and demonstrated parabolic kinetics.

CrAl and Cr coatings demonstrated better oxidation response than FeCrAl coatings. ZrO_2 formation was inhibited for over 20 hours at 700 ℃ steam environment for both CrAl and Cr coatings with the thickness of 1um, while a layer of ZrO_2 with the thickness over 100um was expected to form on an uncoated Zircaloy-2. γ-Al_2O_3 with cubic structure (Fd-3m) was identified on the 57/43 CrAl coating after exposed to 700 ℃ steam. Formation of both Cr_2O_3 and Al_2O_3 was observed on the 67/33 CrAl and 81/19 CrAl coatings at 700 ℃ steam environment for 20 hours. Intermetallic phases were observed on the post-exposed CrAl coated Zircaloy-2 at 700 ℃ steam environment. The combined result of XRD and STEM/EDS give consistent results of the composition and structure formation of the intermetallic phases developed in the 700℃ steam environment. The composition and structure of the intermetallic phase developed at 700 ℃ steam environment depend on the compositions of the coatings.

For oxidation behavior at 1200 ℃, FeCrAl coatings do not provide protection on Zircaloy due to the Fe-Zr eutectic reaction. CrAl and Cr coatings delayed the significant oxidation for 5 minutes. Unfortunately, the subsequent oxidation kinetics is comparable to the uncoated Zircaloy.

Reference

[1] Zhong, Weicheng, et al. "Performance of iron–chromium–aluminum alloy surface coatings on Zircaloy 2 under high-temperature steam and normal BWR operating conditions." Journal of Nuclear Materials 470 (2016): 327-338

[2] Leistikow, S., and S. G. Schanz. "The oxidation behavior of Zircaloy-4 in steam between 600 and 1600° C." Materials and Corrosion 36.3 (1985): 105-116.

[3] Pint, Bruce A., et al. "High temperature oxidation of fuel cladding candidate materials in steam–hydrogen environments." Journal of Nuclear Materials440.1 (2013): 420-427.

[4] Meng, Xianying, and Derek O. Northwood. "Second phase particles in Zircaloy-2." Journal of Nuclear Materials 168.1-2 (1989): 125-136.

[5] Terrani, Kurt A., et al. "Protection of zirconium by alumina-and chromia-forming iron alloys under high-temperature steam exposure." Journal of Nuclear Materials 438.1 (2013): 64-71.

2.2 TEM/STEM study of Zircaloy-2 with protective FeCrAl layers under simulated BWR environment, high-temperature steam exposure, and irradiation

Set up

The FeCrAl coatings with a composition of 62 at% Fe, 4 at% Cr, and 34 at% Al were grown on $10\times10\times1.5mm^3$ Zircaloy-2 coupons using magnetron sputtering at 300 °C in an inert environment with argon working gas. The target was biased at -470V and 90W at the working pressure of 1.6 mTorr. The FeCrAl protective layers were grown for 3 hours at a temperature of 300 ˚C to a thickness of 1.3 microns. The rolled, β-quenched Zircaloy-2 material procured from ATI Specialty Alloys and Compounds.

The autoclave immersion system simulated BWR conditions and consisted of a recirculating Inconel 625 loop that held the temperature at 288 °C, the pressure at 9.5 MPa and maintained a dissolved oxygen concentration of 2ppm. An inlet conductivity of <0.06 μS/cm and an outlet conductivity of <0.15 μS/cm was maintained. The coupons were exposed for 10 days, 20 days, and 40 days. Subsequent steam exposure at 700 °C was conducted using a NEITZCH Jupiter 441 Simultaneous Thermal Analyzer (STA). After sample loading, the system was pumped to 2×10^{-4} Torr and then backfilled with Ar. The system was heated at a rate of 15 °C/minute under a constant of Ar, followed by a 20 minute equilibration hold at 700 °C. The sample was then exposed to steam for 3.6 hours before the system was cooled.

Coupons were irradiated with protons and Fe^{3+} ions using the Tandetron accelerator facility in the Michigan Ion Beam Laboratory (MIBL). Total dose was 6 dpa for proton and 6,12, and 24 for Fe^{3+} ions. The end ranges of irradiation of proton and Fe^{3+} ions were calculated using SRIM code and were about 3μm and 12μm deep from the surface respectively. The temperature was maintained at 360° for each experiment. Table 1 provides details of each coupon such as thickness of the coating layer, exposure/irradiation condition, and analysis performed on each coupon.

To investigate microstructural evolutions of the exposed and/or irradiated coupons, cross sections of each specimen were observed using TEM and scanning transmission electron microscopy (STEM). Electron-transparent TEM specimens were fabricated and bonded to a copper grid using a focused ion beam (FIB) system. The instrument used was a FEI Helios 600i with an acceleration voltage of 30kV and a current of 25pA through 6.5nA. Two TEM instruments were used to investigate the microstructures. A Hitachi 9500 with a LaB_6 electron emission gun to achieve 0.18 nm resolution at an acceleration voltage of 300 kV was used to investigate the morphology by taking bright field (BF) images. Due to the lower limit of area selection of the conventional selected area diffraction (SAD) aperture (approximately 200nm in Hitachi 9500), electron diffraction patterns (DPs) of each nanosized crystals is obtained by nano-area electron diffraction (NAED). When a small condenser aperture is inserted, beam aligning lens can limit a probe size less than several tens nanometers with and focus a parallel transmitted beam on the front focal plane of the objective lens. Diffracted beam from this nano-sized probe smaller than grain size contains crystal information of nano-sized grains. A JEOL 2010F TEM equipped with an Oxford INCA 30 mm ATW detector was used for determination of the chemical composition of post-exposure samples using high angle annular dark field imaging technique (HAADF) and EDS spectra. This (S)TEM operated at 200 kV and used a Schottky field emitter source

Table 1. Sample identification matrix showing coating information, exposure condition, and characterization techniques employed

Sample	Fe/Cr/Al	$T_{coating}$[nm]	Exposure	Time[hr]	Irradiation	Analysis techniques
Zy2-34Al-288C-240h-S*	62/4/34	1200	BWR	240		(S)TEM, SEM, XRD
Zy2-34Al-288C-240h-1	62/4/34	1200	BWR	240		
Zy2-34Al-288C-240h-2	62/4/34	1200	BWR	240		
Zy2-34Al-288C-240h-HTS[†]	62/4/34	1200	BWR→Steam	240→3.6		(S)TEM, SEM, XRD
Zy2-00Al-288C-240h-S*	Uncoated		BWR	240		SEM
Zy2-00Al-288C-240h-1	Uncoated		BWR	240		
Zy2-00Al-288C-240h-2	Uncoated		BWR	240		
Zy2-34Al-288C-480h-S*	62/4/34	1200	BWR	240		(S)TEM
Zy2-34Al-288C-480h-1	62/4/34	1200	BWR	240		SEM, XRD
Zy2-34Al-288C-480h-2	62/4/34	1200	BWR	240		
Zy2-00Al-288C-480h-S*	Uncoated		BWR	240		STEM
Zy2-00Al-288C-480h-1	Uncoated		BWR	240		SEM
Zy2-00Al-288C-480h-2	Uncoated		BWR	240		
Zy2-34Al-288C-960h	62/4/34	1200	BWR	240		
Zy2-00Al-288C-960h	Uncoated		BWR	240		
Zy2-34Al-700C-3.6h	62/4/34	1200	Steam	3.6		(S)TEM, SEM, XRD
Zy2-00Al-700C-10h	Uncoated		Steam	10		
Zy2-34Al-360C-Fe	62/4/34	1200			Fe^{3+} 24dpa	(S)TEM
Zy2-34Al-360C-P	62/4/34	1200			Proton 5dpa	TEM

S* - scratched surface, HTS[†]- high temperature steam

Autoclave Weight Gain

Surface area normalized weight gain data from 10, 20 and 40 days simulated BWR exposure is shown in Fig. 1. The 40 day uncoated weight gain does not follow standard Zircaloy-2 kinetics, likely due to a small ~ 0.02mm^3 fragment breaking off. The 40 days coated sample shows minimal weight gain over the 20 day samples, indicating a passivating layer formation. The weight gain measured for the 10 and 20 days uncoated Zircaloy-2 are in the same range.
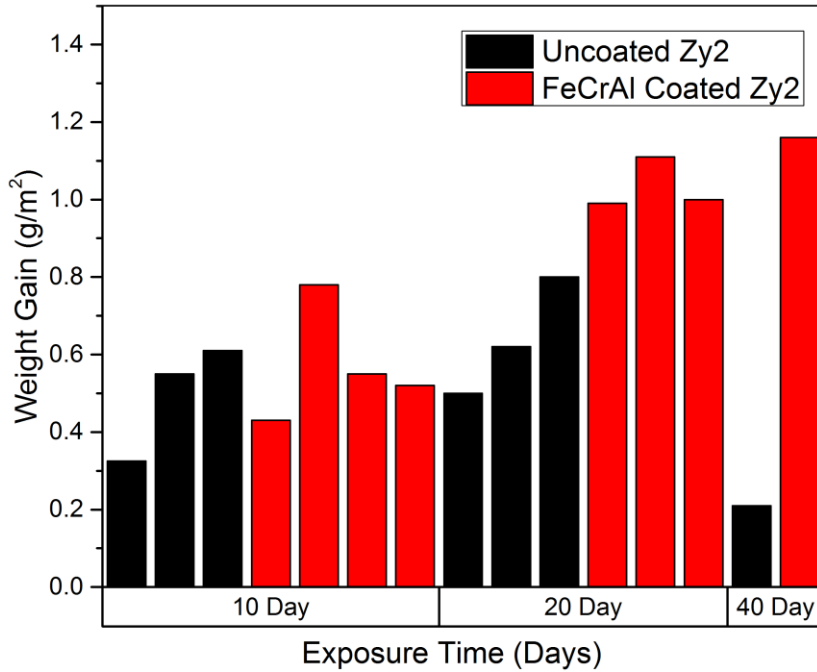

Figure 1: Surface area normalized weight gain data from 10, 20, and 40 day simulated BWR exposed FeCrAl coated, and uncoated Zircaloy-2. Each column represents a different sample. The 40 day uncoated data is not representative of normal behavior.

As received Zircaloy 2 under 20 day simulated BWR exposure

Fig. 2(a) shows a cross-sectional microstructure of Zy2-00Al-288C-480h-S. A dark oxide layer formed on the surface of the uncoated Zircaloy-2 coupon easily identified because of the Z contrast to the bright Zircaloy-2 bulk region. An EDS measurement in this layer shows an oxygen concentration of 52 at%, while no oxygen was present in the Zircaloy matrix. Fine equiaxed oxide grains are typically observed in the outer part of the oxide layer near to the water/oxide interface, and the inner oxide layer consists of large columnar grains growing perpendicular to the oxide/metal interface [1]. Fig. 2(b) shows the oxide layer is divided into two regions of 20nm thick nano-sized small equiaxed grains near the free surface and the columnar grain structure down to the Zircaloy-2 matrix. EDS (not shown) confirmed the elemental composition is uniform throughout the oxide layer. Fig. 2(c) depicts that voids(a bright region in

BF image) are adjacent to intermetallic second phase particles (SPPs). Due to the slower oxidation of SPPs, differences in volume increases near SPPs leads to tensile stress which is relieved by void formation [2-4]. The nanobeam electron DPs of the oxygen rich area with columnar grains in Fig. 2(d) were used to identify monoclinic zirconia, in agreement with previous studies [1, 2, 5, 6]. The thin oxide layer above the columnar grains exhibited ring DPs (not shown) when probed with a 10nm beam. Ring patterns are typically from an amorphous or nano-crystalline region, confirming this layer consists of very fine grains much smaller than the probe size. DPs from the Zircaloy bulk was identified as α-Zr with a= 0.32318nm (PDF 01-089-4791) along the zone axis of ($\bar{3}32$), as indexed in Fig. 2(e). The oxide layer is homogeneous without significant morphology variation except for voids, which are depicted as a dark region in Fig. 2(a).
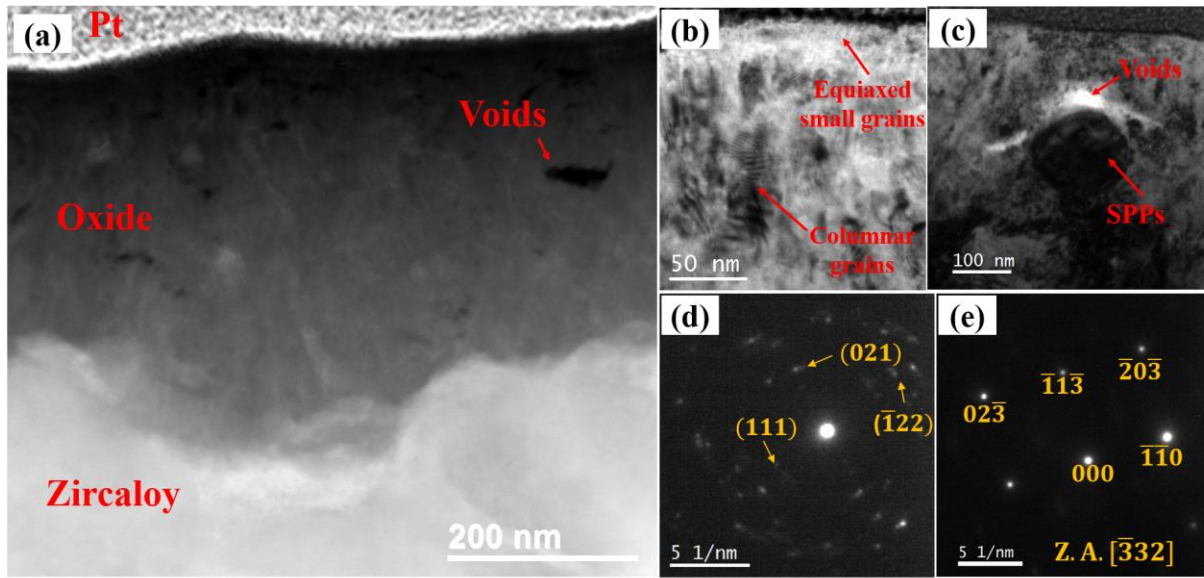
Figure 2. (a)HAADF image of Zy2-00Al-288C-480h-S(as-received Zircaloy-2 coupon after 20 days under simulated BWR environment), (b) BF image of the oxide layer, (c) BF image of the voids adjacent to the SPPs, (d) DPs from the oxide layer, and (e) DPs from the Zircaloy bulk matrix.

FeCrAl Coated Zircaloy-2 under simulated BWR exposure

The HAADF images shown in Fig.3 reveal the microstructural evolution in the FeCrAl coated Zircaloy-2 coupon after 10 day (Zy2-34Al-288C-240h-S) and 20 day (Zy2-34Al-288C-480h-S) simulated BWR exposure. Four distinct layers are observed: (1) Zircaloy-2 substrate, (2) FeCrAl coating, (3) transition layer, and (4) spinel crystals. Columnar grain structures in the FeCrAl coating are evident and grain width ranges from 80 to 100nm. A well-defined interface between the FeCrAl and Zircaloy-2 is maintained for 10 and 20 days with no indication of delamination. The transition layer has an elemental composition rich in Ni, Fe, and O with small concentrations of Cr and Al, as seen in Fig. 4. This layer increases in thickness from 80-100nm after 10 days to 100-200nm after 20 days, while the combined thickness of the FeCrAl and transition layer stays constant at 1200nm. The 1200nm thickness of these combined layers is

consistent with the initial thickness of the coating. This indicates that the transition layer is formed by the inward diffusion of Ni and O from the $NiFe_2O_4$ spinel. No precipitates were observed on the surface of the uncoated sample under simulated BWR exposure. Pyramidal crystallized precipitation with the spinel phase covers the entire surface of the coating.
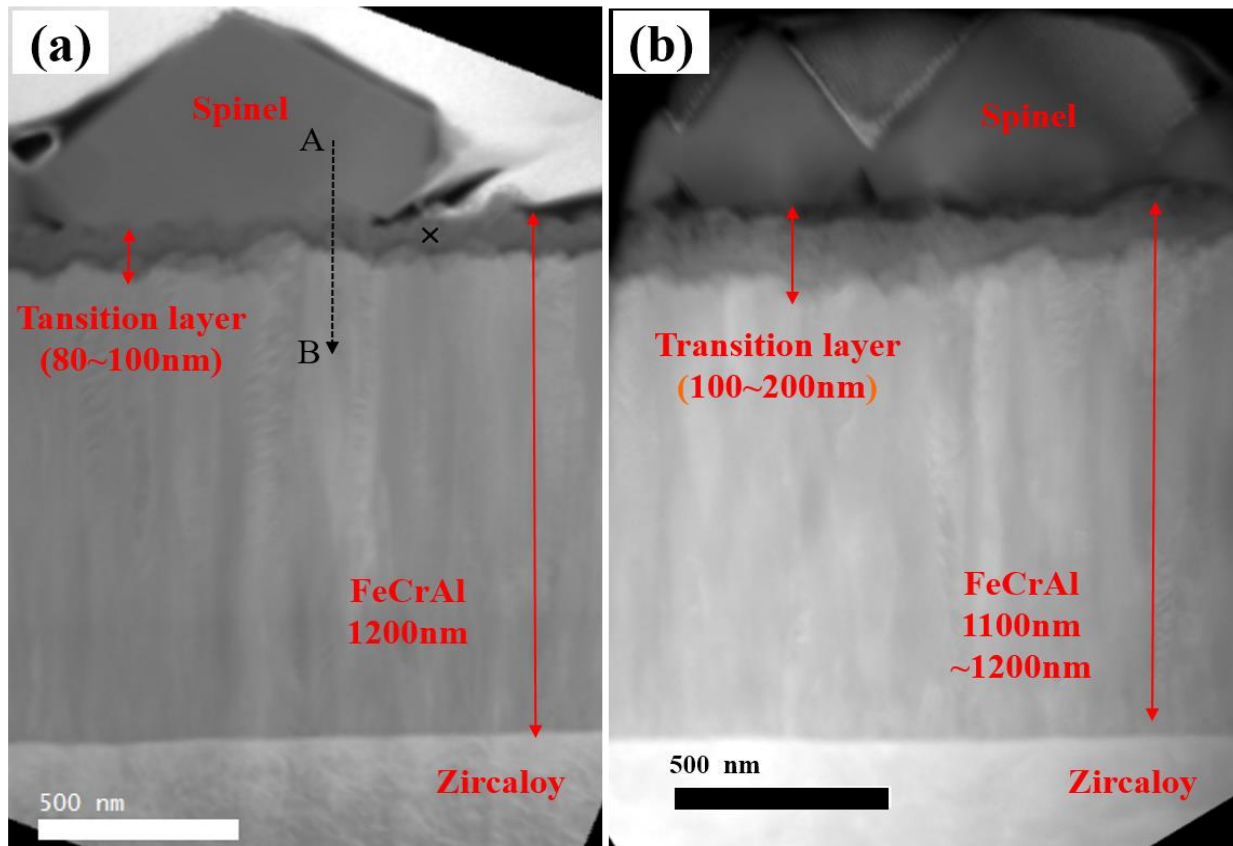

Figure 3. FeCrAl coated Zircaloy-2 under simulated BWR environment : (a)HAADF image of Zy2-34Al-288C-240h-S(10 day); (b)HAADF image of Zy2-34Al-288C-480h-S(20 day). The spinel is precipitated on the exposed surface, and the transition layer forms between the spinel and the FeCrAl layer. A and B are the starting point and the end point of the EDS line scan show in Fig. 4.phases
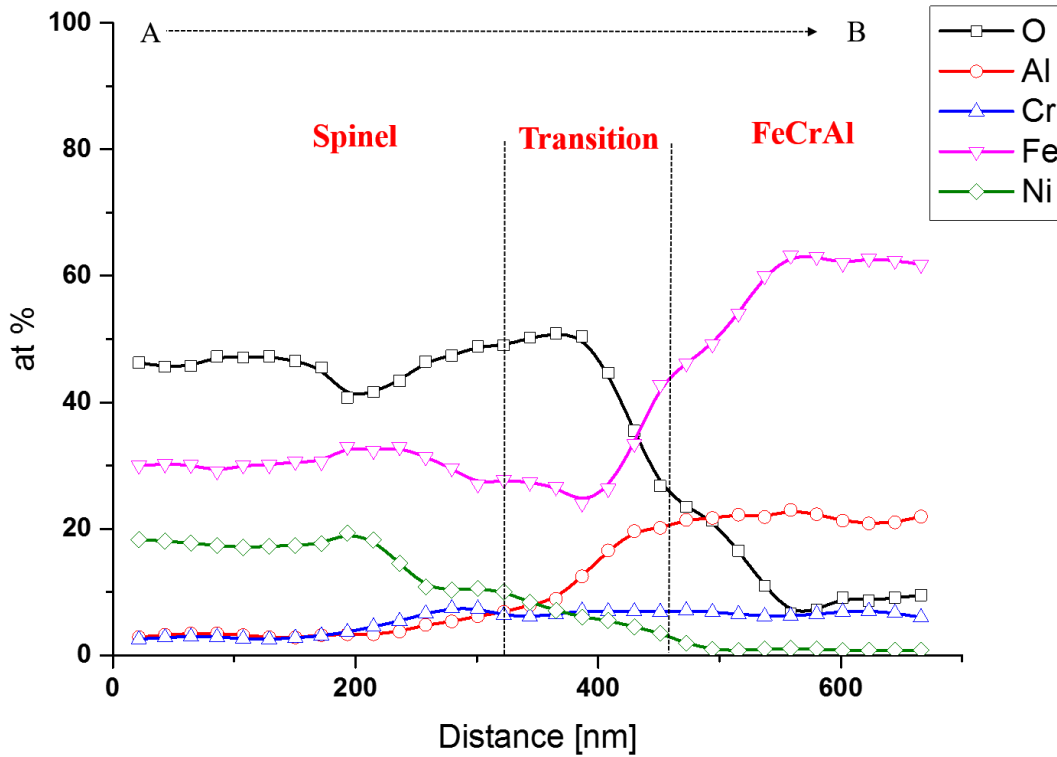
Figure 4. EDS line profile from the spinel (point A) to the FeCrAl layer (point B) of Zy2-34Al-288C-240h-S shown in Fig. 3(a). The transition layer is located between the Spinel and the FeCrAl.

Fig.5 shows the nanobeam electron DPs of the pyramidal spinel structure covering on the top of the transition layer, the transition layer, and the one of FeCrAl grains, respectively. The DPs taken from the pyramidal structure in Fig.5(a) exhibit a diamond cubic structure corresponding to $NiFe_2O_4$ with a lattice parameter a= 0.834nm (PDF 04-002-0637) along the zone axis of ($0\bar{1}1$). Bright, smeared spots in Fig.5(b) suggest the transition layer is nanocrystalline. The diameter of the smallest ring DPs is measured about 8.1 nm^{-1}, the corresponding d-spacing is around 2.47 nm. Several iron- or chromium-based oxide phases are possible with similar d-spacing. We cannot therefore conclusively identify the transition layer phase from the DPs. The DPs of the FeCrAl layer in Fig.5(c) are indexed as a primitive cubic (pm-3m) corresponding to a binary FeAl solid solution phase with a= 0.28854nm (PDF 04-013-9846) along the zone axis of ($\bar{1}1\bar{1}$).
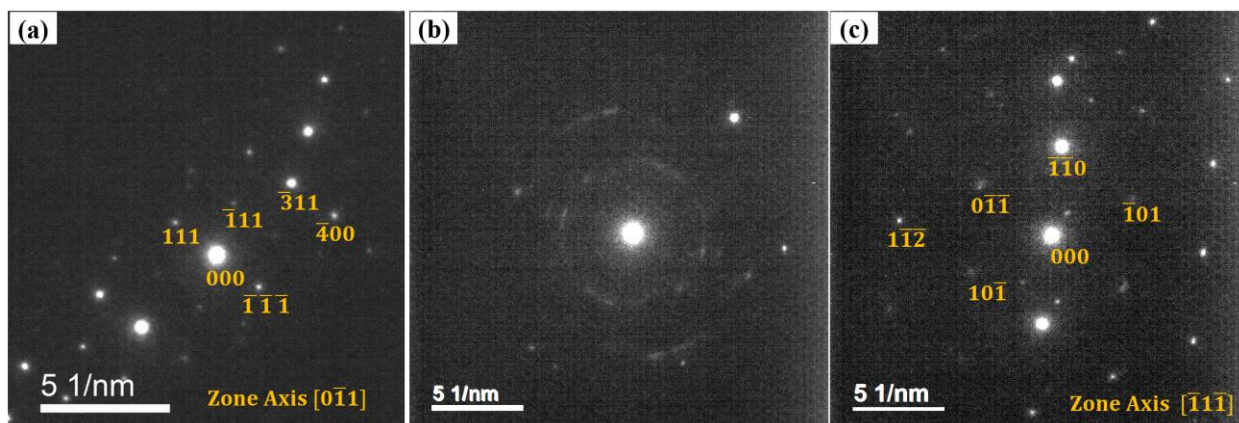
Figure 5. DPs of each layer in Zy2-34Al-288C-240h-S (the FeCrAl coated Zircaloy-2 coupon under 10 day simulated BWR environment) shown in Fig. 3(a): (a) spinel crystal ; (b) transition layer ; (c) FeCrAl coating. (a) is taken at the point A and (c) is taken at the point C. (b) is taken at the point marked as a cross symbol in the center of the transition layer in Fig. 3(a).

The Fe/Cr/Al layer composition measured in EDS after 10 days exposure is 69/7/23 atomic percent and 76/7/17 after 20 days. Compared to the initial composition of Fe/Cr/Al=62/4/34, aluminum was depleted in the FeCrAl layer as the exposure time increased. Aluminum depletion from the bulk alloy during corrosion is widely known. We confirm this in the thin film structure. The transition layer shows an increase in the Cr and Al concentration along with a decrease in the Ni and O compared to spinel layer. The spinel composition from the both samples is consistent with the stoichiometry of $NiFe_2O_4$. An EDS line profile starting from the spinel crystal and traversing through the FeCrAl layer in the 10 day exposed sample was conducted to show the composition variation. The results are shown in Fig.4. The position of the line scanning is marked as a starting point A and an end point B in Fig.3(a). The composition is relatively uniform across the spinel crystals and the FeCrAl coating, and the composition varies across the transition layer. Nickel in the spinel structure originates from the Inconel autoclave loop.

FeCrAl Coated Zircaloy-2 under steam exposure

TEM and STEM were used to investigate the compositional changes that occurred in an as-grown and 10 day autoclave exposed sample after 700°C steam exposures for 3.6 hours. Bright field images of the as-grown coupon (Zy2-34Al-700C-3.6h) are shown in Fig.6, and HAADF images of the autoclave exposed coupon (Zy2-34Al-288C-240h-HTS) are shown in Fig.7. Zy2-34Al-700C-3.6h exhibits the expected changes due to steam exposure. The top layer in Fig. 6(a) has a measured thickness of 100 nm and a stoichiometric alumina composition as shown in Table 2. XRD identified the surface oxide as α-alumina. From the cross-section view, the alumina layer is observed to be uniform, without voids or pores. The EDS mapping in Fig.8, from the yellow box in Fig. 6(a), shows the distribution of each element across the interface between the alumina layer and the FeCrAl layer in bulk Zr. Iron and Cr are depleted in the

22

alumina layer in Fig.8. Therefore, Al diffuses outward to form the oxide layer. The outward growth of oxide layer is also reported in other publications [7,8]. In Zy2-34Al-288C-240h-HTS, the alumina layer formed between the spinel crystals and the FeCrAl coating as shown in Fig.7(a) and (b). Fig.9 shows the elemental line profile orthogonal to the exposed surface and illustrates the location of the 100 nm thick aluminum rich layer. The alumina layer is identified by an Al peak and suppression of Fe and Cr. Diffraction patterns could not be obtained using TEM because of the small thickness of the layer. Glancing angle diffraction at increasing angles, shown in Fig.10, shows that the phase below the spinel is α-alumina.
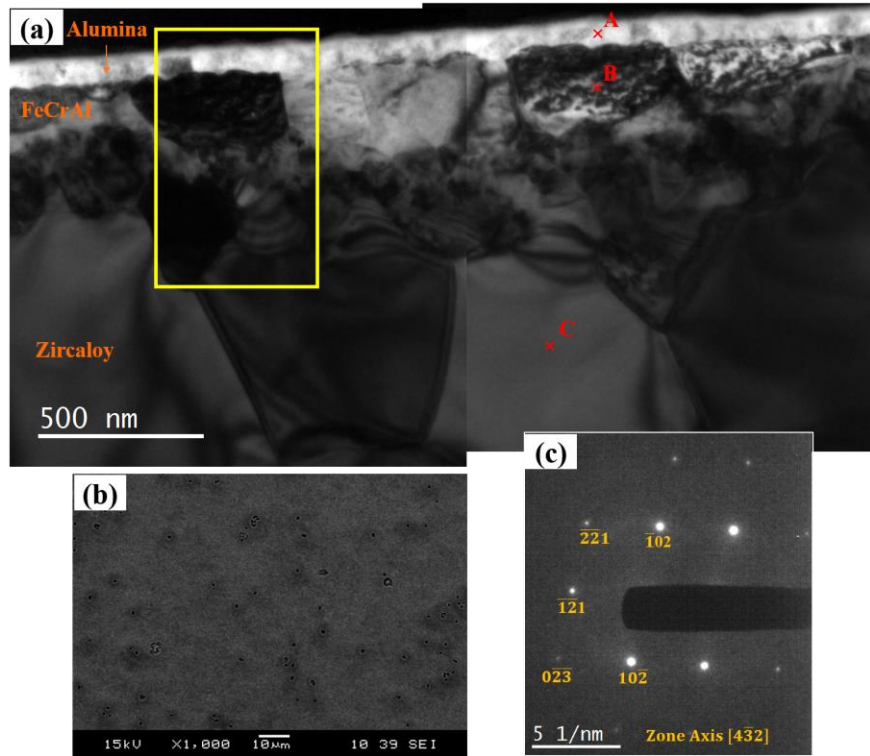
Figure 6. (a)Cross-sectional BF image and (b)plan-view SEM image of the FeCrAl coated Zircaloy-2 coupon after 3.6 hr HTS (Zy2-34Al-700C-3.6h). (c) DPs taken from the FeCrAl layer. HTS exposure resulted in the formation of the alumina layer on the exposed surface and the porosity within the film. EDS measurements from points A, B, and C are shown in Table 2. EDS mapping results within the yellow box is shown in Fig. 8.

The formation of aluminum oxide leads to a variation in the composition and morphology of the FeCrAl layer. Fig.7 shows the presence of large pores within the FeCrAl layer. Although pores are not seen in the cross-sectional image of Fig.6 (a), they were observed in plan view SEM image in Fig. 6(b). Both samples exhibit an increase in the Cr concentration of the FeCrAl layer; the Cr concentration increased from 7 at% in the as-coated sample to 26 at% in Zy2-34Al-700C-3.6h and 14 at% in Zy2-34Al-288C-240h-HTS as shown in Fig.4, Table 2, and Table 3 respectively. While Al and Fe diffuse into the surface and the Zircaloy matrix respectively, as shown in Fig.7, Cr has a relatively low concentration in the Zircaloy matrix. Fig.8 shows that the

Cr segregation is uniform across the thickness of the FeCrAl layer, and this resulted in the formation of ternary intermetallic phase that is indexed to a primitive cubic (pm-3m) $Fe_2(CrAl)$ with lattice parameter a= 0.5811nm (PDF 04-016-4676) (Fig.6(c)).
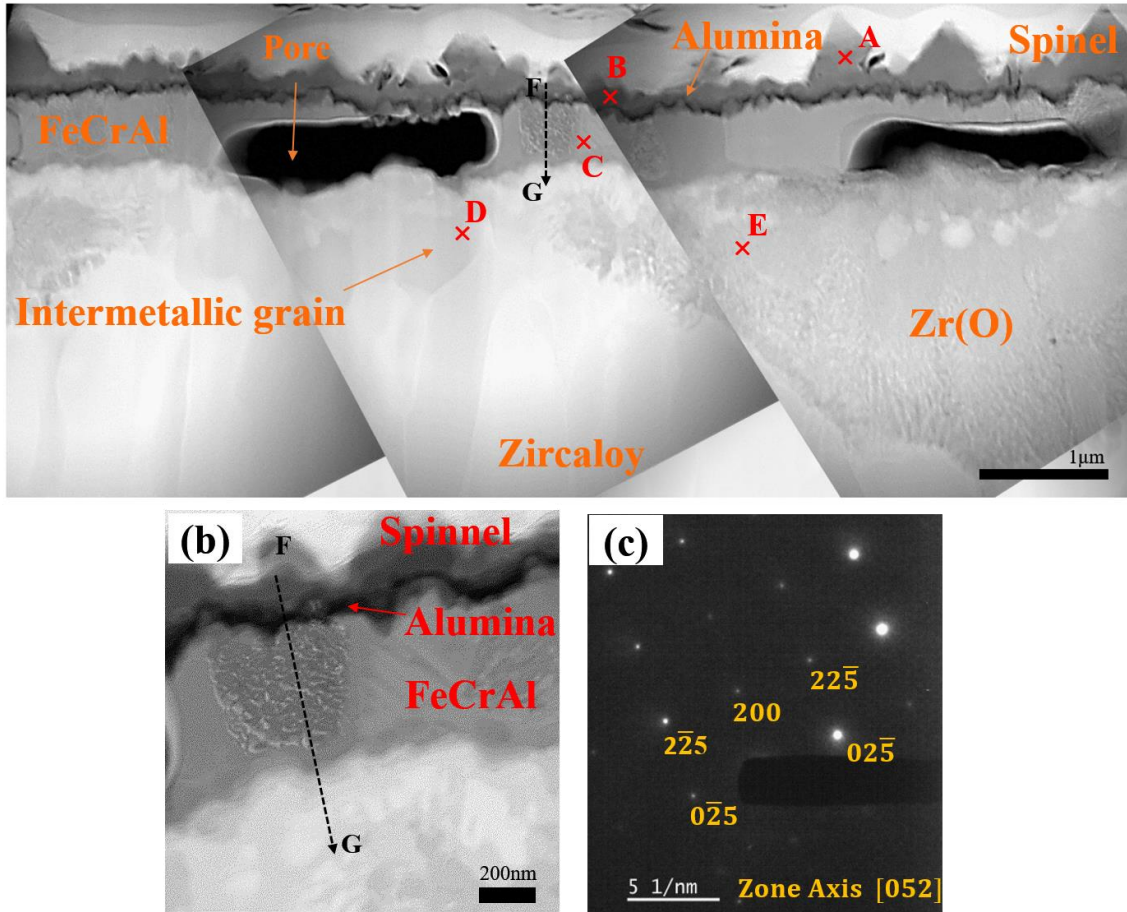

Figure 7. (a)Cross-section HAADF image of the FeCrAl coated Zircaloy-2 after 10 day sim- ulated BWR environment exposure and 3.6h steam exposure (Zy2-34Al-288C-240h-HTS) (b) Magnified HAADF image of the interfaces (c) DPs taken from the intermetallic grain, indexed as Zr_3Fe. EDS data from points A, B, C, D, and E are shown in Table 3. F and G are the starting point and the end point of the EDS line scan shown in Fig. 9.

Cross-sectional images show the film consumption and the grain growth in the FeCrAl coating after HTS exposure. The thickness of the as-grown FeCrAl coating was 900nm. After HTS exposure, the coating/substrate interface becomes wavy, and the thickness varied from 150 to 600nm in Zy2-34Al-700C-3.6h (Fig. 6(a)). In the Zy2-34Al-288C-240h-HTS sample in Fig. 7(a), the initial thickness of 1200 nm FeCrAl layer decreased to 600 nm. From the depletion of nickel throughout the FeCrAl layer (Fig.9), we confirm that the transition layer, which had 12 at% nickel when it developed during the simulated BWR exposure, was entirely consumed by the steam exposure. A protective alumina scale with a thickness of 100nm developed after 50% consumption of the FeCrAl film. Grain growth within the FeCrAl film is also observed. The grain size increases from 100nm to hundreds of nanometer after 3.6 hours post-autoclave exposure.

Table 2. Element concentrations in atomic percent for each layer of the FeCrAl coated Zircaloy-2 after 3.6 hr steam exposure (Zy2-34Al-700C-3.6h, Measuring positions are shown in Fig. 6)

Position	Layer	Zr	Fe	Cr	Al	O
A	Alumina	-	-	-	55	45
B	FeCrAl	-	45	26	30	-
C	Zircaloy	70	12	1	17	-

Table 3. Element concentrations in at% for each layer of FeCrAl coated Zircaloy-2 after 10 day autoclave exposure and 3.6 hr steam exposure (Zy2-34Al-288C-240h-HTS, Measuring positions are shown in Fig. 7)

Position	Layer	Zr	Fe	Cr	Al	Ni	O
A	Spinel	-	36	3	6	15	40
B	Alumina	-	3	6	46	-	45
C	FeCrAl	-	58	14	28	-	-
D	Intermetallic	44	40	3	13	-	-
E	Zr(O)	55	9	-	13	-	23

Fig. 7(a) shows that the initial Zircaloy-2 matrix near the FeCrAl layer evolves into two different regions with distinct contrast after the autoclave exposure and the subsequent steam exposure. A Zircaloy region with high oxygen solubility, confirmed by the EDS measurement in Table 3, grew to 3 um in thickness, but did not form a continuous stoichiometric zirconia layer. Weak ring DPs (not shown) from this phase are consistent with fine grains. Since zirconia had formed after 20 hours of HTS exposure and for long steam exposure times in steam exposure on other coupons, these nano-sized grains would be oxidized to form a stoichiometric zirconia layer if steam exposure extends. Zirconia was not observed in Zy2-34Al-700C-3.6h (steam exposure only). This implies that the zirconia formation in the FeCrAl coated Zircaloy-2 exposed to the steam is not uniform and requires exposure longer than ~ 4 hours and depends on FeCrAl layer thickness. The presence of Fe and Al in the Zircaloy, observed in Fig.9, led to the formation of Zr_3 and Zr_6FeAl_2 intermetallic phases, identified in XRD measurement in Fig.10. These intermetallic precipitates grew to 300nm in diameter. One of the binary Zr_3Fe grains was indexed to the Fd-3m space group as shown in Fig.7(c).
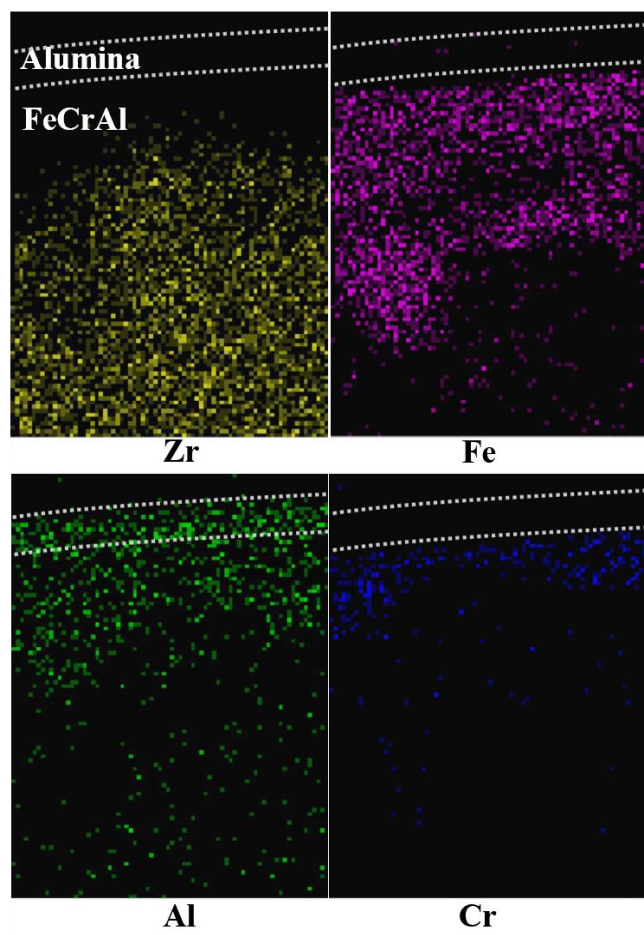
Figure 8. EDS element mapping results in the FeCrAl coated Zircaloy-2 after 3.6h HTS (Zy2-34Al-700C-3.6h). Maps are measured within the region labelled by the yellow box in Fig. 6. The distributions of Zr, Fe, and Cr are confined to the FeCrAl layer and are not observed in the alumina layer(white dotted lines). Oxygen mapping is not shown because of poor sensitivity.
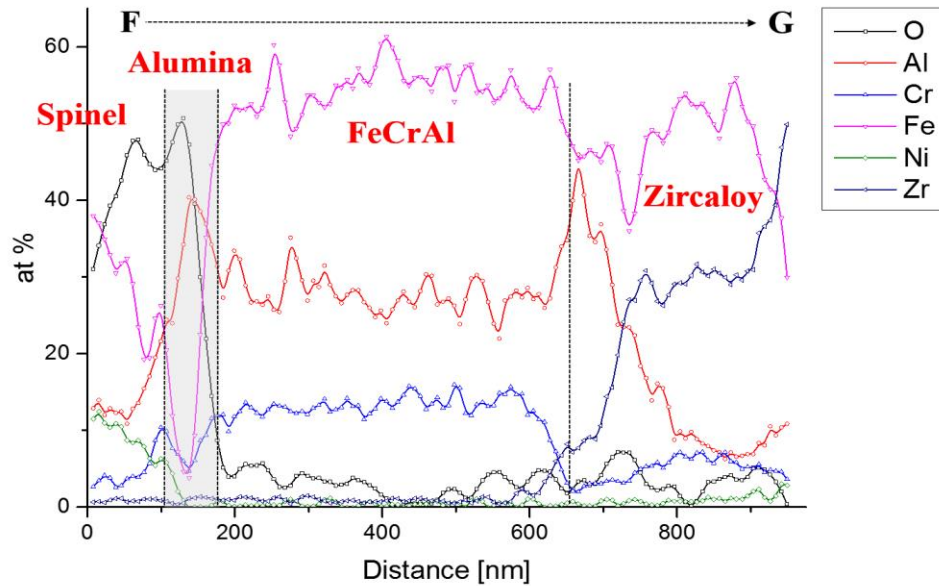
Figure 9. EDS line profile after 10 day simulated BWR environment exposure and 3.6h steam exposure (Zy2-34Al-288C-240h-HTS). It is measured from the spinel (point F) through the Zircaloy-2 bulk (point G) as identified in Fig. 7. The alumina layer is observed between the spinel and the FeCrAl layer. Iron and Al are observed in the Zircaloy-2 below the FeCrAl layer.
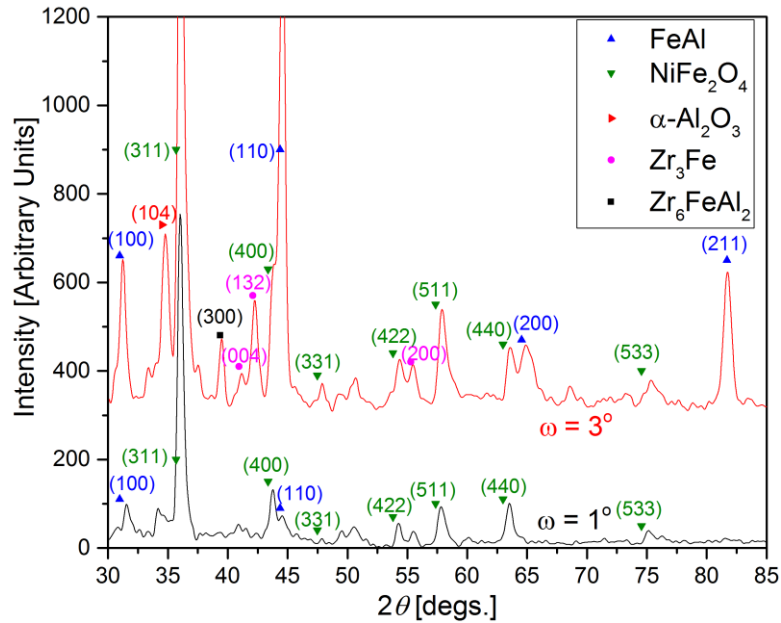
Figure 10. Glancing angle XRD at fixed omega values of a coated 10 day autoclave sample after 3.6h 700_C exposure (Zy2-34Al-288C-240h-HTS). The bottom spectrum is ω fixed at 1°. The spinel layer dominates the spectrum. The top spectrum is is ω fixed at 3°. The peaks of the spinel crystals are suppressed. The signal of the FeCrAl layer and Zr based intermetallics are revealed at is ω=3°. In addition, the (104) reflection from α-Al2O3 is observed at ω = 3°.

A schematic illustration of a process thought to govern the response of the FeCrAl-Zry system during autoclave and HTS exposure is shown in Fig.11. Dissolved Ni in the autoclave loop interacts with Fe from the FeCrAl coating, and precipitates out as spinel crystals on the top of the FeCrAl coating. High temperature steam reacts with the FeCrAl coating layer and the outer layer of the coating is consumed. Aluminum diffuses outward to form a protective uniform alumina layer. The counter flow of vacancies in response to the Al diffusion results in a porosity in the FeCrAl coating. Localized inward oxygen diffusion is attributed to the formation of a zirconia layer. Inward diffusing Fe and Al reacts with Zircaloy-2 matrix to form binary or ternary intermetallic particles.
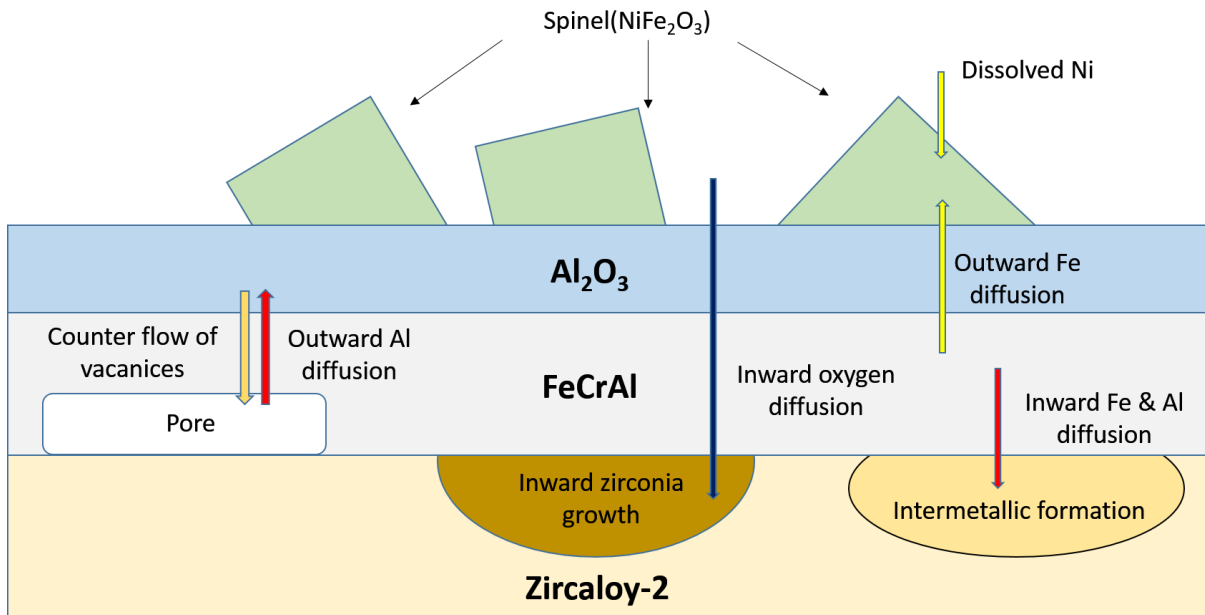
Figure 11. Schematic of the kinetics of the FeCrAl coated Zircaloy-2 under the simulated BWR environment and the steam exposure. This schematic is based on a similar schematic in [9].

Irradiated FeCrAl Coated Zircaloy-2

1 MeV protons and 8.5MeV Fe ions are irradiated to examine stability of the deposited film. BF images shown in Fig.12 reveal a microstructural morphology in the FeCrAl coated Zircaloy-2 coupon after proton irradiation (Zy2-34Al-360C-P) and (b) Fe^{3+} irradiation (Zy2-34Al-360C-Fe). As seen in Fig.12, we cannot observe any changes in morphology except for the interface with discrete contrast. Compared to the interface of the un-irradiated sample shown in Fig.3, the interface is around 30nm thick and darker than the adjacent Zircaloy layer. EDS line profile in Fig.13 shows a ratio of Fe/Cr/Al after irradiation is similar to as-deposited FeCrAl film. While distribution of each element does not vary throughout the film, Cr segregation at the interface between the FeCrAl layer and the Zircaloy matrix was confirmed from the Cr peak in the interface of the irradiated one. Since similar Cr peak(not shown here) is also found in

unirradiated region of the identical sample (Zy2-34Al-360C-Fe), the elevated temperature, 360°C, during irradiation is thought to lead Cr segregation in the interface.
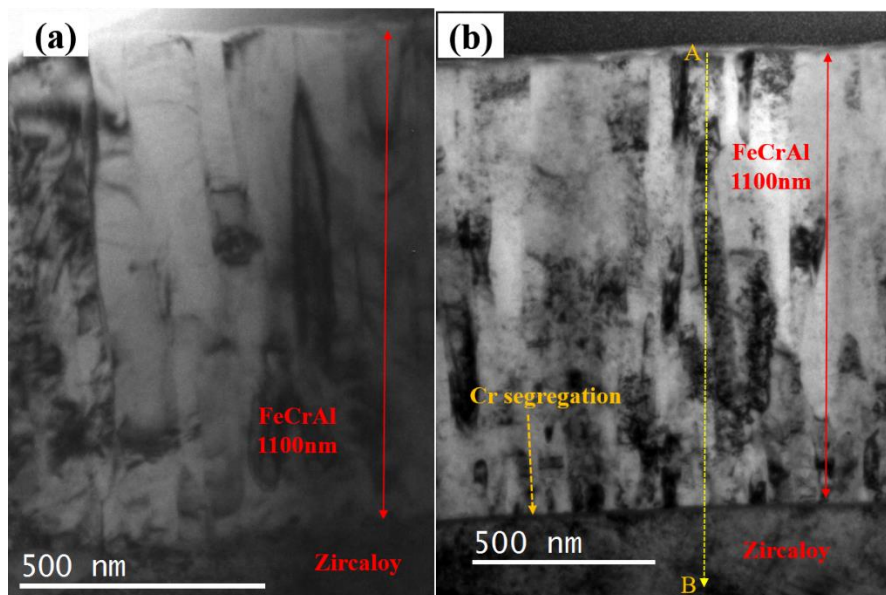

Figure 12. Cross-sectional BF images of irradiated FeCrAl coated Zircaloy-2 : (a) proton irradiated (Zy2-34Al-360C-P); (b) Fe^{3+} irradiated (Zy2-34Al-360C-Fe). Morphological variation is not observed. A and B are the starting point and the end point of the EDS line scan show in Fig. 13
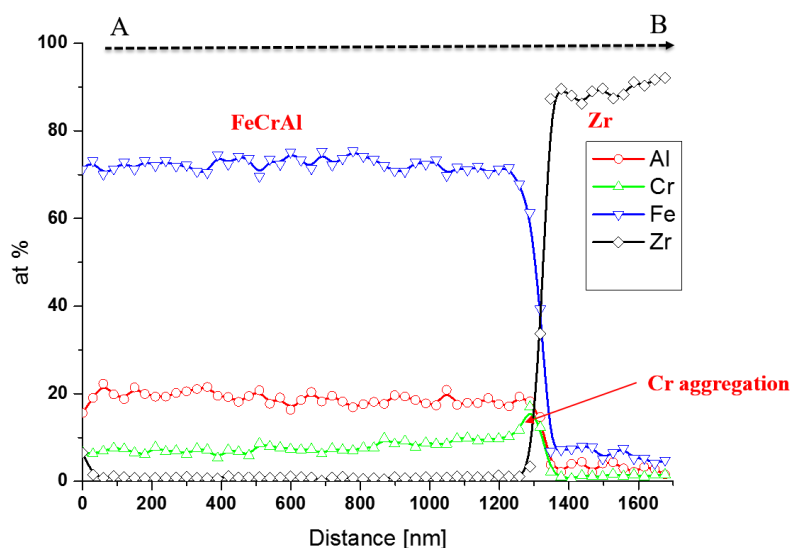

Figure 13. EDS line profile from the FeCrAl (point A) to the Zircaloy bulk (point B) of Zy2-34Al-360C-Fe shown in Fig. 12. The Cr peak is observed in the interface between the FeCrAl film and the Zircaloy substrate

While we didn't observe any iron precipitation or induced second metallic compounds in Fe^{3+} irradiated sample, hydrides are found in proton irradiated sample. Fig. 14 shows DPs taken with the zone axis of ($1\bar{1}0$). Periodic DPs were indexed as α-Zr with a= 0.32318nm (PDF 01-089-4791) from the Zircaloy bulk. Distinct diffraction pattern is observed near ($1\bar{1}0$) diffraction of α-Zr and is identified as δ-ZrH (200) with a= 0.4781nm (PDF 00-034-0649).
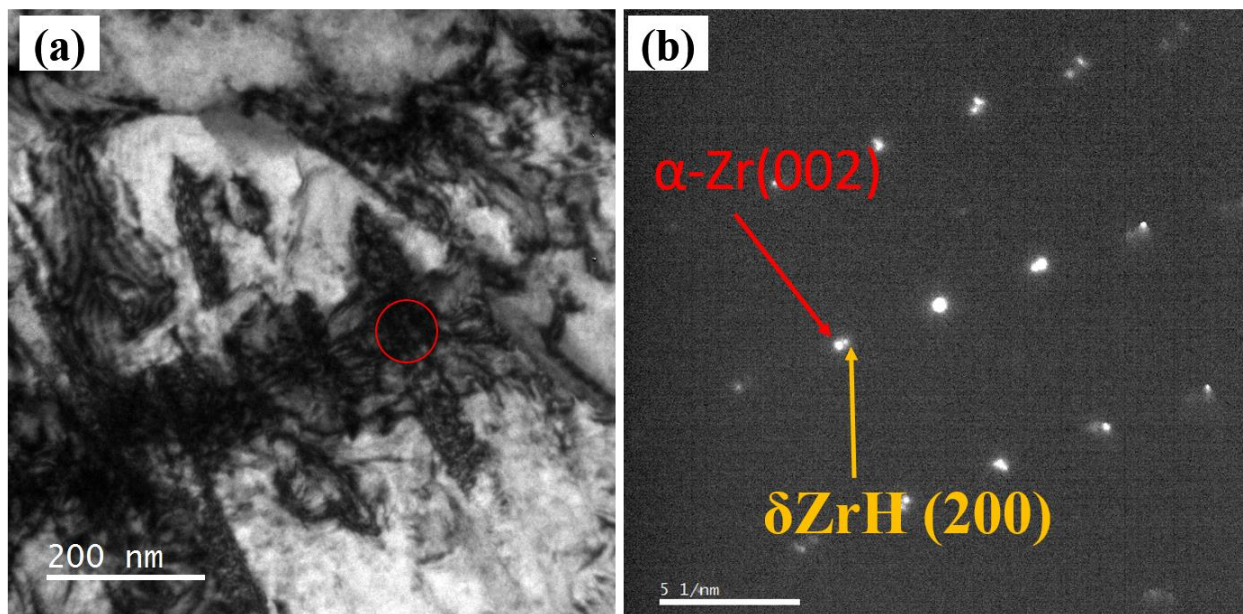
Figure 14. (a) BF image of the Zircaloy bulk near the end range of proton irradiation (Zy2-34-Al-360C-P) that is around 12 um oxide layer (b) DPs from the hydride marked in red circle

[1] S. Nanikawa, Y. Etoh, "The effect of oxide microstructure on kinetic transition in out-of-pile steam corrosion test for zircaloy-2 and nb-added zircaloy-2", Journal of nuclear science and technology 38 (6) (2001) 420-428.

[2] A. Yilmazbayhan, E. Breval, A. T. Motta, R. J. Comstock, "Transmission electron microscopy examination of oxide layers formed on Zr alloys", Journal of Nuclear Materials 349 (3) (2006) 265-281.

[3] P. Tejland, M. Thuvander, H.-O. Andrén, S. Ciurea, T. Andersson, M. Dahlbäck, L. Hallstadius, "Detailed analysis of the microstructure of the metal/oxide interface region in zircaloy-2 after autoclave corrosion testing", in: Zirconium in the Nuclear Industry: 16th International Symposium, ASTM International, 2012.

[4] P. Bossis, G. Lelievre, P. Barberis, X. Iltis, F. Lefebvre, "Multi-scale characterization of the metal-oxide interface of zirconium alloys", in: Zirconium in the Nuclear Industry: Twelfth International Symposium, ASTM International, 2000.

[5] B. de Gabory, A. T. Motta, K. Wang, "Transmission electron microscopy characterization of zircaloy-4 and ZIRLO oxide layers", Journal of Nuclear Materials 456 (2015) 272-280.

[6] M. Oskarsson, E. Ahlberg, K. Pettersson, "Oxidation of zircaloy-2 and zircaloy-4 in water and lithiated water at 360°C", Journal of nuclear materials 295 (1) (2001) 97-108.

[7] K. A. Terrani, S. J. Zinkle, L. L. Snead, "Advanced oxidation-resistant iron based alloys for LWR fuel cladding", Journal of Nuclear Materials 448 (1) (2014) 420-435.

[8] D. J. Park, H. G. Kim, J. Y. Park, Y. I. Jung, J. H. Park, Y. H. Koo, "A study of the oxidation of FeCrAl alloy in pressurized water and high temperature steam environment", Corrosion Science 94 (2015) 459-465.

[9] K. Terrani, B. Pint, Y.-J. Kim, K. Unocic, Y. Yang, C. Silva, H. Meyer, R. Rebak, "Uniform corrosion of FeCrAl alloys in LWR coolant environments", Journal of Nuclear Materials 479 (2016) 36-47.

2.3 Zirconium-Yttrium Alloys

Microscopy

Zirconium-Yttrium alloys containing 0.01, 0.1, 0.5, 1, 2, and 12 wt% yttrium were cast by ATI. The equilibrium Y solubility in Zr is very small, with only 0.4 at% in solution at 800^{oC} [1]. However recent research has found that cast Zr-Y alloys have an extended solid solution solubility of up to 3% [2]. Chemical etching followed by optical microscopy, along with EDS analysis in SEM was performed to determine the microstructure. The etching solution used contained sulfuric acid which aggressively attacks Y [3], allowing for contrast in regions of high Y. Due to the similarity of the characteristic X-ray spectra of Zr and Y, only large Y precipitants could be seen in the SEM. It was found that the Y phase preferentially nucleated at grain boundaries, with only the 12% sample exhibiting intragranular Y phase formation in lines and spheroids as seen in Figure 1. At 2 wt% slight pitting was observed at the grain boundaries indicating the possibility of Y phase formation, however no Y peaks were seen in diffraction of the as received material. The lack
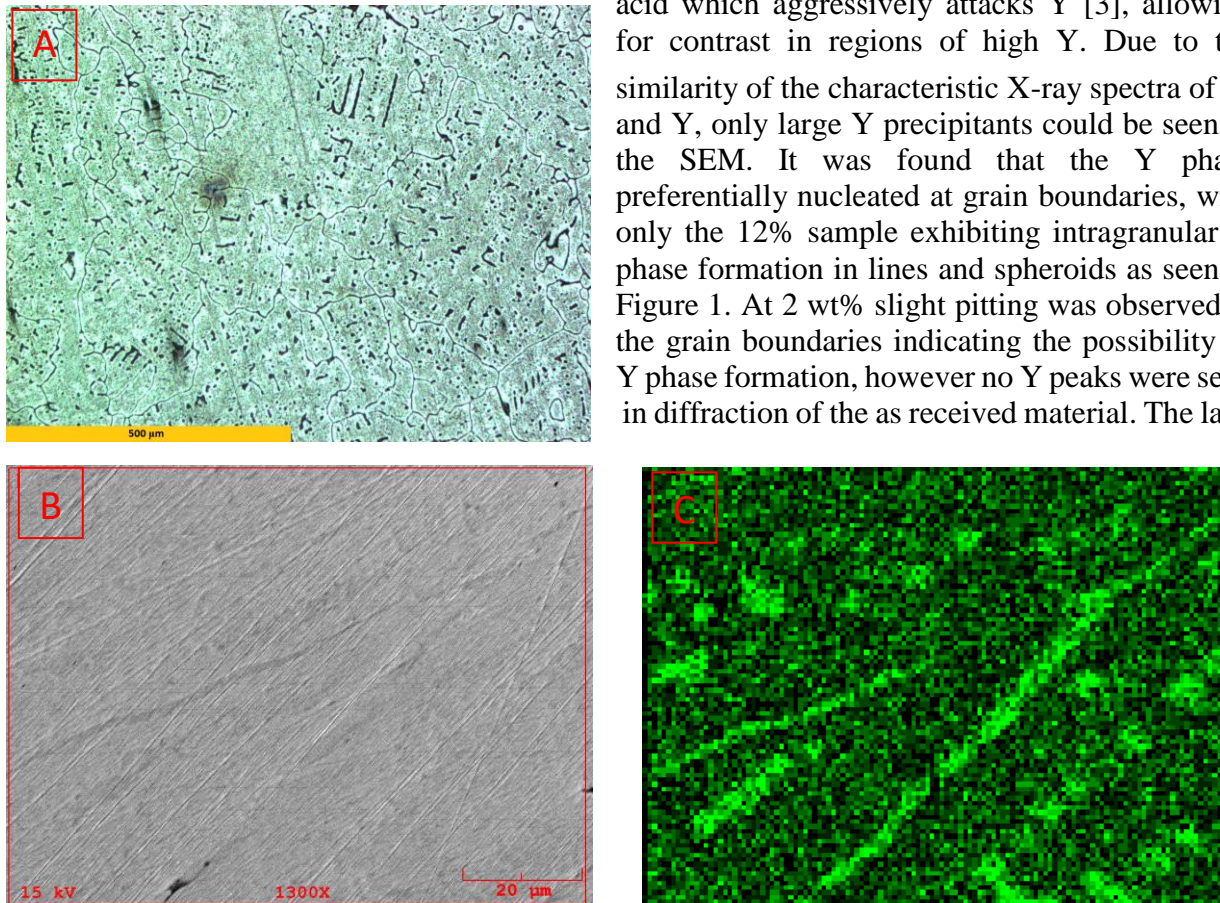
Figure 1. Microscopy of 12 wt% Y material as received. A) Optical image after etching. The regions represent Y rich regions that were preferentially attacked. B) SEM secondary electron of polished 12 wt% Y. C) EDS map showing Y intensity of the region shown in B. Yttrium enrichment along a grain boundary in the center, as well as multiple spheroids shows the formation of α-Y.

of large Y phase formation in the 2 wt% is in agreement with the extended solid solution solubility previously observed [2]. Yttrium diffraction was seen in the 2 wt% sample after a 30 minute 700^{oC} steam exposure. This is due to the nucleation of Y precipitates due to the associated aging while the sample was at an elevated temperature. The grain structure of the as received material formed during cooling is non-uniform with grain sizes ranging from 10 to 500 μm in size. Additionally, dendritic structures associated with cast cooling were observed. These six concentrations cover a range of single and two phase morphologies, focusing on the solid solution regions.

Kinetics

Coupons 1mm x 10mm x 10mm were oxidized in steam at 500^{oC}, 700^{oC}, 900^{oC}, and 1100^{oC}. It was consistently seen that the addition of Y was detrimental to the oxidation kinetics at high temperatures. At 700^{oC}, low Y concentrations resulted in parabolic kinetics as seen in Figure 2. Comparing the 0.01% and 0.1% to Zirconium foil obtained from Alpha Aesar it can be seen that at these low concentrations, there is a minimal effect on the kinetics. The 0.01% showed less weight gain than the Alpha Aesar Zr, most likely due to the Zr at ATI being nuclear grade which includes the removal of hafnium. Alpha Aesar did not quote the exact concentration of hafnium. Starting after the 0.5% Y, cyclic oxidation occurs. The 1% and 2% Y samples exhibit long cycles, with only two occurring during the 10 hours exposure. The breakaway kinetics seen in Zircaloy-2 was not observed indicating that the oxides formed on the Zr-Y samples have greater mechanical stability, even though cycling does occur. The yttrium does increase the diffusion rate of the oxygen through the oxides as seen in Figure 2 by the increased weight gain at shorter time periods. However, the linear kinetics of Zircaloy-2 eventually lead to greater weight gain.

At 500^{oC}, the addition of Y still increased the oxidation rate, only without the presence of cyclic behavior in the 1 wt% Y sample over the 20 hours exposure. The kinetics transition from being parabolic at 0.01% to cubic at 1%. As with 700^{oC}, the addition of Y leads to faster oxygen diffusion through the oxide, an effect is not as pronounced at 1100^{oC}. Additionally, no cycling was observed. One 0.5% coupon was exposed at 350^{oC} for 30 hours. Linear break away kinetics developed after one hour, consistently increasing the weight of the sample at a rate of 0.014038 g/m^2 per minute for the rest of the 29 hour exposure.

Figure 2. Weight gain data from steam exposure at A) 700^{oC} and B) 500^{oC}.

Diffraction

Powder Diffraction

Powder diffraction samples were created from 0.01, 0.5, 2, and 12 wt% Y samples at 700^{0C} and 1100^{oC}. These samples were run in a Siemens/Bruker D-5000. The results were analyzed using GSAS. The monoclinic phases of zirconia were observed in all results, while yttria was only strongly seen in the 2% and 12% samples. Due to the intensity of the device, the yttria peaks for the 0.5 wt% sample were nearly indistinguishable from the background. The
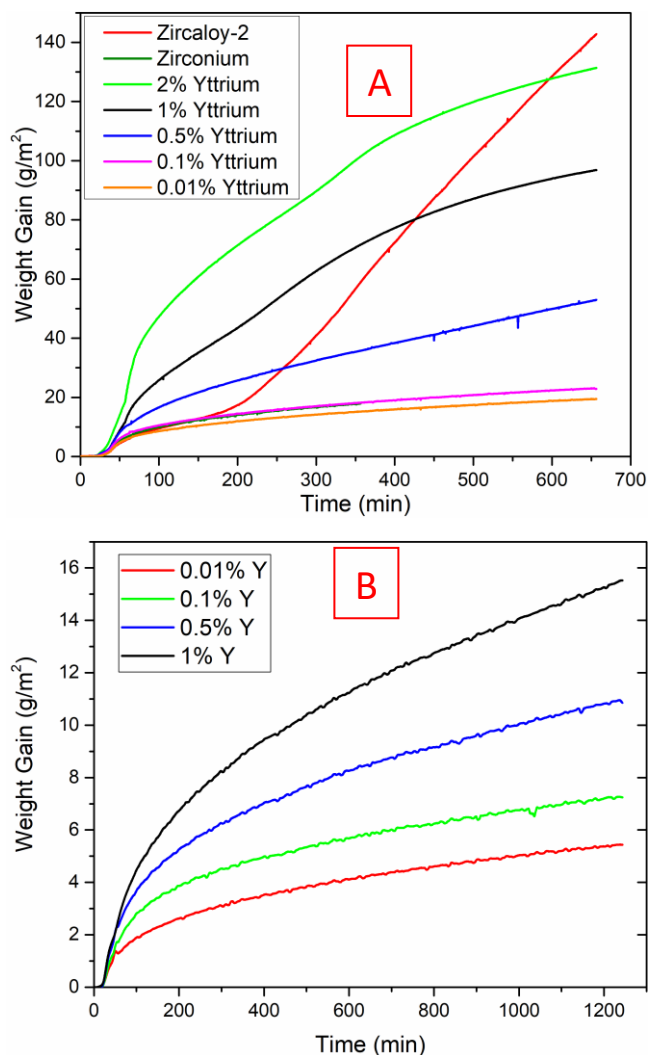
tetragonal phase of zirconia was very weak but present in all samples. One 2% sample was partially oxidized at 1100^{oC} to observe phase structure before complete oxidation occurred. In this case a metastable Zr_3O phase was identified.

From the structural refinement of the powder diffraction data two systematic trends were seen. The lorentzian isotropic strain was larger in the 700^{oC} powders and decreased with decreasing Y concentration. Secondly there was a systematic change in the a and c lattice parameters from being 5.152±0.0002 and 5.318±0.0002 respectively at 1100^{oC} and 5.1495±0.0002 and 5.325±0.0002 respectively at 700^{oC}. This appears to have originated from shifts in the positioning of the two oxygen atoms in the unit cell keeping volume constant. No large lattice parameter shifts were observed as a function of Y concentration indicating that it does not have a high solubility in monoclinic zirconium oxide.

Synchrotron Diffraction Phase Composition

X-ray diffraction on steam oxidized coupons was performed at ANL using APS at the 11-ID-C beamline. The samples (Table 1) were run in transmission with data collected using a CCD panel detector.

Table 1. Exposure conditions for each of the Y concentrations.

	As received	30hr 350C	20hr 500C	0.5hr 700C	10hr 700C	15hr 800C	10hr 900C	3hr 1100C	5hr 1100C
12% Yttrium									
2% Yttrium									
1% Yttrium									
0.5% Yttrium									
0.1% Yttrium									
0.01% Yttrium									
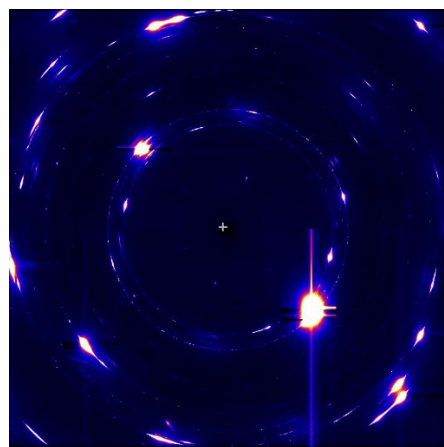
Figure 3. Diffraction data from 0.01 wt% Y exposed to 500^{oC} for 20 hours.

Due to the large grain size of the starting coupons, exact structural refinement of the samples was impossible. Diffraction from one or two grains from the base metal was common, resulting in strong, single crystal diffraction spots as seen in Figure 3.

Additionally, the thermal oxides and hydrides formed at the different temperatures were highly textured. However this also gave a large amount of data in the relationships between thermally grown phases. Table 2 shows the thermally grown phases in addition to the monoclinic and tetragonal phases.

Table 2. Thermally grown oxide and hydride phases at each temperature and concentration

Yttrium wt%	30hr 350C	20hr 500C	0.5hr 700C	10hr 700C	15hr 800C	10hr 900C	3hr 1100C	5hr 1100C
12%			Y_2O_3, $YH_{1.98}$, Zr_3O				Y_2O_3	
2%			$ZrH_{1.65}$, ZrH, Y_2O_3, Zr_3O	$ZrH_{1.65}$, ZrH, $YH_{1.98}$, Y_2O_3, Zr_3O				Y_2O_3, Zr_3O
1%		$ZrH_{1.65}$, ZrH	$ZrH_{1.65}$, ZrH, Y_2O_3, Zr_3O	$ZrH_{1.65}$, ZrH, Y_2O_3, Zr_3O		$ZrH_{1.65}$, ZrH, Y_2O_3, Zr_3O		Y_2O_3, Zr_3O
0.5%	$ZrH_{1.65}$, ZrH	$ZrH_{1.65}$, ZrH	$ZrH_{1.65}$, ZrH, Zr_3O	$ZrH_{1.65}$, ZrH, Y_2O_3, Zr_3O	$ZrH_{1.65}$, ZrH, Y_2O_3, Zr_3O	$ZrH_{1.65}$, ZrH, Y_2O_3, Zr_3O		Y_2O_3, Zr_3O
0.1%		$ZrH_{1.65}$, ZrH	$ZrH_{1.65}$, ZrH, Zr_3O	$ZrH_{1.65}$, ZrH, Zr_3O		$ZrH_{1.65}$, ZrH, Y_2O_3, Zr_3O		Y_2O_3, Zr_3O
0.01%		$ZrH_{1.65}$, ZrH	$ZrH_{1.65}$, ZrH, Zr_3O	$ZrH_{1.65}$, ZrH, Zr_3O	$ZrH_{1.65}$, ZrH, Zr_3O	$ZrH_{1.65}$, ZrH, Zr_3O		Zr_3O

The δ and γ phases of zirconium hydride were seen at all temperatures below 1100^{oC}. The formation of the δ phase was due to the rapid cooling of the samples after oxidation locking in the non-equilibrium phase. Of the non Zr and Zr_3O phases that formed, the hydride phases make up a greater fraction of the thermally grown phases at lower temperatures and at higher Y concentrations. At 500^{oC}, comparing the relative peak areas of the (-111) monoclinic oxide to the (220) δ hydride, it was seen that the ratio of hydride to oxide increased from 1.679, to 10, to 12.8, to 18.7 spanning the concentrations from 0.01wt% Y to 1 wt% Y. Yttrium hydride was only seen in the 12 wt% sample at the 30 minute 700^{oC} exposure, and in the 2 wt% sample at the 10 hour 700^{oC} exposure. Yttrium is a stronger hydride former than Zr, as seen be the lack of Zr hydrides in the 12 wt% sample. However, large concentrations are needed, as well as enough time for the Y hydrides to grow. The 500^{oC} data indicates that even if Y hydrides are not forming, Y in solution can promote the formation of Zr hydrides. At higher temperatures, the Zr_3O phase begins to compete with the hydride phase. In the 1100^{oC} samples all of the Zr formed Zr_3O, and no hydrides were present. The fraction of Zr_3O increased with temperature and exposure time, limiting the hydride formation when cooled.

Yttria phase formation was observed at higher temperatures and higher Y concentrations. No yttria was observed at the 350^{0C} or 500^{oC} temperatures even though yttria has a lower Gibbs free energy of formation than zirconia at these temperatures. Additionally, at 700^{oC}, the 0.5 wt% Y sample did not exhibit yttria diffraction at the 30 minute exposure. The 0.1 wt% Y sample only contained yttria at 900^{oC} and 1100^{oC}. This indicates that a threshold concentration of Y is needed for yttria to form. Therefore oxide thickness plays a role in yttria formation over zirconia. At 1100^{oC} the weight fraction of the Yttria phase from Rietveld refinement showed a close tie with the initial weight fraction of Y in the starting material indicating that minimal Y is incorporated into the Zirconia. As the oxide grows, the Y is forced diffuse towards the center of

the sample, until the concentration is high enough that the oxide forms. This is why sufficient temperature and exposure time is necessary for yttria formation in the 0.1 and 0.5 wt% Y samples.

Synchrotron Texture

Using a panel detector to capture the complete Debye-Scherrer cone allowed for insight into the coupling of phase orientations. The large grain size of the zirconium lead to near single crystal diffraction in many of the samples. The thermally grown phases also showed large degrees of texturing. Observation of the azimuthal intensity dependence between phases shows a strong dependence on the oxide and hydride phases as seen in Figure 4.
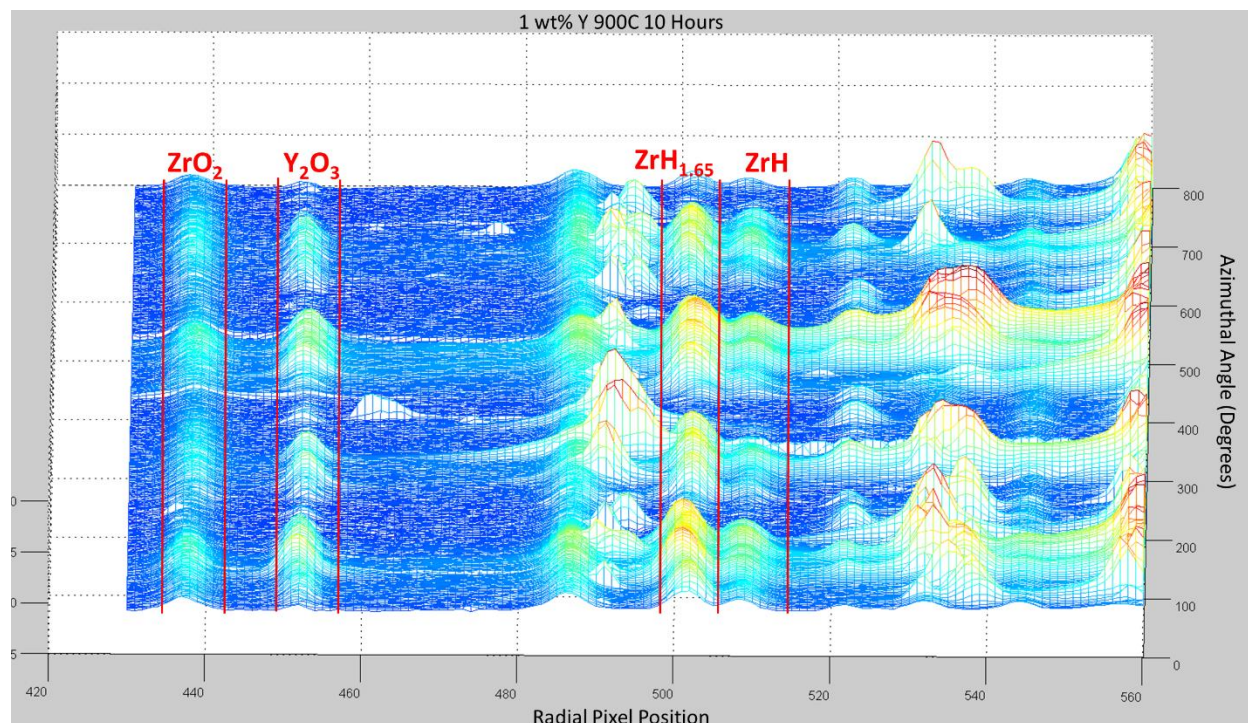
Figure 4. Panel diffraction data from the 1 wt% Y sample after 10 hour exposure to 900^{oC} steam. The ring diffraction has been unwrapped such that the X axis I the radial position along the center, corresponding to the inverse of d-spacing. The Y axis travels along the ring of the diffraction cone giving the azimuthal dependence. The Z axis is the log of the intensity. Similar strong azimuthal variations are seen in the hydride and oxide.
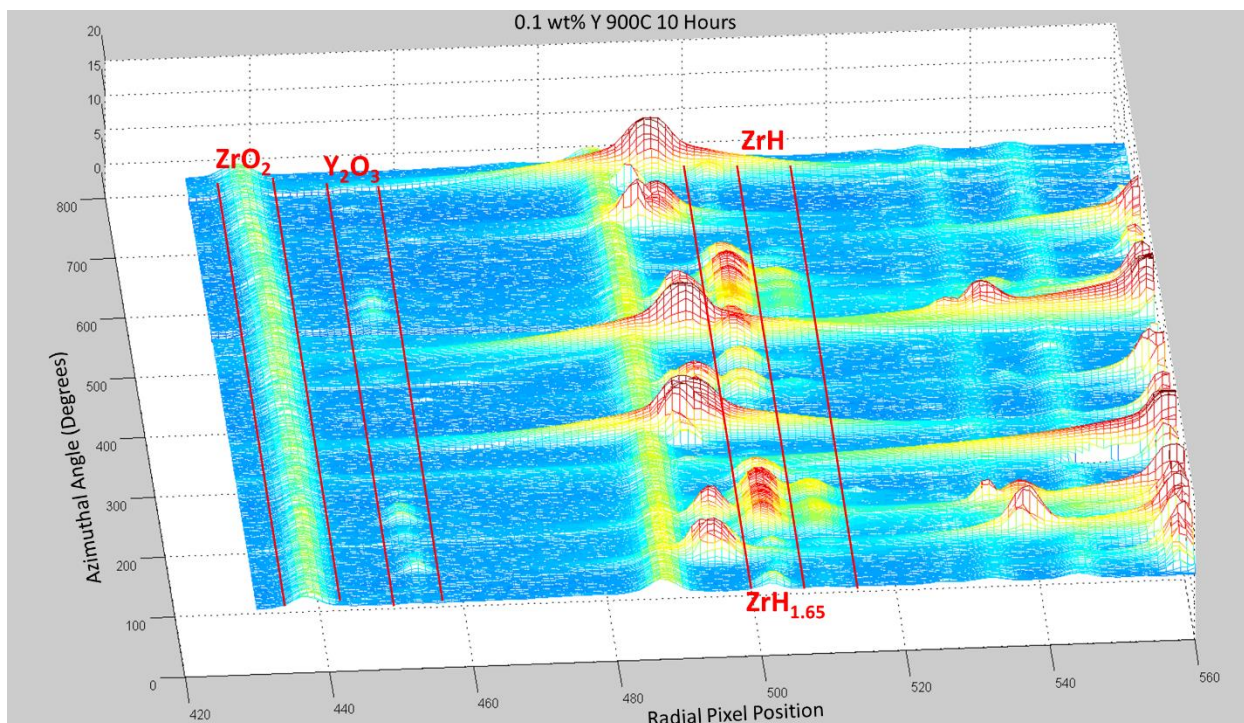
Figure 5. Panel diffraction data from the 0.1 wt% Y sample after 10 hour exposure to 900^{oC} steam. The ring diffraction has been unwrapped such that the X axis I the radial position along the center, corresponding to the inverse of d-spacing. The Y axis travels along the ring of the diffraction cone giving the azimuthal dependence. The Z axis is the log of the intensity. The zirconia shows very little azimuthal dependence, while the yttria and hydrides show matching azimuthal dependence.

In the 1 wt% Y 900^{oC} sample, the zirconia and yttria show a strong azimuthal dependence that matches that of the hydrides. The hydride phases show strong azimuthal anisotropy independent of temperature and yttrium concentration, indicative of large blocky structures that are oriented in the same direction. As the matrix zirconium that the hydrides are forming from is effectively single crystal on the scale of the x-ray probe, the strong hydride azimuthal dependence is expected. These hydrides, however, induce strong texturing into the surrounding yttria and zirconia phases. The texturing of the zirconia may be driven more by the yttria, as its texturing is stronger when yttria is present. The yttria always follows the azimuthal intensity of the hydrides. This can be seen in the 0.1 wt% Y 900^{oC} sample in Figure 5. The intensity of the zirconia is very uniform azimuthally indicating a lack of texture due to randomly oriented grains. The yttria, however, although exhibiting weak intensity, has stronger intensity at the same azimuthal angles as the δ and γ-hydrides. The 0.01 wt% 900^{oC} sample shows no yttria diffraction peaks, and no texturing of the zirconia, the hydrides are still textured. At 1100^{oC} no hydrides formed. Texturing of the zirconia and yttria was still present, with the azimuthal intensity dependence matching when both phases were present.
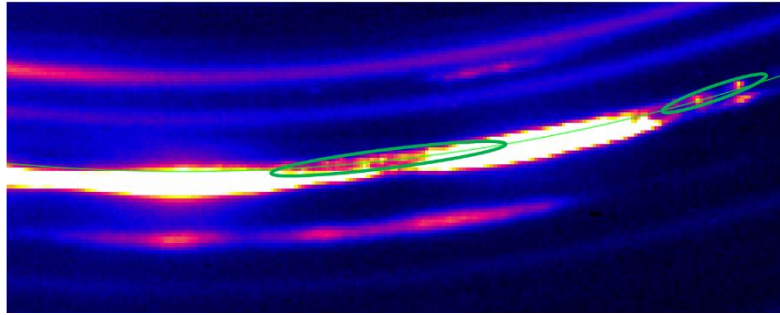
Figure 6. Diffraction data from 1 wt% Y exposed to 700^{oC} for 10 hours. Circled regions show Zr_3O intensity. The white high intensity regions are the Zr reflections.

The Zr_3O phase formation is highly tied to the Zr matrix. At 700^{oC}, the small phase fraction of Zr_3O causes its peaks to be almost indistinguishable from the matrix Zr, with a d-spacing difference of 0.013 at the (101) Zr reflection. Given the strong intensity of the Zr peaks, close azimuthal examination is needed to identify the Zr_3O as its reflections will be overwhelmed if an integration around the azimuthal angle is performed (Figure 6). The Zr_3O peaks are slightly offset azimuthally from the Zr peaks. At 900^{oC} Zr_3O reflections farther away azimuthally from the Zr peaks occur, and the Zr_3O peaks coupled to the Zr peaks increase in intensity making them more easily identifiable after an azimuthal integration.

Conclusions

Alloying yttrium into zirconium has multiple effects on the oxidation behavior of zirconium. It strongly increases the zirconium hydride phase fraction, eventually forming yttrium hydrides at high Y concentrations. This increased flow of hydrogen may be responsible for the increased oxidation kinetics observed in conjunction with increased Y concentrations at all temperatures. At Y higher concentrations, cyclic oxidation occurs in the intermediate temperature range indicating a destabilization of the oxides mechanical stability. At high temperature and exposure times yttria formation occurs adding additional stresses to the oxide. Additionally, strong texturing of the monoclinic zirconia was observed in samples with significant yttria formation.

References

[1] Palenzona, A., and S. Cirafici. "The Y-Zr (Yttrium-Zirconium) system." *Journal of phase equilibria* 12.4 (1991): 485-489.

[2] Peng, Jia-Qing, et al. "Solid solubility extension and microstructure evolution of cast zirconium yttrium alloy." *Rare Metals* 35.4 (2016): 325-330.

[3] Shin, D-W., and J. G. Kim. "Study On The Separation And Extraction Of Rare-Earth Elements From The Phosphor Recovered From End Of Life Fluorescent Lamps." *Archives of Metallurgy and Materials* 60.2 (2015): 1257-1260.

2.4   Aluminization Coating on Zircaloy Cladding for Improved Accident Tolerance of Light Water Reactor Fuel

1. Summary

Zirconium is a strong oxide former when exposed to high temperature water/steam environment at normal and off-normal LWR operation conditions, which leads to severe oxidation and the associated hydrogen production. Degradation of zirconium alloy cladding by waterside corrosion is expected in off-normal scenarios, e.g. loss-of-coolant accidents (LOCAs). Therefore, it is desired to develop a corrosion resistance coating on the surface of zirconium alloys to mitigate oxidation and to improve the accident tolerance of fuel cladding.

The objectives of this proposed work are to modify the current Zircaloy cladding with respect to enhanced corrosion resistance in LWR:
1)   Develop a process for depositing a protective surface coating on the zirconium alloy with a minimum impact on the cladding performance under normal conditions.
2)   Demonstrate the improved accident tolerance (decreased oxidation rate) of modified zirconium alloy cladding upon off-normal scenarios
3)   Scientifically understand the oxidation kinetics and microstructural evolution of diffusion coating and underneath zirconium substrate.

Aluminum was identified as potential candidate coating element due to the formation of compact protective surface oxide scale, and the aluminum oxide acts as oxygen diffusion barrier and significantly slow down the M+O→MO reaction during high-temperature steam exposure expected at LOCAs scenarios. Pack cementation diffusion coating is utilized to diffuse aluminum into the near surface layer of Zircaloy-4. Corrosion tests at static hydrothermal, simulated dynamic LWR environment and off-normal operation conditions were conducted. Corrosion performance of coated Zircaloy-4 was evaluated and compared with the response of un-modified ones. Corrosion kinetics and microstructure development on coating was characterized.

In addition, the feasibility of using electro-spark deposition (ESD) to deposit a layer of FeCrAl alloy on the Zr-4 cladding was studied. It was proved that by using a low power but a high frequency, a smooth layer of coating can be achieved. However, more studies are needed to make conclusive recommendation for this application.

2. Background

2.1 Waterside corrosion of zirconium alloy claddings in LWR

Zirconium alloys generally exhibit excellent corrosion performance under normal BWR and PWR operation conditions. Figure 1 illustrates the process of Zr alloy waterside corrosion. The oxidation of metal occurs at the interface between oxide and metal with the formation of new oxide, H^+ ions are released at the oxide/water interface. The transportation of oxygen and electron through the oxide layer leads to oxide growth. Based on different corrosion conditions

and metallurgical structure of alloys, either oxygen anions or electrons transportation determines the overall oxidation rate [1,2]. Due to the low mobility of zirconium ions, the migration of cations through oxide layer is normally negligible. The chemical reaction between water and zirconium can be summarized as the following equation:

$$Zr + 2H_2O \rightarrow ZrO_2 + 2(1-x)\ H_2 + 4x\ H \quad \text{(Eq. 1)}$$
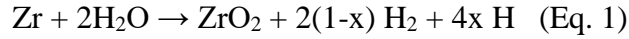
where x is defined as the hydrogen pickup fraction by the zirconium alloy. The hydrogen absorption is deleterious to the Zr alloy, and it will be fatherly illustrated in the following section.

The waterside corrosion of zirconium alloy claddings at high temperatures has been studied extensively. During high temperature/pressure water exposure, a uniform oxide scale forms on the outer surface of Zr alloy cladding and the thickness of this scale grows with time under exposure. The waterside corrosion process of zirconium alloys can be clearly classified as three stages: pre-transition stage with parabolic or cubic time dependence, onset of transition and breakaway oxidation with linear oxide growth with time, as shown in Figure 2 [3]. The oxide layer forms at the pre-transition stage serves as a diffusion barrier to protect the substrate alloys from further oxidation, the diffusion-limited process is described in Figure 1. The onset of transition indicates that oxide layer grows unstably and start to lose its protective properties. There are two major hypotheses attempting to explain the mechanism of transition. Both of the hypotheses explain the transition as a mechanical failure of the oxide scale. One hypothesis explains the lateral cracking due to the stresses generated by the oxide growth is responsible for the transition [4, 5]. Another hypothesis claims that micro-cracks and micro-pores inside the oxide scale generated by the stresses serves as pathway for oxygen diffusion [6-8].

It should be noticed that, as shown in Figure 2, the three-stage corrosion process will then repeat itself at constant time intervals. This cyclic behavior has been observed as a common feature among zirconium alloys [9]. It was also proved that the waterside corrosion behavior change little with variation of oxygen and hydrogen content over a wide range in the water [10].
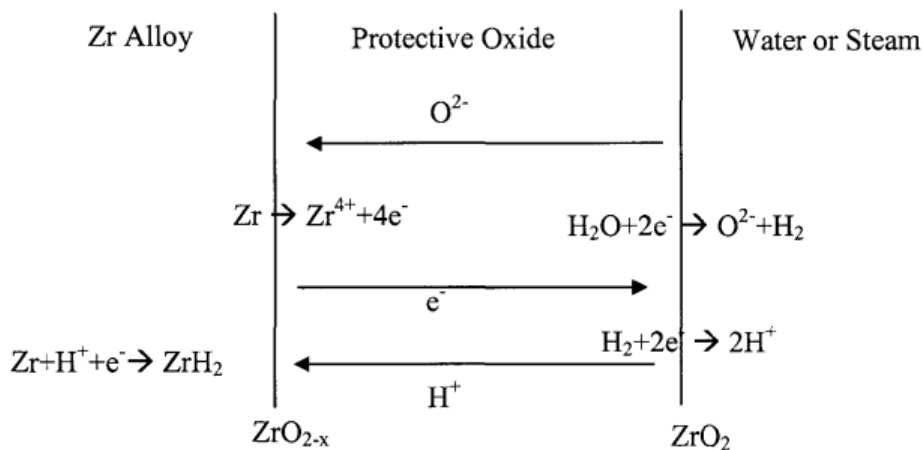
Figure 1. Schematic of waterside corrosion process of zirconium alloys [1]
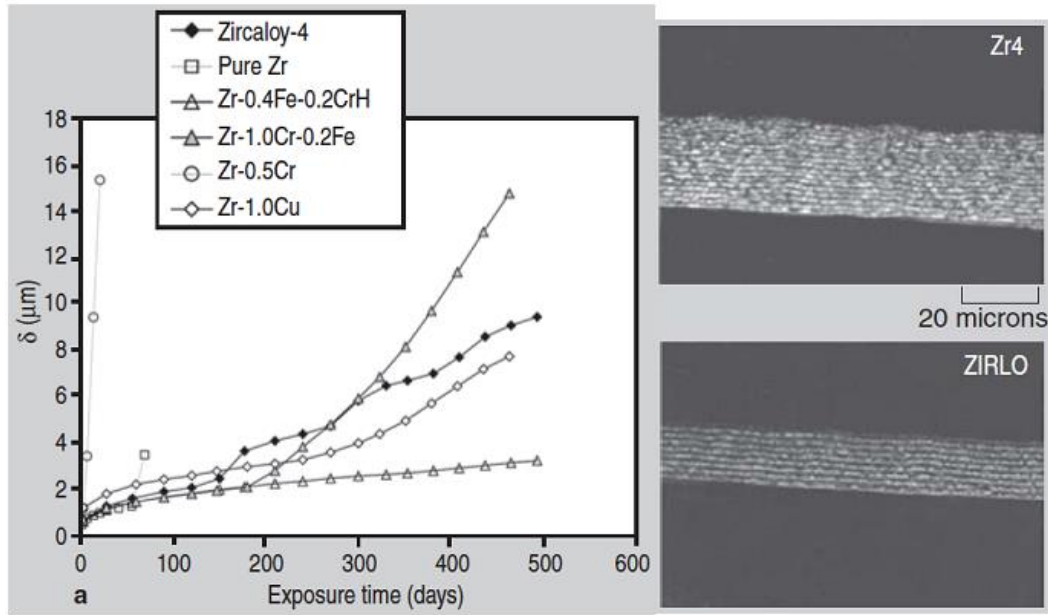
Figure 2. Corrosion kinectics of sevearl Zr alloys under 360C water exposure [3]

The oxidation behavior of Zircaloy-2 and Zircaloy-4 alloys under high-temperature gas (steam/air/CO-CO2 mixture) has also been studied over the latest few decades [11]. Figure 3 gives an example of oxide growth of Zircaloy-4 under different oxidizing environments. At the initial stage, the oxidation kinetics of Zircaloy-4 cladding follows parabolic or quasi-parabolic rates at the temperatures range of 600-950C [12] ; for Zircaloy-2 a cubic rate dependency is followed at 400-600C [13]. The parabolic rate dependence results from the growth of a dense oxide layers, which is diffusion-limited. While electric field effects and point defect concentration constraints in the oxides lead to the cubic rate behavior of Zircaloy-2 [9]. A liner oxide growth can be already observed for Zircaloy-4 below 800C. The linear growth is an indication of breakaway oxidation. In this process, non-protective oxide layers with defects such as porous oxides form and cracking occurs due to the mismatch of specific volume between the oxide layer and metal substrate. The specific volume change of zirconium oxides arises from the structural change of tetragonal zirconia (t-ZrO_2) to more stable monoclinic zirconia (m- ZrO_2) at high temperature [14]. The allotropic forms of zirconia is summarized in Table 1 [15].
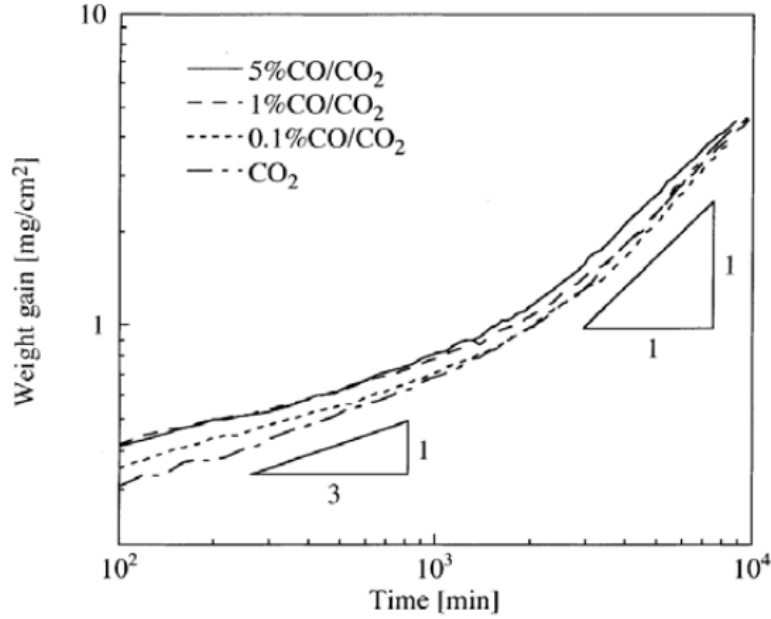
Figure 3. Weight gain vs. time plot of Zircaloy-4 under different environments at 600°C [12]

Table 1. Allotropic forms of zirconia [15]

Phase	Temperature of Stable Existence (°C)	Space Group	Lattice parameters (Å), (angle: degrees)
Monoclinic ZrO_2	<1100	P 2_1/a	a = 5.341, b = 5.232 c = 5.169, β = 99.218 and α = γ = 90
Tetragonal ZrO_2	1100 < t < 2100	P 4_2/nmc	a=3.64, c=5.27 α = β = γ = 90
Cubic ZrO_2	> 2100	F m3m	a=b=c=5.07 α = β = γ = 90

As described above, zirconium alloy claddings are exposed to high-temperature pressurized coolant water in LWRs and generally exhibit satisfied corrosion performance under normal reactor operation conditions. However, during the severe environments with high temperatures at off-normal scenarios, zirconium will be oxidized rapidly by reacting with high temperature water/steam with hydrogen generation as by-product. Zirconium will become strong oxide former with water/steam as the temperatures increases, especially above 800 °C. During accident scenarios, e.g. loss-of-coolant accidents (LOCAs) , the oxidation rate of Zr alloy claddings increases rapidly as temperature arises due to insufficient cooling of the reactor core and significant heat from the exothermic oxidation. Figure 4 shows that a large number of brittle

phases, ZrO_2 and oxygen-stabilized α–Zr(O), are formed under 1200 °C steam attack, which are both mechanically brittle phases, and the metallic β-Zr becomes the only source of ductility [16].
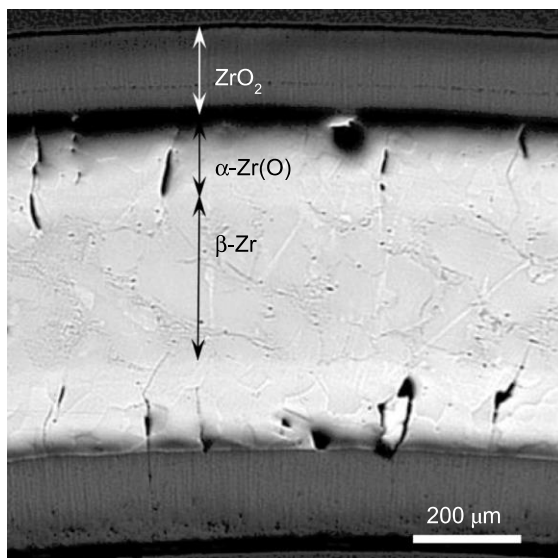
Figure 4. Optical image of Zircaloy cladding oxidized at 1200 °C for 2 h in 1 MPa steam [1].

2.2 Approaches towards improved accident tolerance cladding

There are continuous active studies on improving the oxidation performance of cladding materials during the last several decades [5,6]. After the Fukushima Daiichi accident in 2011, interests are specifically boosted to develop advanced cladding materials for accident tolerant fuel (ATF) systems under significant aggressive accidents scenarios. The strategies for claddings with enhanced oxidation resistance and/or improved accident tolerance can be basically classified as modification of Zr alloys and development of none-Zr materials. Optimization of zirconium alloys for improved oxidation and corrosion performance basically fall into two approaches: 1) Metallurgical modification for better alloys, 2) Surface modification.

2.2.1 Metallurgical modification of zirconium alloys

The corrosion resistance of zirconium alloys has been remarkably improved through decades of development. New series of zirconium alloys with superior oxidation resistance as compared with the conventional Zr-2 and Zr-4 are developed and and some of these have been commercially applied. These novel alloys are mostly doped with Nb by metallurgical methods (E110, E125, E635, M5 AND ZIRLO). These new types of Zr-based alloys are able to provide the expanded fuel burnup and longer fuel cycle for LWR reactors in their normal operation. However, it is unlikely to achieve significant high temperature oxidation resistance to withstand hasher off-normal operation condition by simply adding small amount alloying elements into Zr-based cladding. A remarkable cladding composition modification is urgently needed, while potential changes on structural properties limit the latitude on bulk composition alteration.

2.2.2 Replacement of Zr-based materials

Materials with excellent high-temperature performance, especially very high oxidation resistance have been developed over the past several decades. A variety of materials system are being considered as potential nuclear fuel cladding materials as alternatives to zirconium-based alloys. Among these, advanced iron-based alloys and silicon carbide composites are currently the most promising candidates.

Iron-based alloys were initially used as fuel cladding materials in early prototype of LWRs before the application of zirconium alloys. In recent years, advanced iron-based alloys have been reconsidered as promising potential LWR cladding materials to replace zirconium alloys due to the development of novel types of advanced steels with superior corrosion and mechanical performance as shown in Figure 5. Cheng et al. [17] and Pint et al. [18] reported that Kanthal APMT (Advanced Powder Metallurgy Tube) and austenitic 310 stainless steel present superior oxidation resistances under high-temperature steam corrosion. Figure 6 reveals that the parabolic oxidation rate constants for APMT and 310SS are approximately two to three orders of magnitude lower than these of zirconium alloys [19]. Nevertheless, the major drawback of the iron-based claddings is their high neutron absorption cross section, which requires to increase the enrichment of fuel.
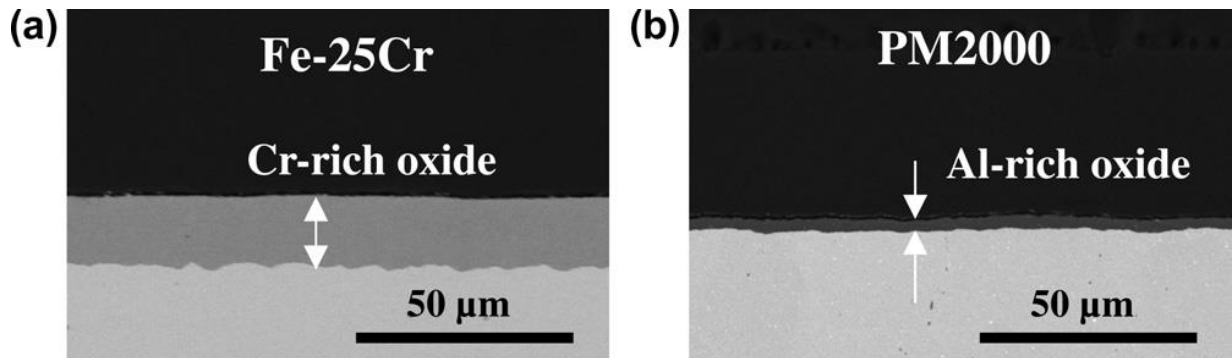
Figure 5. SEM images of Fe–25Cr (a), PM2000 (b), after 8 h exposure at 1200 °C in 0.34 MPa steam [17]
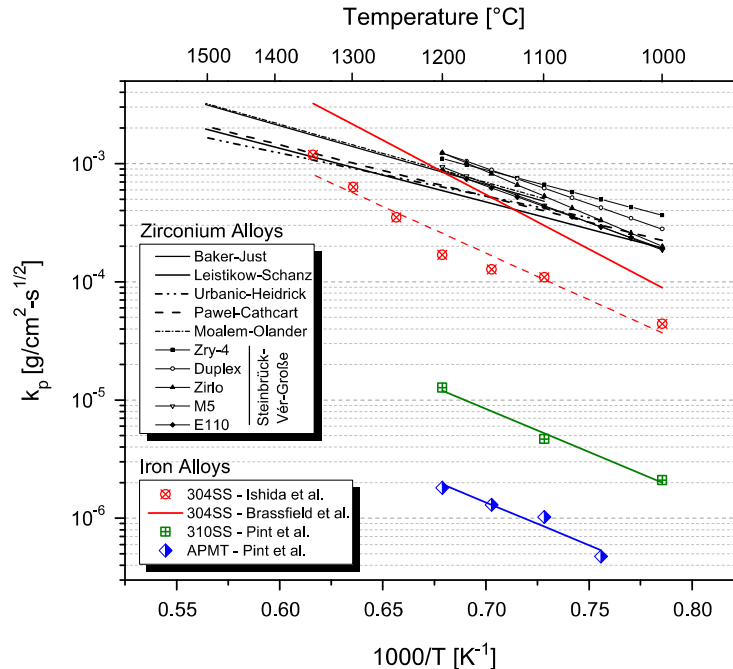
Figure 6. Arrhenius plot of the parabolic weight-gain rate constants for zirconium alloys and iron-based alloys oxidized in pure steam, 1atm [19]

SiC composites: Silicon carbide fiber-reinforced SiC matrix composites（SiC/SiC）have also been proposed as a promising alternative cladding material due to their excellent corrosion resistance [20]. However, the major issue with SiC cladding is the fabrication/joining of cladding tube, in addition, it was recently reported radiolysis induced corrosion can occur for the SiC in a LWR environment.

2.2.3 Coating on Zr-cladding for improved oxidation resistance

Compared with metallurgical alterations on zirconium alloys or a total replacement of Zr-based cladding with iron based alloys or SiC, coating method possesses several benefits due to the fact that materials suitable for fuel cladding in LWRs are extremely limited. It should be also noticed that large concentration of alloying element(s) may undermine the overall performance of the Zr alloys. Neutronics performance is always the major challenge to non-zirconium based materials due to their larger thermal neutron capture cross-section compared with zirconium. In addition, the alloying element can potential change the cladding physical-mechanical properties. One example is that high concentrations addition of aluminum as alloying element will lower down the alloy melting point. While coating composition can be largely adjusted in a wide range and mechanical properties of the existing zirconium alloys will not be significantly affected since there are minimum alterations on the bulk cladding compositions and microstructures.

Coating methods can be basically classified into two categories: 1) overlay coating that coating has minor inter-diffusion with substrate and 2) diffusion coating that modifies the composition and/or the microstructure of the substrate. Currently, under the DOE ATF program, there are several teams working on coating the Zr-cladding tubes with MAX phase, FeCrAl, and other

multilayer ceramics, and the coating methods include thermal spray and sputtering deposition. In this project, we explored another method, pack cementation coating, which was widely used in the industry for coating the iron-base alloys with aluminum or silicon rich protective layer. For nuclear fuel cladding application, diffusion coating method can be favorable compared with overlay coating methods. The coating material is metallurgically bonded into the substrate, and thus coating spallation or other adhesion issues can be largely avoided. Diffusion coating typically exhibits the intrinsic features of functional gradient materials, which can significantly reduce the mismatch of coefficient of thermal expansions (CTEs) between the coating and substrate.

2.3 Description of pack cementation diffusion coating (PCDC) process

The concept of pack cementation was first introduced by Van Aller as a U.S. filled patent in 1911 [21]. The process is illustrated in Figure 7. PCDC has been a common method for improving the oxidation resistance of alloys at elevated temperatures [23], especially for the high-temperature protection of blades and vanes in gas turbine engines and steam tubes in coal power plant [24, 25]. Compared with other coating methods, PCDC is generally easier to achieve controllable, thick coating with sufficient oxidation resistance elements. Aluminzation, chromization and siliconization are generally applied on alloy surface via PCDC in order to form protective oxide scales under high-temperature exposure.
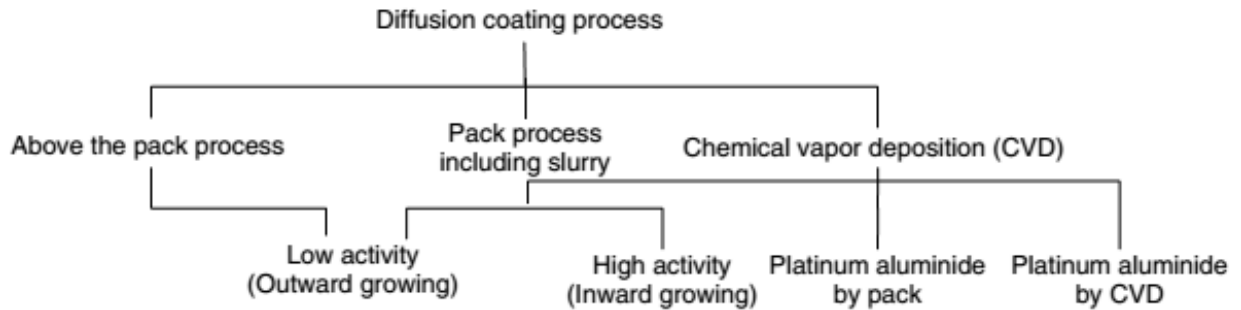
Figure 7. Various diffusion coating processes [22]

Compared with a well-controlled conventional CVD process which requires special furnace and gas manifold systems, pack cementation is a more commercially viable process which presents the advantages of low cost and especially the ability to coating large size parts. In practice, an industry standard PWR Zircaloy-4 alloy fuel cladding can be as long as 12 feet. In addition, pack cementation is particularly convenient for coating components such as cladding tubes in this work with a curved surface since the pack powder can be contact with coating parts directly, while the delivery of precursor can be difficult for conventional CVD.

In nature, PCDC is an *in situ* Chemical vapor deposition (CVD) batch process in which the part(s) to be coated is placed inside a well-mixed pack powder mixture, then the pack is heated to an elevated temperature inside a furnace for a desired interval of time. The process is carried out under inert gas atmosphere. The pack powder generally contains: 1) depositing source element(s), such as Al, Cr, or alloy powders if co-deposition is desired; 2) activator which is one kind of

halide salts, chlorides and fluorides are the most widely utilized; and 3) inert filler that prevents sintering of the deposited particles and provides pathways for the gas phases transportation during the process; Al_2O_3 powders is generally used as the inert filler due to its high stability and low cost.The key factors that control the thermodynamics and kinetics of the packing process and stability and low cost, the resulting microstructures of coating include the type and concentration of the activators, composition of the pack powder and deposition temperature.

Pack cementation is a complex process that involves reactions of between metallic depositing source and activator, gas transportation through pack and the subsequent solid deposition. A number of studies have been carried out to understand the thermodynamics and kinetics during pack cementation process and to determine the factors that control the resulting microstructures of coating. The most applied aluminide coating via pack cementation has been specifically well-understood. In general, three interrelated processes take place in the pack at high temperatures: activation process, gaseous species transportation, substrate surface reaction. Here is list of criteria for an functional oxidation-resistant coating targeted in this work.

1)   Good adhesion to the substrate, which usually requires a thermal expansion coefficient (CET) close to that of the substrate (5.89×10^{-6} K^{-1} for zirconium) in order to minimize interfacial stresses
2)   Smooth surface with low roughness
3)   Free from microspores and through-in cracks
4)   Capability to be processed at low enough temperature to avoid microstructure change on substrate
5)   Minimal adverse effects on neutronics performance

Identification of coating elements

The best oxidation resistance is generally achieved among aluminum, chromium and silicon containing materials through the formation of intact, protective and adherent oxides scales of alumina (Al_2O_3), chromia (Cr_2O_3) and silica (SiO_2) on the surface. The protective properties of the oxide scales origin from the following aspects:

  1) The proper Pilling-Bedworth ratios (PBRs) of these oxides results in low internal stress and good scale integrity;
  2) The compact structures with wide columnar grains with few grain boundaries and small grain-to-grain mis-orientations limit the transportation pathway of metal ions and oxidizing species through scales;
  3) These oxides are highly thermal stable due to the high melting points and low vapor pressures under a various of corrosion atmosphere (Figure 8).

In high temperature steam environments, Cr_2O_3 and SiO_2 become less protective due to the formation of volatile hydroxide species with water. Particularly, the formation of toxic CrO_3 gas also brings out serious environmental issues. Alumina is generally resistant to accelerated oxidation in water vapor conditions. Among the three oxides, alumina provides the best corrosion protection in aqueous and steam condition. Additionally, Al has low thermal neutron

absorption cross-section that comparable with Zr. For these reasons, Al is selected as the candidate element for oxidation resistant coating on zirconium alloys in this work.
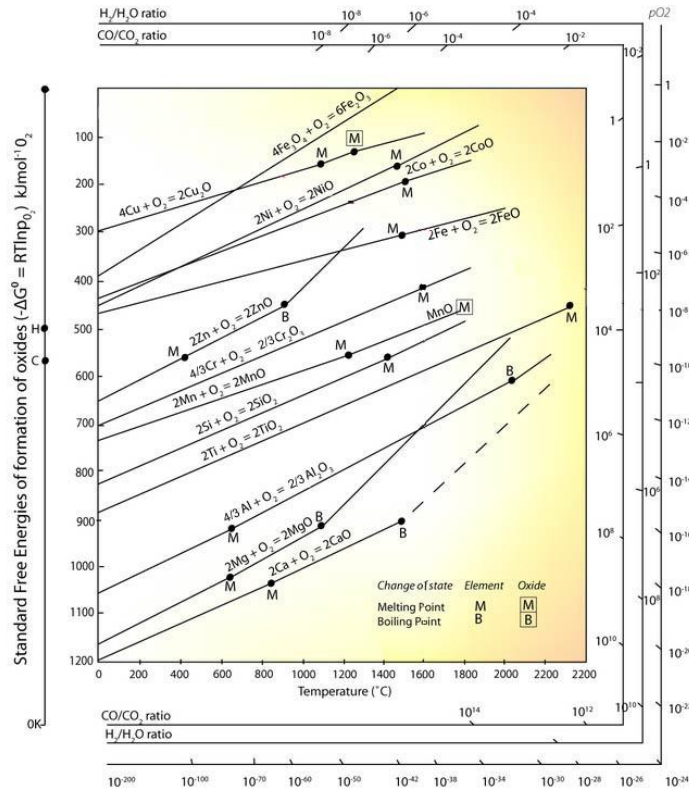

Figure 8. Ellingham diagram for candidate elements

According to the Al-Zr phase diagram Figure 9 , a variety of intermediate phases could form in an Al-Zr binary system. If aluminum that diffusing into zirconium transforms into complex structure with multiple types of intermetallic phases, cracks are likely to be formed during temperature changes because of mismatch of the CTEs of different phases. Moreover, the corrosion behavior of the modified zirconium alloys will be complicated due to the presence of multiple phases. Thus coating with single-phase structure is desirable after aluminization on zirconium alloy. It has been reported that $ZrAl_3$ is the only phase formed through Al-Zr inter-diffusion at temperatures below 650C.

The conclusion indicates that aluminization by PCDC on zirconium alloys will result surface inter-diffusion with a single phase structure, the $ZrAl_3$ phase on cladding surface is expected to act as a substantial reservoir of Al for the formation of a protective alumina scale during oxidation.
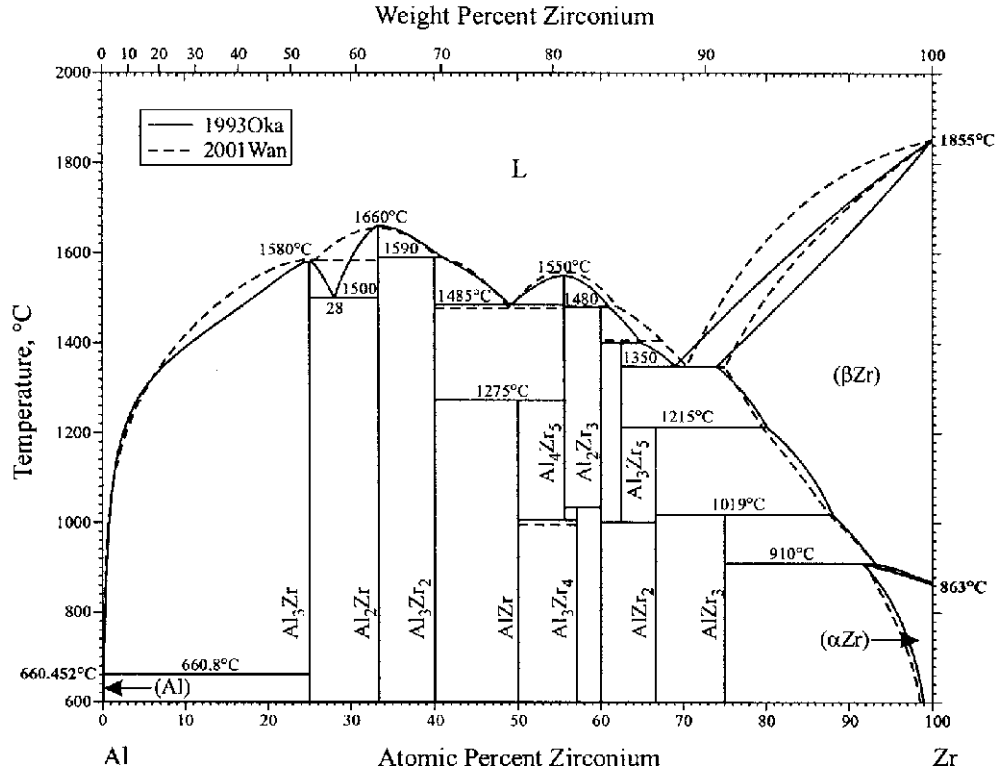
Figure 9. Binary phase diagram of Al-Zr [27]

3. EXPERIMENTAL

3.1 Preparation of substrate materials

Zircaloy-4, the primary alloy utilized in current PWRs, were used in this study. The materials were provided by the project collaborator, ATI Wah Chang, the detailed composition of Zircaloy-4 is given in

Table 2. As a pioneering study, Zr-4 flat samples instead of actual cladding tubes were used in this work. Prior to experiments, Zr-4 samples were cut into flat coupons by high speed diamond saw with dimensions of approximately 15mm x 15mm x 1.5mm. Each sample was then drilled with a 1/16 holes in order to be hung on the sample rack in the following autoclave tests.

The coupon samples were mechanically grinded on silicon carbide papers following an 80,120, 200, 400, 600, 800, 1200 grit sequence. Each grinding step should remove the scratches on the samples from last step. After grinding, the samples were then polished to a mirror surface finish with 3 um diamond suspension followed with 0.06 um silica suspension in order to minimize initial surface unevenness. Following polishing, samples were cleaned by methanol and acetone in ultrasonic bath in sequent.

Table 2. Composition of Zircaloy-4 by weight%

	Sn	Fe	Cr	Zr
Zircaloy-4	1.53%	0.26%	0.1%	Balance

3.2. PCDC aluminization process

Figure 10 shows the equipment setup of the PCDC experimental system used in this study. The experimental process requires two key conditions: inert gas environment and high-temperature n. A single heat zone Lindberg/Blue horizontal tube furnace was used to control the packing cementation temperature. A thermocouple was inserted through alumina foam blocks to monitor the *in-situ* furnace temperature. A rotary vacuum pump was connected to the tube furnace. An argon gas circulation system was connected to the furnace in order to achieve the none-oxygen atmosphere. The chamber pressure was controlled at slightly above 1atm to prevent inward flowing of air by regulating the gas valves connected to the tubing system.
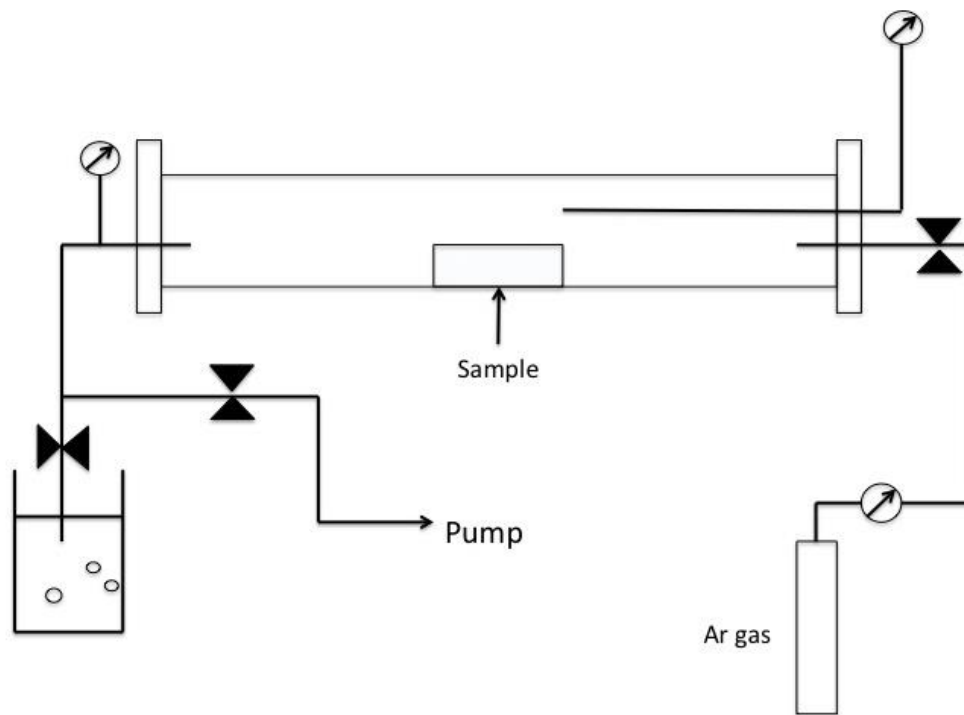
Figure 10. Schematic of the equipment setup for PCDC

Coating procedures

The weights of zircaloy-4 coupon samples were recorded using a Denver Instrument P-314 balance before each experiment. Samples were then buried in pre-mixed pack powder mixture inside an alumina crucible. The vented crucible was placed in the center area of the tube furnace. The pack powder mixture consists of powders of pure Al metal powders as the depositing source, and alumina as the inert filler. In this work, NH_4Cl was selected as the activator. Compared with condensed activator such as AlF_3, NH_4Cl decomposes into vapor species during heating process so there will be no residue activator particles entrapped in the coating. $AlCl_3$ is also a common activator for aluminization, while it is highly reactive to water and moisture resulting in oxygen absorption into the pack. Served as as heat and chemical barriers, alumina foam blocks were placed at the two ends of the alumina tube respectively. One side of alumina blocks were drilled with holes to permit the entry of thermocouple. After sealing the furnace tube, air was pumped out firstly and Ultra High Purity (UHP) grade argon gas flowed through the tube. The exit of argon gas was bubbled into water and exhausted through a fume hood.

The pack cementation experiment was then carried out isothermally at a given temperature for desired hours under the argon gas atmosphere. Once reached the required time, the furnace was turned off and the crucible was allowed to cool down inside the tube. The maximum heating temperature was controlled below 874 °C which is the transformation temperature of zirconium from α(HCP) phase to β(BCC) phase.

The argon gas kept flowing through the system until the experiment finished and the tube cooled down to room temperature. After pack cementation process, the coated samples were removed from the pack and cleaned by acetone and menthol in ultrasonic bath. After cleaned completely, the weight of the coated samples was measured.

3.3 Corrosion test in static autoclave

The corrosion performance of aluminized Zircaloy-4 was accessed by out-of-reactor aqueous corrosion tests in a static autoclave. The static corrosion tests offer more aggressive conditions than real LWR operations, while the behavior of the alloys in this environment correlates well with in-reactor behavior, i.e. alloys that behave well in this test behave reasonably well in-reactor. The static autoclave corrosion tests present basic aqueous corrosion performance of aluminized Zr-4 in at elevated temperature.

3.3.1 Designing of the oxygen detection system
The out-reactor static corrosion tests were conducted in a Parr instrument 4670 pressure vessel with a volume of 2L at in deionized water. An oxygen detection system was attached to the autoclave (Figure 11). The oxygen concentration in water was controlled at 250 ppb by purging 4% hydrogen balanced nitrogen gas mixture into water before heating up the autoclave, and the setup schematic is shown in Figure 12.
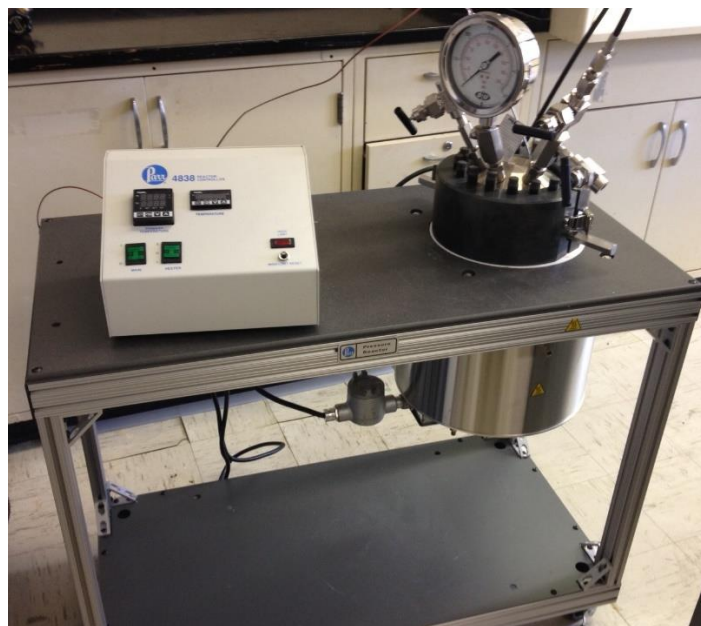
Figure 11. Parr instrument 4670 series high pressure/high temperature vessel
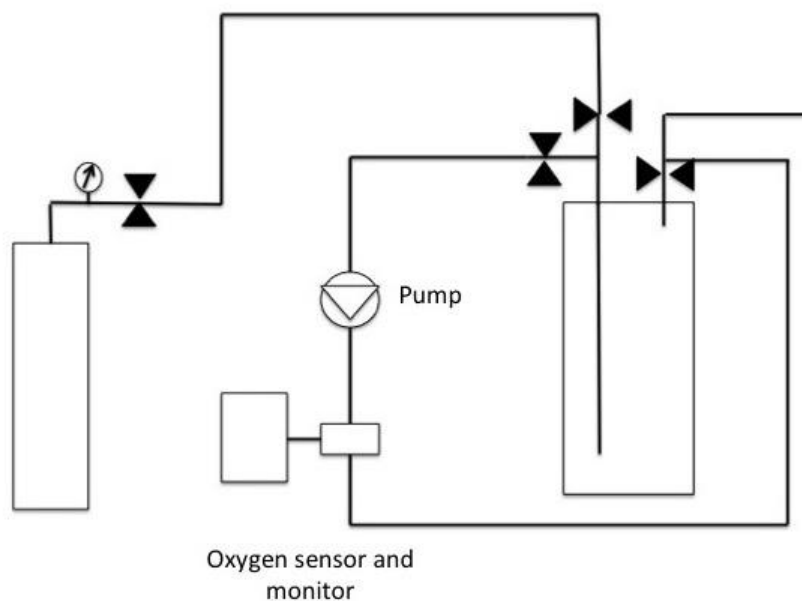

Figure 12. Schematics of the autoclave with oxygen detection system

3.3.2 Static autoclave test procedures

The samples were hang on a 316 stainless steel rack. An impact-resistant polycarbonate plate was attached in front of the autoclave to provide precaution in case of the possible steam or components injection in potential explosion/overpressure accidents. The rupture disc of the

autoclave was vented into water for unexpected burst issues. Before being put into autoclave, the specimens' masses were measured. The tests at 360 °C, 2708 psi were interrupted periodically to for weight gain measurement.

3.4 Corrosion test in simulated off-normal LWR conditions

The oxidation resistance of aluminized Zr-4 under excessive oxidation environment in off-normal LWR conditions was evaluated via high-temperature steam test. The steam corrosion tests at variety of temperatures conducted at the University of Illinois at Urbana-Champaign by using a Simultaneous thermal analyzer (STA), and the facility is shown in Figure 13.

Figure 13. Simultaneous thermal analyzer (STA) at UIUC

Steam tests under normal pressure were performed at 800 °C for up to 12 hours. During exposure, 2g / hr steam was flowed constantly with a 200 ml/min UHP argon as carrier. An *in-situ* specimen weight change measurement was carried out by the thermal gravimetric analysis (TGA) associated with the system.

3.4 Materials characterization

Scanning electron microscope (SEM) was used to characterize the surface morphology and cross-section of coated samples before and after corrosion respectively. Energy dispersive X-ray spectroscopy (EDS) analysis associated with SEM provides quantitative compositional data of the coatings before and after corrosion tests, particularly the depth-composition profiles in the cross-section analysis. X-Ray diffraction (XRD) and X-ray photoelectron spectroscopy (XPS) were used identify the phases formed after coating and oxidation respectively. The micro/nano-structures of oxide scale and oxide/metal interface were studied using transmission electron microscopy (TEM) and the TEM specimens will be prepared using a Focus Ion Beam (FIB).

Scanning electron microscope (SEM) (FEI Phillips XL-40 FEG) was used to characterize the surface morphology and cross-section of coated samples before and after corrosion respectively. The compositional profile of coated and oxidized samples was analyzed by energy dispersive X-ray spectroscopy (EDS). X-Ray diffraction (XRD) (Panalytical XPert Powder, Cu-Kα source) was used to identify the phases formed after coating and oxidation respectively. The microstructures of oxide scale and oxide/substrate interface were studied by transmission electron microscope (TEM) (ARM-200cF), and TEM specimens will be prepared by Focus Ion Beam (FIB) (Dual-Beam Strata DB235).

4. RESULTS AND DISCUSSION

4.1 Characterization of the coating layer prepared using PCDC process

Figure 14 shows the SEM image of surface morphology of Zr-4 after aluminization. Temperature had significant effects on the reaction rate of aluminization and final coating thickness. The thickness of aluminized layers was in the range of 10um at 600 °C and 30um at 650°C respectively (Figure 15). The cross-section EDS line-scan indicates a 1:3 atomic ratios between Zr and Al all cross the coating (Figure 16), the ratio was found in coatings obtained at all conditions. XRD analysis verified that the phase on the surface was a single $ZrAl_3$ intermetallic phase (Figure 17). Similar phenomenon has been reported in Zr-Al inter-diffusion experiments, which could be explained by minimization of lattice distortion [28, 29].
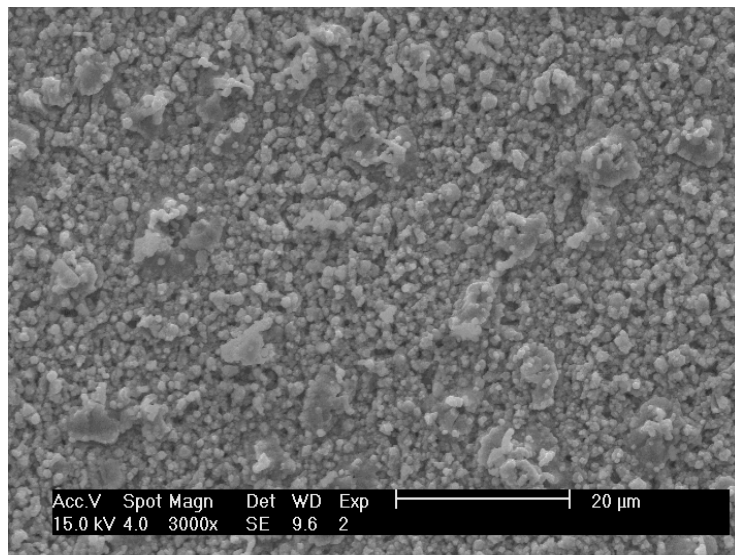
Figure 14. Surface morphology of PCDC aluminized layers at 600°C for 2 hrs.
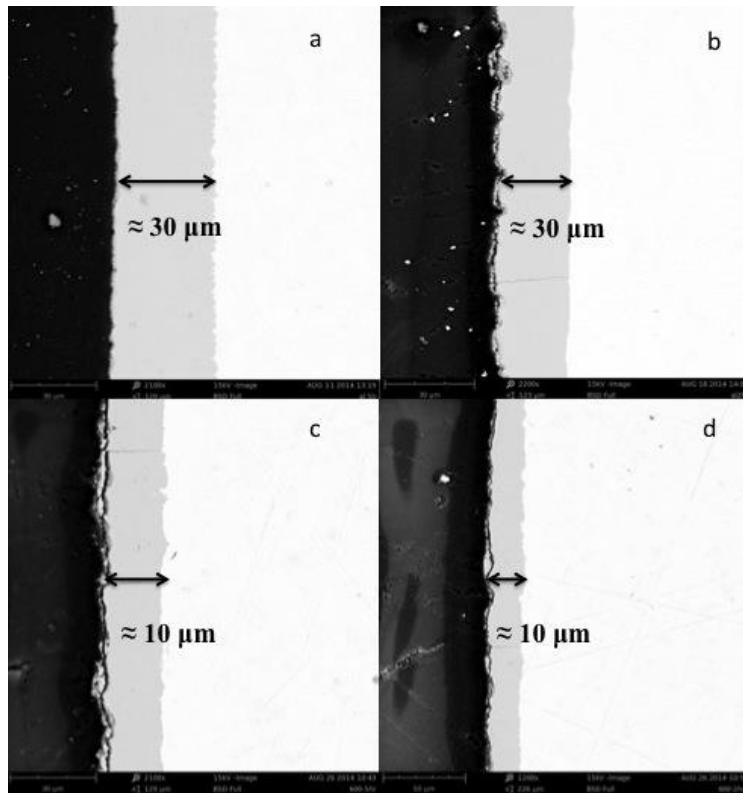
Figure 15. SEM cross-sections of aluminized layers by PCDC at a) 650°C for 5hrs, b) 650°C for 2hrs, c) 600°C for 5hrs and d) 600°C for 2hrs.
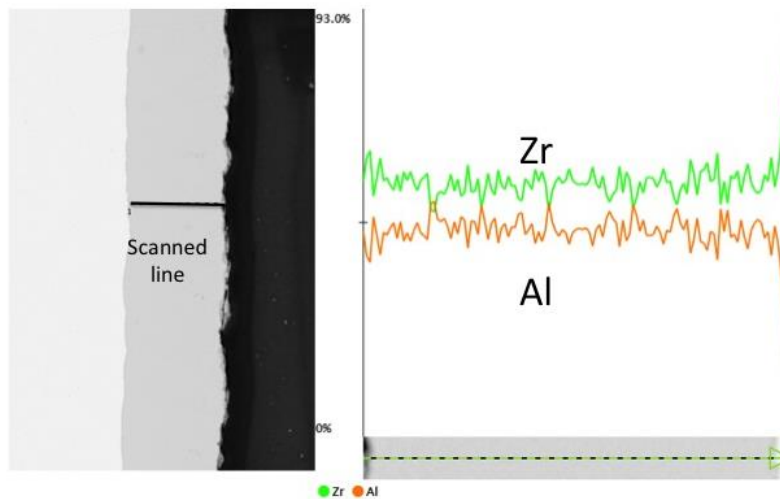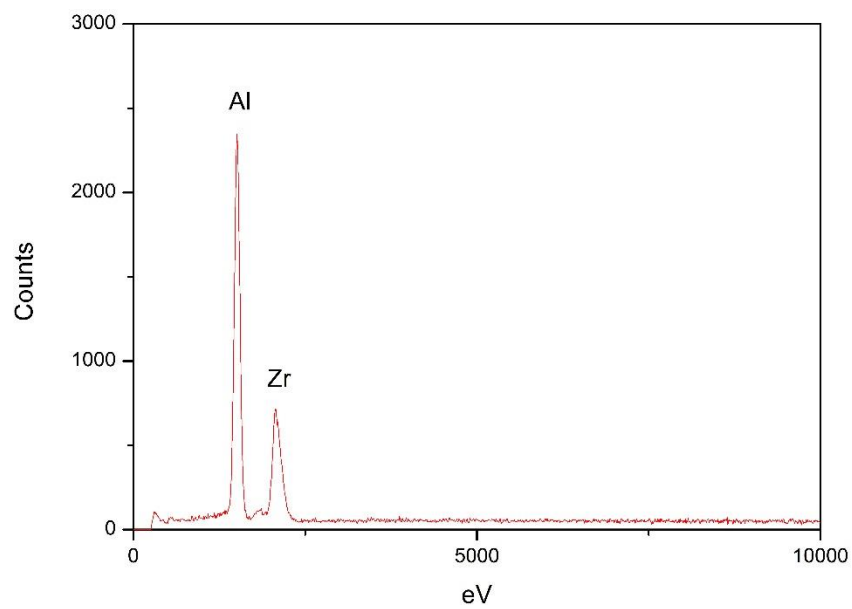
Figure 16. Cross-section EDS line-scan of aluminized layer
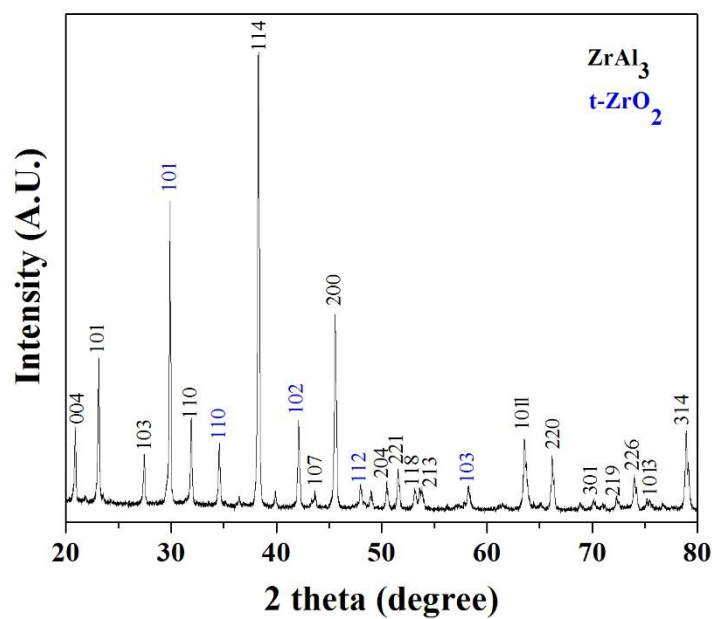
Figure 17. XRD pattern of the as-coated aluminized Zr-4

4.2 Autoclave corrosion testing analysis

Figure 18 shows the weight gain vs. time of aluminized Zr-4 and uncoated counter parts. The coated samples had higher surface roughness than the uncoated samples (mirror surface finish), the larger surface areas of aluminized Zr-4 could pick up more oxygen during initial oxidation. As a result, the initial weigh gains of coated samples were higher than that of uncoated ones. The weight-gain increment of aluminized samples after 10-day corrosion was also higher than that of the uncoated Zr-4, which indicates a relative instability of the coated Zr-4 oxidation product under pressurized water exposure.
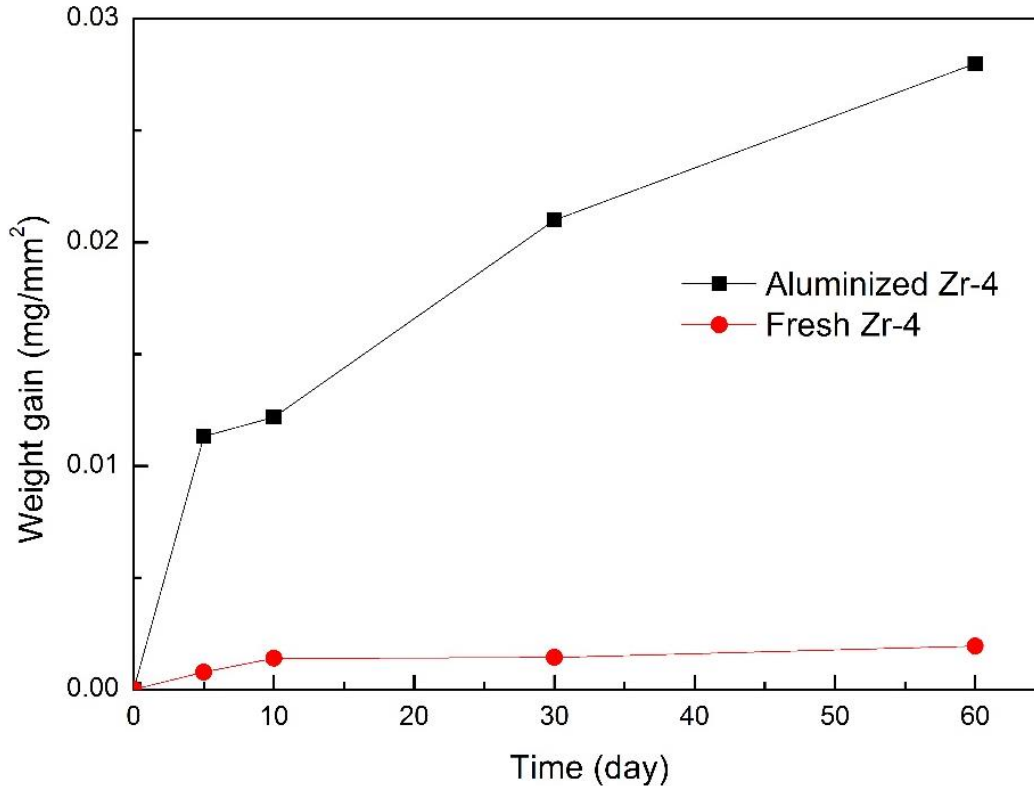
Figure 18. Weight gain vs. time plots for aluminized Zr-4 and fresh Zr4 in autoclave test at 360°C

Figure 19 show the SEM images of layer of surface scale with compact and uniform structure formed after aqueous exposure. The grain size is in the range of approximately 2 μm. Figure 20 of EDS mapping and spot spectrum prove the existence of aluminum and oxygen, while no zirconium. This is an indication of selective oxidation between Al and Zr.
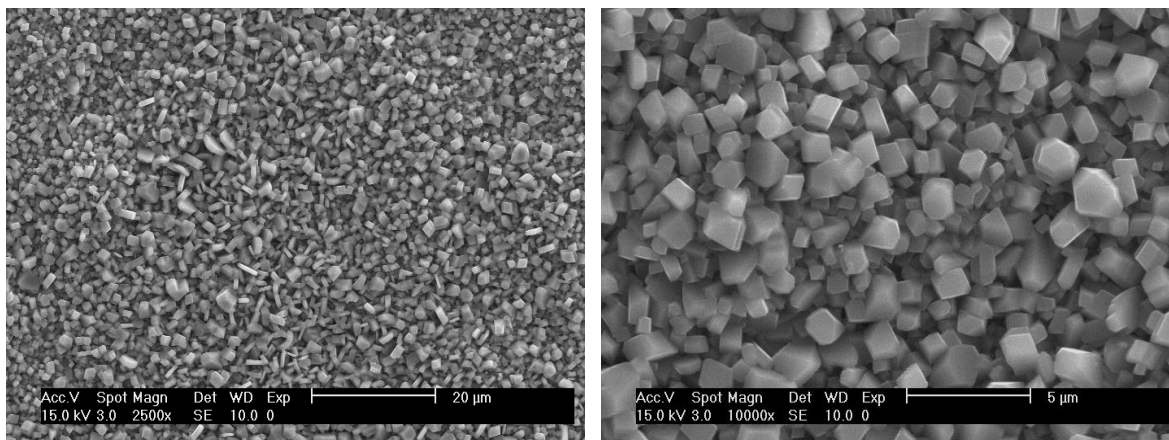
Figure 19. Surface morphology of aluminized Zr-4 after autoclave test
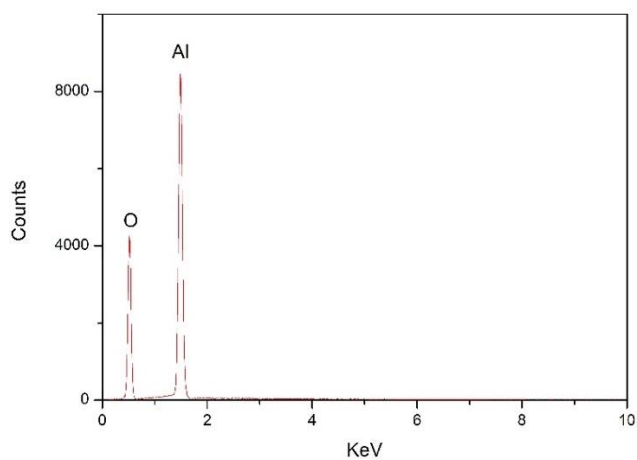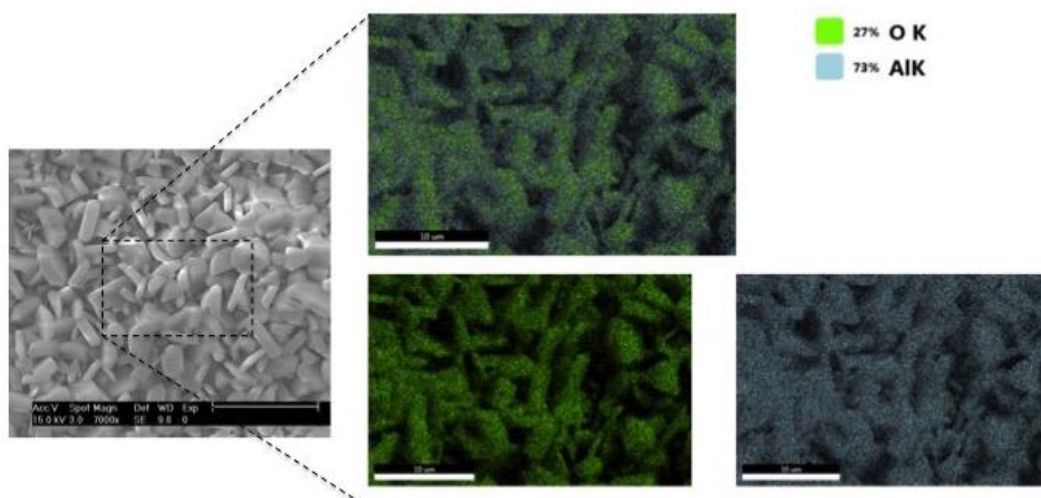
Figure 20. EDS mapping for the surface of aluminized Zr-4 after autoclave for 2 days

The Grazing Incident X-ray diffraction (GIXD) pattern (Figure 21) shows that the major corrosion product formed on the coating surface is Boehmite phase (AlOOH), which was one type of alumina hydroxide.

A possible hydrothermal reaction of metastable alumina ($Al_2O_3 + H_2O \rightarrow 2AlOOH$) could be responsible for the formation of hydroxide phase. TEM image and EELS mapping in Figure 22 also confirm the structure and elemental composition of the oxide scale.
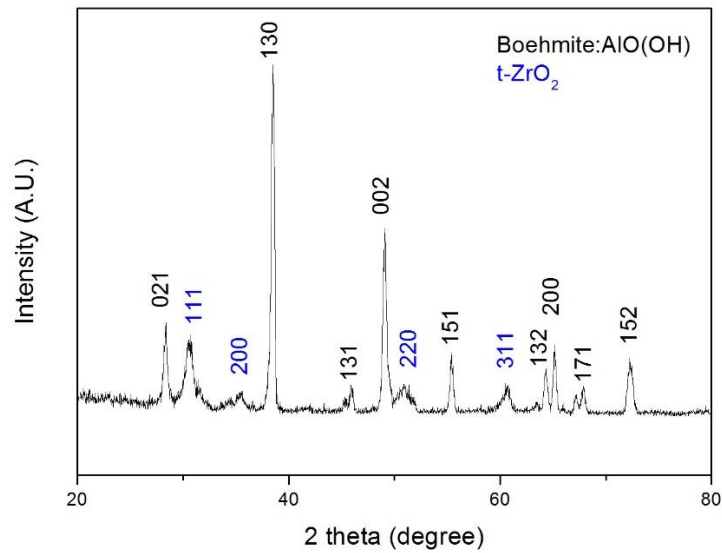
Figure 21. GIXD pattern of aluminized Zr-4 after autoclave test for 2 days

(A)

(B)
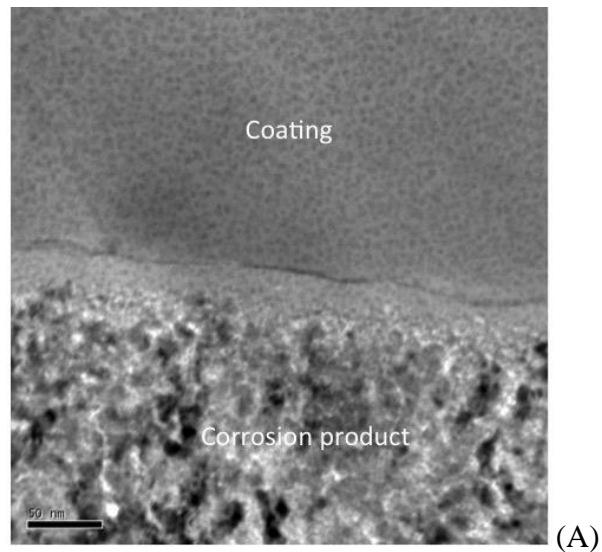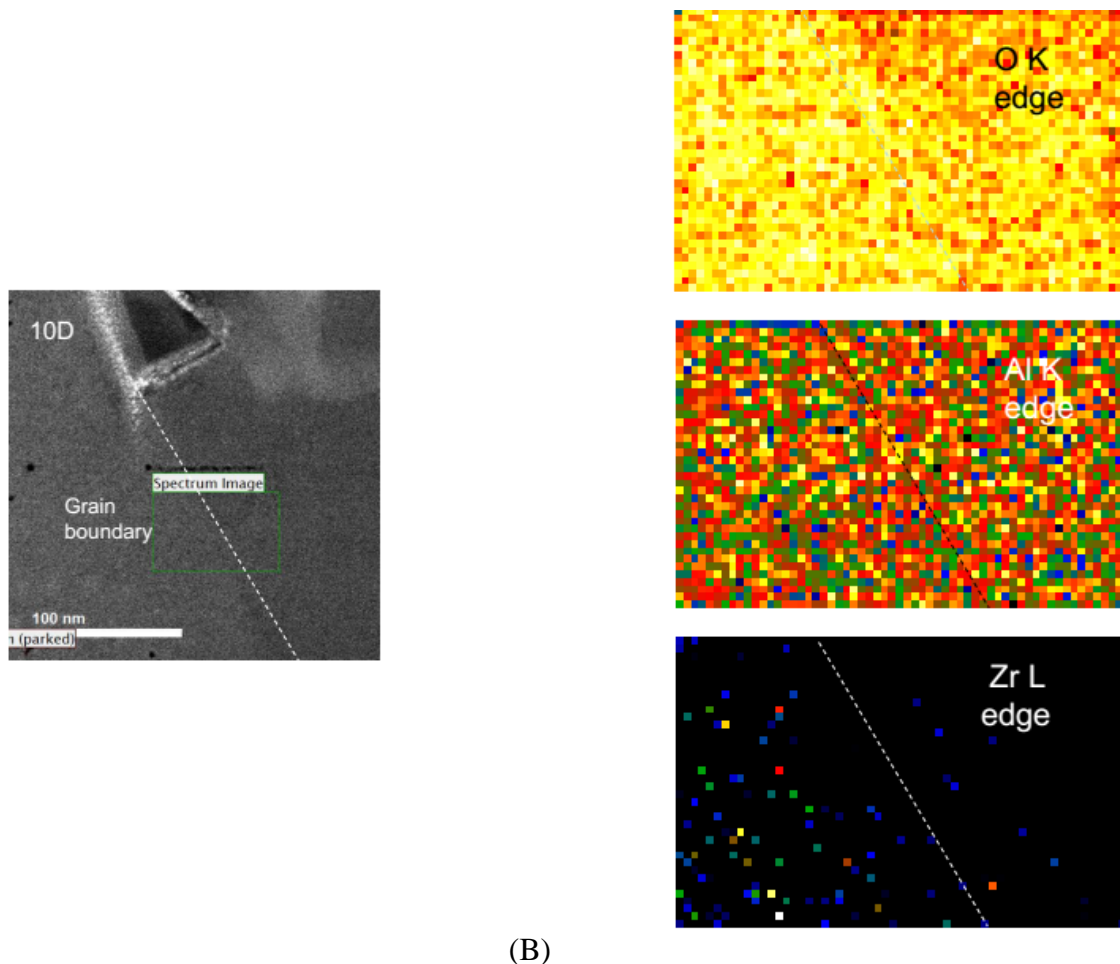
Figure 22. (A) Bright field TEM image surface scale from aluminized sample after 2-day corrosion, and (B) EELS mapping of the boehmite phase

Figure 23 shows cross-section SEM images of aluminized Zr-4 after 30 and 60 days of exposure. As indicated by the EDS line-scan, the surface region is Al-rich and Zr-depleted. Oxygen could penetrate the Boehmite scale and an oxides layer containing both Al and Zr was found between the surface scale and $ZrAl_3$ intermetallic. The thickness of the oxide scale increases with longer exposure, which indicates a growth of Boehmite scale. The low Al concentration in the oxides mixture region was an evidence of the outer diffusion of aluminum during oxidation. The oxidation of zirconium was delayed and Zr had been relatively protected by this phenomenon. The concentration of oxygen dropped significantly along the interface between $ZrAl_3$ and oxides mixture.
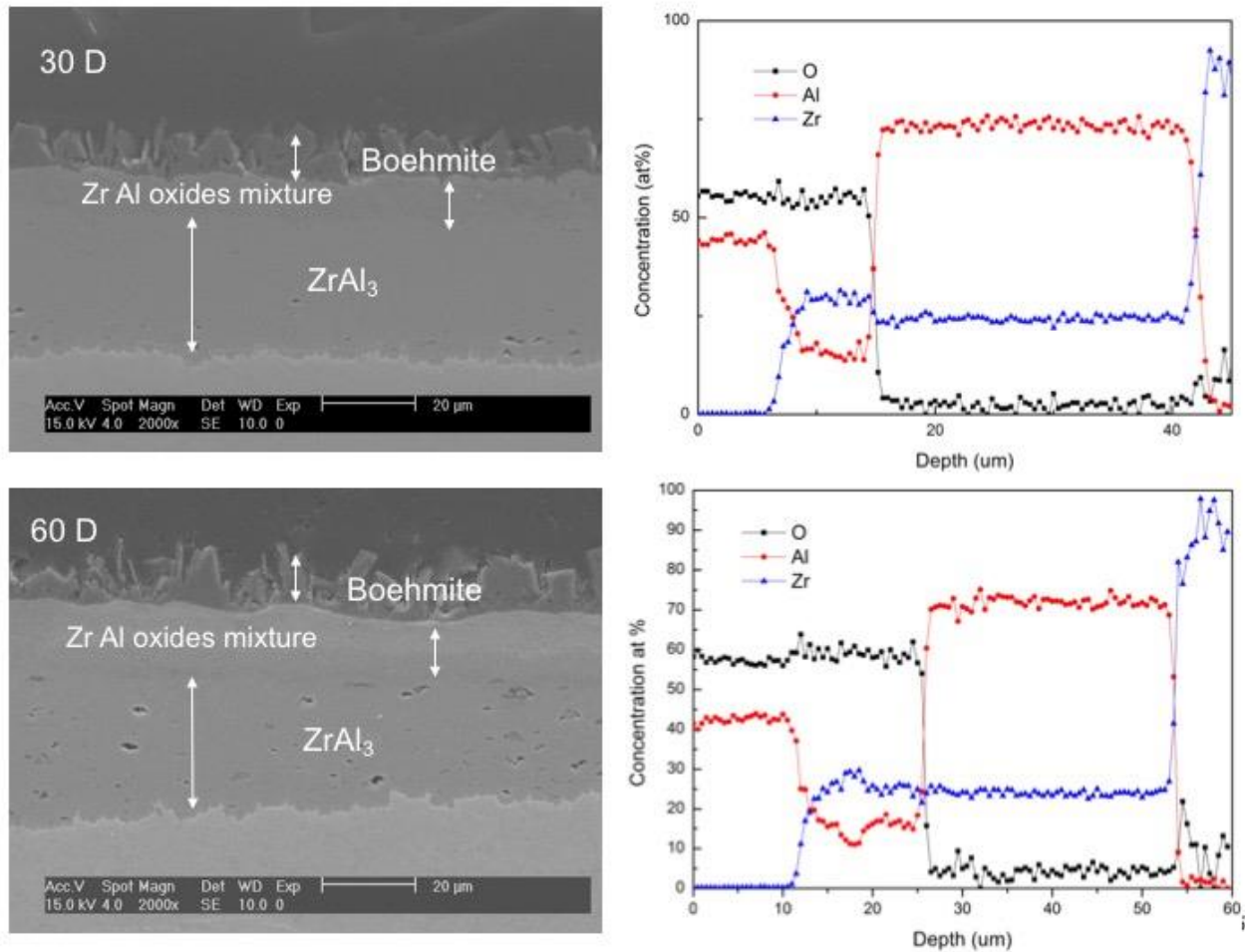
Figure 23. Cross-section EDS line-scan of aluminized Zr-4 after static autoclave test

4.3 Results from high temperature steam tests

Figure 24 shows the weigh-gain as a function of exposure time for each specimen under the 800 °C steam exposure. The aluminized and autoclaved samples exhibited decreased oxidation rates compared with the original Zr-4. The fresh Zr-4 specimens suffered severe spallation after 850 seconds of exposure, while no spallation were observed for as-coated and autoclaved samples. The Zr-4 samples clearly exhibited a linear oxidation growth that the oxidation rate remains constant during the test. The oxidation kinetics of as-coated samples basically obeyed a featured parabolic law. That is the oxidation rate decreased as the corrosion continued. As shown in Figure 24, the parabolic behavior has been well verified by the liner relation of square root of time and sample weight gain. As shown in Figure 25. the slope of linear fitting equation also given that the oxidation rate constant of parabolic kinetics is K=3.361. In this case, diffusion through corrosion products determined the overall oxidation rate. The surface morphologies of the coated samples exposed to steam for 12h and 20h are shown in Figure 26 . EDS spectra in Figure 27 shows the longer exposure promote less Zr in the oxide

surface layer, which indicating a selective oxidation between Al and Zr. The cross section SEM image and associated EDS line-scans in Figure 28 also indicate the enrich of Al in nearly the surface zone.
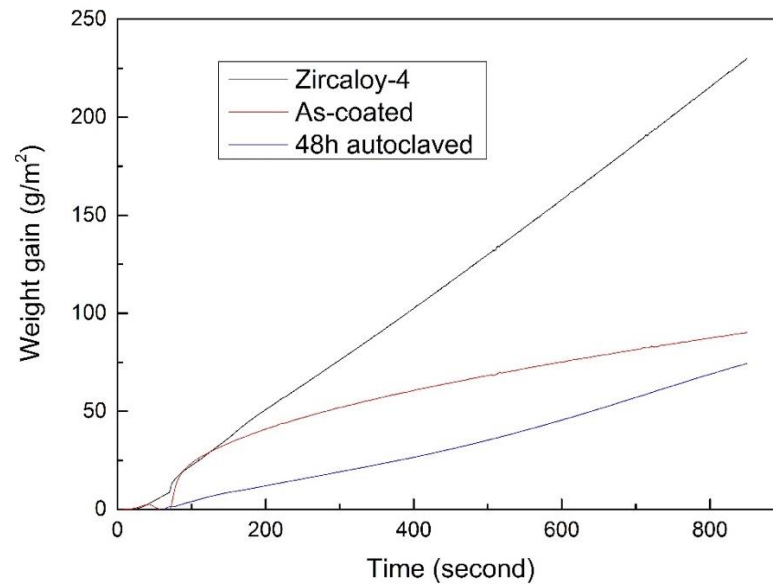

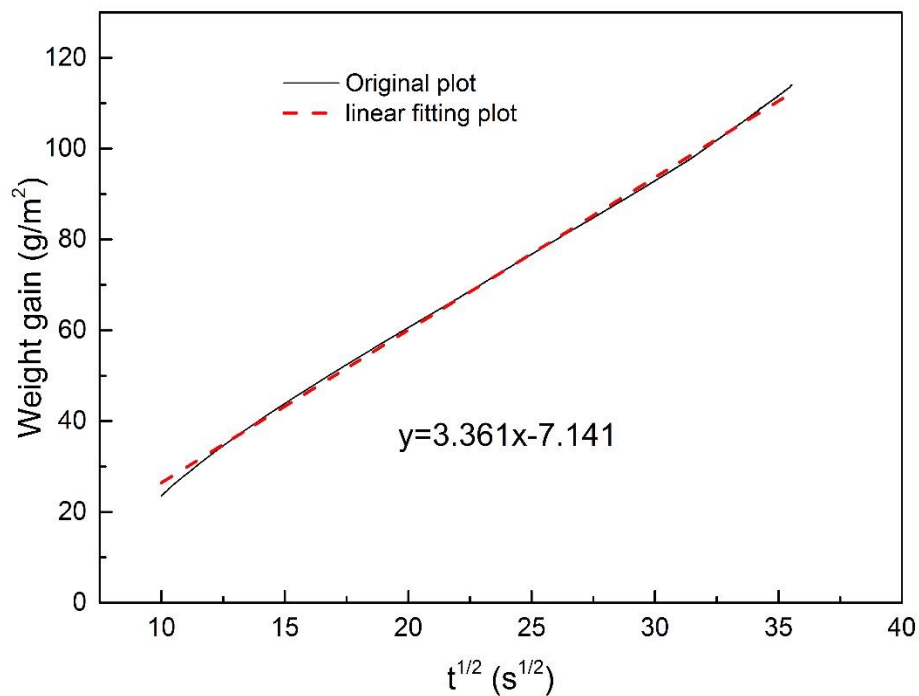Figure 24. Weight-gain vs. time plot of aluminized and fresh Zr-4 during 800 °C steam test

Figure 25. Square root of time vs. weight gain relation of as-coated Zr-4 and its linear fitting plot
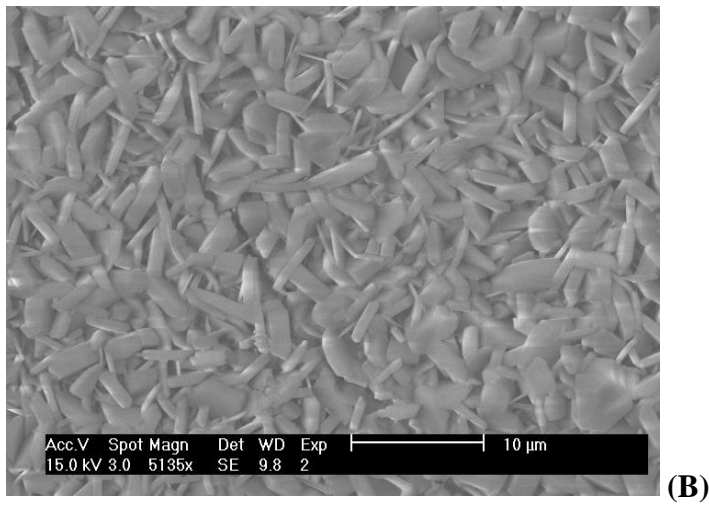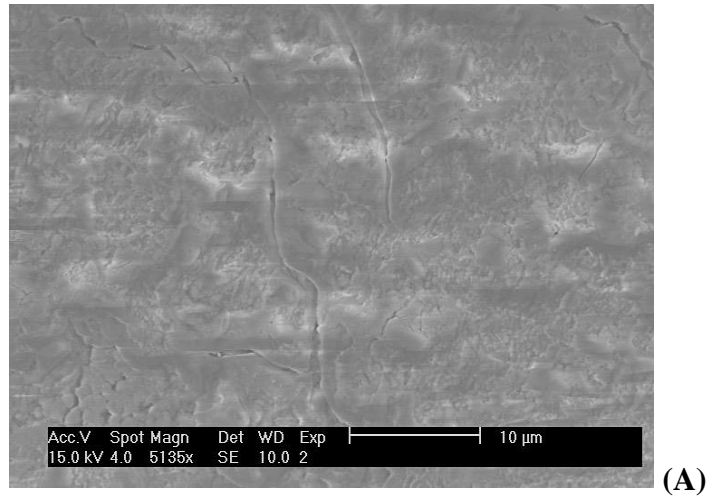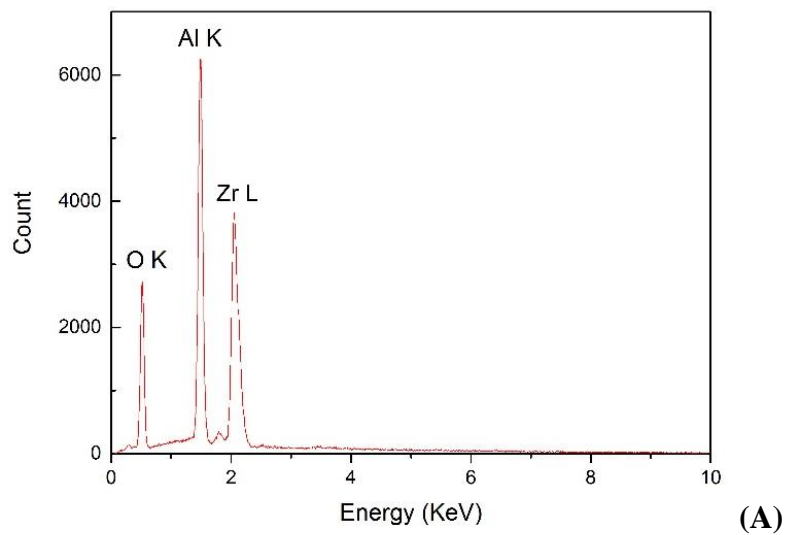
(A)

(B)

Figure 26. SEM image of surface morphology of as-coated sample after (A) 12h and (B) 20 h steam test

(A)
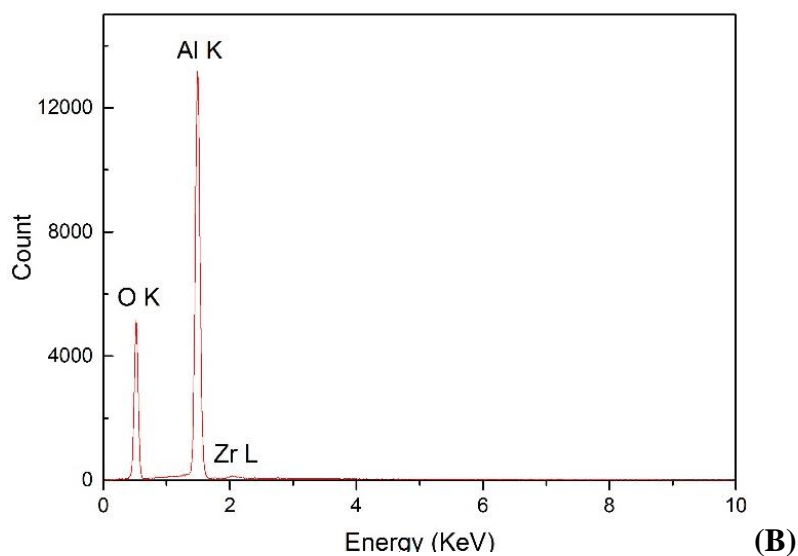
Figure 27. EDS from the steam exposed aluminized specimen (A) 12h and (B) 20h.
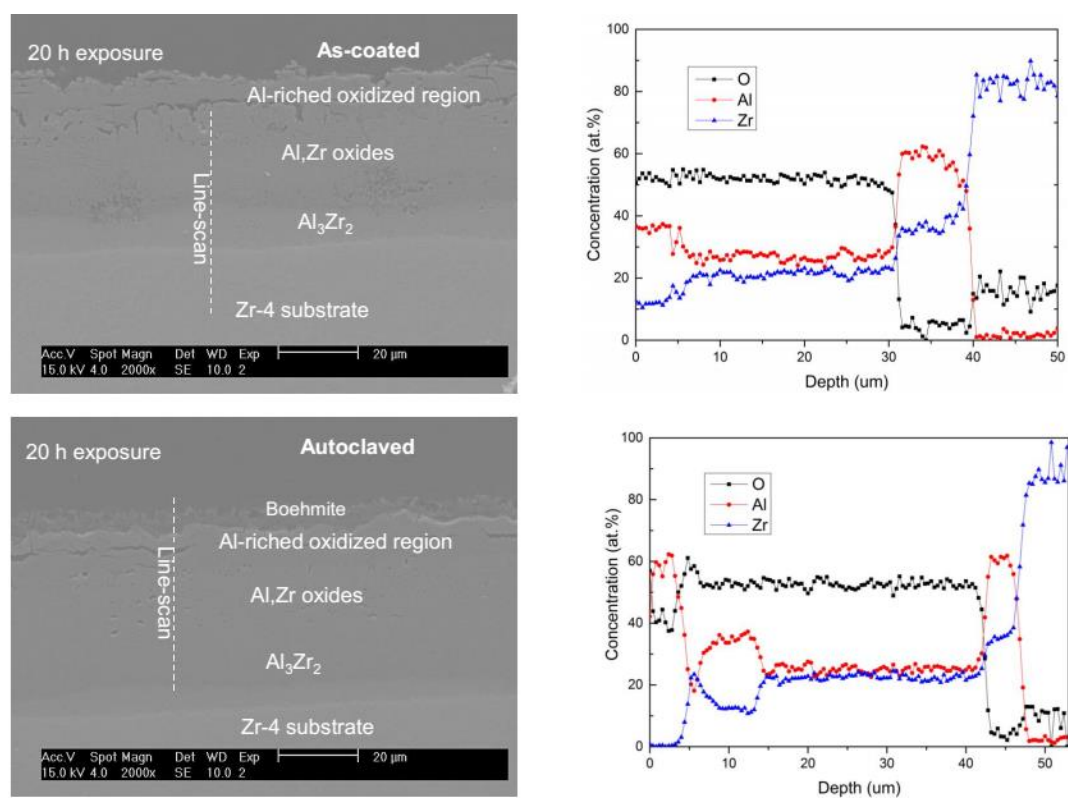
Figure 28. Cross section SEM and EDS line scans from the as-coated and autoclaved samples after 800C steam exposure.

5. SUMMARY AND CONCLUSION

In this work, aluminization via pack cementation diffusion coating (PCDC) technique was conducted in order to obtain a protective coating in high-temperature oxidation. The Zircaloy-4 samples were buried in a pack powder mixture inside alumina crucible. The pack powder mixture consisted of Al powder as the source element, ammonium chloride as the activator and alumina as the inert filler. The optimized mixture of powders is $25Al-2NH_4Cl-73Al_2O_3$ by weight percentage. Coating with a thickness of approximate 20μm was obtained through the aluminization process at 600°C for 20 hours. EDS and XRD analysis verified that the coating was a single $ZrAl_3$ intermetallic phase layer.

The corrosion performance of coated Zr-4 under normal LWR operating conditions was assessed using autoclave static corrosion tests. The tests were conducted at 360 °C, 2708 psi with controlled oxygen concentration at 250 ppb for up to 60 days. A surface scale of boehmite (γ-AlOOH), one type of aluminum hydroxide, was formed over the aluminized layer during the autoclave tests. The scales grew from 2μm (5 days) to 10μm (60 days) approximately while remaining intact during exposure. The weight-gain of aluminized samples was higher than that of the fresh ones (Fig 1) due to a larger surface area of the rough aluminzation surface (larger surface area for oxygen pickup) and a higher growth rate of boehmite scale in pressurized water.

The oxidation resistance of aluminized samples under off-normal LWR conditions were evaluated using 800 °C steam tests conducted on a simultaneous thermal analyzer (STA). Both as-coated samples and 48-hour autoclaved samples were tested in order to better simulate real scenarios that off-normal situations occur after cladding served in normal LWR conditions for a period of time. The aluminized and autoclaved samples exhibited decreased oxidation rates as compared with the uncoated Zr-4. The fresh Zr-4 specimens suffered severe spallation after 850 seconds of exposure, while no spallation was observed for as-coated or autoclaved samples. The Zr-4 samples clearly shows a linear oxidation growth that the oxidation rate remains constant during the tests. The oxidation kinetics of as-coated samples basically obeyed a featured parabolic law that the oxidation rate decreases with exposure time. In this case, diffusion through corrosion products determines the overall oxidation rate. The oxidation of autoclaved samples was even more suppressed as compared with as-coated ones due to the existence of the pre-formed boehmite scale. XRD and SEM analysis confirmed that the boehmite phase remained stable after the 800 °C steam tests, while cracks through the scale were observed in some areas during exposure, which could act as pathway for oxygen penetration.

In summary, the PCDC aluminized Zr-4 exhibits a relatively instability while free from spallation in normal LWR operating conditions; on the other hand, at off-normal conditions, the aluminization has shown an improved oxidation resistance over the uncoated Zircaloy-4 claddings.

Reference

1. Shirvington, P. J., & Cox, B. (1970). A study of charge transport processes during the oxidation of zirconium alloys. Journal of Nuclear Materials, 35(2), 211-222.

2. Hauffe, K. (1965). Oxidation of Metals Plenum. *New York.*

3. Yilmazbayhan, A., Motta, A. T., Comstock, R. J., Sabol, G. P., Lai, B., & Cai, Z. (2004). Structure of zirconium alloy oxides formed in pure water studied with synchrotron radiation and optical microscopy: relation to corrosion rate. Journal of Nuclear Materials, 324(1), 6-22.

4. P. Bossis, G. Lelievre, P. Barberis, X. Iltis, and F. Lefebvre, "Multi-Scale Characterization of the Metal-Oxide Interface of Zirconium Alloys,," in Twelfth International Symposium on Zirconium in the Nuclear Industry, Toronto, 2000, p.918.

5. J. Godlewski, "How the Tetragonal Zirconia is Stabilized in the Oxide Scale that is Formed on a Zirconium Alloy Corroded at 400 C in steam," 10th Int.Symp.on Zr in the Nuclear Industry, vol. STP 1245, pp. 663-686, 1994.

6. B. Cox, "Pore Structure in Oxide Films on Irradiated and Unirradiated Zirconium Alloys," Journal of Nuclear MAterials, vol. 148, pp. 332-343, 1987.

7. B. Cox and Y. Yamaguchi, "The Development of Porosity in Thick Zirconia Films," Journal of Nuclear Materials, vol. 210, pp. 303-317, 1994.

8. E. A. Garcia, "Dynamical diffusion model to simulate the oxide crystallization and grain growth during oxidation of zirconium at 573 and 623 K," Journal of Nuclear Materials, vol. 224, pp. 299-304, 1995.

9. Couet A., Motta, A., and Comstock R. J., (2015), Effect of alloying elements on hydrogen pickup in zirconium alloys, STP 1543 Zirconium in the Nuclear Industry, 479-514

10. Pecheur, D., Godlewski, J., Billot, P., & Thomazet, J. (1996). Microstructure of oxide films formed during the waterside corrosion of the Zircaloy-4 cladding in lithiated environment. ASTM SPECIAL TECHNICAL PUBLICATION, 1295, 94-112

11. T. Arima, K. Moriyama, N. Gaja, H. Furuya, K. Idemitsu, Y. InagakiJ. (1998), Oxidation Kinetic of Zircaloy-2 between 450 and 600C in oxidizing atmosphere Nucl. Mater., 257, 67-77

12. Coindreau, O., Duriez, C., & Ederli, S. (2010). Air oxidation of Zircaloy-4 in the 600–1000° C temperature range: Modeling for ASTEC code application.Journal of Nuclear Materials, 405(3), 207-215.

13. Aima. T, Masuzumi T., Furuya, H., Idemitsu K., and Inagaki Y., (2001), The oxidation kinetics and structure of the oxide film on Zircaloy before and after the kinetic transition, J.N. Matt., 294(1-2), 148-153

14. Cox, B. (1976). Oxidation of Zirconium and its Alloys. Advances in corrosion Science and Technology, Plenum, New York, 5, 173-391

15. Abriata, J. P., Garces, J., & Versaci, R. (1986). The O− Zr (Oxygen-Zirconium) system. Bulletin of Alloy Phase Diagrams, 7(2), 116-124.

16. S.J. Zinkle, K.A. Terrani, J.C. Gehin, L.J. Ott, L.L. Snead, Accident Tolerant Fuels for LWRs: A Perspective, Journal of Nuclear Materials (2013).

17. Cheng, T., Keiser, J. R., Brady, M. P., Terrani, K. A., & Pint, B. A. (2012). Oxidation of fuel cladding candidate materials in steam environments at high temperature and pressure. Journal of Nuclear Materials, 427(1), 396-400.

18. Pint, B. A., Terrani, K. A., Brady, M. P., Cheng, T., & Keiser, J. R. (2013). High temperature oxidation of fuel cladding candidate materials in steam–hydrogen environments. Journal of Nuclear Materials, 440(1), 420-427.

19. Terrani K.A., Zinkle S.J., and Snead L.L. (2014), Advanced oxidation-resistant iron-baed alloys for LWR fuel cladding, J.N.Matt., 448(1-3_, 420-435

20. Yueh, K., & Terrani, K. A. (2013). Silicon Carbide Composite for Light Water Reactor Fuel Assembly Applications. Journal of Nuclear Materials.

21. Van Aller, T. (1915). U.S. Patent No. 1,155,974. Washington, DC: U.S. Patent and Trademark Office.

22. Bose, S. (2011). High temperature coatings. Butterworth-Heinemann

23. Kung, S. C., & Rapp, R. A. (1989). Analyses of the gaseous species in halide-activated cementation coating packs. Oxidation of metals, 32(1-2), 89-109.

24. Goward, G. W., & Cannon, L. W. (1988). Pack cementation coatings for superalloys: a review of history, theory, and practice. Journal of engineering for gas turbines and power, 110(1), 150-154.

25. Goward, G. W. (1998). Progress in coatings for gas turbine airfoils. Surface and Coatings Technology, 108, 73-79.

26. Xiang, Z. D., Rose, S. R., & Datta, P. K. (2003). Codeposition of Al and Si to form oxidation-resistant coatings on γ-TiAl by the pack cementation process. Materials Chemistry and Physics, 80(2), 482-489.

27. Journal of Phase Equilibria Vol. 23 No. 5 2002

28. Kidson, G. V., & Miller, G. D. (1964). Journal of Nuclear Materials, 12(1), 61-69.

29. Laik, A., Bhanumurthy, K., & Kale, G. B. (2004). Intermetallics, 12(1), 69-74.

2.5   SRP/UF Hardness and Deformation Mechanisms of Zr-based Clad from Nanoindentation Simulations

Z. Lu, A. Chernatynskiy, M, J. Noordhoek, S. B. Sinnott and S. R. Phillpot, Nanoindentation of Zr by Molecular Dynamics Simulation, Journal of Nuclear Materials, 467, 742-757 (2015). http://dx.doi.org/10.1016/j.jnucmat.2015.10.042

Z. Lu, A. Chernatynskiy, M. J. Noordhoek, S. B. Sinnott and S. R. Phillpot, Nanoindentation of ZrO₂ and ZrO₂/Zr Systems by Molecular Dynamics Simulation, Journal of Nuclear Materials 486, 250-266 (2017). http://dx.doi.org/10.1016/j.jnucmat.2017.01.022

SRP/UF 1: Introduction

A better understanding of the basic deformation behaviors of Zr, and of zirconia-oxidized zirconium can be expected to help to improve the design and ultimately performance of clad. Nanoindentation is now an important and widely-used method used to probe the mechanical properties of materials at the nanoscale. In particular, it is commonly used for measuring basic mechanical properties such as hardness and elastic modulus [Oliver and Pharr, 1992]. With further development, other mechanical properties can also be determined using nanoindentation [Shuh 2006; Oliver and Pharr 2010]. To observe the nucleation and propagation of dislocations and evolution of defect structures, nanoindentation has been combined with electron microscopy to characterize deformation processes at the nanoscale in real time. Despite the development of in situ nanoindentation, full observation of the nucleation and propagation of dislocations at the atomic level remains challenging.

Here we used Molecular dynamics (MD) simulation to characterize the deformation processes under nanoindentation of Zr, and Zr with a thin ZrO_2 overlayer, representing the oxide. To understand a thick oxide more fully, we have also perform nanoindentation simulations on ZrO_2. The nanoindentation process has been studied using molecular dynamics in fcc [Kelchner et al. 1998; Nair et al.2008], bcc [Remington et al. 2014] and hcp [Verkhovtsev et al.2013] metals. Indeed, computational methods have played a very important role in elucidating the atomic-level mechanisms of dislocation nucleation and propagation under nanoindentation [Shuh 2006].

SRP/UF 2: Nanoindentation of Zr

We perform MD simulations of nanoindentation of a Zr single crystal. Two different empirical potentials were used in the simulation: a Charge Optimized Many Body (COMB) potential [Noordhoek et al. 2013] and the Mendelev and Ackland Embedded Atom Method (MA EAM) potential [Mendelev and Ackland 2007]. All simulations were performed with the LAMMPS code.

The method used to calculate hardness is shown in Fig. 1 SRP/UF. Figure 2 SRP/UF shows the results of our MD simulations of nanoindentation $[11\bar{2}0]$ orientated Zr. The load indentation curve in Fig. 2a SRP/UF resembles the schematic in Fig. 1 SRP/UF. In the elastic region, hardness (H), as defined in as H=P/A (P is the load and A the area) is a strong function of the indentation depth, as shown in Fig. 2b

SRP/UF. However, once the plastic deformation begins, its value stabilizes and only fluctuates slightly, reflecting the various operant deformation processes.
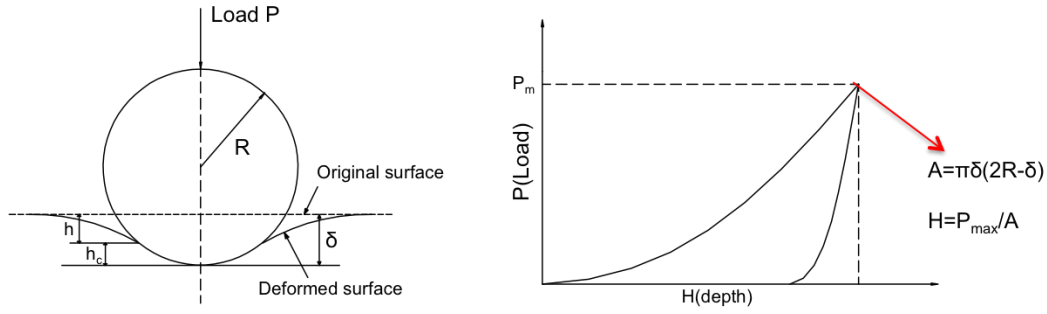

Fig. 1 SRP/UF: Method used to calculate hardness after reference [Oliver et al.1992, 2010].
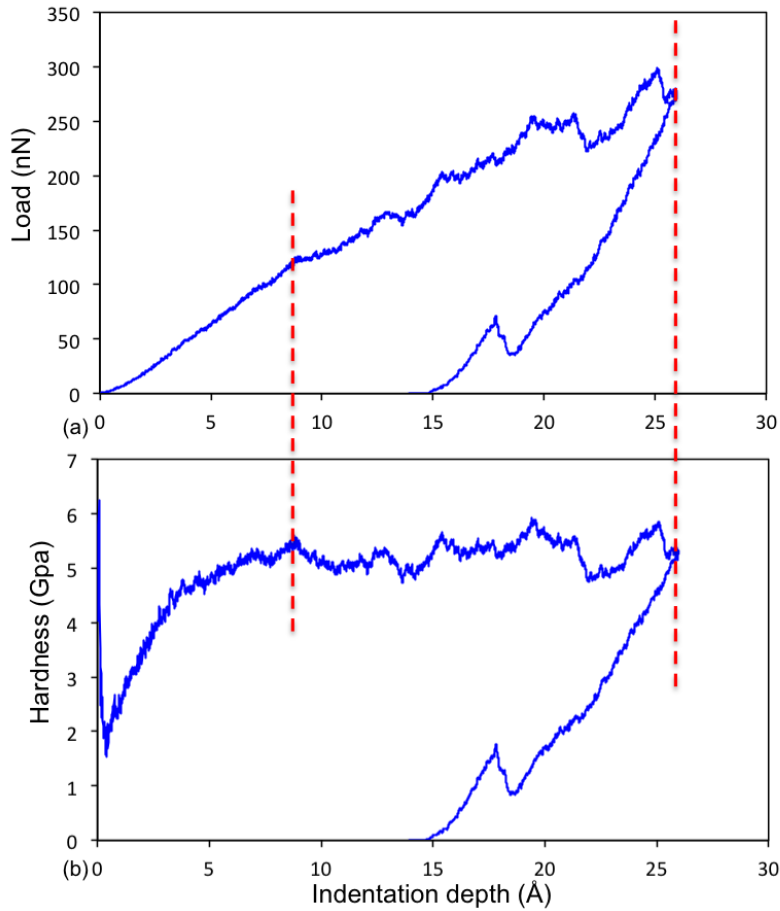

Fig. 2 SRP/UF: Relationship between (a) load and (b) hardness and indentation depth for $[11\bar{2}0]$ orientated Zr crystal. The reported hardness and its uncertainty are obtained for depths bounded by the red dotted lines.
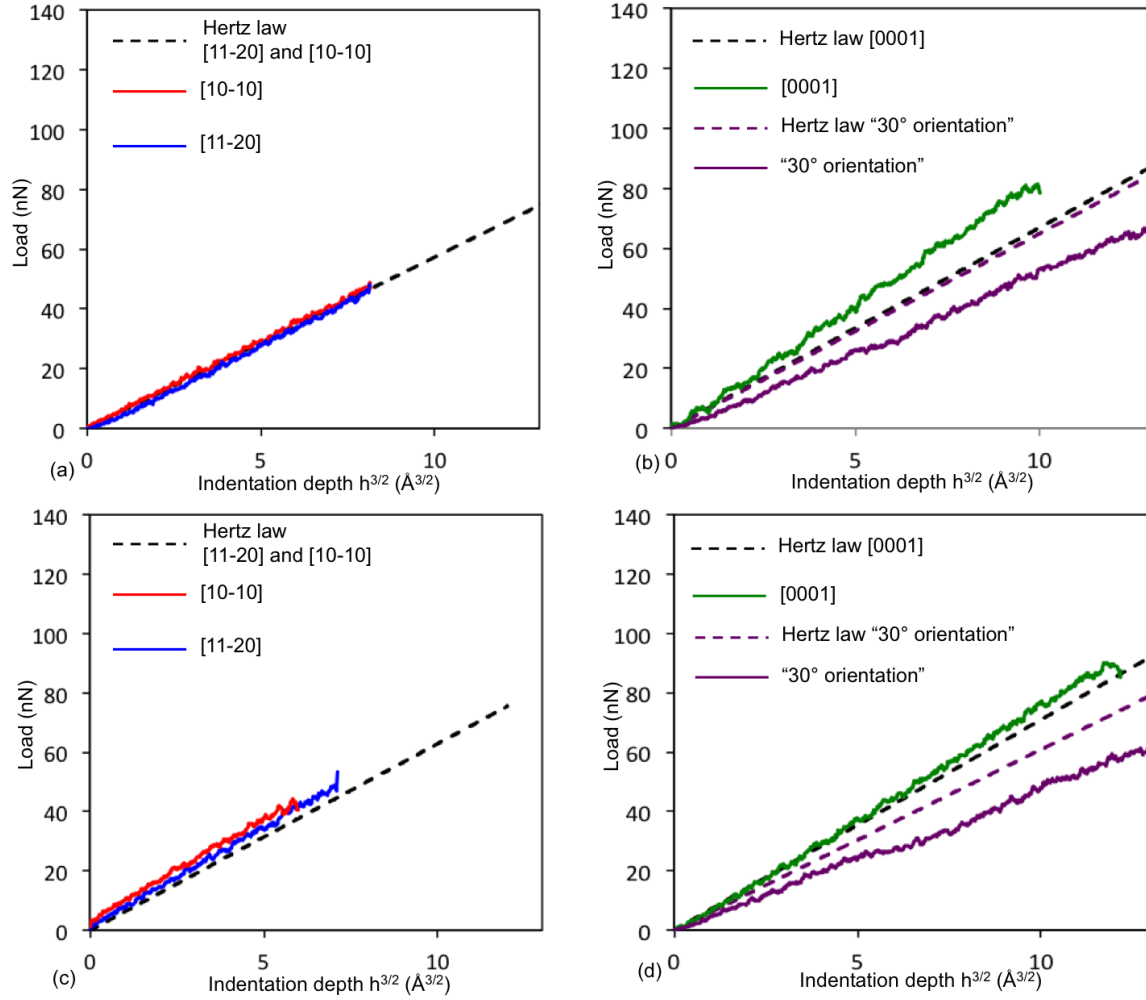
Fig. 3 SRP/UF: Load-displacement curves in the elastic region. (a) MA EAM $[11\bar{2}0]$ and $[10\bar{1}0]$ orientation, (b) MA EAM [0001] orientation and 30° orientation, (c) COMB $[11\bar{2}0]$ and $[10\bar{1}0]$ orientation (d) COMB [0001] orientation and 30° orientation. All the data from the MD simulations are fitted using a moving average method.

In indentation of a single crystal, the crystallographic orientation of the indented surface will promote some deformation modes and hinder others, thus eliciting different mechanical responses [Tenckhoff 1988]. In this work, four different orientations are chosen to perform the indentation tests: [0001], $[11\bar{2}0]$, $[10\bar{1}0]$ and the [0001] orientation rotated by 30° about the c-axis, commonly used in zircaloy [Murty 2006]. From a crystallography point of view the $[11\bar{2}0]$ and $[10\bar{1}0]$ orientations promote prismatic <a> slip and basal <a> slip. The [0001] orientation promotes pyramidal <a+c> slip. The 30° orientation promotes pyramidal <a+c> slip and basal <a> slip. The load-displacement curves for the two potentials in the

elastic region are shown in Fig. 3 SRP/UF, while complete load-displacement curves are shown in Fig. 4 SRP/UF. The hardness values calculated from these data are shown in Fig. 5 SRP/UF. The experimental hardness value is for a Zr-1Nb-0.05Cu zirconium alloy [Yan et al. 2015] is also shown. The polycrystalline zirconium alloy has grain boundary structures and a wide range of grain orientations, which can make it easier for the dislocations to nucleate. So it is reasonable that the hardness value of the tested zirconium alloy is smaller than that of the simulation results.
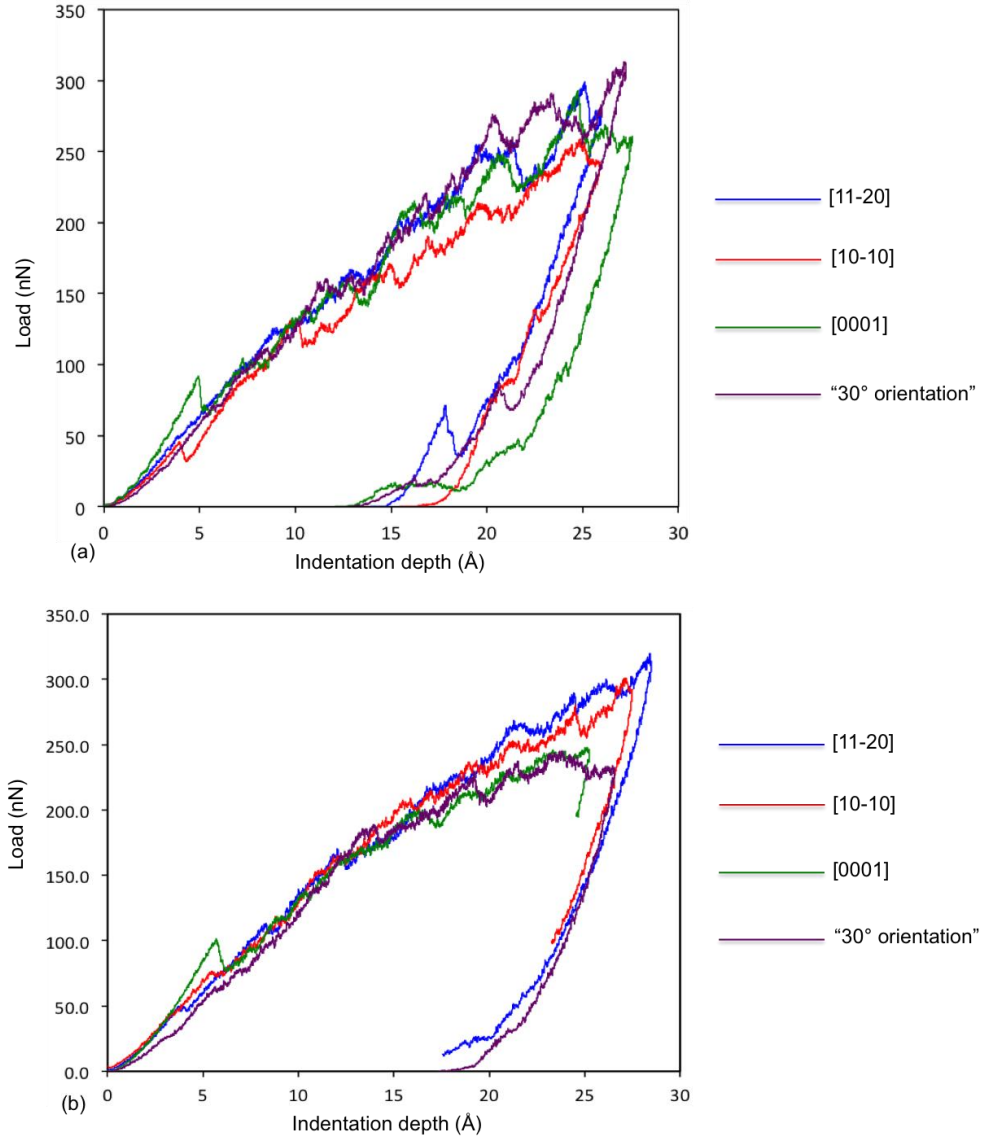
Fig. 4 SRP/UF: Load-displacement curve of four different orientations for the nanoindentation simulation: (a) MA EAM potential, (b) COMB potential.

Before the first dislocation activity, the characteristic of the load-displacement curve lies in the elastic regime. The MD results are consistent with the Hertz analysis; in particular, in the elastic regions shown in Fig. 3 SRP/UF, the load varies with the predicted as $h^{3/2}$ dependence for both potentials and for all four surface orientations. The derived E* values indicate that the slope of the load-displacement curve for the [0001] orientation should be steeper than that of the. $[11\bar{2}0]$ orientation and $[10\bar{1}0]$ orientations. From classical theory, $E^*_{[11\bar{2}0]} = E^*_{[10\bar{1}0]}$; thus the load displacement curves of $[11\bar{2}0]$ and $[10\bar{1}0]$ orientations should be the same in the elastic region. For the MA EAM potential Fig. 3(a) SRP/UF, they match exactly with each, while for the COMB potential, Fig. 3(c) SRP/UF, there is a small deviation. The $[11\bar{2}0]$ and $[10\bar{1}0]$ orientations from the simulations also quite closely match the Hertz law for the two potentials, particularly for the MA EAM potential.

By contrast, the load-displacement curves obtained from the simulations for the [0001] orientation are steeper than the Hertz Law predictions for both potentials, with the disagreement being larger for the MA EAM potential than for the COMB potential. For the 30° orientation, the load-displacement curves predicted by the Hertz Law are steeper than the simulation results for both potentials. Although the deviation of the simulation results from the Hertz Law predictions for [0001] and the 30° orientation are slightly larger, the load-displacement curves still show elastic behavior. In summary, the overall elastic response can be quite well represented by Hertz theory.

The plastic deformation begins at the first load drop in the load-displacement curve. It is most pronounced for the [0001] orientation, and less so for the other orientations considered. As shown in Fig. 4(a) SRP/UF for the MA EAM potential, the 30° orientations support the largest load, while the $[10\bar{1}0]$ support the lowest load. As shown in Fig. 4(b)SRP/UF for the COMB potential, the $[11\bar{2}0]$ orientation supports the largest load, while the 30° orientation supports the lowest load. The load drops in the load-displacement curve represent the plastic deformation events throughout the indentation simulation. The magnitude of the load drop and the indentation depth where the load drop happens all varies slightly for different orientations of different potentials. One obvious similarity for both potentials is that the [0001] orientation has the largest first load drop at around 5 Å indentation depth. The details of the plastic deformation events are discussed later.

The comparison of hardness for the four simulated orientations of two potentials is shown in Fig. 5 SRP/UF. The 30° orientation (MA EAM) and $[11\bar{2}0]$ orientation (COMB) have the highest hardness values, while the $[10\bar{1}0]$ orientation (MA EAM) and the 30° orientation (COMB) have the lowest. However, as shown in Fig. 4 SRP/UF, the hardness fluctuates with the indention depth. So when taking into account the fluctuations represented by the errors bars in Fig. 5 SRP/UF, the difference of the hardness value for different orientations of the two potentials is not significant.
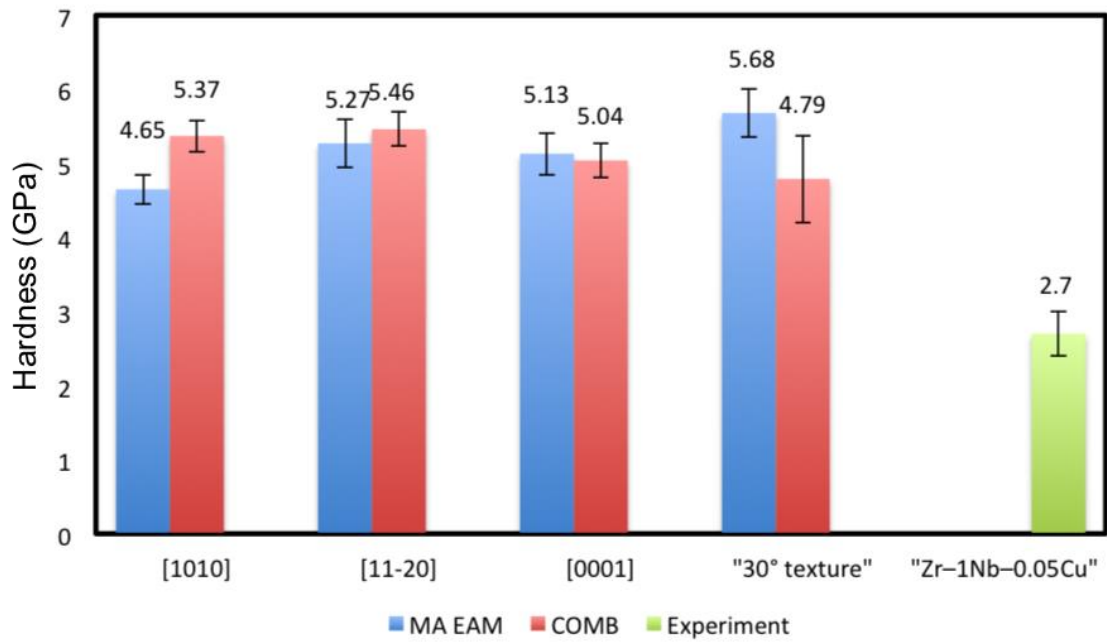
Fig. 5 SRP/UF: Hardness of four orientations using MA EAM and COMB potential. The experiment value is from reference [Yan et al. 2015].

MD simulation has the capability to characterize the plastic response of the system with atomic-scale resolution. From the deformed structures of four different orientations shown in Fig. 6 SRP/UF, we can see that dislocation loops are commonly activated for the MA EAM potential. The dislocation loop consists of partial dislocations on the basal plane and dislocations on the prismatic planes. Dislocation loops are only observed traveling along the <a> direction on prismatic plane inside the bulk or on the surface in this nanoindentation simulation. The dislocation loop observed in this nanoindentation turns out to be the most stable interstitial loop in Zr, and has been observed in simulation work [Serra and Bacon 2010]. They found that the rectangular self-interstitial loop that consists of prismatic dislocations and basal partial dislocations has the lowest formation energy and highest binding energy [Serra and Bacon 2010].

For the $[10\bar{1}0]$ and $[11\bar{2}0]$ orientations, as shown in Figs 6(a) and 6(b) SRP/UF, the dislocation loops for under the indenter and travel along the <a> direction on the prismatic plane. With regards to the plastic deformation contribution, the Schmid factors for prismatic and basal slips along<a> are commonly observed in these nanoindentation simulations. For the 30° and [0001] orientations, as shown in Figs. 6 (c) and (d) SRP/UF, dislocation loops form under the indenter. For both orientations, the dislocation loops only travel along the surface. The second basal partial dislocation cannot nucleate to form a full

73

dislocation loop. It is thus not surprising that dislocation loops are not observed to leave the surface to travel inside the bulk. Pyramidal slip is observed along with the dislocation loops.

Considering the elastic deformation, the reduced modulus of the [0001] orientation has the highest value among the four orientations. The reduced modulus of the 30° orientation (129 GPa) lies between those of the [0001] orientation (133 GPa) and $[11\bar{2}0]$ orientation (114 GPa) but very close to [0001] orientation. Thus, from the viewpoint of elasticity, the [0001] orientation should have the highest load response and the steepest slope of the load-displacement curve in the elastic region, which agrees with the simulation results as shown in Fig. 4 (a) SRP/UF.

Comparing the details of the plastic deformation of these two orientations may give some insights to the difference in the magnitude of the load drop. As shown in Fig. 6 (c) and (d) SRP/UF, the dislocation density is much higher for the [0001] orientation than for the 30° orientation. In addition, the calculations from the Crystal Analysis Tool show that the [0001] orientation has a total length of dislocation of 1132 Å compared to 765 Å for the 30° orientation, confirming that the 30° orientation has the lowest dislocation density. This lower dislocation density is consistent with the small load drop. The small dislocation density combined with the moderately reduced modulus results in the largest hardness value (5.68 GPa) for the 30° orientation among the four orientations. Although it has the largest reduced modulus, the [0001] orientation has a hardness of only 5.13 GPa due to the relative ease with which plastic events are nucleated. Furthermore, this ease of nucleation for [0001] orientation is consistent with the crystallography: the dislocation loop glides in the <a> direction on prismatic plane, which is parallel to the surface for the [0001] orientation.

A corresponding analysis was performed for simulations using the COMB potential. For all four orientations, the COMB nanoindentation simulations display prismatic dislocations rather than basal dislocations. Because the stacking fault energies for the COMB potential is higher than for the MA EAM potential [Luet al. 2015], the dislocation density for MA EAM potential is higher than COMB potential. This can be attributed to differences in the stacking fault energies and the energy barriers to their motion. DFT calculations generally offer higher materials fidelity than calculations with classical potentials; thus the DFT results should more closely match experiment. While nanoindentation with DFT is not computationally feasible, the fact that the energy barrier ratio for DFT lies between the values for COMB and MA EAM suggests that formation and propagation of dislocation loops in Zr metal should take place, but not to the same degree as predicted by MA EAM potential.
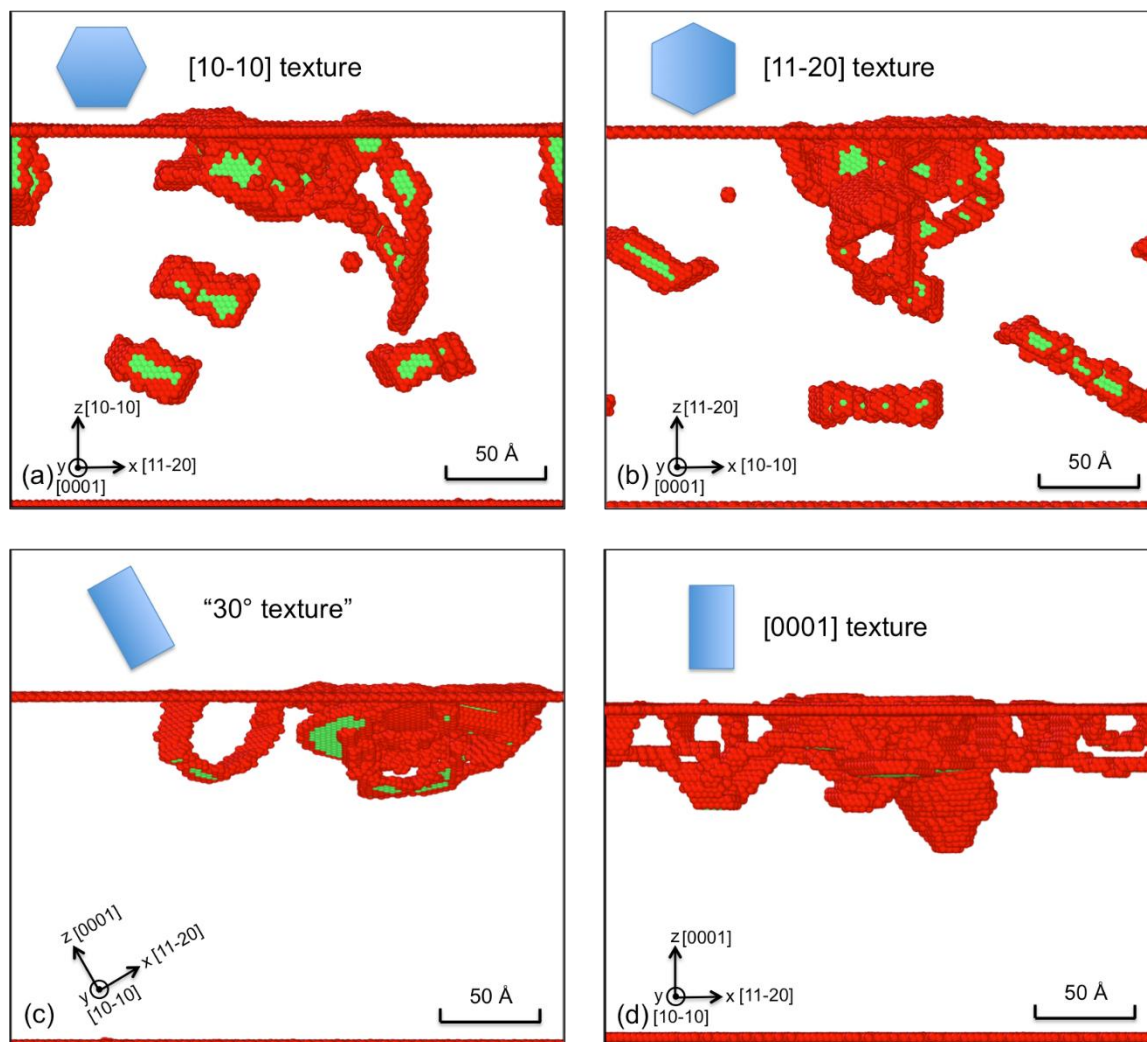
Fig. 6 SRP/UF: Common neighbor analysis of Zr indentation at around 26 Å indentation depth using MA EAM. (a) $[10\bar{1}0]$ orientation (b) $[11\bar{2}0]$ orientation (c) 30° orientation along c-axis. (d) [0001] orientation. Red atoms represent the disordered atoms. Green atoms represent the atoms in fcc environment. The atoms in hcp environment are not shown.

SRP/UF 3: Nanoindentation of ZrO_2/Zr and ZrO_2

Under reactor operating conditions, the cladding experiences extremes of temperature, stress, radiation and corrosion. One of the major products of the corrosion process is zirconia. The three zero pressure phases of zirconia display monoclinic, tetragonal and cubic symmetry; the tetragonal phase and monoclinic phase are derivatives of the cubic fluorite phase [Leger et al. 1993]. At ambient pressure, the monoclinic phase is stable at room temperature, transforming to the tetragonal phase at 1205°C, which transforms to the cubic phase at about 2370°C. The cubic phase of zirconia can be stabilized at room temperature by doping, most prominently with Y_2O_3 at concentrations of 8-10 mol% [Messerschmidt et al. 1997].

At the beginning of the indentation test, the system deforms elastically. As shown in Fig. 6 SRP/UF, the load vs. $h^{3/2}$ curves obtained from the simulation are linear, which represents elastic behavior in the Hertz Law. The reduced modulus calculated using the COMB3 potential predicted elastic constants for the [110] and [100] orientations are 370 GPa and 468 GPa, respectively. The slope of the [100] orientation from simulation is initially slightly steeper than that of the [110] orientation, which is consistent with the order predicted by the Hertz law. However the [100] orientation exhibits a softening with increasing load. The slope of the load vs. $h^{3/2}$ curves calculated from the Hertz Law is steeper than those from the simulations. The above difference may be caused by the effects of system size observed in the Zr nanoindentation simulations described above.

Having established that the elastic part of the indentation obeys Hertz Law, we can rescale the length scale of the MD system size to allow for direct comparison with experimental results that are obtained for much larger indenters (350nm) and indentation depths at the micrometer scale. Our simulation results for ZrO_2 are compared to the nanoindentation experiments carried on YSZ with 10 mole% yttria [Fujikane et al. 2007]. According to an experimental study of YSZ with yttria doping ranging from 11% to 18% mole%, the Young's modulus and shear modulus decreases as the mole% of yttria increases, while the anisotropy factor increases as the mole% of yttria increases [Gadag et al. 2006].

As illustrated in Fig. 7 SRP/UF, the rescaled load-displacement curves from the MD simulations match quite well with those from the indentation experiments on single crystal YSZ. The simulation results for the [110] orientation show the better match with the experimental data. For the [100] orientation, the simulation results agree well with the experiment for low loads prior to the softening discussed above. This softening could also be caused by system size effects, or could arise from the surface reconstruction.
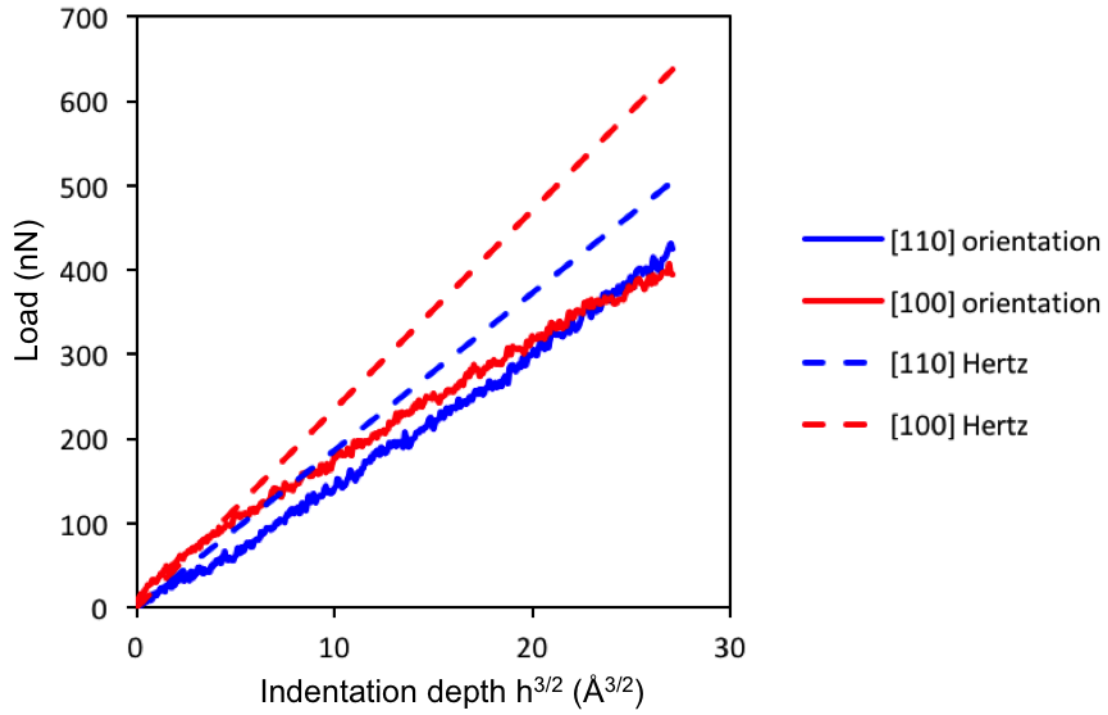
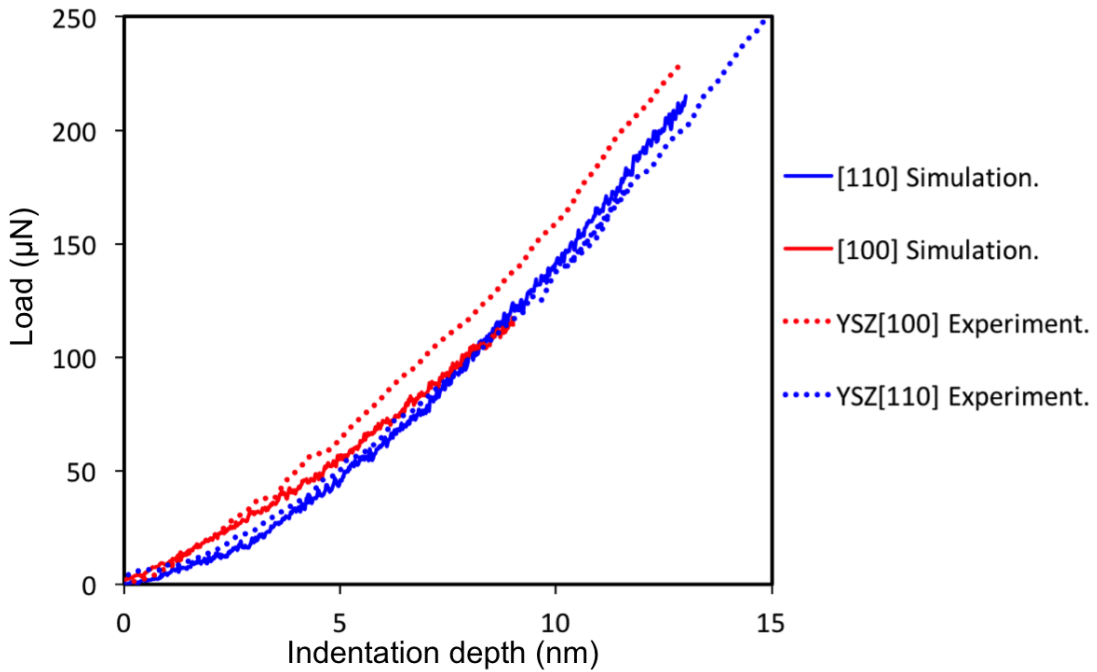Fig. 6 SRP/UF: Load vs. $h^{3/2}$ in the elastic region for [110] and [100] orientations.

Fig. 7 SRP/UF: Comparison of load-displacement curves from rescaled MD data and experimental data. The experimental data shown were obtained from reference [Fujikane et al. 2007].

The first load drop typically represents the initiation of plastic deformation. As indicated in Fig. 8 SRP/UF, the first load drop for the [110] orientation takes place at an indentation depth of ~13Å, while for [100] orientation, the first load drop is at ~10 Å. After rescaling, the first load drop should be at ~10nm for the [100] orientation and ~13nm for the [110] orientation. The earlier yield for the [100] orientation simulation agrees reasonably well with the indentation experiments on YSZ, for which the first load drop for the [100] and [110] orientations occurs at 14nm and 22nm, respectively [Fujikane et al. 2007]. The simulated yield strength of the [110] orientation (~800nN) is twice as much as that of the [100] orientation (~400nN). This is also consistent with the experimental results [Fujikane et al. 2007] where the yield strength of the [110] and [100] orientations are ~500μN and ~250μN, respectively.
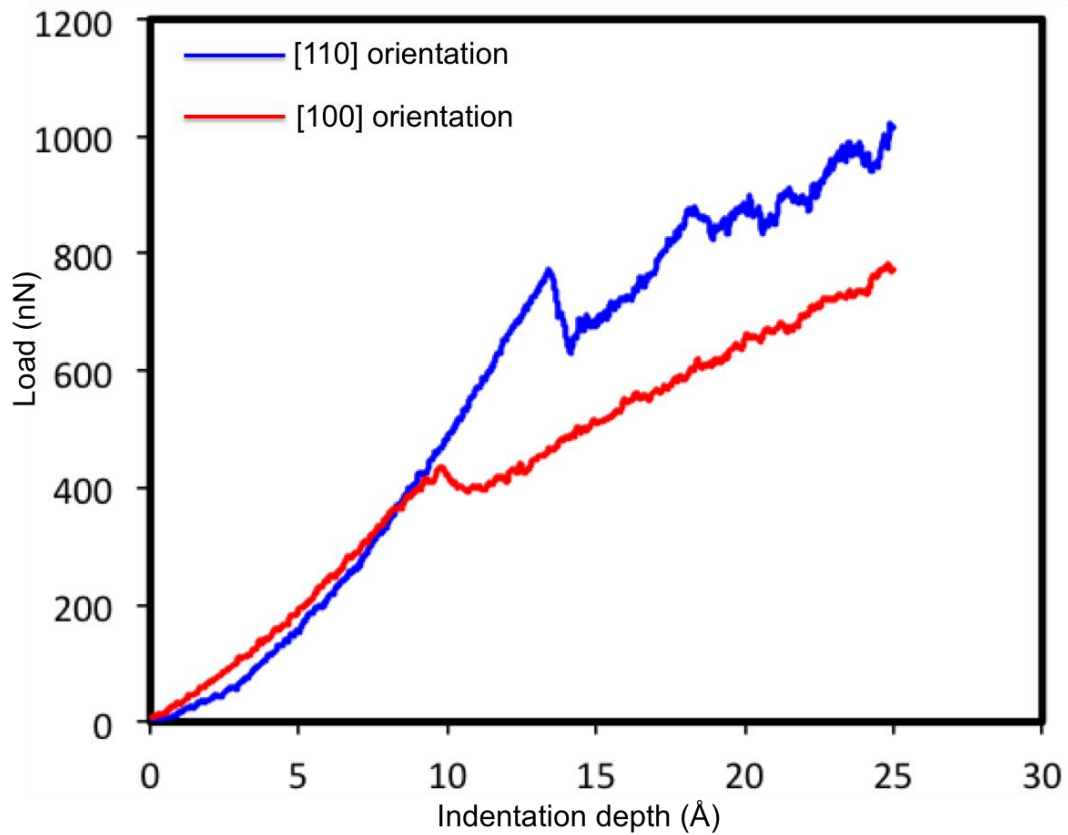
Fig. 8 SRP/UF Load-displacement curves for [110] and [100] orientation under indentation at 300K.

The deformed atomic structures at an indentation depth of 25Å are provided in Fig. 9 SRP/UF. The atomic pileups represented by the miscoordinated atoms in Fig. 8 SRP/UF are seen in both the [110] and [001] orientations. It is evident that the shapes of the deformed regions are very different for the two orientations. The origin of this difference resides in the anisotropy and the limited slip systems available in ZrO_2. For the [110] orientation, as we can see from the side view (001) plane, Fig. 9(a) SRP/UF, and from the side view (110) plane, Fig. 9(b) SRP/UF, the boundaries between the deformed and the un-deformed

78

regions lie along the <110> direction. The boundary between the deformed region and un-deformed region in the [100] orientation is also along the <110> direction, as shown in Figs. 8(c) and (d) SRP/UF. This preference for deformation along the <110> direction during nanoindentation is consistent with <110> being the dominant slip direction for the ZrO_2 system. The Dislocation Extraction Algorithm (DXA) [Stukowski and Albe 2010] can be used to capture dislocation structures. The DXA is applied to the Zr fcc sublattice, but captures no dislocations. By contrast indentation simulations of fluorite-structured CaF_2 did show the generation of dislocations as the first plastic event took place [Lodes et al. 2011].
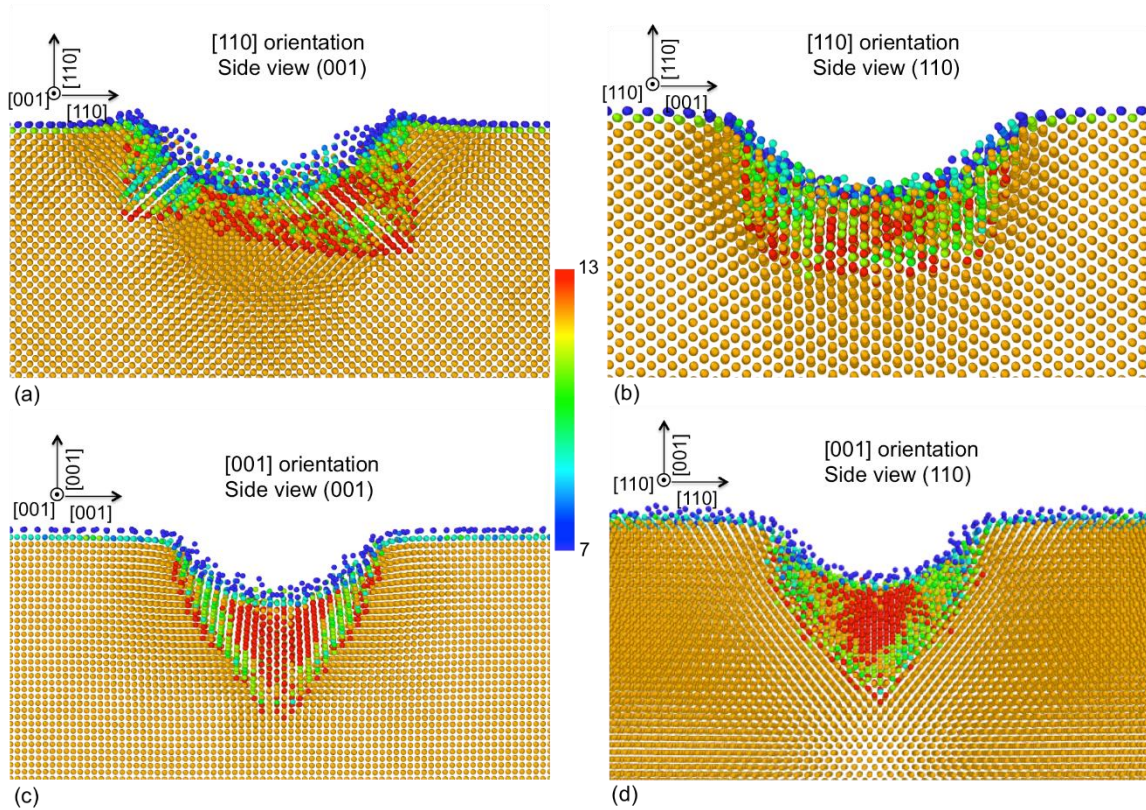
Fig. 9 SRP/UF Side views of deformed structures of ZrO_2 at indentation depth of 25Å. (a) [110] orientation side view of (001) plane. (b) [110] orientation side view of (110) plane. (c) [001] orientation side view of (001) plane. (d) [001] orientation side view of (110) plane. The color scheme represents the coordination number. Only Zr atoms are shown in the figure.

The [110] orientation of ZrO_2 has been observed in oxidized Zr by electron diffraction [Ploc 1982]; the (110) plane is charge neutral plane without dipole moment normal to the surface plane. The [0001] orientation is one of those commonly observed in Zircaloy [Goel et al. 2014]. While the surface formed by a 30° of the [0001] orientation around the c-axis is also commonly observed, it is not computational convenient. Therefore, the Zr-[0001] orientation with ZrO_2-[100] orientation on top is chosen for these simulations. In order to reduce the lattice mismatch between Zr and ZrO_2, the number of unit cells of Zr

and ZrO_2 along x and y directions has been chosen such that total strain is less than 1% along the x direction and less than 3% along the y direction; reduction of the strain in the y-direction below this value would necessitate the use of a prohibitively large simulation cell. The work of adhesion of our simulated system is 2.31 Jm^{-2}, which is comparable to the DFT results, 1.96 Jm^{-2} for the Cu-(001)/ZrO_2-(110) interface [Kul'kova et al. 2013].

The load-displacement curve and the hardness vs. indentation depth are provided in Fig. 10 SRP/UF. In the load-displacement curve, no significant yielding takes place until an indentation depth of 18 Å, at which point the load and the calculated hardness start to decrease. The hardness first increases with the indentation depth, then becomes stable with small fluctuations between 13 Å and 18 Å.
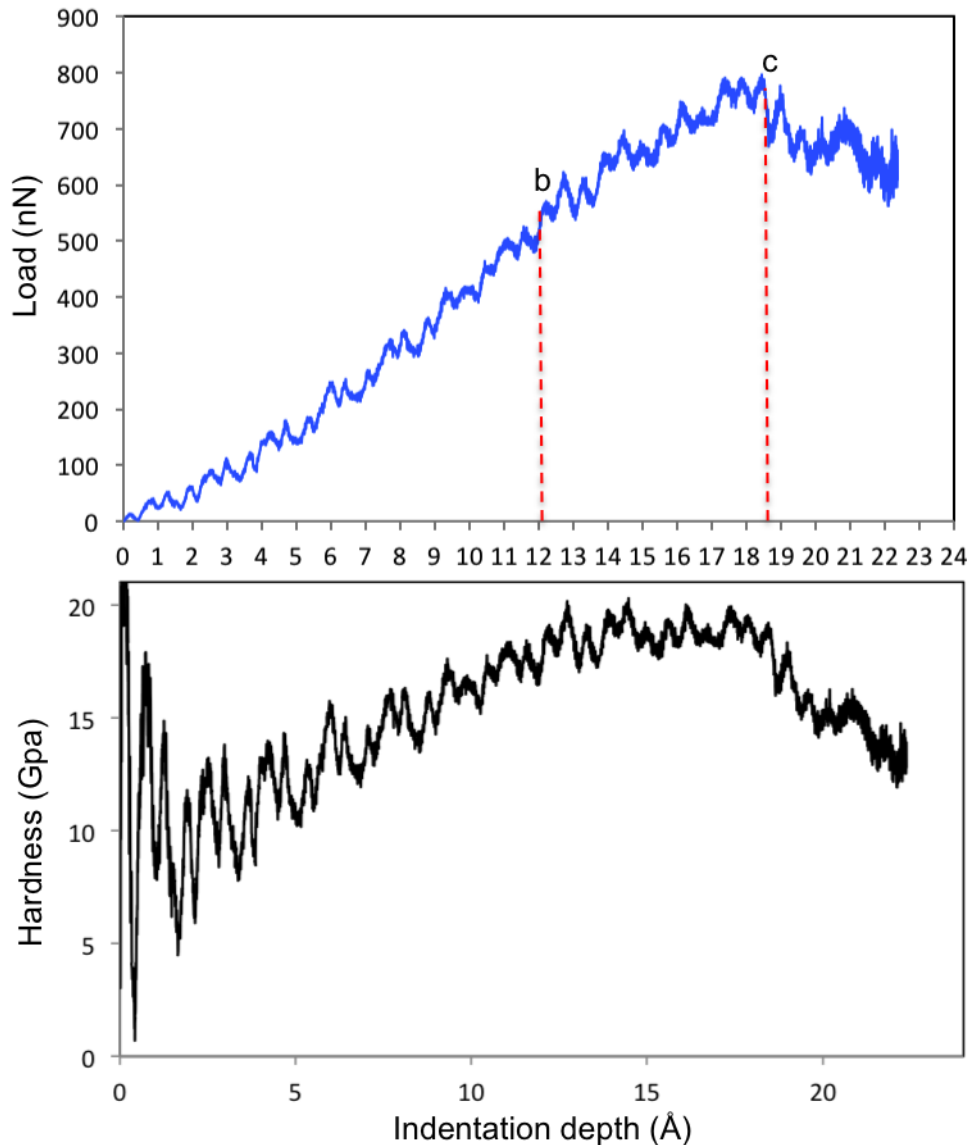
Fig. 10 SRP/UF Load-displacement curve and hardness vs. indentation depth for the ZrO_2/Zr system

The deformed structure during the nanoindentation simulation (with oxygen atoms removed from the image for clarity) is illustrated in Fig. 11 SRP/UF. The Zr atoms are in an fcc environment in the ZrO_2 layer and in an hcp environment in the Zr substrate. Thus, common neighbor analysis (CNA) [Clarke and Jonsson 1993] has to be applied separately in Zr and ZrO_2 to identify fcc-like atoms, hcp-like atoms and disordered atoms. DXA is then used to identify dislocation lines. Pyramidal <a+c> dislocations start to nucleate in the Zr substrate at an indentation of ~12 Å as revealed by Fig. 11(a) SRP/UF. This 12 Å indentation depth corresponds to point *b* in the load-displacement curve in Fig. 10 SRP/UF. It answers the question raised previously, showing that the Zr substrate starts to deform plastically at 12 Å, before the yield point *c* in Fig. 10 SRP/UF at 18 Å. However unlike the pure Zr system, no significant load drop is predicted in the load-displacement curve for the ZrO_2/Zr system when plastic deformation takes place in Zr substrate. That is, the presence of the ZrO_2 layer delays the plastic deformation in the Zr substrate relative to the pure Zr system.
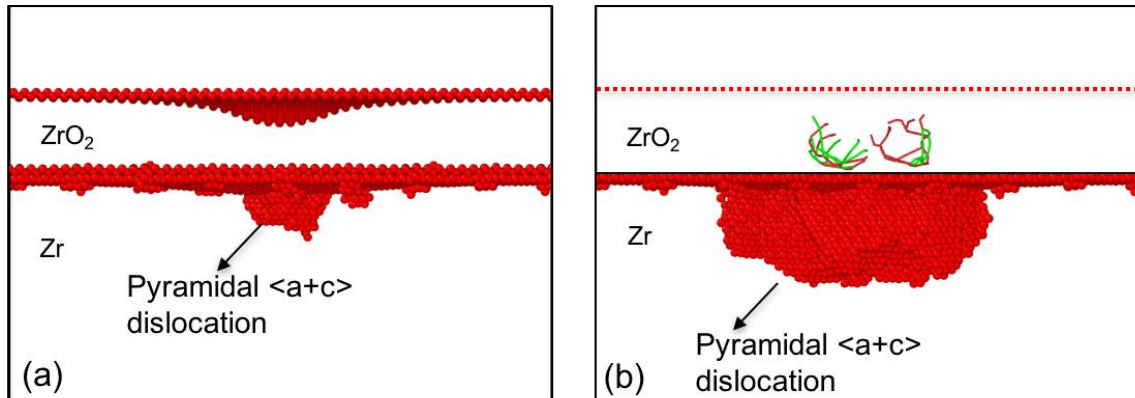

Fig. 11 SRP/UF Deformed structure of ZrO_2/Zr system after nanoindentation. (a) Deformed structure at 12.4 Å indentation depth. The red atoms represent disordered atoms. Atoms in fcc and hcp environment have been removed. (b) Deformed structure at 19 Å indentation depth. The atoms in ZrO_2 layer have been removed. Only dislocation lines are shown. Green lines represent the Shockley partials. Red lines represent other dislocations types. The dislocation lines are captured using DXA.

References SRP/UF

Clarke A., H. Jonsson, Physical Review E, 47 (1993) 3975-3984.
Fujikane M., D. Setoyama, S. Nagao, R. Nowak, S. Yamanaka, J Alloy Compd, 431 (2007) 250-255.
Gadag S., G. Subbarayan, W. Barker, J Mater Sci, 41 (2006) 1221-1232.
Goel S., R. Jayaganthan, I. Singh, D. Srivastava, G. Dey, N. Saibaba, Mater Design, 55 (2014) 612-618.
Kelchner C. L., S.J. Plimpton, J.C. Hamilton, Phys Rev B, 58 (1998) 11085-11088.
Kul'kova S., A. Bakulin, S. Hocker, S. Schmauder, Technical Physics, 58 (2013) 325-334.
Leger M. , P. Tomaszewski, A. Atouf, A.S. Pereira, Phys Rev B, 47 (1993) 14075.
Lodes M. A., A. Hartmaier, M. Goken, K. Durst, Acta Materialia, 59 (2011) 4264-4273.
Lu Z. Z., M.J. Noordhoek, A. Chernatynskiy, S.B. Sinnott, S.R. Phillpot, Journal of Nuclear Materials, 462 (2015) 147-159.

Mendelev M., G. Ackland, Philosophical Magazine Letters, 87 (2007) 349-359.

Messerschmidt U., D. Baither, B. Baufeld, M. Bartsch, Mat Sci Eng a-Struct, 233 (1997) 61-74.

Murty K. L., I. Charit, Prog Nucl Energ, 48 (2006) 325-359.

Nair A. K. , E. Parker, P. Gaudreau, D. Farkas, R.D. Kriz, Int J Plasticity, 24 (2008) 2016-2031.

Noordhoek M., T. Liang, Z. Lu, T. Shan, S. Sinnott, S. Phillpot, Journal of Nuclear Materials, 441 (2013) 274-279.

Oliver W.C., G.M. Pharr, J Mater Res, 7 (1992) 1564-1583.

Oliver W. C., G.M. Pharr, MRS Bull, 35 (2010) 897-907.

Ploc R., Journal of Nuclear Materials, 110 (1982) 59-64.

Remington T. P., C.J. Ruestes, E.M. Bringa, B.A. Remington, C.H. Lu, B. Kad, M.A. Meyers, Acta Materialia, 78 (2014) 378-393.

Schuh C. A., Mater Today, 9 (2006) 32-40.

Serra A., D.J. Bacon, Philos Mag, 90 (2010) 845-861.

Stukowski A., K. Albe, Modelling and Simulation in Materials Science and Engineering, 18 (2010) 085001.

Tenckhoff E. , Deformation Mechanisms, Texture, and Anisotropy in Zirconium and Zircaloy, ASTM International, 1988..

Verkhovtsev A. V., M. Hanauske, A.V. Yakubovich, A.V. Solov'yov, Computational Materials Science, 76 (2013) 80-88.

Yan C., R. Wang, Y. Wang, X. Wang, Z. Lin, G. Bai, Y. Zhang, Materials Science and Engineering: A, 628 (2015) 50-55.

Introduction

To improve the accident tolerance of zircaloy as a fuel cladding material, we considered a few possible design approaches based on computational studies: (1) identify a more stable protective oxide for zirconium, (2) identify diffusion routes for solutes to migrate to a surface during irradiation. For the first, we considered Be and its preference to segregate to Zr surfaces, as BeO is more stable than zirconia. For the second, we computed solute diffusivities from first principles, including the off-diagonal "drag coefficient," L^{sv}, which quantifies the flux of solutes caused by *vacancy motion* in a material (hence, a diffusion mechanism that should be prevalent under irradiation, but not in normal equilibrium conditions).

Be segregation to Zr surfaces

High-temperature oxidation of zircaloys poses a serious safety risk for nuclear fuel cladding applications, thus driving the search for oxidation resistant alloys. Ellingham diagrams suggest preferential oxidation of beryllium over zirconium, but the atomic-scale behavior of Be near Zr surfaces is unknown. We performed first principle calculations using density functional theory to investigate the stability of Be at possible sites in the Zr surfaces and bulk [Jain and Trinkle 2017]. Our calculations predict that Be favors substitutional sites and prefers to segregate to the surface layers. Charge density analysis showed charge redistribution around the solute atom in substitutional sites which leads to increased bonding and explains the high stability of these sites. The calculated surface segregation energy suggests that Be migrates towards the surface at high temperatures, which could enhance oxidation resistance.

Solute diffusivity in Zr: Fe, Cr, Al, Be, Sn, Ni

We considered multiple solutes in Zr: the primary zircaloy additions, the elements in FeCrAl, and finally possible Be additions. Our goal was to, from first-principles, predict solute diffusivity including the solute-vacancy drag coefficient. Two main complications arose: (1) in zirconium, the vacancy hops through a metastable configuration that complicates the prediction of transport coefficients directly from atomic-scale jump information, and (2) several elements can diffuse either as a substitutional solute with a vacancy-mediated mechanism, or as a higher energy interstitial solute in the lattice. Fortunately, we have sufficiently developed the theory [Trinkle 2016, Trinkle 2017] along with the open-source software [Onsager] to be able to treat these complications.

We performed first principles calculations using density function theory to investigate the interaction of Sn, Cr, Fe, Be, Al and Ni with vacancies in the HCP Zr matrix. We developed a methodology to accurately model the metastable vacancy states along the basal migration path, known to occur in Group IV metals. We computed the vacancy mediated solution diffusion coefficients and drag ratios using both kinetic Monte Carlo and a new analytic Greens function method. The computed diffusion coefficients of Sn and Al show good agreement with the experimental data, which indicates that vacancy mediated transport is the dominant mechanism for these solutes. The diffusion coefficients for Cr, Fe, Be and Ni are much lower than the experimental values, and the interstitial mechanism is expected to be dominant for these solutes. The drag ratios for Cr, Fe, Be and Ni are positive from 600 K to 1235 K, which suggests that non-equilibrium vacancy fluxes could drag these solutes towards sinks. We also compute the transport coefficients by omitting all the metastable states, and our results show that proper treatment of the metastable states is essential for accurate prediction of drag ratios, however these states have a negligible influence on the diffusion coefficients.

We followed our simulation of vacancy-mediated transport with interstitial diffusion mechanisms for Be, Cr, Fe, and Ni. This includes the calculation of the interstitial site energies relative to the substitutional sites; for all solutes we considered, the interstitial sites are higher in energy than substitutional sites. However, we also find that the activation barrier for diffusion when added to the increased site energy is still *lower* than the diffusion barrier predicted by the vacancy mechanism alone. This suggests that the interstitial diffusion mechanism contributes more to the diffusion than the vacancy mediated mechanism for these solutes. The transport coefficients are in good agreement with available experimental data.
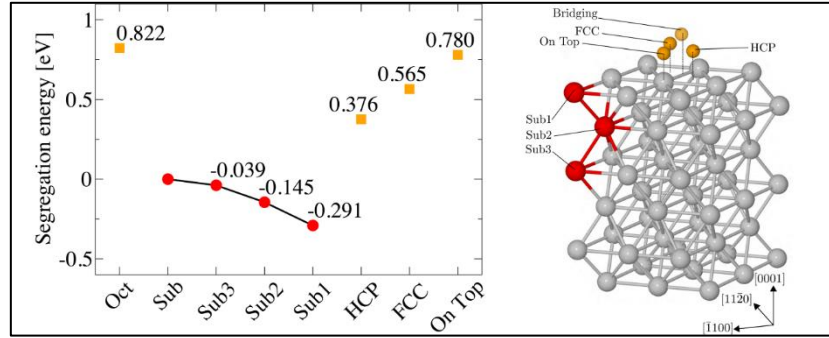
Figure 1. Segregation energy of Be at various sites in the Zr(0001) basal surface. For comparison, we also show the energy of the bulk Oct site. The symbols for adatom and Oct sites are orange, and the symbols for the substitutional sites are red. All energies are relative to the energy of Sub site, the substitutional site in bulk. The most stable site in the basal surface is the Sub1 site. The most stable adatom site in the basal surface is the HCP site but it is higher in energy compared to the substitutional sites in the surface. In the bulk, the Sub site is more stable than the Oct site. We connect the substitutional sites in the basal surface to indicate a possible migration path from bulk to surface.
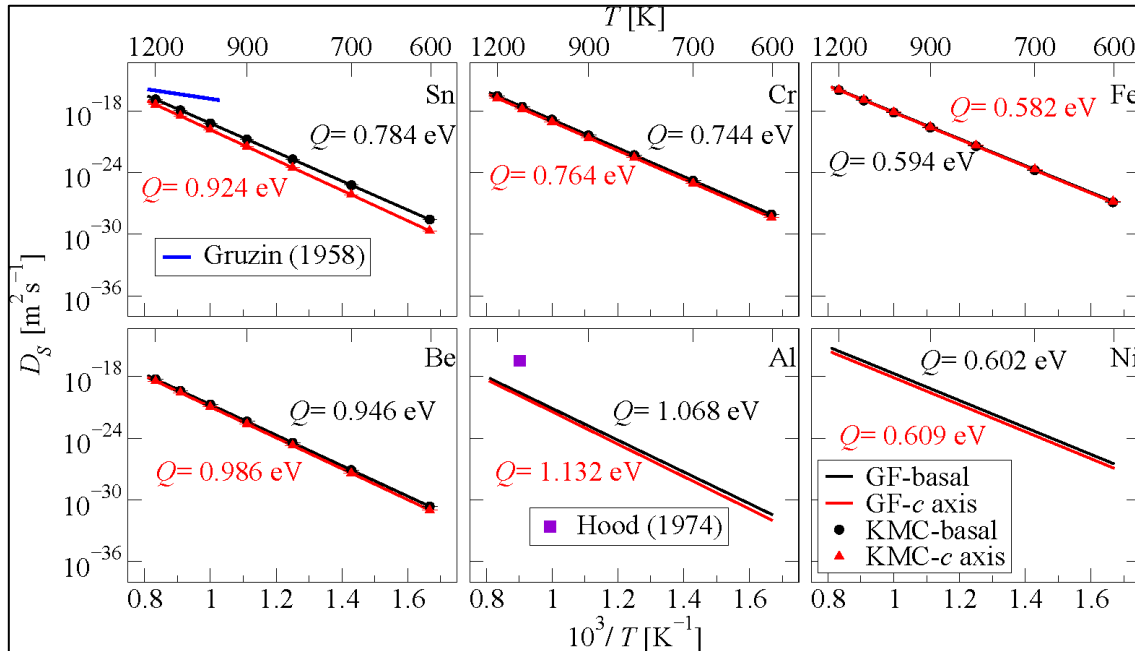

Figure 2. Diffusion coefficients for vacancy mediated transport of the solutes Sn, Cr, Fe, Be, Al and Ni in Zr along the basal plane and parallel to the *c* axis. For Sn, Cr, Fe and Be, we compare the diffusivities computed using Greens function method (GF) and kinetic Monte Carlo (KMC), and the results are in good agreement. The calculated diffusivities and the corresponding activation energies *Q* obtained from Arrhenius fits are in black for basal plane and in red for *c* axis. We also plot the available experimental data for Sn [Gruzin et al. 1958] and Al [Hood and Schultz 1974]. The diffusivity is nearly isotropic in the basal plane and parallel to *c* axis for all solutes except Sn.
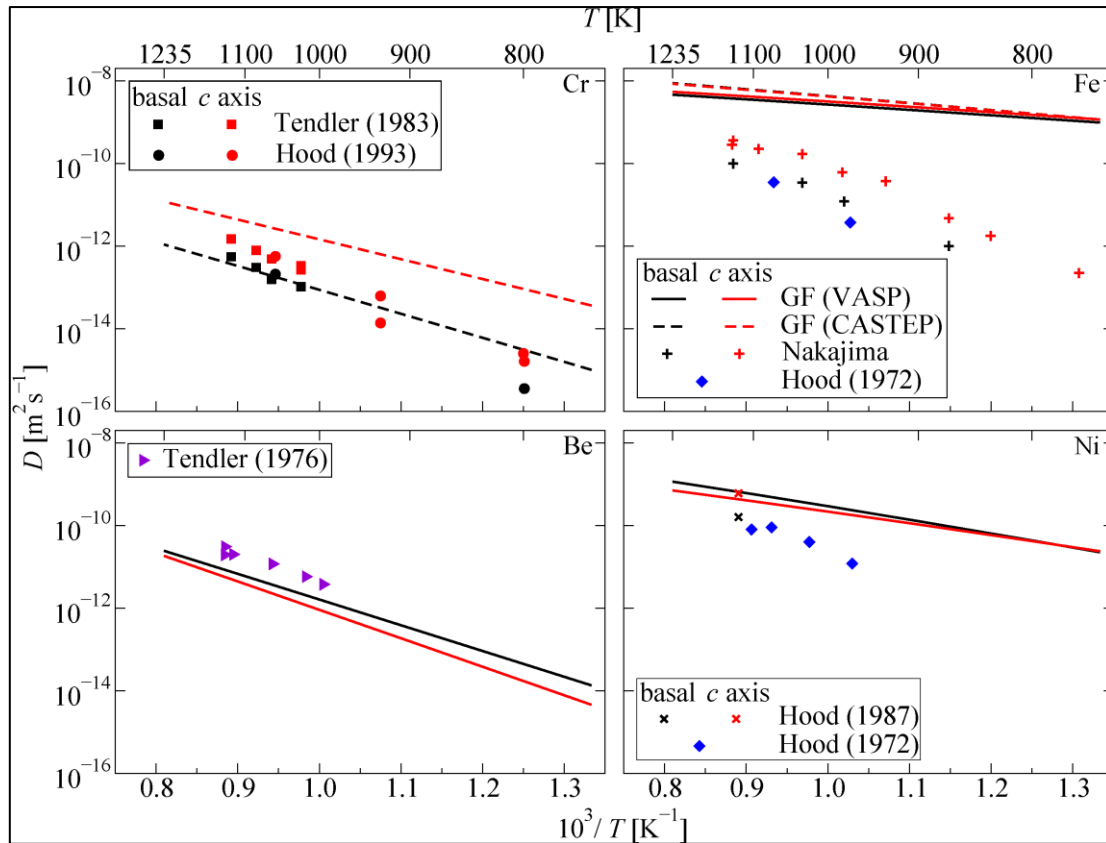
Figure 3. The calculated diffusion coefficients compared to the experimental data for the solutes Cr [Balart et al. 1983, Hood and Schultz 1993], Fe [Nakajim et al. 1988, Hood and Schultz 1972], Be [Tendler et al. 1976] and Ni [Hood and Schultz 1972, Hood and Schultz 1987] in Zr. The basal and c-axis diffusion coefficients are in black and red, respectively. The diffusion coefficients for Cr, Be and Ni agree well with the experimental data. The VASP and CASTEP calculations for Fe are in good agreement but the calculated diffusion coefficients are two orders of magnitude higher than the experimental data.

Bibliography:

- Balart et al. 1983: S. N. Balart, N. Varela, and R. H. de Tendler, J. Nuc. Mater. 119, 59 (1983).
- Gruzin et al. 1958: B. P. L. Gruzin, V. S. Emelyanov, G. G. Ryabova, and G. B. Fedorov, in *Proceedings of the Second United Nations International Conference on the Peaceful Uses of Atomic Energy*, Vol. 19 (United Nations, Geneva, 1958) p. 187.
- Hood and Schultz 1972: G. M. Hood and R. J. Schultz, Philos. Mag. 26, 329 (1972).
- Hood and Schultz 1974: G. M. Hood and R. J. Schultz, Acta Metallurgica 22, 459 (1974).
- Hood and Schultz 1987: G. Hood and R. Schultz, Mater. Sci. Forum 15-18, 475 (1987).
- Hood and Schultz 1993: G. M. Hood and R. J. Schultz, J. Nuc. Mater. 200, 141 (1993).
- Jain and Trinkle 2017: A. C. P. Jain and D. R. Trinkle, "First principles calculations of beryllium stability in zirconium surfaces." *Acta mater.* **122**, 359–368 (2017), doi://10.1016/j.actamat.2016.10.003
- Nakajima et al. 1988: H. Nakajima, G. M. Hood, and R. J. Schultz, Philos. Mag. B 58, 319 (1988), http://dx.doi.org/10.1080/13642818808208473.
- Onsager: Software, D. R. Trinkle, ONSAGER (http://dallastrinkle.github.io/Onsager/) v.1.2.2
- Tendler et al. 1976: R. Tendler, J. Abriata, and C. Varotto, J. Nuc. Mater. 59, 215 (1976).
- Trinkle 2016: D. R. Trinkle, "Diffusivity and derivatives for interstitial solutes: Activation energy, volume, and elastodiffusion tensors." *Philos. Mag.* **96**, 2714–2735 (2016), doi://10.1080/14786435.2016.1212175
- Trinkle 2017: D. R. Trinkle, "Automatic numerical evaluation of vacancy-mediated transport for arbitrary crystals: On- sager coefficients in the dilute limit using a Green function approach." (accepted) *Philos. Mag.* (2017), arXiv:1608.01252

2.7   Advanced reactor simulations

List of publications

Heuser, B. J., Kozlowski, T., Wu, X., "Engineered Zircaloy Cladding Modifications for Improved Accident Tolerance of LWR Fuel: A Summary," Proc. of the 2013 LWR Fuel Performance Meeting/TopFuel, Charlotte, North Carolina, USA, September 15–19, 2013.

Wu, X., Sabharwall, P., Hales, J. & Kozlowski, T., (2014). Neutronic sand Fuel Performance Evaluation of Accident Tolerant Fuel under Norma lOperation Conditions. Technical Report INL/EXT-14-32591, Idaho NationalLaboratory.

Wu, X., Kozlowski, T. & Heuser, B. J., (2014). Neutronics Analysis of Improved Accident Tolerance of LWR Fuel by Modifying Zircaloy Cladding of Fuel Pins, In: Proceedings of ICAPP-2014, Charlotte, USA, April 6-9.

Rose, M., Downar, T., Wu, X. & Kozlowski, T., (2015), Evaluation of Accident Tolerant FeCrAl Coating for PWR Cladding under Normal Operating Conditions with Coupled Neutron Transport and Fuel Performance, In:Proceedings of M&C-2015, Nashville, TN, April 19-23.

Wu, X., Kozlowski, T., & Hales, J. D., (2015). Neutronics and Fuel Performance Evaluation of Accident Tolerant FeCrAl Cladding under Normal Operation Conditions. Annals of Nuclear Energy, 85, 763-775.

TK/UIUC 1: Phenomenological models

- Phenomenological models used in the thermal-hydraulics and fuel performance codes related to the following will need to be reviewed and updated, if necessary, for the new fuel/clad system
- Task 1.a.: Review the current set of models, generally applicable to UO_2-Zr system, used in the safety (and fuels) codes.
- Task 1.b. Evaluate the applicability of the existing models to the modified fuel-clad system.
- Task 1.c. Implement the database of properties and correlations developed in TMA2 for clad properties as well as for PCI in the safety codes.

Milestone 1: Phenomenological models used in the thermal-hydraulics, neutronics and fuel performance codes reviewed and updated for the new clad system.

- Deliverable 1.a.: Status report with review of the current set of models applicable to the UO_2-Zr system used in the safety (and fuels) codes, including evaluation of the applicability of the existing models to the modified clad system.
- Deliverable 1.b.: Implementation of properties and correlations developed in TMA2 for clad properties in the appropriate safety codes.

TK/UIUC 1.1: Overview

Following the Fukushima Daiichi nuclear disaster in 2011, the emphasis for nuclear fuel R&D activities has shifted from fuel reliability and waste minimization to enhancing the accident-tolerance of Light Water Reactor (LWR) fuels. By definition, enhanced Accident Tolerant Fuels (ATFs) can tolerate the loss of active cooling in the core for a considerably longer time period (depending on the LWR system and accident scenario) compared with the standard UO_2-zircaloy system currently used [Goldner, 2012]. Furthermore, the ATF fuel/cladding system should maintain or improve the fuel performance during normal operations, operational transients, as well as design-basis (DB) and beyond design-basis (BDB) events [Goldner, 2012].

Three potential approaches are proposed for the development of fuel/cladding systems that have enhanced accident tolerance [Ott et al., 2014] [Zinkle et al., 2014].

1. Improve or replace the ceramic oxide fuel

2. Modify current zircaloy cladding to achieve improved oxidation resistance, including application of coating layer

3. Replace zircaloy cladding with an alternative oxidation-resistant high-performance cladding.

The evaluation of ATF should involve the assessment of its performance under normal operations and accident scenarios. One of the potential approaches that has been extensively explored is improving the oxidation resistance of the cladding. Currently, the heat transfer coefficient between the zircaloy cladding exterior surface and the coolant is on the order of 1 W/(cm^2 K), under normal operating conditions [Terrani et al., 2014a]. However, under accident conditions, when the fuel rods are exposed to a slow-flowing or stagnant steam, this parameter could decrease by four orders of magnitude, resulting in poor fuel cladding-to-coolant heat convection. Consequently, decay heat will drive up the fuel temperature, and a rapid exothermic zircaloy oxidation reaction will happen in the high-temperature steam environment, accompanied by significant hydrogen production. Zirconium cladding oxidation in high-temperature steam environments with poor heat transfer to the gaseous phase is characteristic of a self-catalytic process (at a temperature higher than 1200°C) [Terrani et al., 2014a]. The enthalpy production from oxidation reaction, along with the decay heat, will keep increasing the fuel temperature to the melting point. Therefore, cladding with improved oxidation resistance and less heat/hydrogen generation is expected to achieve larger margins of safety against severe accident scenarios.

Iron-based alloys, like standard commercial austenitic SS-310: Fe–25Cr–20Ni–2Mn, as well as Kanthal APMT (a commercial oxide dispersion strengthened [ODS] FeCrAl alloy) ferritic alloy: Fe–22Cr–5Al–3Mo, were reexamined for their potential application as nuclear fuel cladding to replace zirconium alloys [Terrani et al., 2014a]. Two standard DB scenarios were investigated: Loss-Of-Coolant Accidents (LOCAs) and Reactivity Insertion Accidents (RIAs). The magnitude of the parabolic oxidation rate constant for APMT and SS-310 were found to be roughly two to three orders of magnitude lower than what is observed for zirconium alloys.

Some other studies also identified a slow-growing alumina surface oxide formation during steam oxidation of APMT alloy [Cheng et al., 2012]. This indicates a promising choice for nuclear fuel cladding under high-temperature accident conditions. Post-quench ductility studies were conducted with Zircaloy-4, stainless steel- (SS) 317, SS-347, and APMT alloy cladding samples at temperatures of 1200°C, followed by cooling to 800°C and then a water quench at room temperature to simulate the design basis LOCA conditions and beyond [Yan et al., 2014]. Among all the materials examined, the APMT sample showed the lowest oxidation rate.

Silicon Carbide (SiC) has also been proposed as a potential cladding material due to its low thermal neutron absorption cross-section, improved irradiation and oxidation resistance in air and steam up to temperatures of at least 1600°C [Terrani et al., 2014b]. A known issue that limits the application of SiC in LWR fuel is the current lack of engineering familiarity in design and application. More engineering familiarity in the design and fabrication is required, as well as the test standards in nuclear applications. SiC is also known to be difficult to fabricate, and has low ductility compared with metallic cladding. These issues should be resolved before SiC finds application as nuclear fuel cladding. Nevertheless, its high thermal conductivity, excellent creep resistance, low thermal neutron absorption cross-section, and irradiation stability (minimal swelling) make it an excellent candidate material for future nuclear fuel/cladding systems.

TK/UIUC 1.2: Thermal-physical properties of FeCrAl

FeCrAl alloy and SS-310 represent the two major types of oxidation-resistant alloys at high temperature. The types of protective surface oxides or scales formed via selective oxidation are Al_2O_3 on APMT and Cr_2O_3 on SS-310 [Terrani et al., 2014a]. However, the material composition of a standard commercial austenitic 310 stainless steel (Fe–25Cr–20Ni–2Mn) has very high nickel concentration. The thermal neutron absorption cross-section of nickel is about twice that of iron. The parameter for iron is about 12-16 times higher than that of zirconium [Terrani et al., 2014a]. Therefore, SS-310 cladding is expected to have significant neutron penalty. Meanwhile, nickel could produce radioactive cobalt via the ^{58}Ni (n,p) ^{58}Co reaction. For these reasons, SS-310 is not considered as candidate cladding in this study. Kanthal APMT FeCrAl alloy is one example of a class of alumina-forming ferritic alloys. The material composition used is 75% Fe, 20% Cr, and 5% Al. It includes ODS variants with increased creep resistance at high temperature [Terrani et al., 2014a].

Possible forms for the application of the candidate cladding material are: (1) using it as monolithic cladding to replace zircaloy; (2) using it as a thin coating layer on the surface of zircaloy cladding. A thin coating layer (100-micron thickness) is applied to the cladding surface. When exposed to steam during temperature excursions, this coating layer is expected to shift the M+O→MO reaction away from oxide growth to protect LWR fuel cladding [Heuser et al., 2013] [Wu et al., 2014a]. However, recently researchers from ORNL identified some major drawbacks for this kind of cladding/coating system [Zinkle et al., 2014] [Terrani et al., 2014a] [Terrani et al., 2013], which include:

1. Careful matching of the thermal expansion coefficient for coating and cladding is necessary to minimize interfacial stresses and delamination during cycling [Zinkle et al., 2014].

2. Diametrical compression that results from reactor pressurization makes the application of coating layer problematic (generally requiring thin and highly adherent coatings) [Zinkle et al., 2014].

3. Different volumetric and microstructural evolution between the coating and underlying cladding under neutron irradiation can lead to coating spallation [Zinkle et al., 2014].

4. Once the fuel rod bursts, the inner zircaloy surface would be exposed to steam under accident conditions, resulting in rapid oxidation, heat generation and hydrogen production. Therefore, high-temperature oxidation protection, especially in steam, is more readily and robustly accomplished by selective oxidation of one bulk component of the alloy than via coatings [Terrani et al., 2014a].

5. Recently, it is reported SS-310 and FeCrAl could experience significant interdiffusion with zirconium [Terrani et al., 2013], which leads to an intermetallic layer with considerable thickness. The monolithic FeCrAl cladding is expected to perform better under high-temperature steam environments in the absence of detrimental iron alloy-zirconium interactions.

Given the above considerations, FeCrAl should be applied as monolithic cladding rather than a coating. However, one important disadvantage of FeCrAl application is in neutron penalty and consequent cycle length reduction, because iron has a thermal neutron absorption cross-section that is about 12-16 times higher than that of zirconium. There are several possible ways to enhance the end-of-cycle reactivity and thus increase the cycle length for nuclear fuel with monolithic iron based alloy cladding:

1. Increase the oxide fuel enrichment.

2. Minimize the cladding thickness. The advanced iron based alloys could enable fabrication of fuel cladding with thinner walls, because of their better strength, corrosion, and embrittlement properties.

3. Increase the mass of fuel inside the nuclear reactor. Since cladding thickness could be reduced, if the volume of fuel pins is maintained, the extra space gained could be filled with oxide fuels.

A most recent study [George et al., 2015] reported a good balance between option 2 and 3 by establishing an end-of-cycle (EOC) reactivity method to quantify the overall reactivity difference between different cladding models during

an 18-month Pressurized Water Reactor (PWR) operating cycle. This article investigated austenitic type 310 and 304 stainless steel, ferritic Fe-20Cr-5Al (FeCrAl) and APMT™ alloys, and SiC-based materials as alternate cladding materials in a PWR, from the neutronics aspect. After a detailed parametric study on the geometric conditions, it is reported that by using a thinner cladding of 350 µm and keeping a constant outer diameter, austenitic stainless steels require an increase of no more than 0.5 wt% enriched ^{235}U to match fuel cycle length requirements, while the required increase for FeCrAl is 0.16%.

[Figure 1.1 TK/UIUC] - [Figure 1.3 TK/UIUC] show various thermal-physical properties for zircaloy, UO_2 FeCrAl. Most of the properties are the same as those used in [Ott et al., 2014], with a minor difference in UO_2 thermal conductivity. Here the Fink-Lucuta model defined in BISON theory manual [Hales et al., 2014] is used for UO_2 thermal conductivity.

Note that all the parameters shown in [Figure 1.1 TK/UIUC] - [Figure 1.3 TK/UIUC] are at zero burnup. In BISON, while the parameters for UO_2 and Zircaloy have a dependence on both temperature and either burnup or neutron flux and fluence, those for FeCrAl have only dependence on temperature. In addition, thermal conductivity values shown do not consider the effects of neutron irradiation. Tabulated material properties used in the report are provided in the appendix of [Wu et al., 2014b] [Wu et al., 2015]. For the specific heat capacity, the sharp spike for Zircaloy is a result of a phase change (alpha to beta) from 1090 K to 1248 K. Similarly, the peak around 800 K for FeCrAl is due to a magnetic phase transition. The volumetric heat capacity and melting temperature could be found in [Ott et al., 2014].

TK/UIUC 2: Operating Conditions and Fuel Cycle Analysis

Steady-state neutronics and thermal-hydraulics performance during normal operation and anticipated operational occurrences (AOO), Specified Acceptable Fuel Design Limits (SAFDLs) are to be respected.

- Task 2.a.: Fuel pin and fuel assembly reactivity effect of the new cladding, comparison with a reference PWR design.
- Task 2.b.: Evaluation of core peaking factor, peak fuel centerline and clad surface temperature, boron concentration (for PWRs), reactivity coefficients and shutdown margin.
- Task 2.c.: Evaluation of core life, enrichment, batch and peak burnup.

Milestone 2: Demonstrate that the proposed cladding modifications are not detrimental to LWR steady-state neutronics and thermal-hydraulics performance during normal operation and anticipated operational occurrences (AOO).

- Deliverable 2.a.: Report on fuel pin and fuel assembly reactivity effect of the new fuel and cladding, comparison with a reference PWR design.
- Deliverable 2.b.: Report on the evaluation of core peaking factor, peak fuel centerline and clad surface temperature, boron concentration (for PWRs), reactivity coefficients and shutdown margin.
- Deliverable 2.c.: Report on the evaluation of core life, enrichment, batch and peak burnup.

TK/UIUC 2.1: Model for neutronics analysis

A recent study [Terrani et al., 2013] [George et al., 2015] suggested an optimized design for FeCrAl cladding to replace current zircaloy cladding. Given the higher strength of iron-based alloys when compared with zirconium-based alloys, a reduced thickness of 350 µm (from 571.5 µm for zircaloy) for FeCrAl is suggested to meet lifetime requirements with only a slightly increased enrichment (0.16%), as well as maintaining cladding integrity during operations. For the cases studied in [George et al., 2015], an outer rod diameter of 0.94996 cm is kept constant, therefore maintaining a pitch-to-rod ratio of 1.326 so that the thermal hydraulics in the PWR system would not be affected drastically if commercialized.

Before moving to fuel performance analysis, a neutronics study is carried out to confirm the results reported in [George et al., 2015], in which simple two-dimensional pin cell analyses were performed using SCALE/TRITON from SCALE 6.1.2. In this report, FeCrAl cladding is used to replace Zircaloy cladding in a PWR single assembly, which is based on the 17×17 Westinghouse design. Each assembly has 264 fuel pins and 25 guide tubes (here the central instrumentation tube is treated as a guide tube). The single assembly configuration is shown in [Figure 2.1 TK/UIUC].

A three-dimensional continuous-energy Monte Carlo reactor physics calculation code, Serpent, is used as the reactor neutronics code [Leppänen et al., 2007]. To achieve sufficiently high calculation precision, 200 K neutrons per cycle are used with 100 inactive cycles and 1,000 active cycles. This is sufficient to achieve eigenvalue statistical uncertainty of about 3 pcm. At the top and bottom of the single assemblies, 30 cm of coolant is added as an axial reflector. [Table 2.1 TK/UIUC] shows the neutronics model specifications. The same type of Zircaloy-4 material is used as cladding for the fuel pins and guide tubes. All the dimensions, material compositions and operating conditions are same with that from [George et al., 2015], except that here we use single assembly instead of a simple two-dimensional pin cell. Note that the specific power in megawatts per metric kilogram of uranium (MW/kgU) corresponds to the constant power of 18.0 KW/assembly modeled through the depletion cycle [George et al., 2015]. The specific power density for fuel with FeCrAl clad is scaled down to keep a constant power per assembly.

TK/UIUC 2.2: Model for fuel performance analysis

INL's finite element-based nuclear fuel performance code BISON [Williamson et al., 2012] is used to model LWR nuclear fuel pin performance under normal operating conditions. BISON solves the fully-coupled equations of thermomechanics and species diffusion, for either 1-D spherical, 2-D axisymmetric or 3-D geometries [Williamson et al., 2012] [Hales et al., 2014] [Williamson et al., 2014]. It incorporates a wide variety of material models for both fuel and zircaloy cladding. Temperature- and burnup-dependent thermal properties, as well as fission product swelling, densification, thermal and irradiation creep, fracture, and fission gas production and release are included for fuel models. For the cladding material, plasticity, irradiation growth, and thermal and irradiation creep models are implemented. Furthermore, BISON has models to simulate gas-gap heat transfer, mechanical contact, and the evolution of the gap/plenum pressure with plenum volume, gas temperature, and fission gas addition.

Detailed descriptions of all models and methods can be found in the BISON theory manual [Hales et al., 2014]. The LWR fuel pin model and mesh used in BISON are shown in [Figure 2.2 TK/UIUC] and [Table 2.2 TK/UIUC]. They include the model configuration, power history, and operational parameters. These parameters are based on the 2D-RZ 10-pellet rodlet example from the BISON workshop manual [Williamson et al., 2014]. It is a well-established example and does not require excessive computational effort.

It is known from experiments the oxidation rate of FeCrAl is lower than that of zircaloy by at least two orders of magnitude [Ott et al., 2014]. Also, oxidation under normal operation is not as important as that in accident conditions such as LOCA. Therefore, oxidation rates are set to 0 for both FeCrAl in the fuel performance analysis. Also, thermal or irradiation creep for FeCrAl is currently not available. For the fuel performance analysis in BISON, one case is executed with no creep for FeCrAl, while in another case, zircaloy creep model is used for FeCrAl. These two cases are used to bound the range of possible creep behavior of FeCrAl. This is a very optimistic estimate, since the creep for FeCrAl is assumed to be smaller than zircaloy in magnitude.

TK/UIUC 2.3: Neutronics analysis results

As mentioned earlier, to enhance the reactivity and increase the cycle length when using FeCrAl as cladding, modified fuel rod geometries or increased enrichment in the fuel are necessary. By reducing the cladding thickness (from 571.5

µm to 350 µm), keep the fuel rod outer diameter gap thickness, filling extra space with fuel and slightly increase the fuel enrichment (from 4.90% to 5.06%), the multiplication factor k_{eff} evolution with effective full power days (EFPD) is shown in [Figure 2.3 TK/UIUC]. Clearly the suggested design of FeCrAl cladding is able to maintain the required PWR cycle length. At the beginning of depletion, fuel with higher absorbing FeCrAl cladding shows a reduction in reactivity but a slight upsurge in reactivity near EOL. This phenomenon is due to greater accumulation of plutonium near EOL and is demonstrated in [Figure 2.4 TK/UIUC].

[Figure 2.4 TK/UIUC] (left) shows the total Plutonium production over the depletion. It is indicated that despite differences in neutron absorption between Zircaloy and FeCrAl, the total Plutonium production will not change significantly. [Figure 2.4 TK/UIUC] (right) shows the radial distribution of ^{239}Pu in the pins at middle-of-life (MOL) and end-of-life (EOL), as ^{239}Pu is the largest contributor of fission reaction after ^{235}U in the fuel pin. Plutonium will accumulate on the periphery of fuel pellets as the depletion continues, because of spatial self-shielding of neutrons. The accumulation of additional fissile material will cause a sharp increase in fission near the edge of fuel pellets, known as the "Rim Effects". It is shown that fuel with FeCrAl cladding has a higher ^{239}Pu accumulation than fuel with zircaloy cladding and therefore a higher power, due to the harder neutron spectrum in the system causing more ^{239}Pu breeding.

Also, an economic assessment from [George et al., 2015] shows that the increase in fuel pellet production costs for FeCrAl cladding is about 15%, which is the minimum among all the candidate materials considered, including austenitic type 310 and 304 stainless steel, ferritic Fe-20Cr-5Al (FeCrAl) and APMT™ alloys, and SiC-based materials. The increase in fuel pellet production costs is due to slightly increased ^{235}U enrichment and the additional UO_2 pellet volume enabled by decreasing clad thickness to nearly half to meet PWR lifetime requirements.

TK/UIUC 2.4: Fuel performance analysis results

The simulation time for the BISON models is 10^8 seconds, which is about 1,160 days (3.2 years). A uniform convective boundary at the clad outer wall is used to simulate heat transfer from the cladding surface to the coolant. The thermal-hydraulics model is simplified to a coolant channel, and details can be found in the BISON theory manual [Hales et al., 2014]. The rodlet model uses discrete pellets.

[Figure 2.5 TK/UIUC] (left) shows fuel average burnup with respect to time for the three cases. Note that "FeCrAl cladding with creep" means zircaloy thermal and irradiation creep model is used for FeCrAl while keeping all the other properties for FeCrAl. Power history and axial power peaking factors are same for all three cases. Because fuel with FeCrAl cladding has a slightly higher enrichment, the burnup at the same time is lower than fuel with zircaloy cladding.

In [Figure 2.5 TK/UIUC] (right) the average fuel temperature evolution with burnup is presented. The average fuel temperature is defined as the average temperature of all the elements in the fuel region. To better interpret these results, a brief description of the nominal fuel temperature evolution in a PWR fuel rod is provided as the following stages:

1. At the beginning of depletion, fuel densification leads to the increase of the gap, thus the heat conduction gets worse, and fuel temperature increases,

2. Fuel swelling and clad creep are combined to reduce gap size, which causes fuel temperature to decrease.

3. Fission gas release begins at a burnup of around 10 MWd/kgU. The mixing of fission gas with helium in the plenum decreases thermal conductivity of gas gap, and fuel temperature increases.

4. This temperature increase is gradually reversed by continuing gap closure, until the gap is fully closed at approximately 36 MWd/kgU.

5. UO$_2$ thermal conductivity decreases with burnup; therefore, fuel temperature increases.

Note the time scale mentioned above is for a nominal PWR core modeled by BISON, not for the rodlet used here. From the above five steps, it is obvious fuel temperature is affected by many factors, such as fuel densification, fuel swelling, cladding thermal and irradiation creep, cladding thermal expansion, and cladding thermal conductivity. Special attention should be paid to Step 3 because fission gas release and fuel temperature increase from a positive feedback over a long burnup period. High fuel temperature will cause more fission gas release, and with the exacerbation of the gap conductance caused by fission gas, fuel temperature will increase. This positive feedback will be most pronounced while the gap is open.

[Figure 2.6 TK/UIUC] shows fission gas production and release over burnup. At each integration point, BISON computes the fission gas produced by a numerical time integration of the gas production rate, which is given as the product of fission rate and fractional yield of gas atoms per fission (with a value of 0.3017) [Williamson et al., 2012]. Therefore, for all the cases, fission gas produced is the same as long as the power history is the same. So the three cases have the same fission gas production rate. But since the two cases with FeCrAl cladding have lower burnup at a given time, they have higher fission gas production at a given burnup compared with zircaloy cladding, as shown in [Figure 2.6 TK/UIUC] (left).

FeCrAl cladding with no creep has slightly higher fission gas release because the average fuel temperature is higher than the other cases, as indicated in [Figure 2.5 TK/UIUC] (right). To find out the reason for this phenomenon we need to look at [Figure 2.7 TK/UIUC], which shows the fuel rod internal volume and plenum pressure. Since there is not creep for this FeCrAl case, in stage 2 of the above temperature evolution, the gap size for this case will be larger, resulting in higher temperature. The subsequent fission gas release and fuel temperature increase from a positive feedback until it is reversed by continuing gap closure. Also, since cladding is not creeping inward, the interval volume is the highest and plenum pressure is the lowest among the three. Also, when we look at Zircaloy and FeCrAl with creep cases, FeCrAl has a similar thermal conductivity but a much higher specific heat capacity compared with zircaloy. This explains the lower average fuel temperature for FeCrAl cladding with creep.

[Figure 2.8 TK/UIUC] shows the axial temperature distribution and axial displacement of fuel centerline, at low burnup (10 MWd/KgU), medium burnup (30 MWd/KgU) and high burnup (50 MWd/KgU) for the three cases respectively. With the increase of burnup, the difference in axial temperatures of the fuel centerline decreases. Furthermore, the axial temperature profile is flattened for FeCrAl cladding with no creep, also the axial displacement is lowest at medium to high burnup for this case.

[Figure 2.9 TK/UIUC] shows the radial temperature profile and radial displacement of the horizontal line at the center of the 5th pellet from the bottom (which is close to the center of the fuel rod), at low, medium and high burnup steps. Similarly, the difference in axial temperature profiles for the three cases decreases with the increase of burnup, but generally temperature profiles for zircaloy case fall between the two FeCrAl cases. In [Figure 2.9 TK/UIUC] (right), the left part (before the sudden drop) indicates the radial displacement in the fuel region, and the right part (after the sudden drop) means radial displacement for the cladding region. The cladding region clearly demonstrates that FeCrAl with creep case and zircaloy case are creeping inward, while FeCrAl with no creep case only has a very small radial displacement at high burnup. The radial displacement in the fuel region is due to thermal expansion and swelling of UO$_2$.

[Figure 2.10 TK/UIUC] shows the radial power factor and radial ^{239}Pu distribution of the horizontal line at the center of the 5th pellet from the bottom, at low, medium and high burnup steps. The "Rim Effect" needs to be captured in order to calculate the heat generation and temperature distribution in the pellet accurately. BISON uses the TUBRNP model of Lassmann [Lassmann et al., 1994]. From [Figure 2.10 TK/UIUC], there is no considerable difference in the

radial power factors and ^{239}Pu accumulation. The difference in radial positions is due to the different radial geometries between fuel rods with Zircaloy and FeCrAl cladding.

[Figure 2.11 TK/UIUC] demonstrates the distribution of hoop stress of the same horizontal line at different burnup steps. Maximum cladding hoop stress and maximum fuel rod centerline temperature are primary parameters to identify the regions for potential failure. It is noticed that hoop stress is largest at low burnup, while the coolant pressure is the primary contributor to the stress state in the cladding. The figure shows that FeCrAl cladding with no creep has much larger hoop stress at each burnup (especially for low to medium burnup). The reason is related to the creep behavior of the cladding. Cladding creeping inward will cause the gap size to decrease which causes earlier contact of fuel pellet and cladding (as shown in [Figure 2.12 TK/UIUC]). Since we know that there will be thermal and irradiation creep for FeCrAl, the hoop stress will not be as large as shown by the red lines in [Figure 2.11 TK/UIUC]. However, special attention should be paid to FeCrAl cladding to make sure it will not fail because of hoop stress at low to medium burnup.

[Figure 2.12 TK/UIUC] presents the gap sizes behavior of two nodes on the pellet surface. Point 1 is at the height of 0.012 m (around the center of the first pellet from bottom), and point 2 is at height of 0.07 m (center of the fifth pellet from bottom). It is summarized that:

1. At the beginning of simulation (power ramp over 3 hours), gap width rapidly decreased from 0.08 mm to 0.03-0.04 mm due to fuel densification.

2. Gap will continue to decrease as a combination of fuel densification, fuel swelling, fuel thermal expansion and clad creep. But within the first 50 days of depletion, FeCrAl case with no creep undergo a slight gap increase because there is no cladding creep inward to counteract the decrease in gap size.

3. FeCrAl clad with no creep shows that gap closure can be delayed greatly, by more than 400 days. This means Pellet-Cladding Mechanical Interaction (PCMI) is significantly delayed.

4. Gap closure occurs at a very different time for a different location in the fuel pins.

TK/UIUC 2.5: Comparison of Zircaloy and FeCrAl

The excellent performance of FeCrAl alloy has already been validated in experimental investigation [Zinkle et al., 2014] [Terrani et al., 2014a] [Cheng et al., 2012] [Yan et al., 2014] [Terrani et al., 2013] and system simulation using TRACE and MELCOR [Ott et al., 2014]. Based on the results from Serpent and BISON, an evaluation of FeCrAl based on neutronics and fuel performance analysis will be discussed here.

1. The utilization of FeCrAl to replace current zircaloy cladding requires a reduction in cladding thickness and a slight increase in fuel enrichment, in order to overcome the neutron penalty and resulting decrease in PWR cycle length.

2. The optimized design proposed in [Terrani et al., 2013] is confirmed with a PWR single assembly neutronics analysis with Serpent code. This design includes keeping the fuel rod outer radius and gap size, reducing cladding thickness from 571.5 µm to 350 µm, and increasing fuel enrichment from 4.9% to 5.06%. The PWR cycle length will be preserved in this way, but the fuel pellet production costs for FeCrAl cladding will increase by about 15%.

3. It is shown that higher thermal conductivity does not necessarily lead to lower fuel temperature and lower initial stored energy upon LOCA, unless the gap is closed. Creep, either caused by heat or irradiation, is proven to play an important role in the evolution of fuel temperatures. Creep of cladding could reduce gap size and decrease fuel temperature over the burnup.

4. However, irradiation creep of zirconium is known to be a primary contributor to geometrical changes in fuel rods, which may be not desirable. For example, in a PWR reactor, permanent deformation of the fuel assemblies (like bowing) could lead to serious issues such as control rod drop failure or increased drop time, exacerbated local cooling, etc.

5. Other impacts of using FeCrAl include reduced plenum pressure, flattened axial power profile, as well as greatly delayed gap closure time.

TK/UIUC 2.6: Depletion analysis of Zircaloy and FeCrAl cladding

The work of the neutronics group was to develop and test the core level multicycle features in PARCS reactor code simulator. Here we describe the core model development, fuel shuffling scheme, and results of the multicycle depletion. This demonstrates that the proposed cladding modifications are not detrimental to LWR steady-state neutronics and thermal-hydraulics performance during normal operation.

The cross sections used in these core calculations were generated from the 15x15 Westinghouse-based design fuel assembly design shown in previous reports. Similar to the comparisons made between fuels using SERPENT, HELIOS results were compared as well. [UM Figure 1] shows the comparison of the reference fuel with a FeCrAl coated cladding fuel.

As can be seen in the figure, the reactivity bias from the coating decreases with burnup. Because the Fe is not burned like a burnable poison, the bias is negative for the life of the fuel. This confirms the earlier findings with SERPENT calculations.
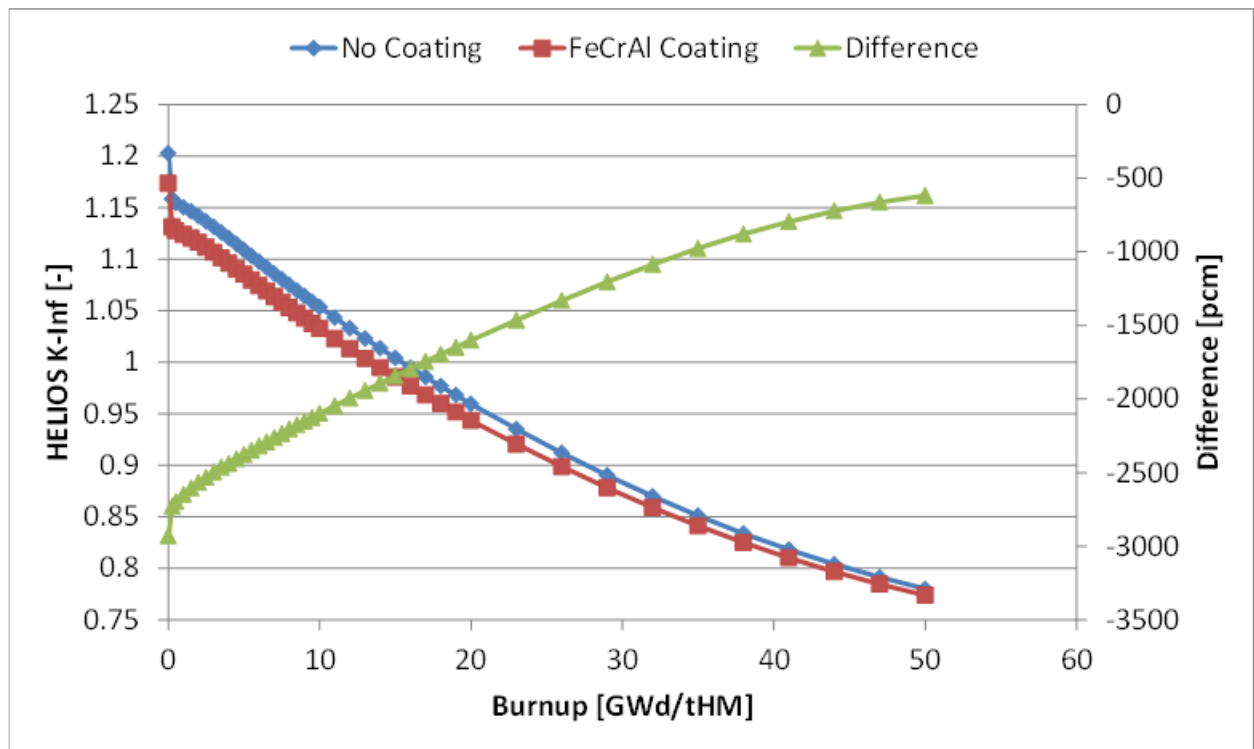
[UM Figure 1]: HELIOS results comparing uncoated and FeCrAl coated fuels

The core layout is based upon a Surry Unit 1, which is a three loop Westinghouse design rated (in the late 1970s) at 2441 MWt. There are 157 fuel assemblies, with 49 control rod locations. [UM Figure 2] shows the core layout. A three batch core reloading scheme was created, which shuffles the fuel individually. Optimization was limited in this approach, but this can be improved in future analysis.
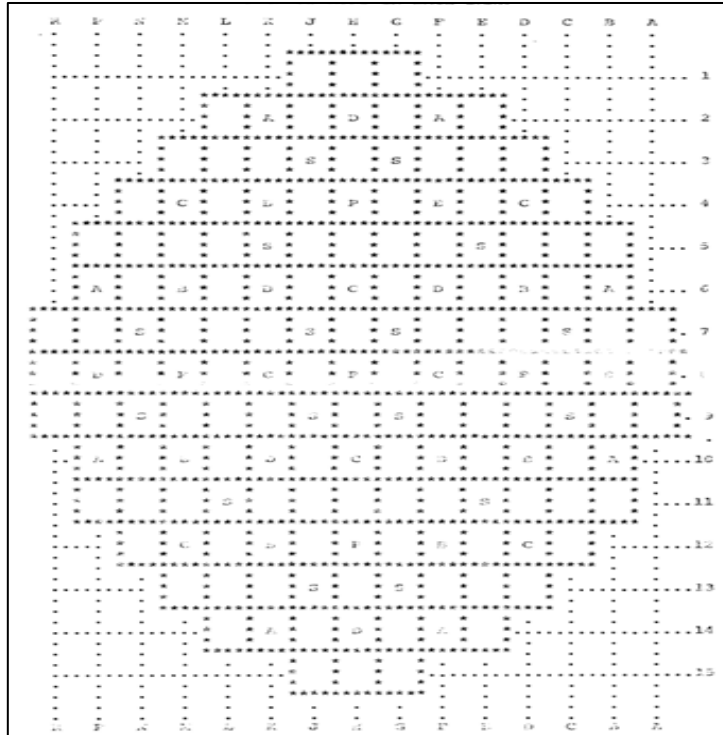
[UM Figure 2]: Surry Unit 1 Core Layout

PARCS utilizes a simple mass energy solver for the calculation of cross section feedback. The user must input the assembly specific geometry, along with the core inlet conditions and power levels. It is then assumed that each assembly has a dedicated coolant flow – no flow mixing between channels – and the calculation takes place between each PARCS iteration. This is similar to the approach used in SIMULATE.

A standard set of core conditions was used for the multicycle search. The data is provided below, for testing purposes, [UM Tables 1-3].

[UM Table 1]: Core Conditions for Depletion.

Parameter	[unit]	Value
Core Power	[%]	100.0
Core Flow	[kg/s/assm]	82.12
Inlet Temperature	[C]	286.0

[UM Table 2]: Depletion Conditions

Depletion Steps	[-]	15
Length Step	[days]	30

[UM Table 3]: Bank Positions

Step	Banks 1-3,5,7 [cm]	Steps
1	0.0	1-2
2	38.0	3-4
3	76.0	5-6
4	114.0	7-8
5	152.0	9-10
6	190.0	11-12
7	228.0	13-15

*Banks 4,6 are ARO=228.0

The results for a converged equilibrium cycle can be seen in [UM Figure 3]. The CR positions can likely be improved to reduce the peaking, and the boron control may likely be improved. Overall, the reactivity bias noted in the lattice calculation can be observed in the core calculations. This provides confidence that the modelling is consistent throughout the calculations system.
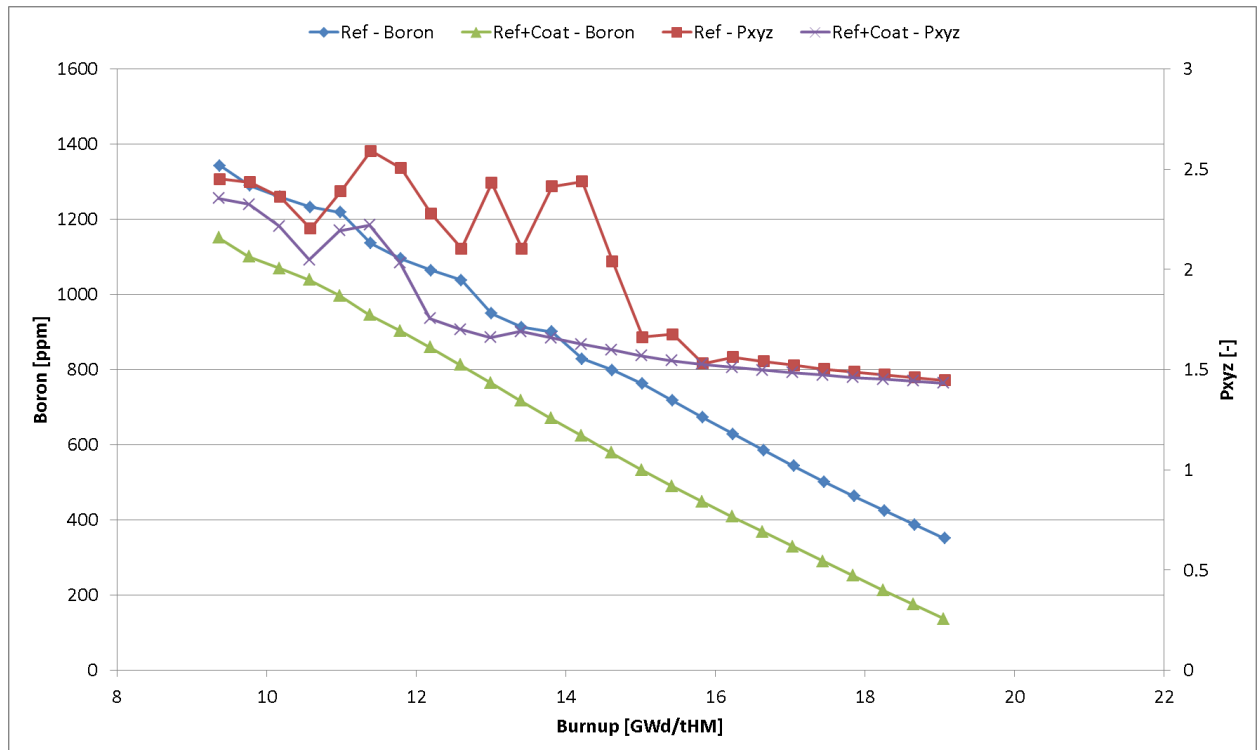
[UM Figure 3]: Multicycle Search Results

97

The PARCS PWR multicycle calculation with coated fuel shows the difference in core behavior between Zr and FeCrAl cladding. Results are physical, while improvement in some of the depletion conditions could be made to improve the peaking and let down curve. The results demonstrate that the proposed cladding modifications are not detrimental to LWR steady-state neutronics and thermal-hydraulics performance during normal operation.

TK/UIUC 2.7: Summary

Neutronics and fuel performance analysis are done for enhanced accident tolerance fuel, with the Monte Carlo reactor physics code Serpent and INL's fuel performance code BISON. The purpose is to evaluate the most promising candidate material FeCrAl, which has excellent oxidation resistance, as fuel cladding under normal operational conditions. Due to several major disadvantages of FeCrAl coating, such as difficulty in fabrication, diametrical compression from reactor pressurization, coating spallation and interdiffusion with zirconium, the monolithic FeCrAl cladding design is chosen. However, a substantial neutron penalty is expected when FeCrAl is used as cladding for current oxide fuel. To compensate for the decrease in reactivity, several approaches are discussed in [Wu et al., 2015], including: (1) increasing the oxide fuel enrichment; (2) minimizing the cladding thickness to reduce the neutron penalty; and (3) reducing the cladding thickness and filling the extra volume with oxide fuel.

We adopted the optimized FeCrAl cladding design from a detailed parametric study reported in [Terrani et al., 2013], which suggests reducing the cladding thickness and slightly increasing the fuel enrichment. A neutronics analysis is done that implementing this FeCrAl cladding design in a PWR single assembly. The results confirm that the PWR cycle length requirements will be matched, with a slight increase in total plutonium production. However, it is also reported in [Terrani et al., 2013] that this optimized design will cause a 15% increase in fuel pellet production cost.

Fuel performance analysis under normal operating conditions with INL code BISON is carried out to investigate the effects with this FeCrAl cladding design. The results from fuel performance analysis demonstrate that the application of FeCrAl cladding could improve performance. For example, the axial temperature profile is flattened. The gap closure is significantly delayed, which means the pellet-cladding mechanical interaction is greatly delayed. The disadvantages for FeCrAl cladding are that: (1) fission gas release is increased; and (2) fuel temperature is increased, but the increase is less than 50 K even at high burnup.

Based on the above discussion, applying FeCrAl as monolithic cladding to replace current zircaloy cladding will help avoid the major disadvantages for FeCrAl coating design. The better strength, corrosion, and embrittlement properties of FeCrAl enable the fabrication of FeCrAl cladding with thinner walls. With the optimized design suggested in [Terrani et al., 2013], FeCrAl cladding proves to be a good alternate for Zircaloy cladding, given the advantages and insignificant disadvantages shown by fuel performance analysis.

TK/UIUC 3: Simulation of off-normal conditions

For accident analysis, fuel rod fragmentation must not occur, and temperature and oxidation limits must not be exceeded. Moreover, the geometry must not alter significantly, and it should always be possible to insert control rods.

- Task 3.a.: Performance under accidents conditions, such as LB-LOCA and rod ejection.
- Task 3.b.: Evaluation of clad surface temperature (magnitude and duration) to assess the rate of hydrogen production under accident scenarios.

Milestone 3: Demonstrate that proposed fuel and cladding modifications are not detrimental during LWR accident conditions with respect to neutronics and thermal-hydraulics, demonstrate that fuel rod fragmentation does not occur and temperature and oxidation limits are not exceeded under accident conditions.

- Deliverable 3.a.: Report on the performance of new cladding under LBLOCA, including evaluation of clad surface temperature and assessment of the rate of hydrogen production under LB-LOCA.
- Deliverable 3.b.: Report on the performance of new cladding under rod ejection accident, including evaluation of clad surface temperature, assessment of the rate of hydrogen production.

In this section, the influence of adding a thin layer of coating material on the fuel cladding is studied based on a reflooding experiment. Temperature measurements at various axial locations during reflood are taken as experiment responses. The experimental and code (TRACE) results are shown to illustrate the effect of adding a coating layer. *Alumina* and *FeCrAl* are the two coating materials studied.

FEBA (Flooding Experiment with Blocked Array) test facility was designed to study fuel pin cladding behavior during LOCA. It was designed for reflooding tests with a capability of constant flooding rate and back pressure. It consisted of 5×5 rod bundle simulating PWR fuel pins which were heated electrically and had a cosine power profile. The rod bundle was housed in stainless steel enclosure which was further insulated with Triton Kao Wool to minimize heat loss. A cross-sectional view of FEBA test facility is shown in [Figure 3.1 TK/UIUC]. The axial view of a single FEBA heater rod, locations of grid spacers and axial power profile is shown in [Figure 3.2 TK/UIUC]. Relevant geometrical dimensions are presented in [Table 3.1 TK/UIUC].

TK/UIUC 3.1: Experimental Description

Tests with varying flooding rates and back-pressure were performed. These tests simulated the re-flooding phase of Large Break LOCA in PWRs. Test #216 was chosen as the base case for which the computational model was built. Prior to the start of the transient, the rods were heated in stagnant steam under low power until the desired initial cladding temperature was reached. The stainless steel housing was heated up only by radiation from the rods. At the start of the transient, the heater rod power was increased to a power level that simulated decay heat according to 120% ANS-standard about 40 seconds after reactor shutdown. Relevant initial and boundary conditions corresponding to Test #216 are presented in [Table 3.2 TK/UIUC]. The initial temperature distribution of the heater rods and housing are taken from Karlsruhe Research Center Report 3657. The transient temperature profile of the fuel pin cladding at various axial locations are presented in [Figure 3.3 TK/UIUC] In this figure, the reference level (0 mm) corresponds to the upper end of the housing (see [Figure 3.2 TK/UIUC]). The coolant enters the test section at axial level 4114 mm (bottom of the section as shown in [Figure 3.2 TK/UIUC]).

TK/UIUC 3.2: Computational Model In TRACE

TRACE (TRAC/RELAP Advanced Computational Engine) is a modernized thermal-hydraulics code designed to merge and extend three NRC's legacy safety codes – TRAC-P, TRAC-B and RELAP. It can be used to analyze large and small break LOCA (Loss of Coolant Accident) and system transients in PWRs and BWRs. TRACE models thermal-hydraulics phenomena in one-dimension (1D), although it includes 3D flow capability through the VESSEL component.

The computational model for TRACE was built with SNAP (Symbolic Nuclear Analysis Package). The FEBA test facility was modeled using a single vertical pipe (PIPE component) with appropriate inlet and outlet boundary conditions. The heater rods simulating fuel pins were modeled using heat structures. The latter was also used to model the stainless-steel enclosure. Heat loss from the outer surface of the housing was not modeled, it was assumed to be a perfect thermal insulator. The total axial length of the pipe was divided into 41 cells. The first (bottom-most) and last (top-most) cells in the pipe correspond to the unheated portion of the pipe. The remaining 39 cells in the middle of the pipe correspond to the heated section. The inlet, outlet and operating conditions are the same as experimental conditions (see [Table 3.2 TK/UIUC]). [Figure 3.4 TK/UIUC] shows the TRACE nodalization. The nodalization

dimensions are presented in [Table 3.3 TK/UIUC]. Junctions where grid spacers were present were modeled with reduced flow area. Pressure loss at grid spacers were modeled via abrupt area change model and additional form loss coefficients were set to 0. Choking model was not used. Fine mesh reflood was activated.

TK/UIUC 3.3: Results

The time evolution of pin cladding temperature for various axial levels as calculated by TRACE are shown below in [Figure 3.5 TK/UIUC]. The selected axial locations are the same as measured and shown in [Figure 3.3 TK/UIUC]. [Figure 3.6 TK/UIUC] shows a comparison between measured and calculated temperatures for 3 axial elevations. From [Figure 3.6 TK/UIUC], it is seen that the initial rate of increase in cladding temperature is over-predicted by TRACE, especially for elevations 590 mm and 2225 mm. The difference in Peak Cladding Temperature (PCT) between the experiment and TRACE is larger for cells that are located closer to the outlet. For instance, $\delta(PCT_{z=590mm}) \approx 150K$ whereas $\delta(PCT_{z=2225mm}) \approx 30K$. For locations close to the bottom (inlet) these deviations are much lower, for instance $\delta(PCT_{z=3860mm}) < 5K$.

[Table 3.4 TK/UIUC] shows the comparison of maximum cladding temperature between the experiment and TRACE for each axial level along with the time at which the cladding temperature peaked. Furthermore, for any given axial level, the PCT is observed to occur at an earlier time in TRACE simulation compared to the experiment. The discrepancies in predicting PCT may be attributed to the limitation in modeling heat losses. The failure to dissipate heat through lateral walls during transient may be the cause for a faster increase in temperature for each axial level. Slight discrepancy in the prediction of quenching time can also be seen from [Table 3.4 TK/UIUC]. The largest difference $\delta t_{quench} = 35$ seconds is observed for $z = 1135$ mm. The quenching times are predicted fairly accurately by TRACE for lower axial levels i.e. $z > 1135$ mm.

A thin coating of Alumina (Al_2O_3) and $FeCrAl$, each of thickness *1 mm* was applied to the heater rods. The power profile, geometry and other operating conditions were left unchanged. In recent accident-resistant-coating studies for nuclear rods, alumina and $FeCrAl$ alloy was proposed as viable choices as coating materials due to the their relatively lower neutron absorption cross-sections and lack of chemical reactivity with steam. Transient temperature profiles of the cladding after application of these coatings are presented here for selected axial locations (*z =590 mm, z = 2225 mm, z = 3860 mm*) in [Figure 3.7 TK/UIUC] to [Figure 3.9 TK/UIUC]. It can be seen from the following figures that the temperature profiles do not change significantly on addition of thin layers of coating. Moreover, [Figure 3.10 TK/UIUC] shows the quenching times are more or less the same as the base case on addition of either coating.

TK/UIUC 3.4: Conclusions

These analyses show that the addition of a thin layer of coating on top of the base cladding does not affect the temperature profile significantly and hence serve as a viable means to prevent oxidation of Zr-based conventional claddings. This demonstrates that proposed fuel and cladding modifications are not detrimental during LWR accident conditions with respect to thermal-hydraulics.
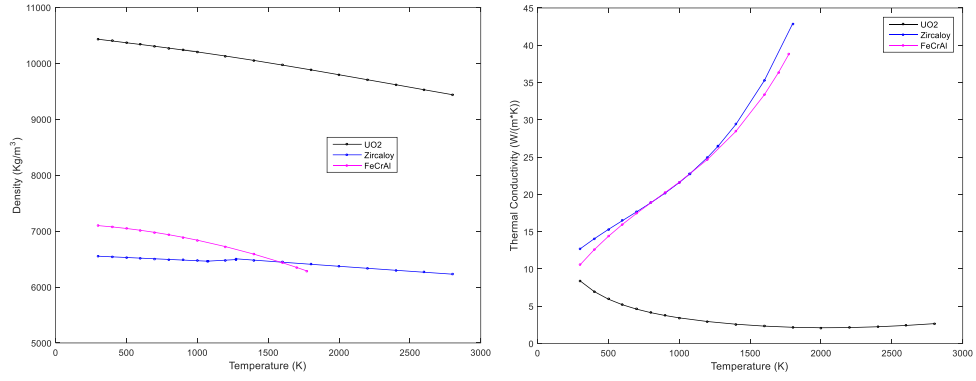
[Figure 1.1 TK/UIUC]: Material density (left), thermal conductivity (right).
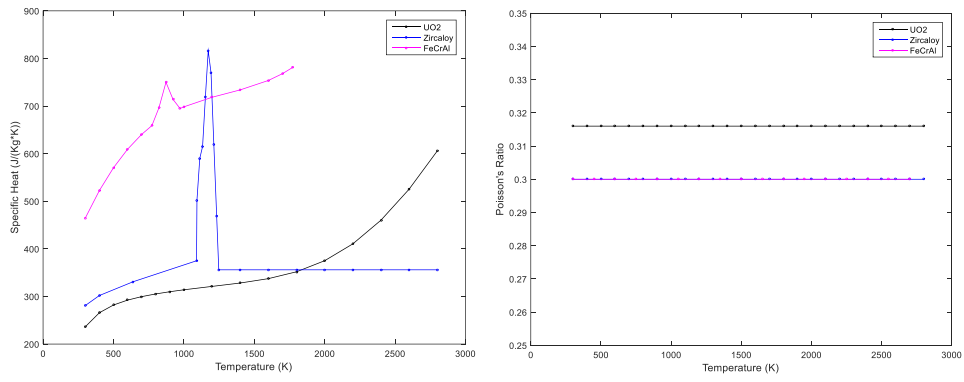
[Figure 1.2 TK/UIUC]: Specific heat capacity (left), Poisson's ratio (right).
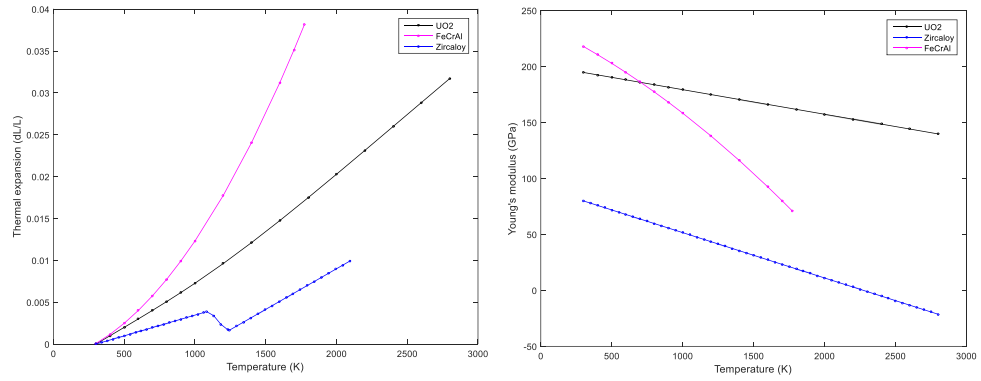
[Figure 1.3 TK/UIUC]: Thermal expansion coefficient (left), Young's modulus (right).
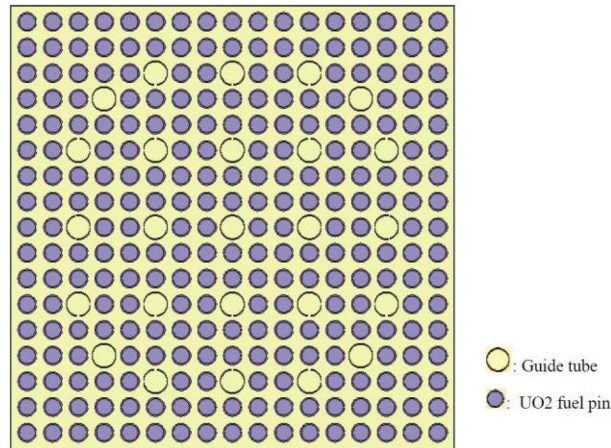
[Figure 2.1 TK/UIUC]: UO$_2$ fuel assembly used for neutronics analysis
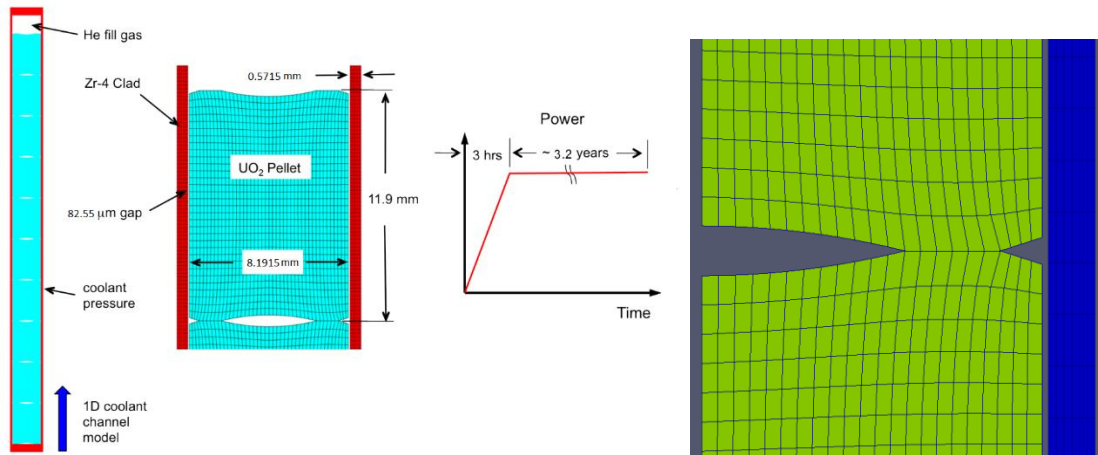
[Figure 2.2 TK/UIUC]: Ten-pellet rodlet model [Williamson et al., 2012] and mesh.
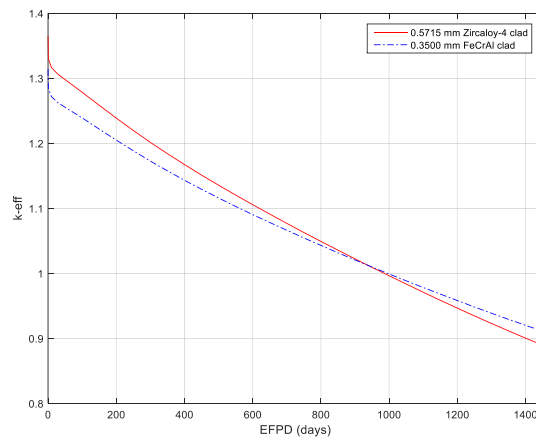
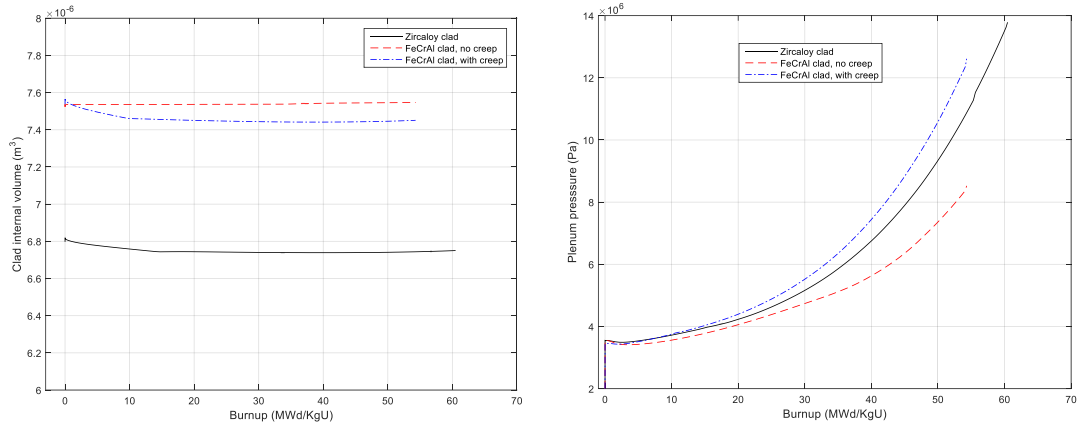[Figure 2.3 TK/UIUC]: Comparison of k$_{eff}$ versus burnup for PWR single assembly
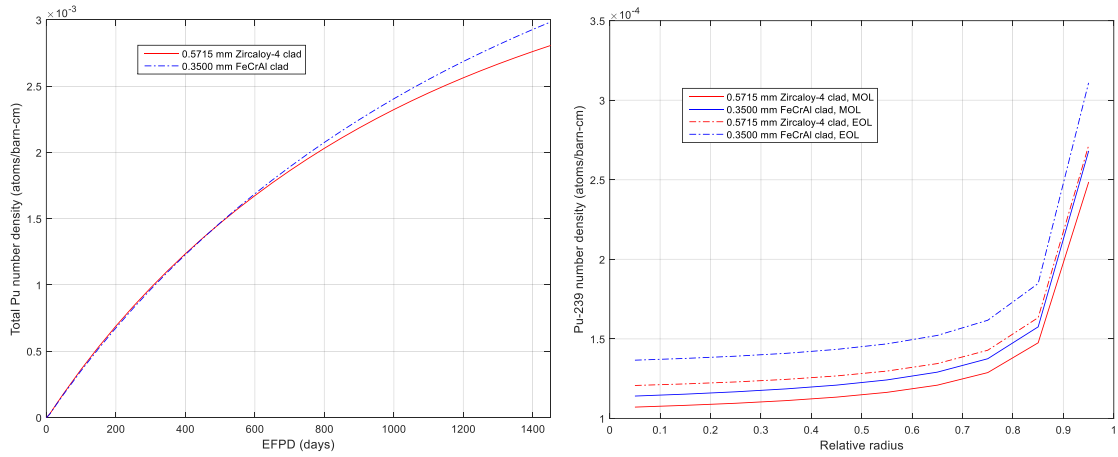
[Figure 2.4 TK/UIUC]: Total Plutonium production (left) and ^{239}Pu radial distribution (right)
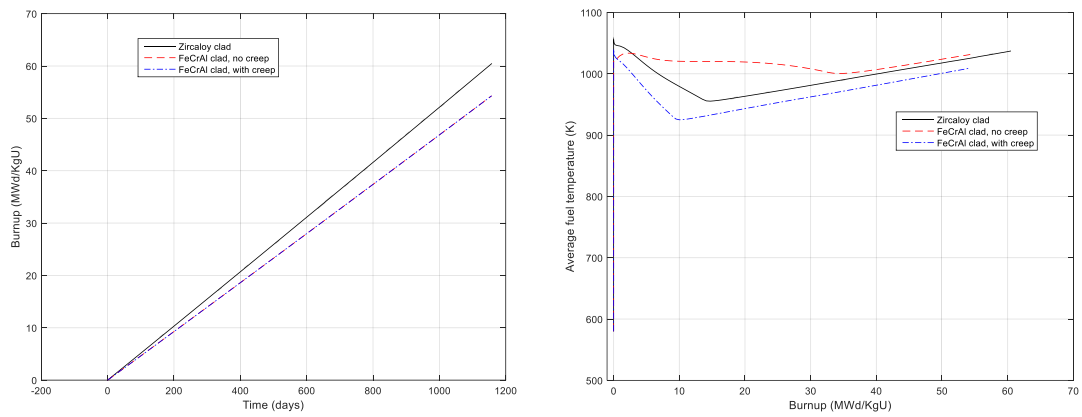
[Figure 2.5 TK/UIUC]: (Left) burnup vs time, (right) average fuel temperature
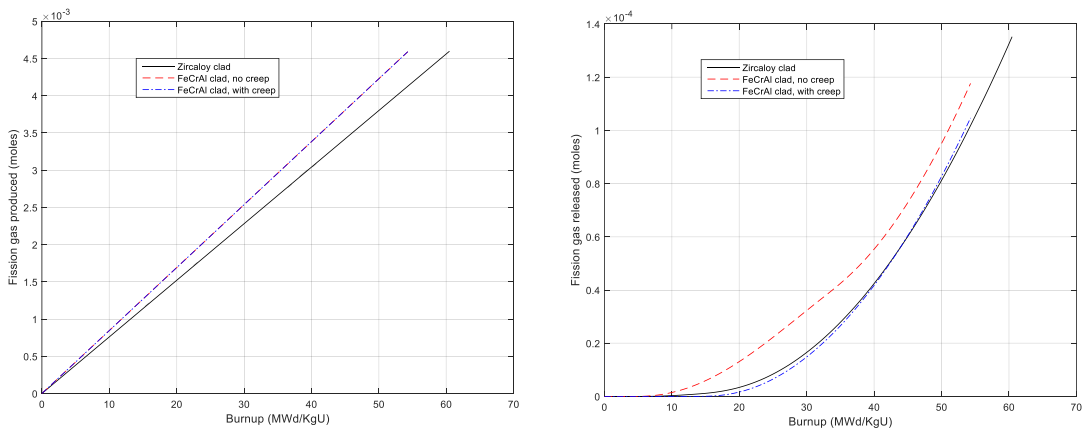
[Figure 2.6 TK/UIUC]: (Left) Fission gas produced, (right) fission gas released

[Figure 2.7 TK/UIUC]: (Left) Internal volume, (right) plenum pressure
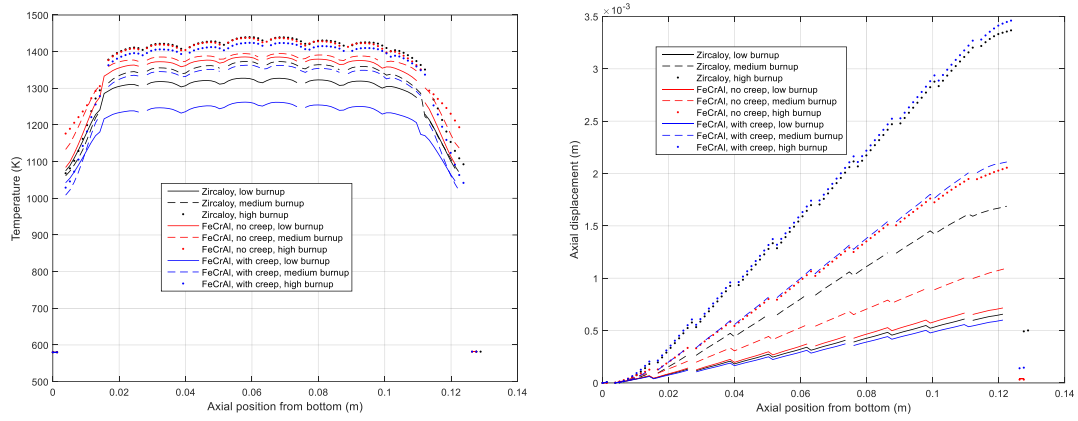
[Figure 2.8 TK/UIUC]: (Left) Temperature distribution over the fuel centerline at different burnup, (right) axial displacement over the fuel centerline at different burnup.
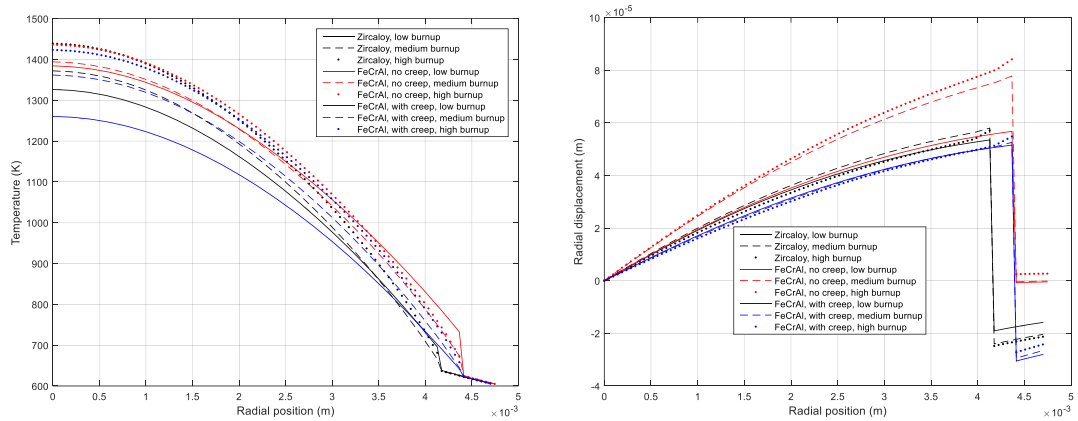
[Figure 2.9 TK/UIUC]: Plot over the horizontal center line of the fifth fuel pellet from bottom at different burnup, (left): radial temperature distribution, (right): radial displacement.
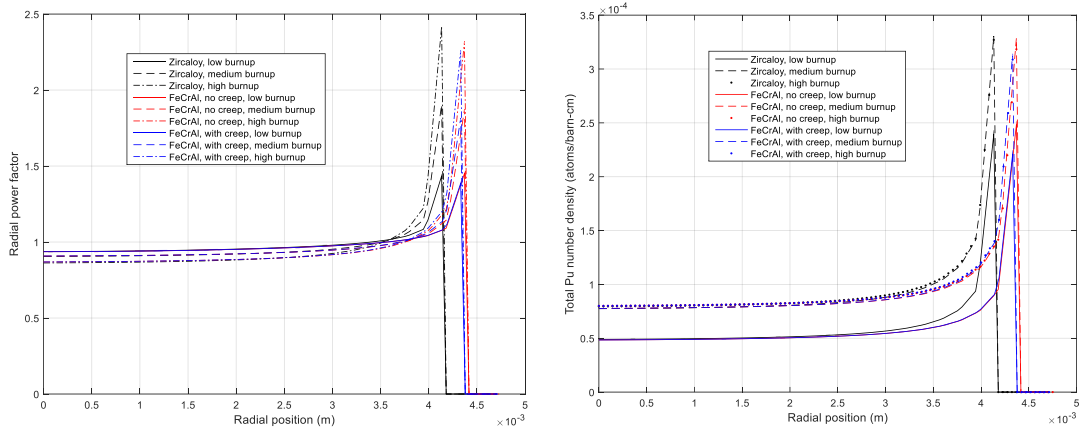
[Figure 2.10 TK/UIUC]: Plot over the horizontal center line of the fifth fuel pellet from bottom at different burnup, (left): radial power factor, (right) radial ^{239}Pu distribution.
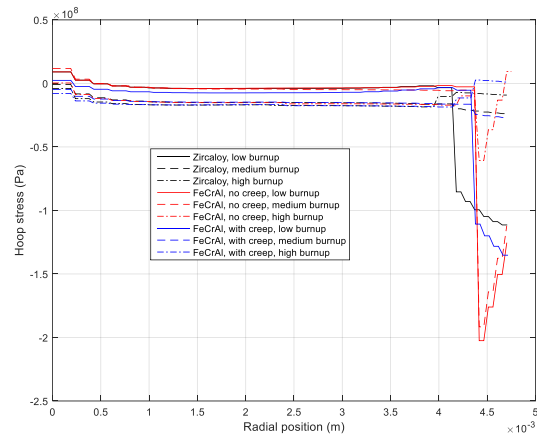
[Figure 2.11 TK/UIUC]: Hoop stress over the horizontal center line of the fifth fuel pellet from bottom at different burnup.
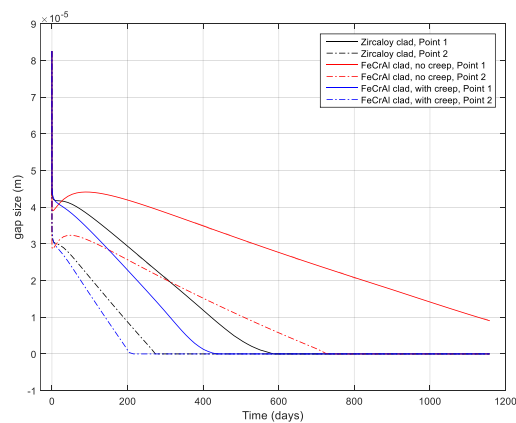
[Figure 2.12 TK/UIUC]: Plot of gap sizes for two nodes on fuel pellet surface, point 1 is at the height of 0.012 m, point 2 is at the height of 0.07 m.

[Figure 3.1 TK/UIUC]: Cross-sectional view of FEBA test facility

[Figure 3.2 TK/UIUC]: Axial view of the simulator heater rod
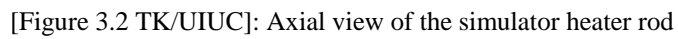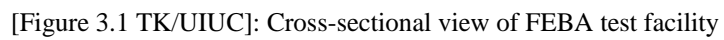
[Figure 3.3 TK/UIUC]: Transient temperature distribution at various axial levels
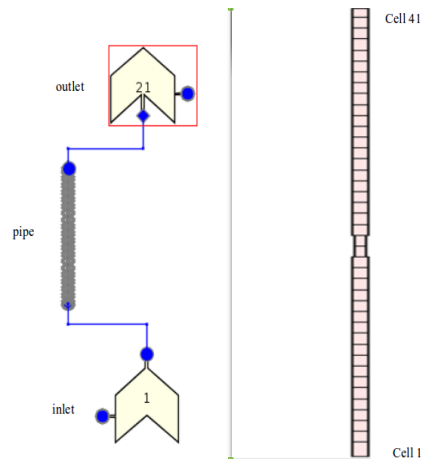
[Figure 3.4 TK/UIUC]: Nodalization diagram in TRACE
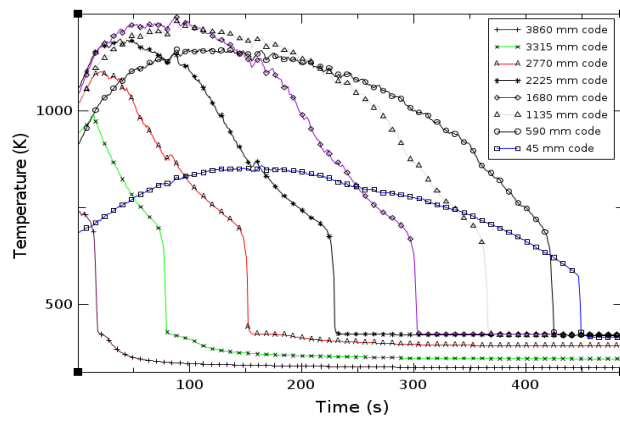
[Figure 3.5 TK/UIUC]: Transient clad temperature computed using TRACE
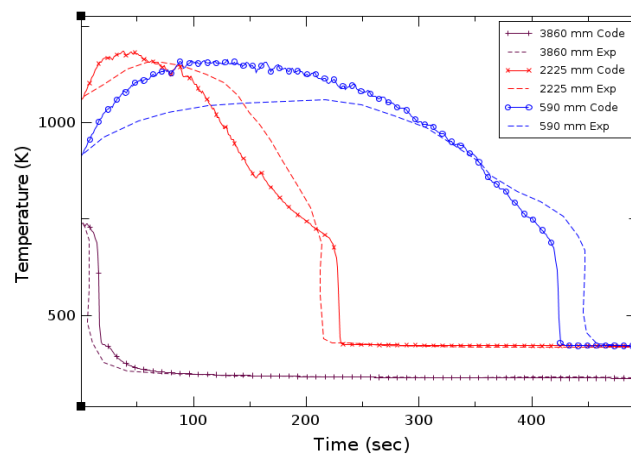
[Figure 3.6 TK/UIUC]: Transient clad temperature for selected axial levels
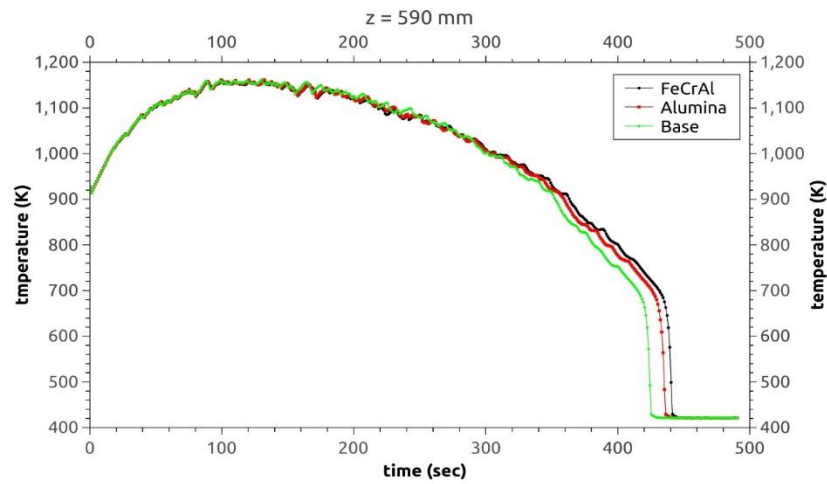
[Figure 3.7 TK/UIUC]: Temperature profiles at z = 590 mm
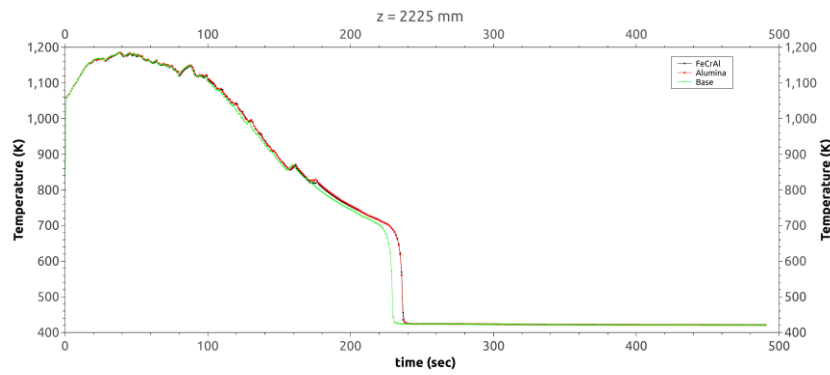
[Figure 3.8 TK/UIUC]: Temperature profiles at z = 2225 mm
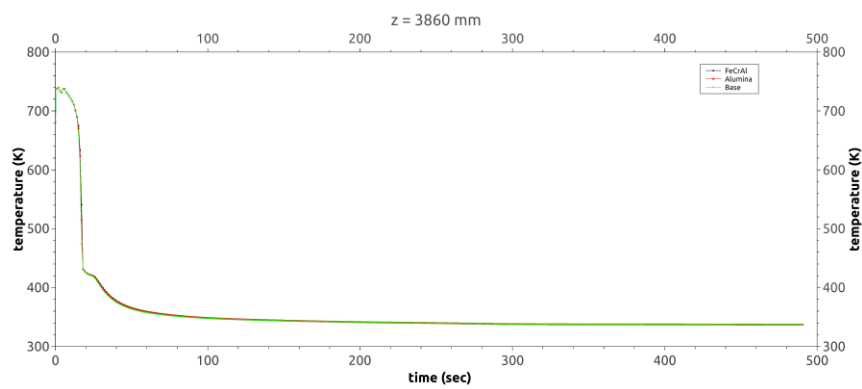
[Figure 3.9 TK/UIUC]: Temperature profiles at z = 3860 mm
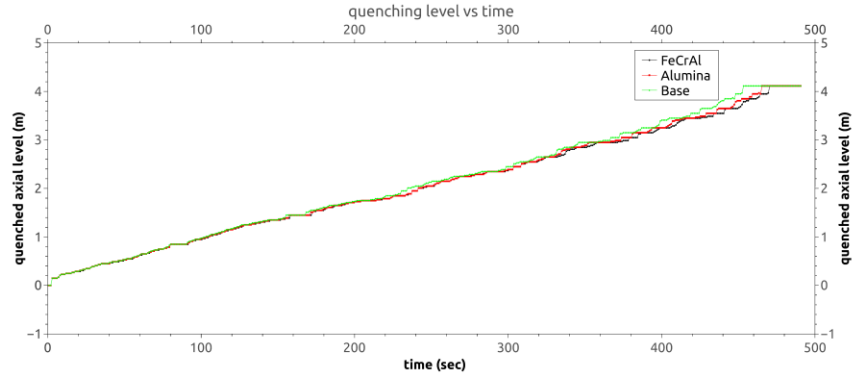
[Figure 3.10 TK/UIUC]: Quench time comparison

[Table 2.1 TK/UIUC]: Serpent model specifications.

Property	Value	
	Zircaloy-4 clad	FeCrAl clad
Assembly fuel height (cm)	365.76	
Clad composition:	Fe/Cr/Zr/Sn = 0.15/0.1/98.26/1.49 wt.%	Fe/Cr/Al = 75/20/5 wt.%
Fuel pellet radius (mm)	4.09575	4.31725
Gap thickness (µm)	82.55	
Cladding ID (mm)	4.1783	4.3998
Cladding thickness (µm)	571.5	350
Cladding OD (mm)	9.4996	
pitch-to-rod-diameter ratio	1.326	
Cladding ID (mm)	5.624	
Cladding OD (mm)	6.032	
Number of guide tubes	25	
Fuel enrichment	4.90 %	5.06 %
Fuel density	10.47 g/cm^3	
Coolant density	0.7119 g/cm^3	
Cladding density	6.56 g/cm^3	7.10 g/cm^3
Specific power density (MW/KgU)	38.3300E-03	34.4798E-03
Simulated time (days)	1500.0	
Coolant temperature	580 K	
Fuel temperature	900 K	
Clad and gap temperature	600 K	
Boron concentration	630 ppm	
Neutron library	ENDF/B-VII	
Boundary conditions	Reflective	
Assembly design	Westinghouse 17 by 17 PWR fuel rod	

[Table 2.2 TK/UIUC]: BISON model specifications

Property	Value	
	Zircaloy-4 clad	FeCrAl clad
Active fuel rodlet height (cm)	11.90	
Fuel pellet radius (mm)	4.09575	4.31725
Gap thickness (µm)	82.55	
Cladding ID (mm)	4.1783	4.3998
Cladding thickness (µm)	571.5	350
Cladding OD (mm)	9.4996	
pitch-to-rod-diameter ratio	1.326	
Fuel enrichment	4.90%	5.06%
Fuel theoretical density	96%	
Cladding density	6.56 g/cm^3	7.10 g/cm^3
Linear heat rate (W/cm)	250	
Simulated time (days)	1157.4	
Fast neutron flux (n/m^{2}s)	7.5 x 10^{17}	
Initial and inlet temperature	580 K	
Coolant pressure	15.5 MPa	
Coolant inlet mass flux	3800 kg/m^2-s	
Initial Helium pressure	2.0 MPa	

[Table 3.1 TK/UIUC]: Dimensions of the heater rod

Stainless steel housing thickness (mm)	6.5
Outer diameter of heater rod (mm)	10.75
Heater rod pitch (mm)	14.3
Inner length of square housing (mm)	78.5

[Table 3.2 TK/UIUC]: System operating conditions

Fluid inlet velocity (cm/s)	3.8
System outlet pressure (bar)	14.12
Feed water temperature (^{o}C) (0-30 s)	48
Feed water temperature (^{o}C) (30s-end)	37
Bundle power (kW) at 0 s	200
Bundle power (kW) during transient	120% ANS standard

[Table 3.3 TK/UIUC]: Computational model dimensions

Cell 1 length (m) (lower unheated portion)	0.139
Cells 2-40 length (m) (middle heated portion)	0.1
Cell 41 length (m) (upper unheated portion)	0.075
Cells 1-18, 21-41 flow area (m^2)	3.893 10^{-3}
Cells 19, 20 flow area (m^2)	3.115 10^{-3}
Junction hydraulic diameter (m) (cells 3-4, 8-9, 14-15, 18-19, 19-20, 24-25, 30-31, 35-36)	0.01075
Junction hydraulic diameter (m) (Remaining junctions)	0.01344
Junction area (m^2) (cells 3-4, 8-9, 14-15, 18-19, 19-20, 24-25, 30-31, 35-36)	3.115 10^{-3}
Junction area (m^2) (remaining cells)	3.893 10^{-3}
Wall roughness (Cells 1-41)	1.0 10^{-5}
Hydraulic diameter (m)	0.01344
Heated diameter (m)	0.01844

[Table 3.4 TK/UIUC]: Comparison of Peak Cladding Temperature

Axial height (mm)	PCT (K)	Quench time (sec)		
	TRACE		Experiment	
45	857	450	802	477
590	1155	425	1055	456
1135	1227	367	1133	402
1680	1240	304	1200	316
2225	1180	231	1155	218
2770	1090	154	1050	138
3315	973	80	955	75
3860	730	60	730	64

TK/UIUC: References

[Cheng et al., 2012] Cheng, T., J. Keiser, M. Brady, K. Terrani, B. Pint, "Oxidation of fuel cladding candidate materials in steam environments at high temperature and pressure," Journal of Nuclear Materials, Vol. 427, No.1, August 2012, pp. 396–400.

[Gaston et al., 2009] Gaston, D., C. Newman, G. Hansen, D. Lebrun-Grandie. "MOOSE: A parallel computational framework for coupled systems of nonlinear equations," Nuclear Engineering and Design, Vol. 239, No. 10, October 2009, pp. 1768–1778.

[George et al., 2015] George, N. M., K. Terrani, J. Powers, A. Worrall, and I. Maldonado, "Neutronic analysis of candidate accident-tolerant cladding concepts in pressurized water reactors," Annals of Nuclear Energy, vol. 75, pp. 703-712, 2015.

[Goldner, 2012] Goldner, F., "Development Strategy for Advanced LWR Fuels with Enhanced Accident Tolerance," Enhanced Accident Tolerant LWR Fuels National Metrics Workshop, Germantown, Maryland, October 2012.

[Hales et al., 2014] Hales, J. D., S. Novascone, G. Pastore, D. Perez, B. Spencer, R. Williamson, BISON Theory Manual: The Equations behind Nuclear Fuel Analysis, Fuels Modeling & Simulation Department, Idaho National Laboratory, Idaho Falls, Idaho, June 2014.

[Heuser et al., 2013] Heuser, B. J., T. Kozlowski, X. Wu, "Engineered Zircaloy Cladding Modifications for Improved Accident Tolerance of LWR Fuel: A Summary," Proc. of the 2013 LWR Fuel Performance Meeting/TopFuel, Charlotte, North Carolina, USA, September 15–19, 2013.

[Lassmann et al., 1994] Lassmann K., O'Carroll C., J. van de Laar, and Walker C. T. The radial distribution of plutonium in high burnup UO2 fuels. J. Nucl. Materials, 208:223–231, 1994.

[Leppänen et al., 2007] Leppänen, J., 2007, Development of a New Monte Carlo Reactor Physics Code, Ph.D. Thesis: VTT Technical Research Centre of Finland, Espoo, Finland.

[Ott et al., 2014] Ott, L. J., K. Robb, D. Wang, "Preliminary assessment of accident tolerant fuels on LWR performance during normal operation and under DB and BDB accident condition," Journal of Nuclear Materials, 448.1, 2014, 520–533.

[Terrani et al., 2013] Terrani, K. A., C. Parish, D. Shin, B. Pint, "Protection of zirconium by alumina and chromia forming iron alloys under high temperature steam exposure," Journal of Nuclear Materials, Vol. 438, No. 1, July 2013, pp. 64–71.

[Terrani et al., 2014a] Terrani, K. A., S. Zinkle, L. Snead, "Advanced oxidation resistant iron based alloys for LWR fuel cladding," Journal of Nuclear Materials, Vol. 448, No. 1, May 2014, pp. 420–435.

[Terrani et al., 2014b] Terrani, K. A., B. A. Pint, C. M. Parish, C. M. Silva, L. L. Snead, and Y. Katoh, "Silicon Carbide Oxidation in Steam up to 2 MPa," Journal of American Ceramic Society, vol. 97, pp. 2331-2352, 2014.

[Williamson et al., 2012] Williamson, R. L., J. Hales, S. Novascone, M. Tonks, D. Gaston, C. Permann, D. Andrs, R. Martineau, "Multidimensional multiphysics simulation of nuclear fuel behavior," Journal of Nuclear Materials, Vol. 423, No. 1, April 2012, pp. 149–163.

[Williamson et al., 2014] Williamson, R. L., et al. "Implicit, parallel, fully coupled nuclear fuel performance analysis," Fuels Modeling & Simulation Department BISON Workshop, Idaho National Laboratory, Idaho Falls, Idaho, June 2014.

[Wu et al., 2014a] Wu, X., T. Kozlowski, and B. Heuser, "Neutronics Analysis of Improved Accident Tolerance of LWR Fuel by Modifying Zircaloy Cladding of Fuel Pins," Proceedings of ICAPP 2014, Charlotte, USA, April 6–9, 2014.

[Wu et al., 2014b] Wu, X., Sabharwall, P., Hales, J., Kozlowski, T., (2014). Neutronics and Fuel Performance Evaluation of Accident Tolerant Fuel under Normal Operation Conditions. Technical Report INL/EXT-14-32591, Idaho National Laboratory.

[Wu et al., 2015] Wu, X., Kozlowski, T., & Hales, J. D., (2015). Neutronics and Fuel Performance Evaluation of Accident Tolerant FeCrAl Cladding under Normal Operation Conditions. Annals of Nuclear Energy, 85, 763-775.

[Yan et al., 2014] Yan, Y., J. Keiser, K. Terrani, G. Bell, L. Snead, "Post quench ductility evaluation of Zircaloy 4 and select iron alloys under design basis and extended LOCA conditions," Journal of Nuclear Materials, Vol. 448, No. 1, May 2014, pp. 436–440.

[Zinkle et al., 2014] Zinkle, S. J., K. Terrani, J. Gehin, L. Ott, L. Snead, "Accident tolerant fuels for LWRs: A perspective," Journal of Nuclear Materials, Vol. 448, No. 1, May 2014, pp. 374–379.

2.8   Numerical simulation of heat transport

We conducted the thermal analysis of the ATF with a protective coating, under increasingly realistic conditions — both at the fuel rod level as well as at the system level. In the next few sections, analysis and results for the temperature distributions in the fuel rod (fuel-gap-cladding-coating) obtained using different methods are reported.

RU/UIUC 1 An analytical solution of temperature distribution for fuel gap clad and coating

The goal is to solve the temperature distribution, *T1(r), T2(r), T3(r)* and *T4(r)* shown in Figure 1. Three methods are applied to solve for the temperature distribution.

RU/UIUC 1.1 Method 1: Constant k1, k2, k3 and k4

For each region (fuel, gap, cladding and coating), the heat conduction equation is used to obtain the analytical solution.

Region 1 (fuel):

Governing Equations (GE):

$$\frac{1}{r}\frac{d}{dr}(k_1 r \frac{dT_1}{dr}) + S_0 = 0$$

$$=> \frac{d}{dr}(k_1 r \frac{dT_1}{dr}) = -S_0 r$$

$$=> k_1 r \frac{dT_1}{dr} = -\frac{S_0 r^2}{2} + C_1$$

$$=> \frac{dT_1}{dr} = -\frac{S_0 r^2}{2k_1} + \frac{C_1}{k_1}\frac{1}{r}$$

$$=> T_1(r) = -\frac{S_0 r^2}{4k_1} + \frac{C_1}{k_1}\ln(r) + C_2$$

Region 2 (gap):

GE:

$$\frac{1}{r}\frac{d}{dr}(k_2 r \frac{dT_2}{dr}) = 0$$

$$=> k_2 \frac{d}{dr}(r \frac{dT_2}{dr}) = 0$$

$$=> \frac{d}{dr}(r \frac{dT_2}{dr}) = 0$$

$$=> r \frac{dT_2}{dr} = C_3$$

$$=> \frac{dT_2}{dr} = \frac{C_3}{r}$$

$$=> T_2(r) = C_3 \ln(r) + C_4$$

Similarly,

Region 3(cladding): $T_3(r) = C_5 \ln(r) + C_6$

Region 4(coating): $T_4(r) = C_7 \ln(r) + C_8$

Apply 8 boundary conditions to solve the 8 unknown coefficients.

Boundary and Interface Conditions:

BC1: $T_1(r = 0) = finite => C_1 = 0$,   BC2: $-k_4 \frac{dT_4}{dr}|_{r=R4} = h(T_4|_{r=R4} - T_\infty)$

BC3: $T_1(r = R1) = T_2(r = R1)$,   BC4: $-k_1 \frac{dT_1}{dr}|_{r=R1} = -k_2 \frac{dT_2}{dr}|_{r=R1}$

BC5: $T_2(r = R2) = T_3(r = R2)$,   BC6: $-k_2 \frac{dT_2}{dr}|_{r=R2} = -k_3 \frac{dT_3}{dr}|_{r=R2}$

BC7: $T_3(r = R3) = T_4(r = R3)$,   BC8: $-k_3 \frac{dT_3}{dr}|_{r=R3} = -k_4 \frac{dT_4}{dr}|_{r=R3}$

The eight coefficients are:

$$C_1 = 0$$

$$C_2 = \frac{R1^2 S_0}{2k_2}\left(\frac{k_2}{k_3}\left(\frac{k_3}{k_4}\left(\frac{k_4}{hR4} - \ln(R3) + \ln(R4)\right) - \ln(R2) + \ln(R3)\right) - \ln(R1) + \ln(R2)\right) + \frac{R1^2 S_0}{4k_1} + T_\infty$$

$$C_3 = -\frac{R1^2 S_0}{2k_2}$$

$$C_4 = \frac{R1^2 S_0}{2k_2}\left(\frac{k_2}{k_3}\left(\frac{k_3}{k_4}\left(\frac{k_4}{hR4} - \ln(R3) + \ln(R4)\right) - \ln(R2) + \ln(R3)\right) + \ln(R2)\right) + T_\infty$$

$$C_5 = -\frac{R1^2 S_0}{2k_3}$$

$$C_6 = \frac{R1^2 S_0}{2k_3}\left(\frac{k_3}{k_4}\left(\frac{k_4}{hR4} - \ln(R3) + \ln(R4)\right) + \ln(R3)\right) + T_\infty$$

$$C_7 = -\frac{R1^2 S_0}{2k_4}$$

$$C_8 = \frac{R1^2 S_0(hR4\ln(R4) + k_4)}{2hk_4 R4} + T_\infty$$

Therefore, the analytical solutions for the four regions:

$$T_1(r) = -\frac{S_0 r^2}{4k_1} + C_2 \tag{1}$$

$$T_2(r) = C_3\ln(r) + C_4 \tag{2}$$

$$T_3(r) = C_5\ln(r) + C_6 \tag{3}$$

$$T_4(r) = C_7\ln(r) + C_8 \tag{4}$$

Some parameters:

The volume of one rod is $V = \pi R1^2 H = 1.7937 \times 10^{-4} m^3$. The power density of one rod is,

$$S_0 = \frac{3565 \, MW}{193 \, assemblies \cdot 264 \, rods/assembly \cdot V} = 390.07 \, MW/m^3.$$

The values of the pertinent parameters are listed below:

R1=0.003951m

R2=0.004010 m

R3=0.004583 m

R4=0.0047 m

$k1$ = 5.3046 W/m-K (assumed, at T=578.5 K)

$k2$ = 1 W/m-K

$k3$= 13 W/m-K

$k4$= 2 W/m-K (assumed).

However, the thermal conductivity variation in fuel region could be significant due to large temperature difference (Figure 2). The following methods are trying to incorporate the effect of temperature dependent thermal conductivity. Thus, $k1$ in the next section is a function of temperature, $k1(T)$.

RU/UIUC 1.2 Method 2: $k1=k1(T)$, $k2$, $k3$, and $k4$ are constants

To reasonably approximate the temperature distributions in the accident tolerant nuclear fuel, the temperature-dependent thermal conductivity of fuel needs to be considered. The effective fuel temperature T_{eff} can be viewed as a representative of fuel temperature. There are different formulae to evaluate T_{eff} and they usually have the form (de Kruijf,1994):

$$T_{eff} = aT_{ave} + bT_0 + cT_f \tag{5}$$

The volume average temperature is $T_{ave} = \int Trdr / \int rdr$. T_0 is the temperature at center of the fuel and T_f is the fuel surface temperature. According to a report by Kozlowski and Downar (2006), $a = 0, b = 3/10$ and $c = 7/10$. Thus, eq. (1) - eq. (4) are still used to calculate the temperature distribution but $k1$ in $T1(r)$ will be updated by $k1(T_{eff})$. T_{eff} is evaluated using eq. (5).

From the report (Kozlowski and Downar, 2006) the thermal conductivities for each region are:

$$k1 = k_{UO2,fuel} = 1.05 + 2150 \cdot (T - 73.15)^{-1} \ W/m\text{-}K$$
$$k2 = 1 \ W/m\text{-}K$$
$$k3 = 13 \ W/m\text{-}K$$
$$k4 = 2 \ W/m\text{-}K \ \text{(assumed)}$$

The temperature distribution with this method is shown in Figure 3.

RU/UIUC 1.3 Method 3: Kirchhoff Transformation

Kirchhoff transformation defines a new thermal conductivity to transform the heat conduction equation and solve it analytically.

$$k(T) = 1.05 + \frac{2150}{T - 73.15} \tag{6}$$

$k(T_o) = k_o$, and define

$$U \equiv \int_{T_o}^{T} \frac{k(T\prime)}{k(T_o)} dT', \tag{7}$$

We get

$$U = \frac{1}{k_o}[1.05 \cdot (T - T_0) + 2150 \cdot \ln(\frac{73.15 - T}{73.15 - T_0})] \tag{8}$$

From the definition of eq. (7) , the heat conductivity equation produces:

$$U(r) = -\frac{\dot{q}}{2k_o}r^2 + C_2 \tag{9}$$

equate eq. (8) and eq. (9), we get,

$$\frac{1}{k_o}[1.05 \cdot (T - T_0) + 2150 \cdot \ln(\frac{73.15 - T}{73.15 - T_0})] = -\frac{\dot{q}}{2k_o}r^2 + C_2. \tag{10}$$

Assume U(R1) = $T1$ to solve C_2. From eq. (9) , if C_2 is known, then eq. (10) can be used to solve T at each location in fuel numerically. For this problem, mathematica is used to solve eq. (10) for T analytically. The analytical solution for temperature is

$$T(r) = 73.15 + 2047.62 ProductLog[0.000471e^{-0.000233\dot{q}\cdot r^2 + 0.000488 \cdot T_0}(e^{0.000465 C_2 \cdot k_0}(T_0 - 73.15))]$$

The advantage of this method is that it considers the variation of thermal conductivity at each location in fuel. However, if eq.(6) *k(T)* in fuel is a more complicated expression, eq. (10) is likely to be a transcendental function. Another difficulty is that usually the unknown coefficient C_2 is determined by the interface boundary condition at the interface of fuel and gap. This increases the complexity of solving eq. (10). A literature (Tomatis, 2013) also tried to apply Kirchhoff transformation to solve fuel temperature. The author used polynomial equation to approximate *k(T)* and conducted the integration in eq. (7) by splines approximation.

RU/UIUC 1.4 Method 4: Solve the temperature in the fuel analytically in Matlab

The heat conduction equation with temperature-dependent thermal conductivity can also be solved analytically in Matlab.
The governing equation is

$$\frac{1}{r}\frac{d}{dr}[k(T)r\frac{dT(r)}{dr}] + S_0 = 0.$$

The expression for temperature-dependent thermal conductivity is,

$$k(T) = 1.05 + \frac{2150}{T - 73.15}$$

The analytical solution for the temperature distribution in fuel solved in Matlab is

$$T(r) = 2047.6 \times wrightOmega(C_1 \text{-}0.00011628 \times S_0 \times r^2 + C_2 \times ln(r^{1/43000}) \text{-}7.6602) + 73.15.$$

The difficulty in this method is that unknown coefficients C_1 and C_2 are inside a special function. When solving fuel region with other regions (gap-cladding-coating), C_1 and C_2 are hard to be determined.

RU/UIUC 1.5 Evaluations of each method

To evaluate the accuracy of each method, a one region (fuel) problem is solved with surface temperature at 435 K.
case_1: *k1= constant* = 5.3046 W/m-K (assumed, at T = 578.5 K)

From eq. (1) ➔ $C_2 = 721.9723$

case_2: *k1* = k (T_{eff} = 0.3*T(r = 0) + 0.7 * T(r = R1)) = 5.9522 W/m-K

From eq. (1) ➔ $C_2 = 690.7473$

case_3: Kirchhoff Transformation

From eq. (7) and eq. (8), when $T = T_0 = 435\ K\ at\ r\ =\ R1$, we get $U(r\ = R1) = 0$

From eq. (9) , $U(r) = -\frac{\dot{q}}{2k_o} r^2 + C_2$, the value of C_2 is

$$C_2 = \frac{\dot{q}}{2k_o(T = 435K)} R1^2 = 435.4563$$

, where

$$k_0 = k(T = 435K) = 6.9917.$$

Solving eq. (10) numerically can determine the temperature distribution at each location. The results for case_1 - case_3 are shown in Figure 4.

In conclusion, Kirchhoff Transformation should be used to calculate the temperature distribution for the region with large variation in thermal conductivity.

RU/UIUC 2 Evaluate the effects of different coating materials with relap5 model

The relap5 input deck in this work is originally used to simulate a main steam line break (MSLB) transient applying the operational data for the Three Mile Island Unit 1, which is a PWR type nuclear reactor. Since zirconium will react with water at high temperature the cladding oxidation is what we are concerned. A coating on the surface of cladding could probably protect the fuel. This TMI-1 model is modified to evaluate the thermal-hydraulic effects of a coating layer. The properties of iron with thickness of 0.1 mm are used to evaluate the effect of coating layer. Figure 5 and Figure 6 compare the maximum temperature in the core and the pressure at hot leg. It can be observed that the differences are very small with iron as the coating material.

Other coating materials, Al, Cr, and FeCrAl are also evaluated with the same thickness (0.1 mm). The results are shown in Figures 7-12. Compared to the case without coating, since the thickness of coating is very small and the thermal conductivities of coatings are not very different from cladding, no apparent effects can be observed. If we highly reduce the thermal conductivities of coating to 10 % (Figures 13 and 14) and 5% (Figures 15 and 16) of cladding the temperatures with coating would drop on the onset of accident (MSLB). The reason is that the heat is blocked by the low conductive coating so the maximum calculated fluid temperature in core is lower.

RU/UIUC 3 Effects of different coating thickness and thermal conductivities

The results in Figure 17., Table 1, and Table 2 are from analytical analysis. Figure 17 shows that the effects of different thermal conductivities of the 0.117 mm thickness coating material. If the conductivity is the same as the cladding (k = 13 W/m-K), the maximum temperature is 1607 K. It increases to 1740 K when the conductivity decreases to 1 W/m-K. Table 1 shows that the maximum temperature in fuel in a range of coating thermal conductivities and thicknesses. For a thin coating (0.05 mm), the maximum temperature is around 1600 K if the thermal conductivity is above 10 W/m-K. It can also be observed that the coating thickness effect increases dramatically as the thermal conductivity of the coating material drops below 5 W/m-K. The maximum fuel temperature without coating is 1597 K. Table 2 shows the maximum fuel temperature difference between the fuel with and without the coating.

RU/UIUC 4 Impacts of fuel burnup on thermal conductivity

In previous sections, Kirchhoff transformation (Tomatis, 2013) is used to solve the heat conduction equation with a temperature dependent fuel thermal conductivity for UO_2 given by Finnemann et al. (1991):

$$k_f(T) = 1.05 + \frac{2150}{T - 73.15} \tag{11}$$

However, the impact of fuel burnup on thermal conductivity is not considered. In this section, a burnup and temperature dependent thermal conductivity for UO_2 proposed by Wiesenack et al. (1996) was applied to evaluate the temperature distribution in fuel.

The correlation is:

$$k_f(T) = \frac{1}{0.1148 + 0.0035\beta + (2.474\times10^{-4} - 8\times10^{-7}\beta)(T-273.15)} + 0.0132\exp(0.00188(T - \tag{12}$$

$$273.15))$$

,where β is fuel burnup [MWd/kgUO2].

The Kirchhoff transformation is

$$U(T) \equiv \int_{T_s}^{T} \frac{k_f(T')}{k_f(T_s)} dT' \tag{13}$$

,where T_s is fuel surface temperature and $k_f(T_s)=k_s$, and the transformed variable is

$$U(T) = 1/[(\beta - 309.25)k_s]$$

$$\times \left\{ 4.20142\beta \times (e^{0.00188T} - e^{0.00188T_s}) - 1299.29 \times (e^{0.00188T} \right.$$

$$- e^{0.00188T_s}) + 1.25 \times 10^6 \tag{14}$$

$$\left. \times \left(\ln \left[\frac{59028.4 + 4648.15\beta + (309.25 - \beta)T_s}{59028.4 + 4648.15\beta + (309.25 - \beta)T} \right] \right) \right\}$$

Apply the transformation on heat conduction equation leads to U(r)

$$U(r) = -\frac{\dot{q}}{2k_s}r^2 + C_2 \tag{15}$$

From boundary conditions,

$T_s = 695.8$ K, $C_2 = 676.138$, $k_s = 4.5$ w/m-K

The temperature distribution at each location r can be evaluated by solving eq. (14) and eq. (15) simultaneously.

Figure 18 shows the thermal conductivity variation in fuel when fuel burnup is considered. The temperature distributions without burnup effect calculated via Finnemann et al. (1991) and Wiesenack et al. (1996) correlations are presented in Figure 19. The difference of maximum fuel temperature is only 13 K since the thermal conductivities evaluated by these two correlations are very close when no fuel burnup is considered. The impact

of fuel burnup is considered via Wiesenack et al.'s (1996) correlation and Kirchhoff Transformation to analytically determine the temperature distribution in the Fuel-gap-cladding-coating region. The temperature distributions with burnup from 0 to 20 MWd/kg-UO2 is shown in Figure 20. The maximum fuel temperatures corresponding to zero burnup, 5, 10, 15 and 20 MWd/kg-UO2 are 1656 K, 1713 K,1768 K, 1822 K, and 1874 K. The maximum fuel temperature difference without burnup and with 20 MWd/kg-UO2 burnup is significant, which is 218 K. The temperature distributions with burnup from 20 to 80 MWd/kg-UO2 are shown in Figure 21. As shown Figure 21, since the thermal conductivity decreases with increase in temperature (Figure 18), the maximum temperature in fuel rod increases dramatically.

In conclusion, to accurately estimate the temperature distribution in nuclear fuel, the temperature-dependent thermal conductivity should be considered due to large temperature gradient in the fuel. For the coating materials of Fe, Cr, Al or FeCrAl with thickness of 0.1 mm, there is no apparent effects on temperature distributions in a fuel rod. Usually the thickness of the coating is in the order of nanometer (nm), which is much thinner than 0.1 mm. Therefore, the effect of the coating on temperature is ignorable.
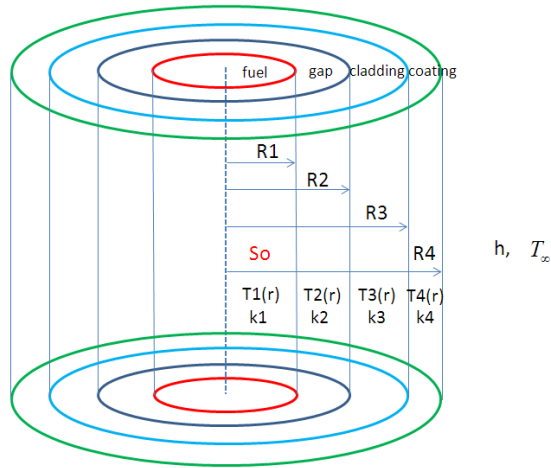
Figure 1 RU/UIUC Geometry of the 4-region (fuel-gap-cladding-coating) problem
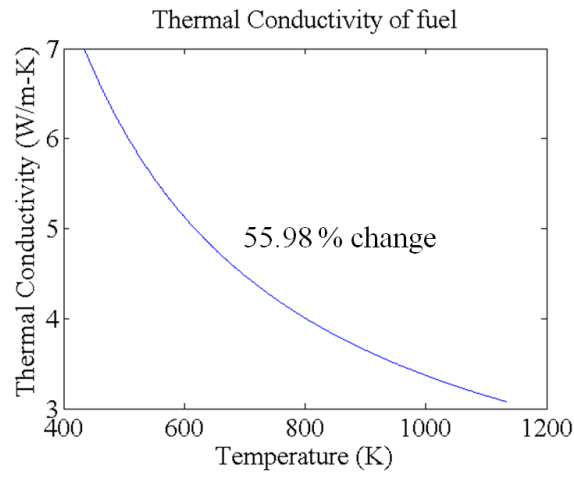
Figure 2 RU/UIUC Variation of thermal conductivity in fuel
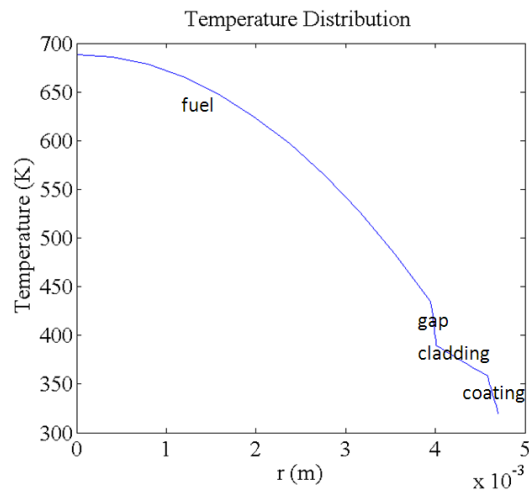
Figure 3 RU/UIUC Temperature distribution by method 2
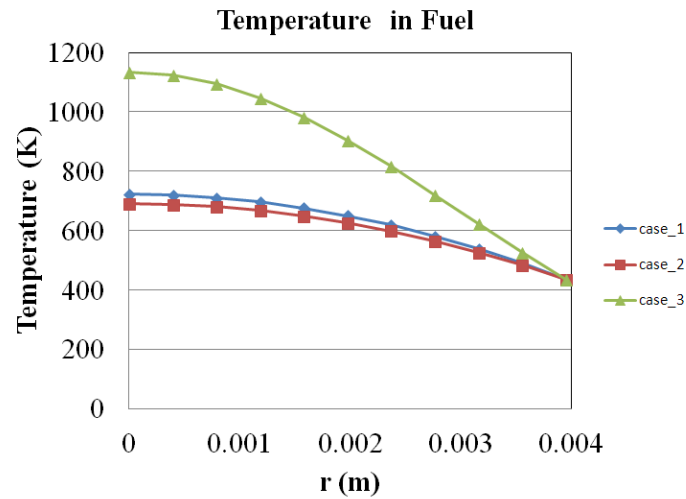
Figure 4 RU/UIUC Temperature distributions from different approaches
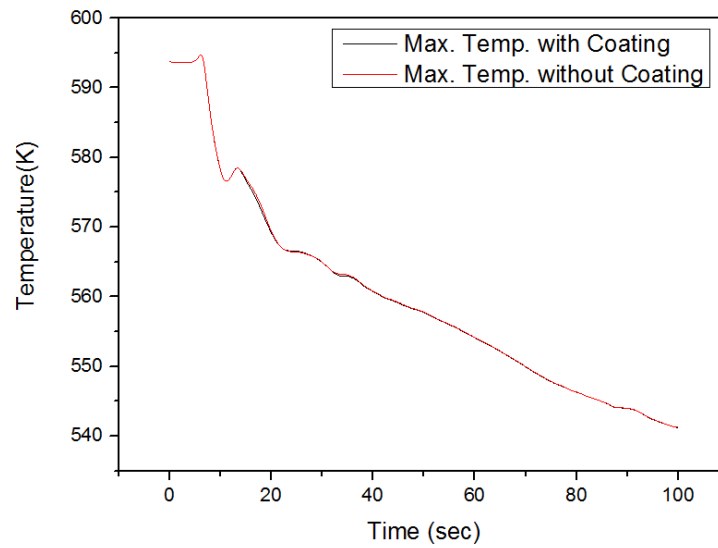
Figure 5 RU/UIUC Maximum temperature in core with Fe coating
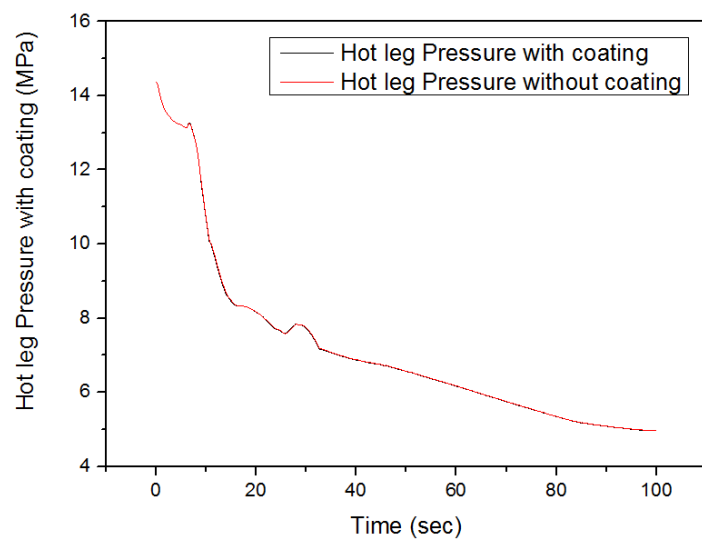
Figure 6 RU/UIUC Pressure at hot leg with Fe coating
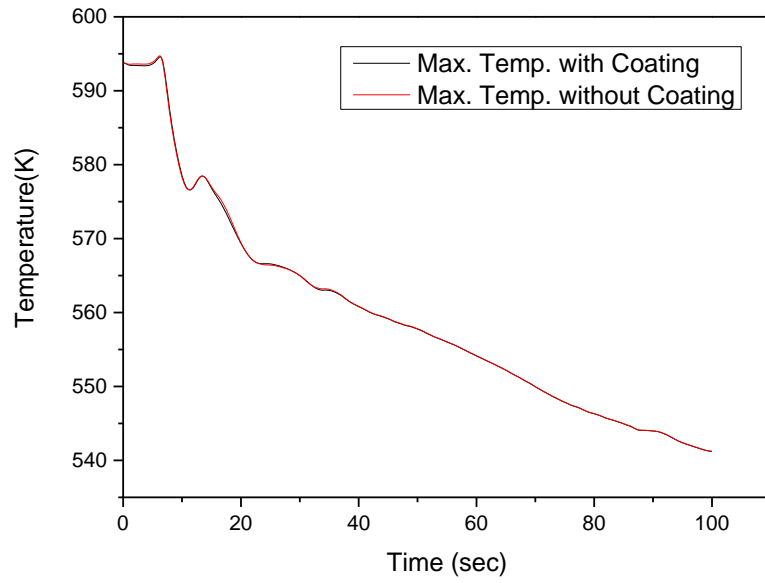
Figure 7 RU/UIUC Maximum temperature in core with Al coating
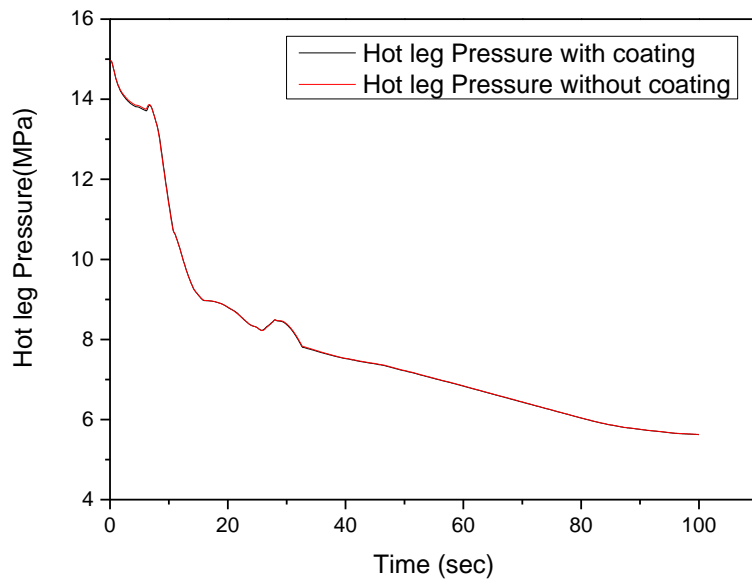
Figure 8 RU/UIUC Pressure at hot leg with Al coating
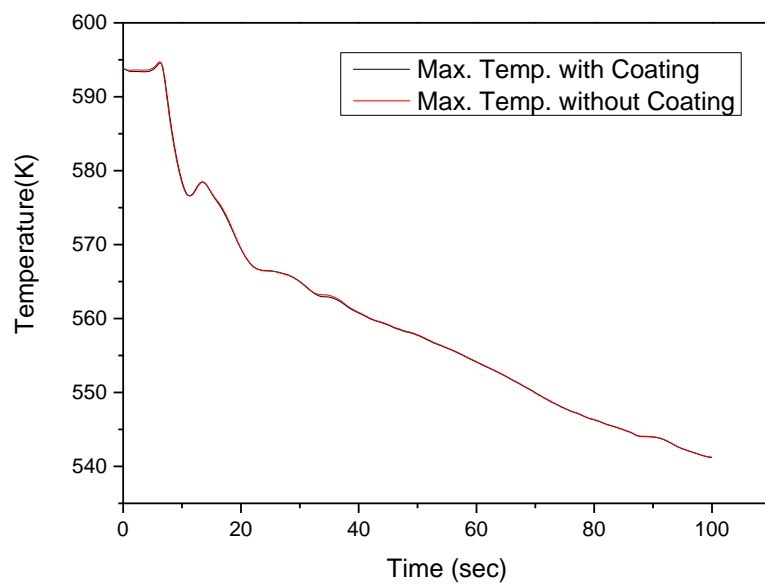
Figure 9 RU/UIUC Maximum temperature in core with Cr coating
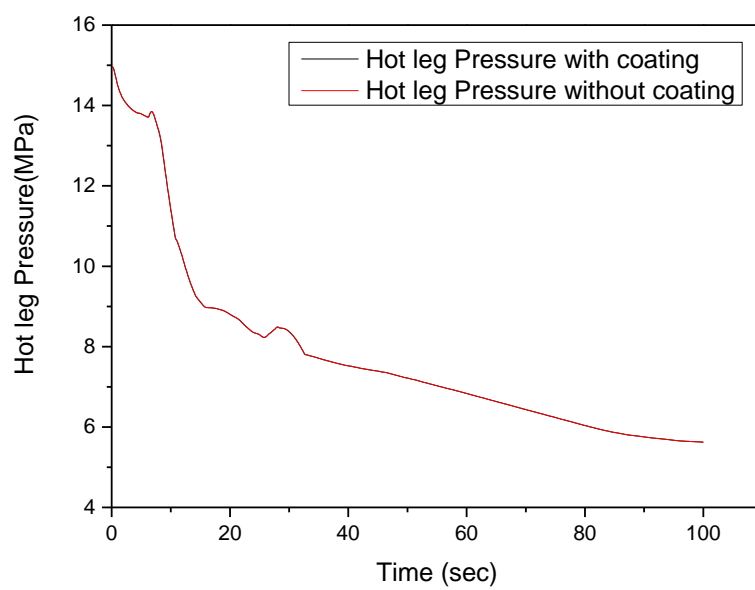
Figure 10 RU/UIUC Pressure at hot leg with Cr coating
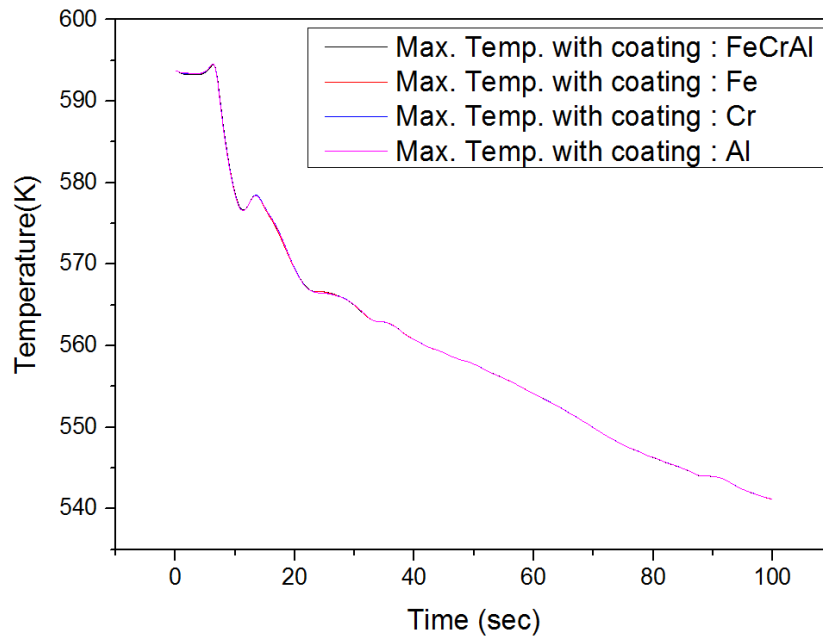
Figure 11 RU/UIUC Maximum Temperature in Core with FeCrAl coating
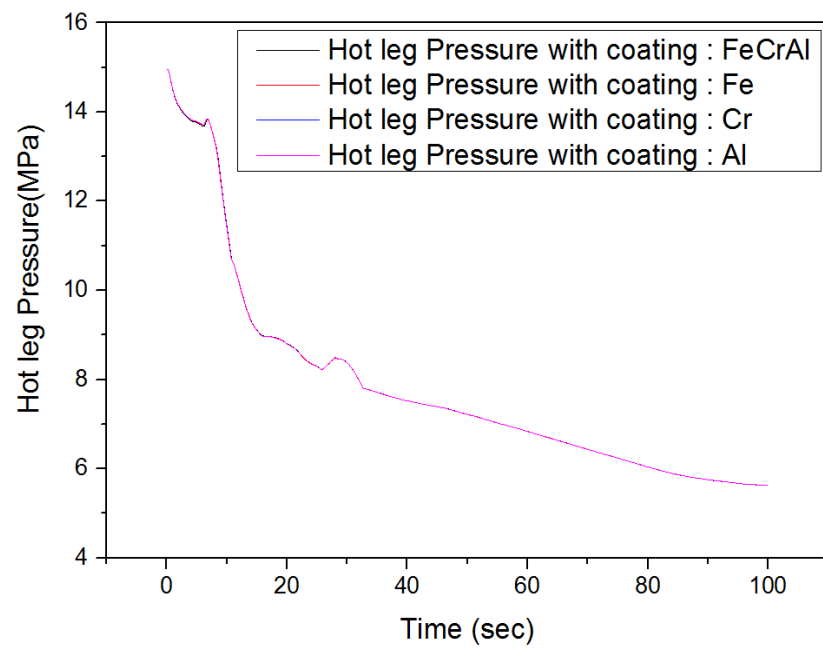
Figure 12 RU/UIUC Hot leg Pressure with FeCrAl coating
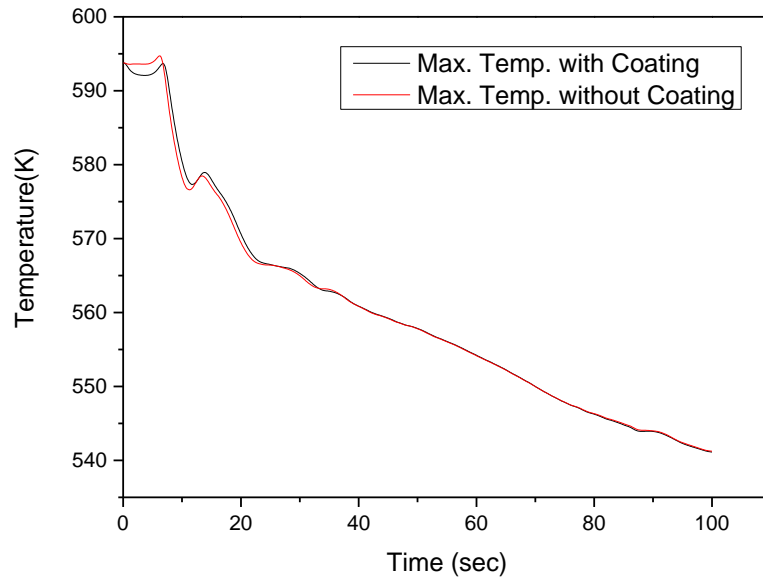
Figure 13 RU/UIUC Maximum temperature in core with $k_{coating} = 0.1k_{clad}$
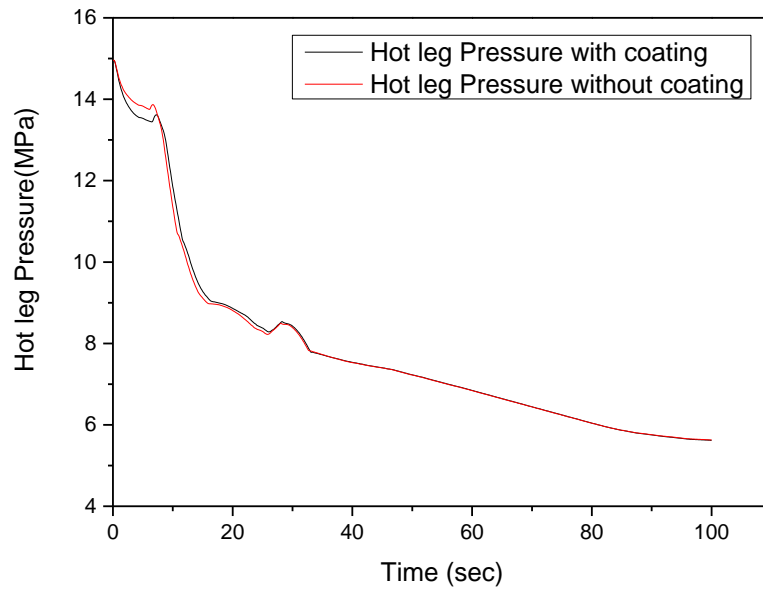
Figure 14 RU/UIUC Pressure at hot leg with $k_{coating} = 0.1k_{clad}$
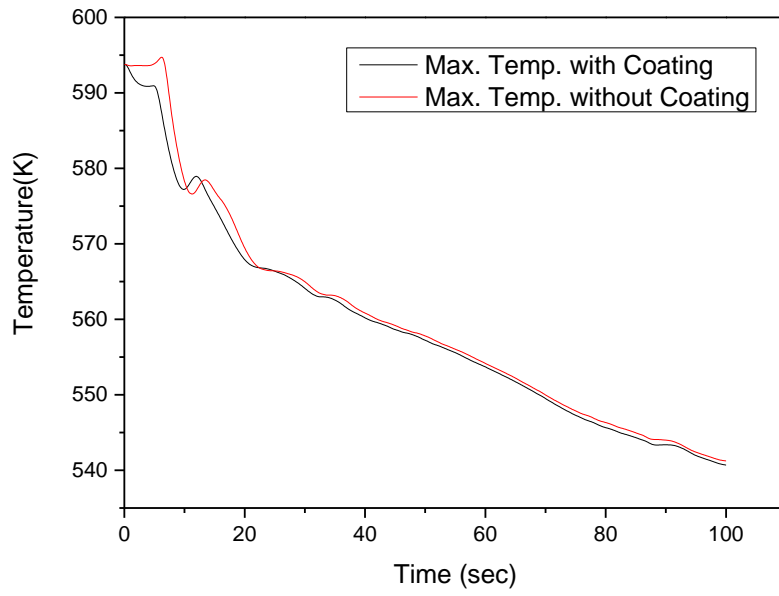
Figure 15 RU/UIUC Maximum temperature in core with $k_{coating} = 0.05k_{clad}$
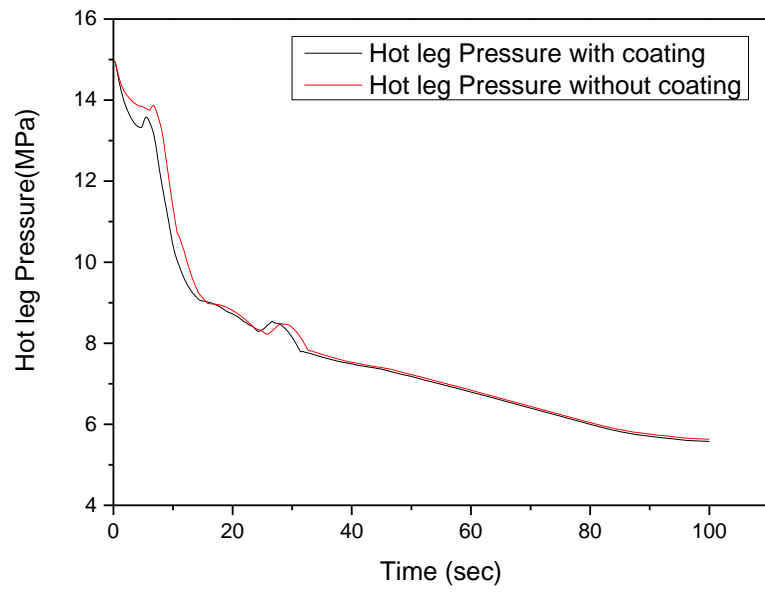
Figure 16 RU/UIUC Pressure at hot leg with $k_{coating} = 0.05k_{clad}$
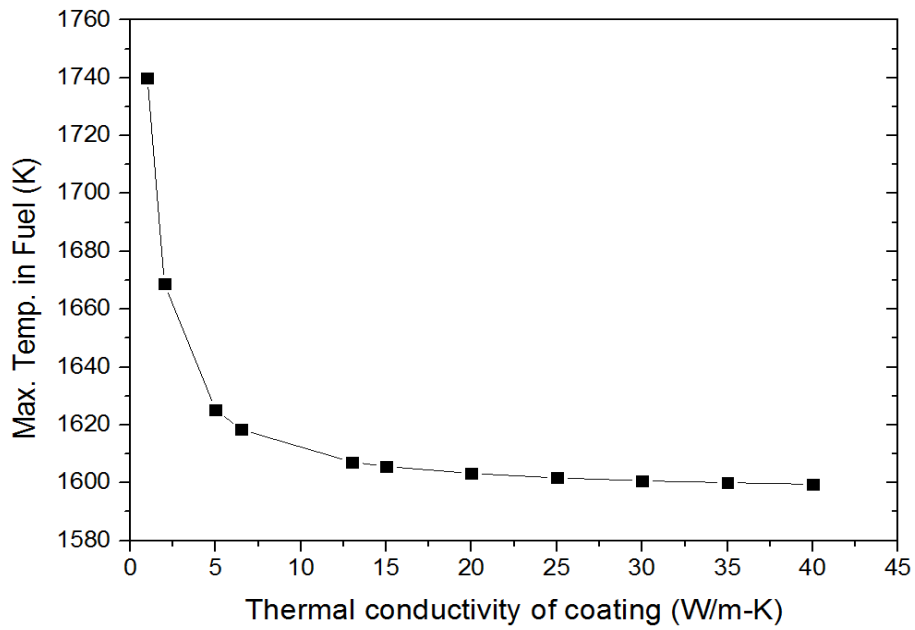
Figure 17 RU/UIUC Maximum temperature in fuel as a function of coating thermal conductivity (coating thickness = 0.117 mm)
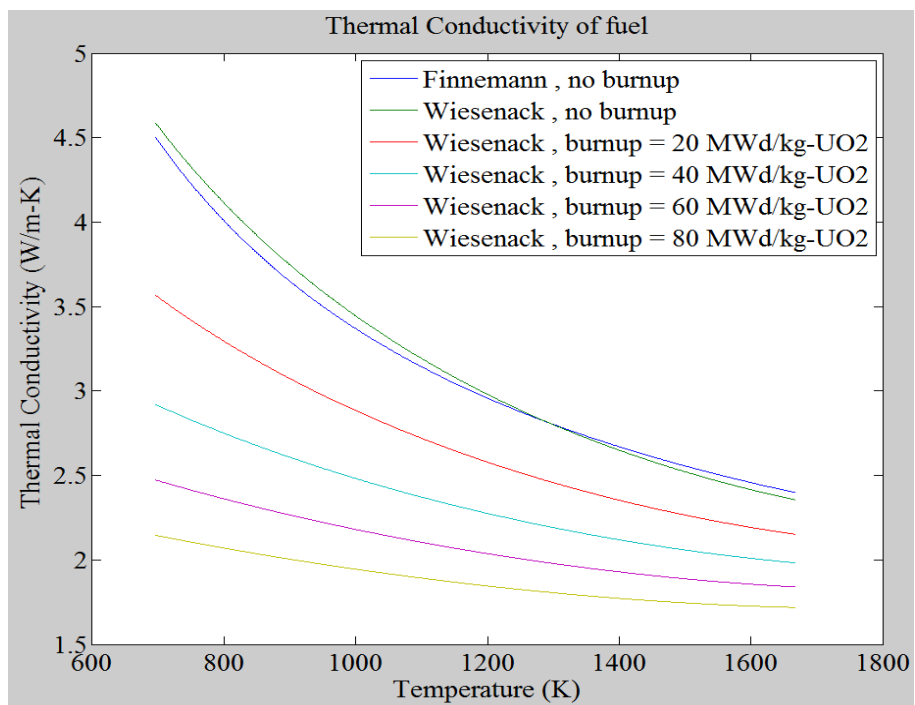
Figure 18 RU/UIUC Thermal conductivity of fuel under different burnup conditions
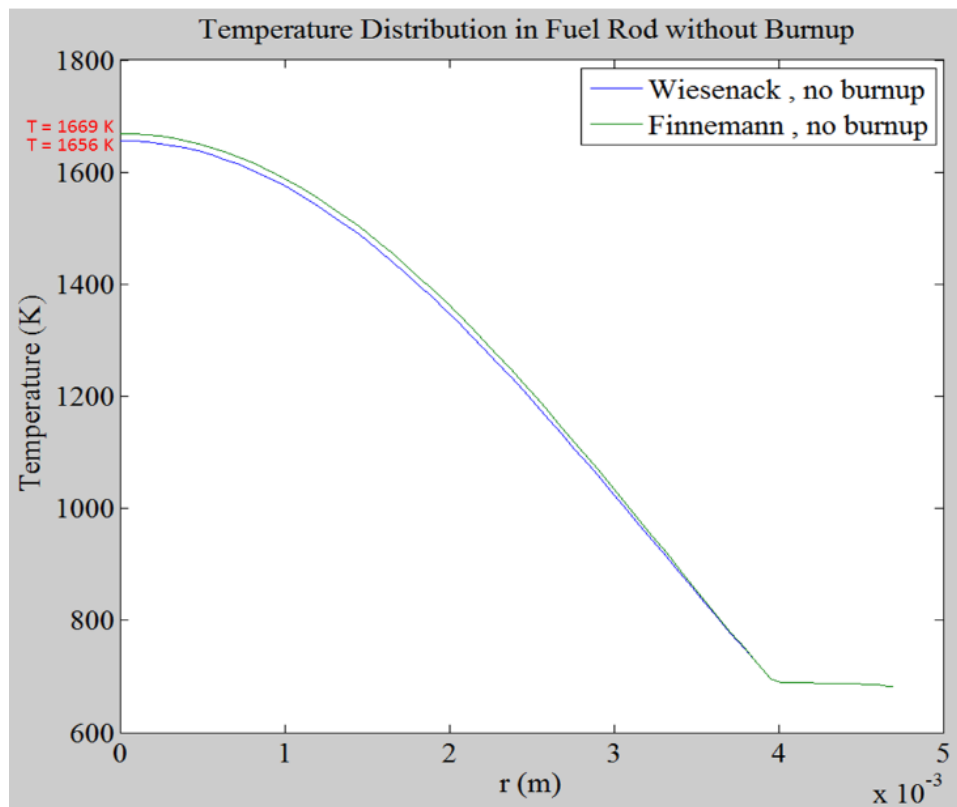
Figure 19 RU/UIUC Temperature distributions in fuel rod using different thermal conductivity correlations, no burnup
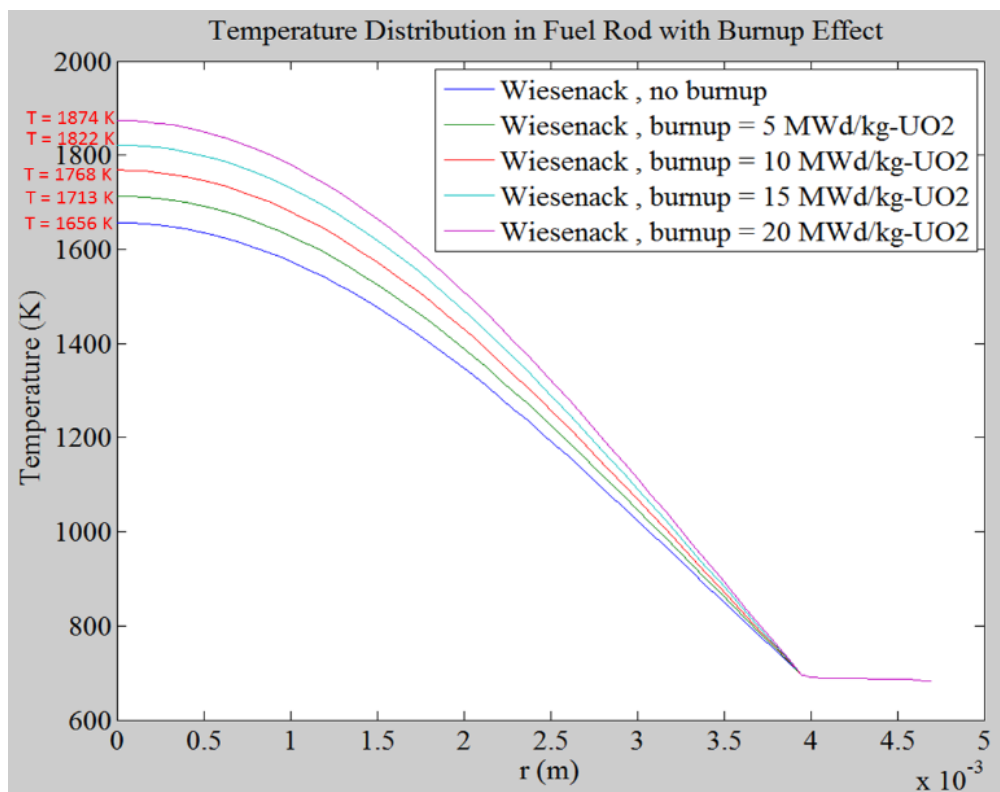
Figure 20 RU/UIUC Temperature distributions in fuel rod with burnup effects
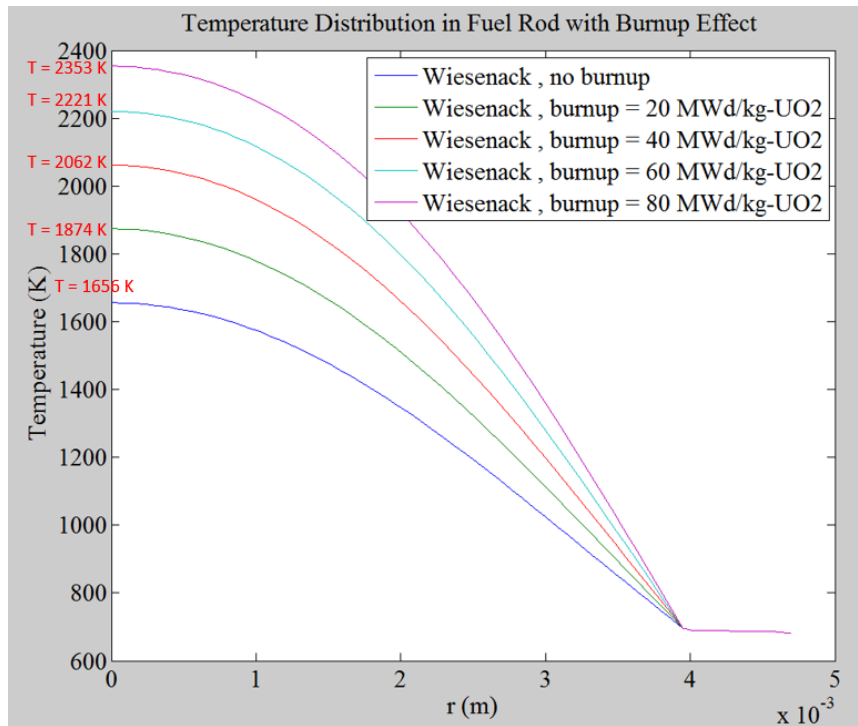
Figure 21 RU/UIUC Temperature distributions corresponding to different burnup effects

Tables

Table 1 RU/UIUC Max. fuel temperature (K) for different coating thicknesses and thermal conductivities

thickness (mm) k (W/m-K)	0.05	0.075	0.1	0.15	0.2
1	1659.2	1689.7	1719.8	1778.7	1836.0
2	1627.9	1643.3	1658.5	1688.4	1717.7
5	1609.0	1615.1	1621.1	1633.0	1644.7
6.5	1606.1	1610.7	1615.3	1624.4	1633.4
13	1601.3	1603.5	1605.7	1610.0	1614.3
15	1600.6	1602.5	1604.4	1608.1	1611.8
20	1599.6	1600.9	1602.3	1605.0	1607.6
25	1598.9	1600.0	1601.0	1603.1	1605.1
30	1598.5	1599.3	1600.2	1601.8	1603.5
35	1598.2	1598.9	1599.6	1600.9	1602.3
40	1598.0	1598.5	1599.1	1600.3	1601.4

Table 2 RU/UIUC Max. fuel temperature difference (K) with and without coating,

$$\Delta T_{\max} (\equiv T_{\max,w/coating} - T_{\max,w/o\ coating})$$

thickness (mm) k (W/m-K)	0.05	0.075	0.1	0.15	0.2
1	62.4	92.9	123.0	181.9	239.2
2	31.1	46.5	61.7	91.6	120.9
5	12.2	18.3	24.3	36.2	47.9
6.5	9.3	13.9	18.5	27.6	36.6
13	4.5	6.7	8.9	13.2	17.5
15	3.8	5.7	7.6	11.3	15.0
20	2.8	4.1	5.5	8.2	10.8
25	2.1	3.2	4.2	6.3	8.3
30	1.7	2.5	3.4	5.0	6.7
35	1.4	2.1	2.8	4.1	5.5
40	1.2	1.7	2.3	3.5	4.6

Bibliography

de Kruijf, W., (1994). Reactor physics analysis of the Pin-Cell Doppler effect in a
thermal nuclear reactor, ECN-R-94-033. Technol. Univ. Delft.

Finnemann, H., Galati,A., (1991). NEACRP 3-D LWR Core Transient Benchmark, NEACRP-L-335, http://www.nea.fr/html/science/docs/1991

Kozlowski, T., Downar, T., (2006). Pressurized Water Reactor MOX/UO2 Core
Transient Benchmark Final Report, NEA/NSC/DOC (2006)20. Technical Report. OECD/NEA and US NRC.

Tomatis, D., (2013). Heat conduction in nuclear fuel by the kirchhoff transformation. Annals of Nuclear Energy, (57), 100-105.

Wiesenack, W., Vankeerberghen, M., Thankappan, R., (1996). Assessment of UO2 conductivity degradation based on in-pile temperature data, HWR-469, lnstitutt for energiteknikk, OECD Halden Reactor Project.

2.9.   Oxidation of Ti-coated Zircaloy -2 and Zr-Ti alloys [Stubbins]

Two kinds of zirconium alloy plates, Zircaloy-2 manufactured by ATI Wah Chang and Zr-8Ti fabricated by American Elements, were used study the oxidation behavior at 700 °C steam as well as the protection of titanium coating on zirconium alloy. The composition of the Zr-8Ti plate is listed in Table 1. All Specimens were cut into 10 mm x 10 mm, as shown in Fig. 0. Three of Zircaloy-2 coupons were further coated a layer of titanium by using the DC magnetron sputtering deposition technique. Information including sample ID, material type, the thickness of titanium coating, initial weight and dimension of the sample before oxidation test are summarized in Table 2. The steam oxidation tests were performed in a thermal gravimetric analysis (TGA) systems, STA 449 F1 Jupiter. Once the samples were placed inside the STA 449 F1 system, the steam temperature was raised from 150°C to 700°C at 15°C /min rate, and then steam temperature would stabilize at 700°C be held for 10 hours.

Table 1: Certificate of Analysis for Zr-Ti Foil, Determine by American Elements

Zr	Ti	Fe	Ni	Si	Cr	Cu
92	8	0.025	0.0145	0.0055	0.0054	0.0048

Figure 0. The photographs of samples right after cutting. Left: Zircaloy-2. Right: Zr-8Ti
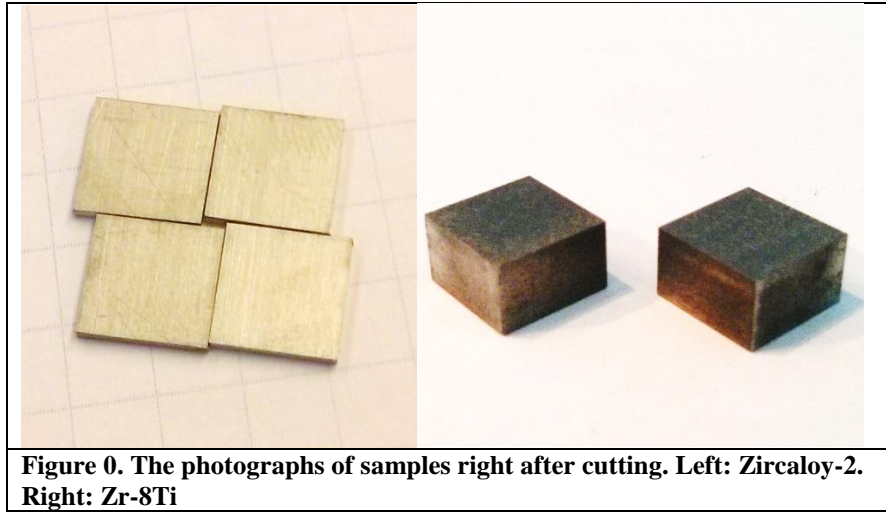
Table 2: List of specimens parameters before oxidation tests

Sample ID#	Substrate Material	Ti-Coating Thickness [nm]	Initial Mass [mg]	Thickness [mm]
1	Zircaloy-2	--	701.1	1
2	Zircaloy-2	21.5	703.0	1
3	Zircaloy-2	43.0	710.8	1
4	Zircaloy-2	64.5	740.3	1
5	Zr-8Ti	--	3807.5	3

The mass change of sample 1 as a function of time under 700°C steam and the corresponding history of temperature are provided in Fig. 1, which indicates the oxidation behavior of as-received Zircaloy-2. Fig. 2, Fig. 3 and Fig. 4 demonstrate oxidation behavior of the Zircaloy-2 coated with a Ti-layer with a thickness of 21.5 nm, 43.0 nm and 64.5 nm, respectively. As demonstrated in Fig. 5, since the mass curves of sample from 1 to 3 are almost overlapped each other, their oxidation behavior and weight gain are close to each other. In 20 minutes at about 350°C during the heating stage of steam, noted as t1, the first detectable result of the weight gain was acquired. The moment to divide the oxidation curve into a parabolic region and a linear region is at about 174 minutes, noted as t2. However, comparing to the results of Sample 1 to 3, sample 4 with a Ti-layer of 64.5 nm exhibits a significant oxidation resistance due to the increase in both t1 and t2 as well as the decrease in the final weight gain. Consequently, titanium coating begin to bring a measureable benefit on the oxidation resistance at 700°C steam. The image in Fig. 6 illustrated the surface morphology of Ti-coated Zircaloy-2 specimen before and after steam oxidation. The key results of weight change curve are summarized in Table 3.

The mass change versus time for Sample 5 under 700°C Steam Oxidation is plotted in Fig. 7. The mass change for the bare Zircaloy stays at zero for the first 10 minutes as the temperature rises from 137°C to 189°C. At that point, it is at 65.5 minutes as the 5 mg weight gain was measured. From then on the weight change acts very volatilely, spiking to a value of 1769 mg. After several strong resonances, the weight change stabilizes around 498 minutes an unreasonable negative value of -144 mg. This negative value is resulted from the fully oxidation which happened in the middle of the test. This material appeared to have completed degraded during the experimentation as shown in the before and after form found in Fig. 8. The oxidation kinetics as a function of these Zr specimens are shown in Fig. 9. The small bumps for the Samples 1-4 (bare and coated Zircaloy-2) are governed by electrical potential that develops across the oxide film during oxidation. For Sample 5 (Zr-8Ti), there never seemed a point in time where the material could be characterized as having cyclical oxidation.
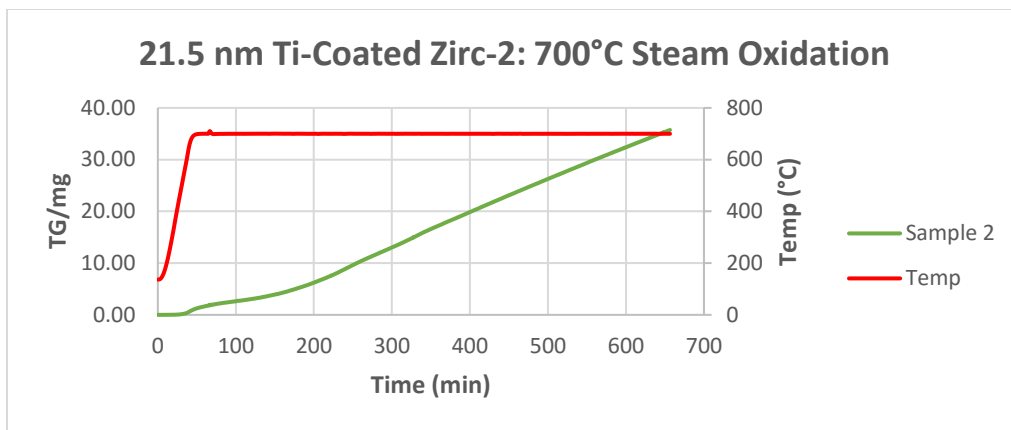
Table 3: List of specimens parameters before oxidation tests

| Sample #	t1, Time to Measure the First Weight Change	t2,Time to increase 5 mg	Linear Behavior Rate	Net Weight Gain
UNITS	min	min	mg/min.	mg
1	20	171	0.0556	35.54
2	20	177	0.0627	35.73
3	19	175	0.0524	35.44
4	25	190	0.0561	33.95
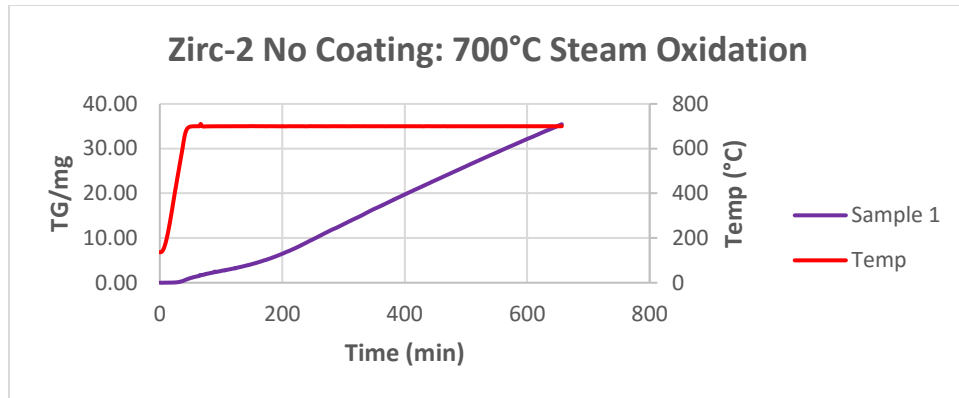
Figure 1: Mass Change vs. Time for Sample 1 (Zirc-2, No Coating) under 700°C Steam Oxidation
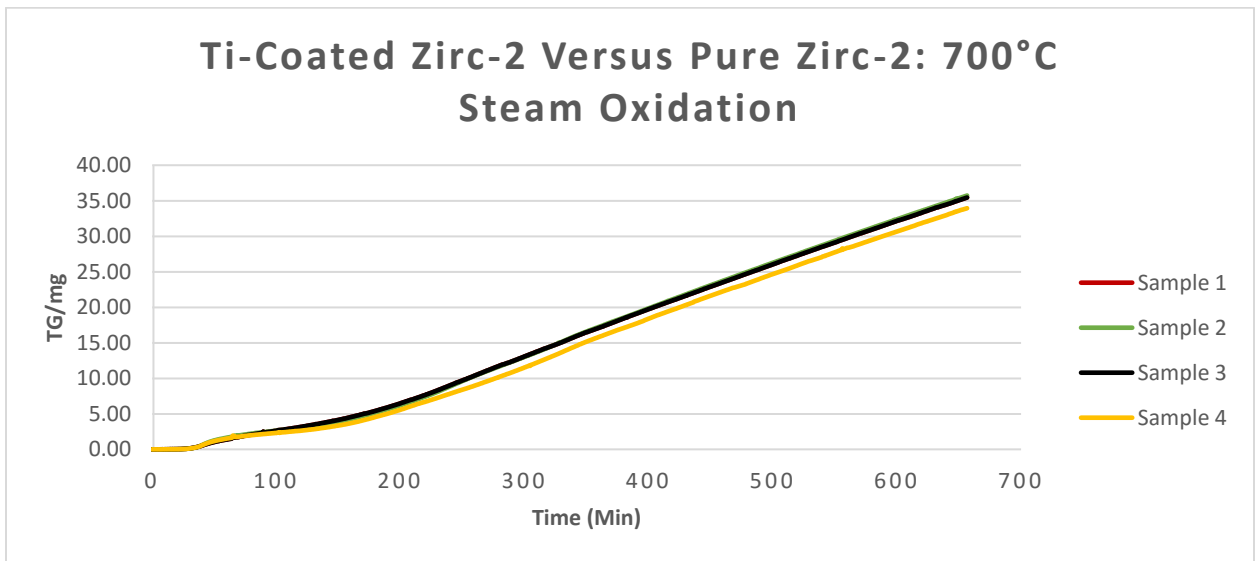

Figure 2: Mass Change vs. Time for Sample 2 (Zirc-2, 21.5 nm Ti-Coated) under 700°C Steam Oxidation
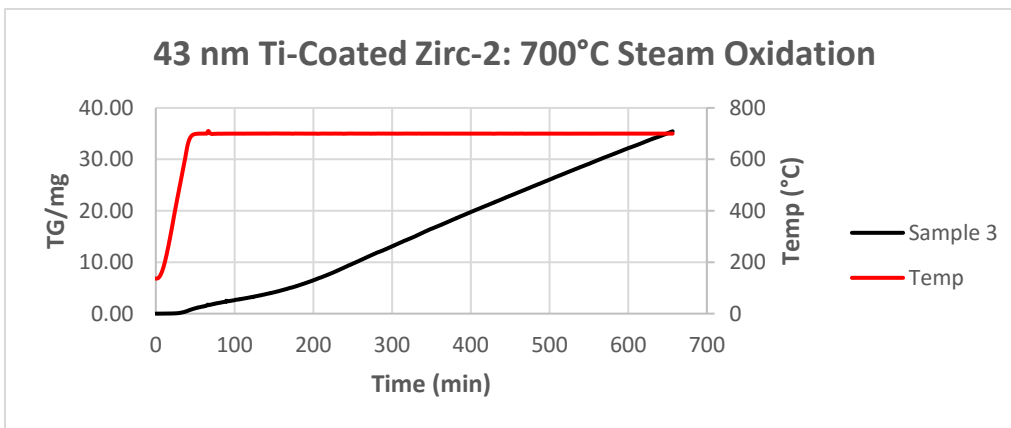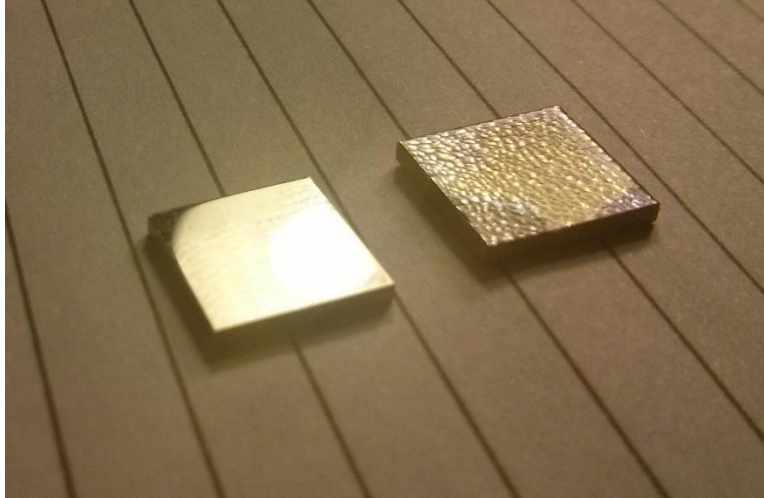

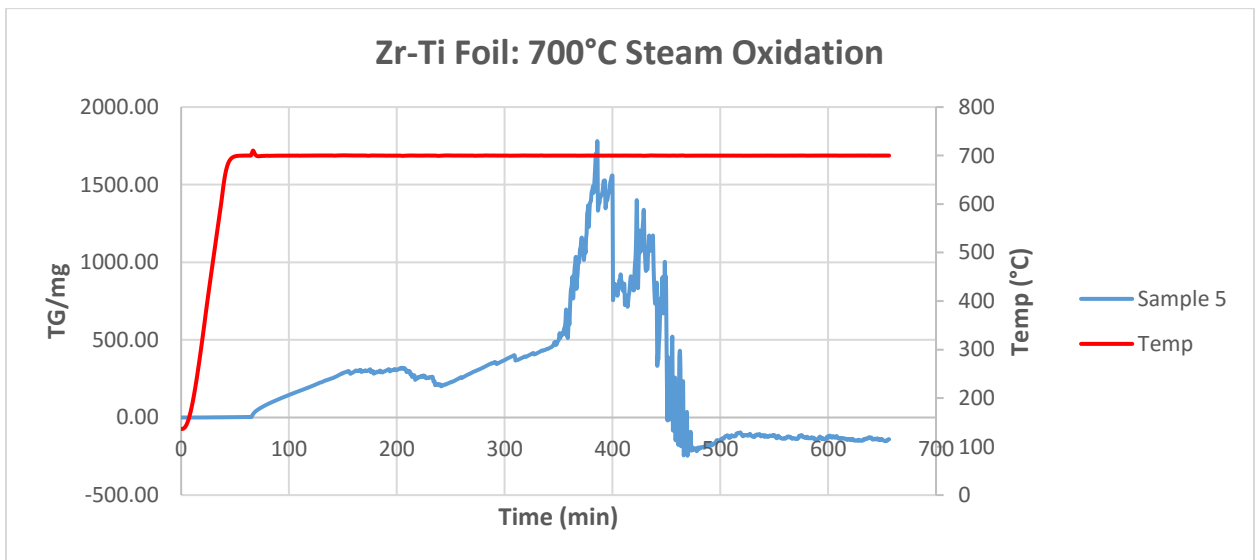**Figure 3: Mass Change vs. Time for Sample 3 (Zircalot-2, 43 nm Ti-Coated) under 700°C Steam Oxidation**
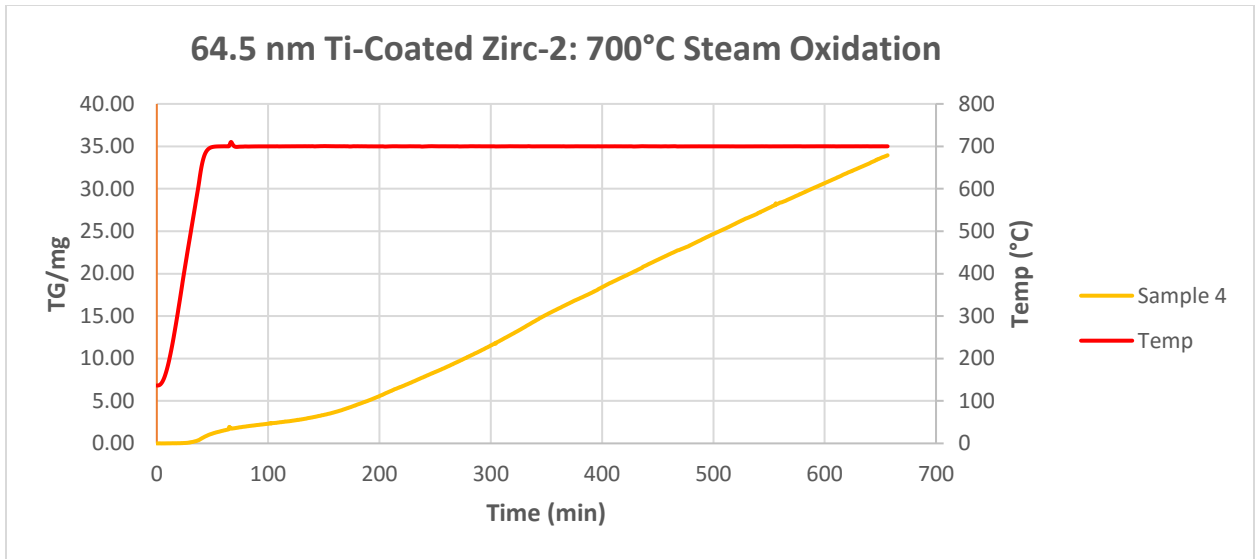
Figure 4: Mass Change vs. Time for Sample 4 (Zircaloy-2, 64.5 nm Ti-Coated) under 700°C Steam Oxidation

Figure 5: Comparison of the Mass Change vs. Time for Zircaloy-2, Ti-Coated Zircaloy-2, and the Zr-Ti Foil under 700°C Steam Oxidation Conditions

Figure 6: Zircaloy-2 Sample Before Steam Oxidation (LEFT) and After Steam Oxidation (RIGHT)

Figure 7: Mass Change vs. Time for Sample 5 (Zr-8Ti) under 700°C Steam Oxidation Conditions

Figure 8: Zr-8Ti coupon Before Steam Oxidation (LEFT), and After Steam Oxidation (RIGHT)
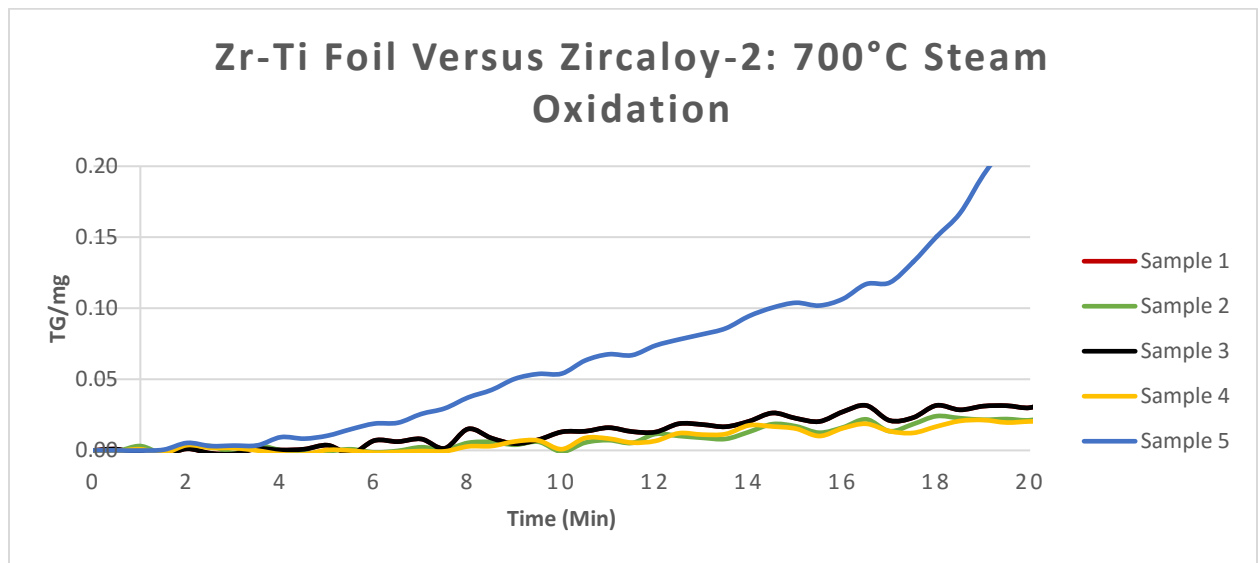
Figure 9: Comparison of the Mass Change vs. Time for Zircaloy-2, Ti-Coated Zircaloy-2, and the Zr-8Ti under 700°C Steam Oxidation Conditions

To identify the oxide growth in the air at 500°C, the oxidation test of zircaloy-4 plate in recrystallized metallurgic state has been conducted. Several 10 mm x 15 mm x 1.6 mm Zircaloy-4 plates was placed in a tube furnace were exposed in the 500°C air for 1, 5, 10, 30, and 100 hours, and the growth oxide layer as well as the both oxide thickness and weight gain are demonstrated in Fig. 1 and Fig. by SEM-FIB technique and pre-/post-weight measurement, respectively. Some micro crack can be overserved as the thickness of the oxide increases. The thickness of the oxide layer is 5.6 um for the sample growth at

500°C air for 100 hours. The trend of measured weight gain is consistent with the trend of the oxide growth as shown in Fig 2.
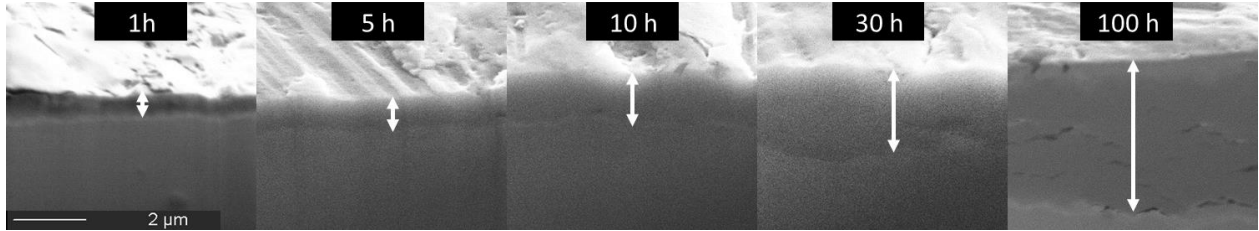
Fig. 1 Growth of thermal oxide on zircaloy-4 plate in the air at 500°C
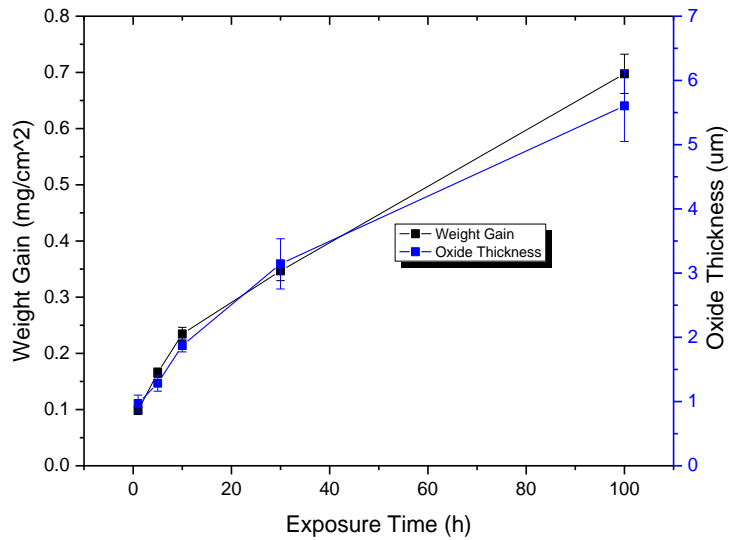
Fig. 2 Growth of thermal oxide on zircaloy-4 plate in the air at 500°C

The phase identification of surface oxide using XRD analysis indicates the oxide layer is composed of monoclinic and tetragonal zirconia, as shown in Fig. . Monoclinic ZrO_2 (111) is the most distinct peak among spectrums of the oxide phase, and minor tetragonal ZrO_2 peaks can be also be detected. It implies the oxide layer of the Zircaloy-4 plate is dominated by the monoclinic ZrO_2 phase.
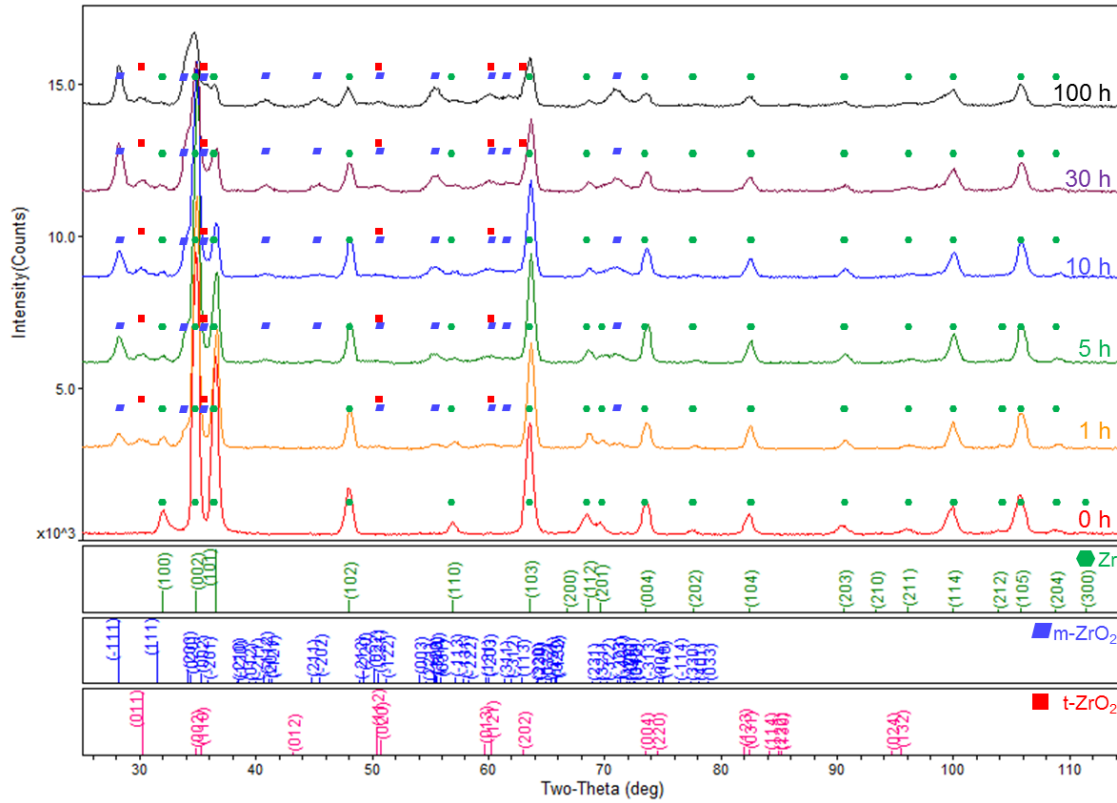
Fig. 3 The XRD patterns for the specimens oxidized in the air at 500°C

By using STA, oxidation tests also been applied to CWSR Zircaloy-4 cladding tubes for the as-received specimen, the as-hydrided with 300 wppm H, the as-hydrided with 750 wppm H. One half ring of the sample was placed in STA furnace with lab air at 500°C air for 100 hours. The weight gain per unit area as a function of time was presented in Fig 4. The weight gain tendency of the sample with 300 wppm H are close to that of the as-received. Interestingly, the weight gain of the sample with 750 wppm is significantly smaller than that of that of the sample with 0 and 300 wppm H during the whole 100 hours oxidation exposure.
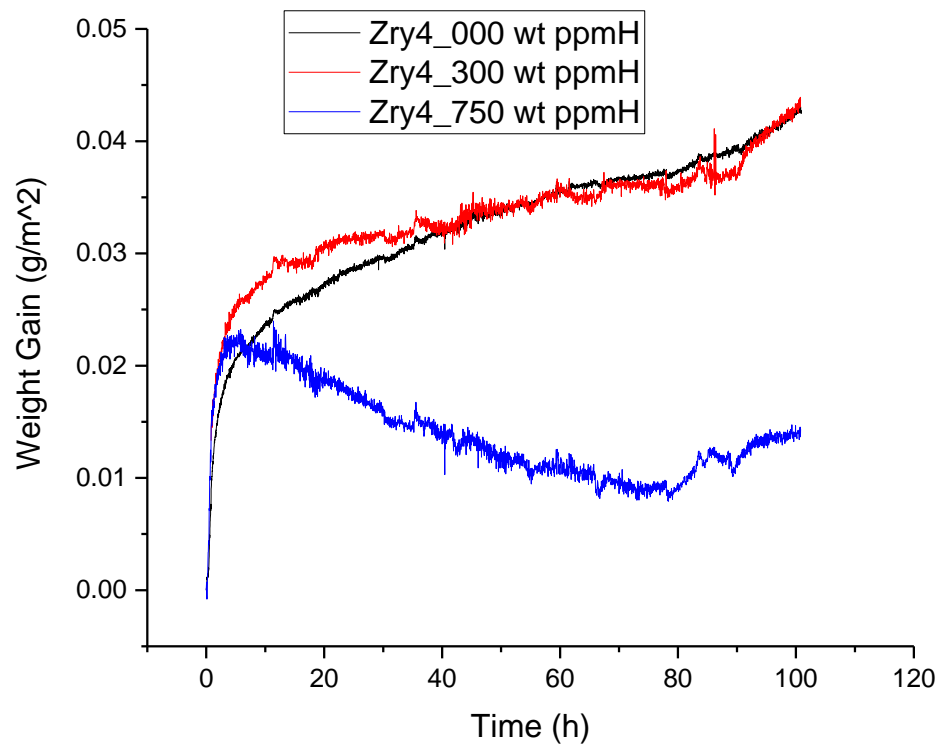
Fig. 4 Weight gain evolution of STA oxidation tests of CWSR Zircaloy-4 tubes at 500°C for 100 hours. Black: as-received tube. Red: tube as-hydrided with 300 wppm H. Blue: tube as-hydrided with 750 wppm H.

2.10   Fuel Cladding Analysis Based on Computational Thermodynamics and Surface Modeling of Zr for Improved Accident Tolerance of Nuclear Fuel [INL]

This project focuses on development of accident-tolerant nuclear fuel for light water reactors (LWRs) with modification of near-surface composition of Zircaloy-2, Zircaloy-4, ZIRLO, and M-5 to mitigate or eliminate hydrogen-gas production in off normal scenarios.

Introduction

ThermoCalc and its sister software, the DICTRA, is used for thermodynamic and diffusion computations, respectively. The existing experimental phase diagrams for the Zr-H binary system indicate that the formation of two hydrides could take place under appropriate conditions: the δ–phase $ZrH_{1.6}$ and the ε – phase, as shown in Figures 1 and 2 [1]. However, from literature it is well known that the third modification also exists, the γ–phase, or ~ZrH [2]. Even for the model binary system discrepancies still exist as to the phase composition of hydrogen – bearing zirconium alloys as a function of their thermo-mechanical histories.
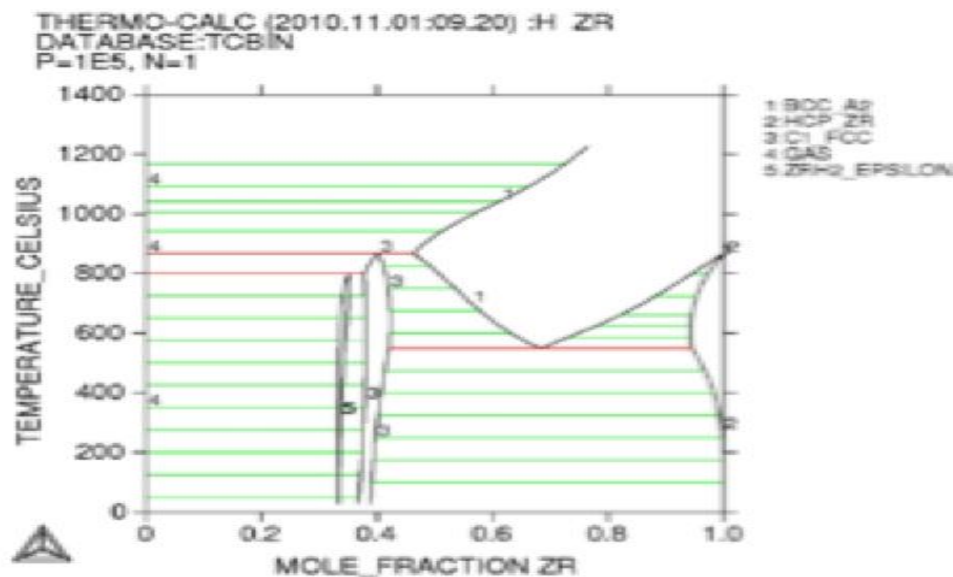

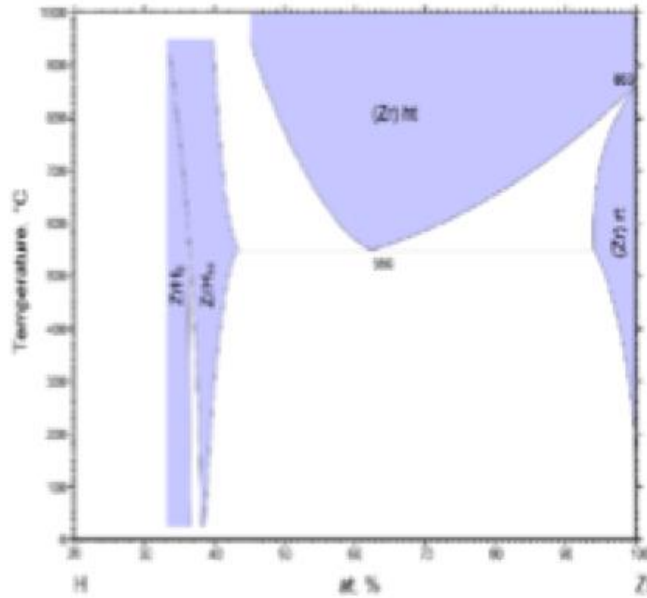Figure 1. Results of Thermodynamic Calculations Using Software Package Thermo-Calc.

Figure 2. Experimental Phase Diagram Constructed by Zuzek and Abriata [1].

Hydrogen Solubility

Hydrogen uptake, facilitates oxidation of Zr. At equilibrium state, hydrogen solubility is same for all three alloys, but Zr-4 is better than Zr-2 in terms of less hydrogen uptake, so hydrogen uptake is not a thermodynamic controlled phenomenon but driven by kinetics. There is even more need to have a detailed self-consistent description of the hydride formation in real-life for alloys such as Zr-2 and Zr-4, which may contain up to 5 different alloying elements and have a different phase composition as a function of the dissolved hydrogen concentration. An example of the so-called "isopleth" (or pseudo-binary) diagram constructed for Zr-4 is presented in Figure 3. The results indicate that the zirconium hydride(s) get dissolved in the matrix at temperature around 560°C, as shown in Figure 4. These results clearly indicate that the need exists to have a detailed understanding of the phase composition of Zr-based alloys as a function of temperature and the concentration of dissolved hydrogen. These commercial alloys possess much more complex phase composition than the binary Zr-H alloys. In turn, this affects the driving forces (the second derivatives of the Gibbs free energy with respect to temperature) that, along with the corresponding mobility, enter all diffusion calculations, including the mesoscale phase-field simulations of microstructure of such materials. Coupled to the development of an advanced non-associated plasticity models for HCP-materials, this thermo-mechanical modeling will result in a detailed understanding of the reasons that might cause undesirable behavior of Zr-alloy nuclear fuel rods.
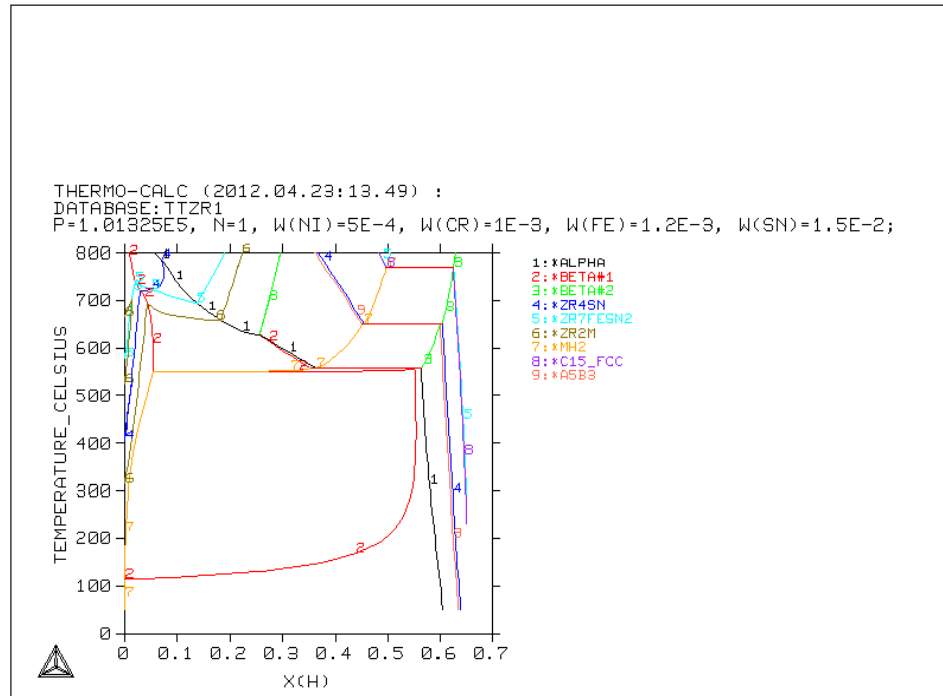
Figure 3. Phases present in the Zr-2 plus hydrogen system as a
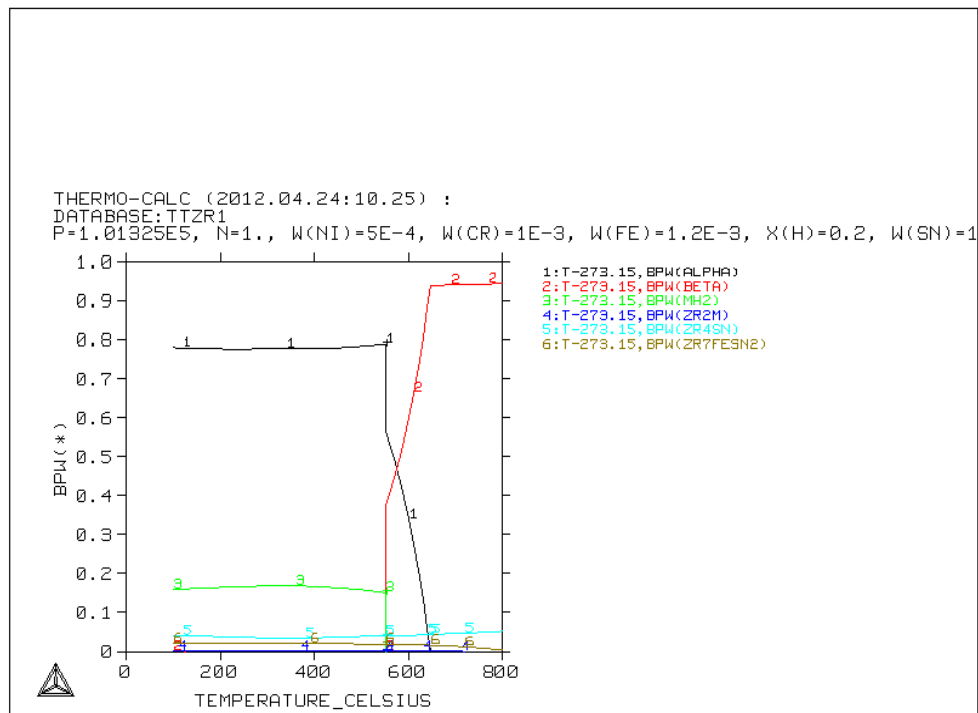function of molar concentration of hydrogen.

Figure 4. Zirconium Hydride(s) get dissolved in the matrix at temperature around 560°C.

Thermodynamic Properties and Phase Equilibria

Thermodynamic properties and phase equilibria are determined for Zirconium, Zr-2, and Zr-4. First, principles atomistic simulations are used to elucidate kinetic aspects of hydriding. Formation of Zr_3O emphasized in slowing down zirconium hydriding process. The phase composition of Zr-2, Zr-4, M5, ZIRLO^{TM} as a function of Temperature is shown in Figure 5, 6, 7, and 8 respectively.
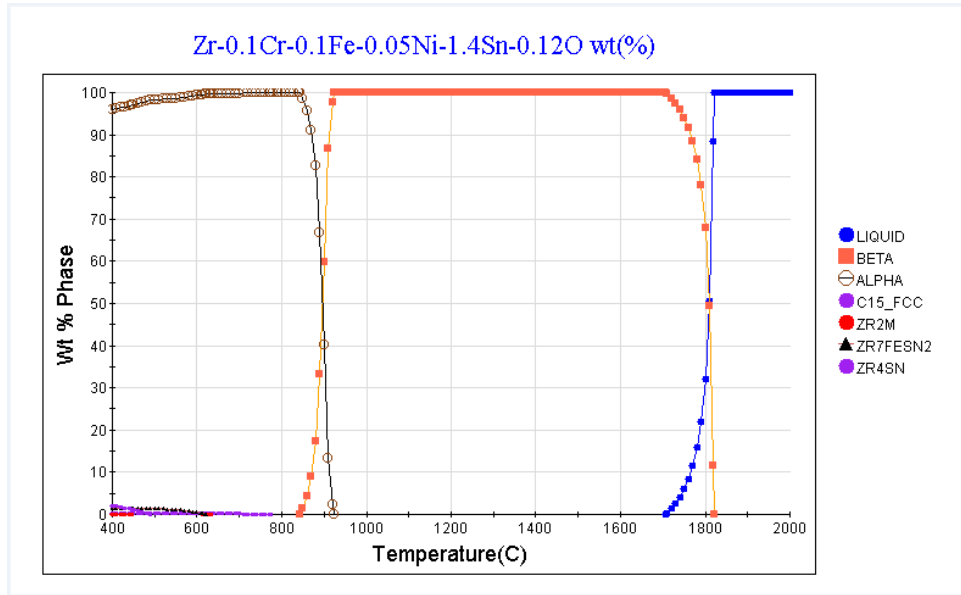

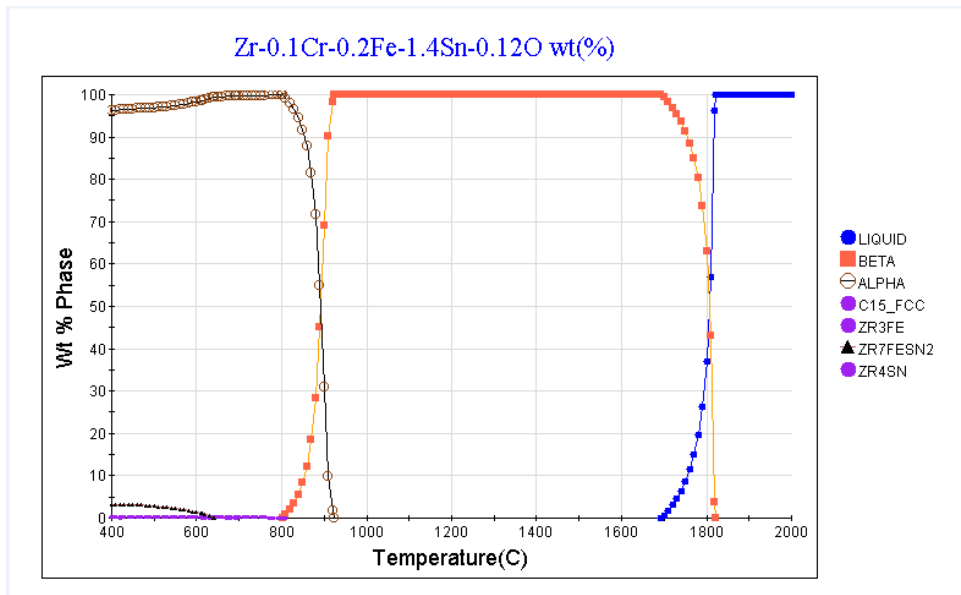Figure 5. Phase Composition of Zr-2 as a function of Temperature.

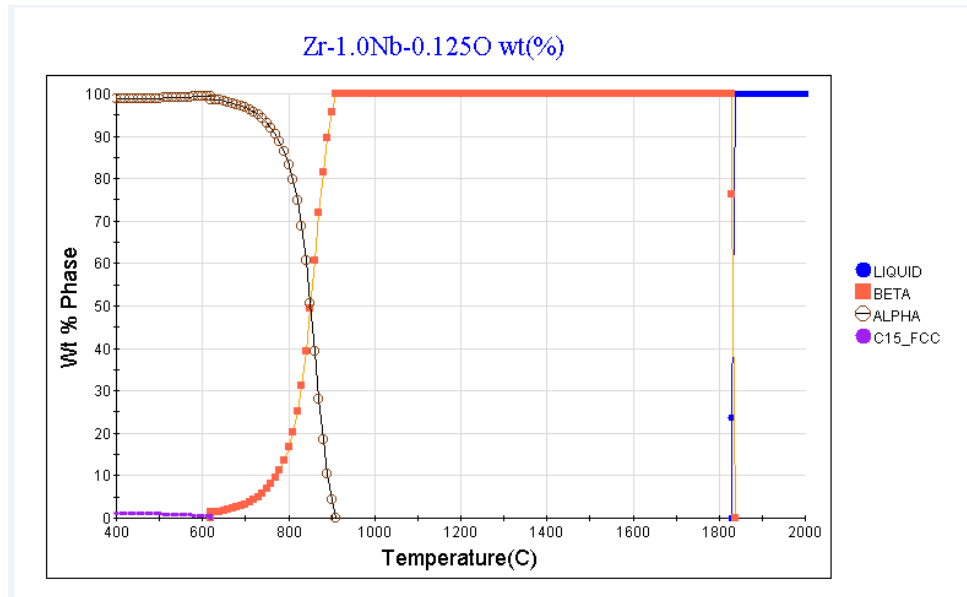Figure 6. Phase Composition of Zr-4 as a function of Temperature.

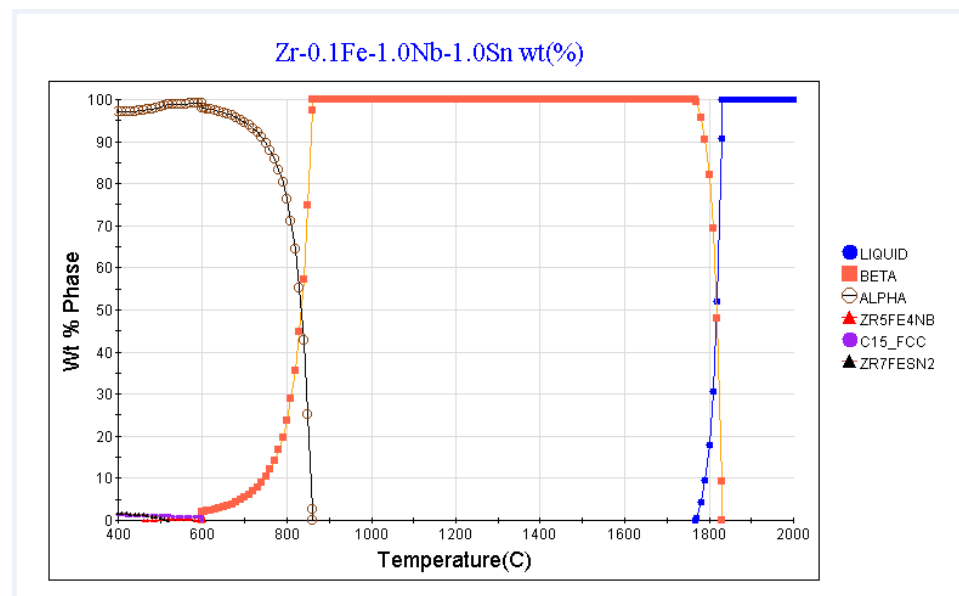Figure 7. Phase Composition of M5 as a function of Temperature.

Figure 8. Phase Composition of ZIRLO^{TM} as a function of Temperature.

Change in density and molar volume occurs at phase transformation, taking that information into account molar volume as a function of temperature has been computed and is shown in Figure 9. As can be seen from the figure, there is a substantial drop and then increase of molar volume with respect to temperature. Any coating that is applied to the zirconium surface should be able to accommodate this change without cracking. Plastic deformation of Zr is unusual/unique (i.e., at lower temperature up to roughly 300°C) it takes place by twinning and at elevated temperatures the mechanism changes to conventional

crystallographic slip. Also, current efforts are being made to update the plastic deformation model for Zr in BISON by using new yield equation for plastic behavior of Zr and then with the availability of Fe-Cr-Al thermo-physical and mechanical properties, the new cladding material will be added to the BISON repository for future fuel performance calculations.
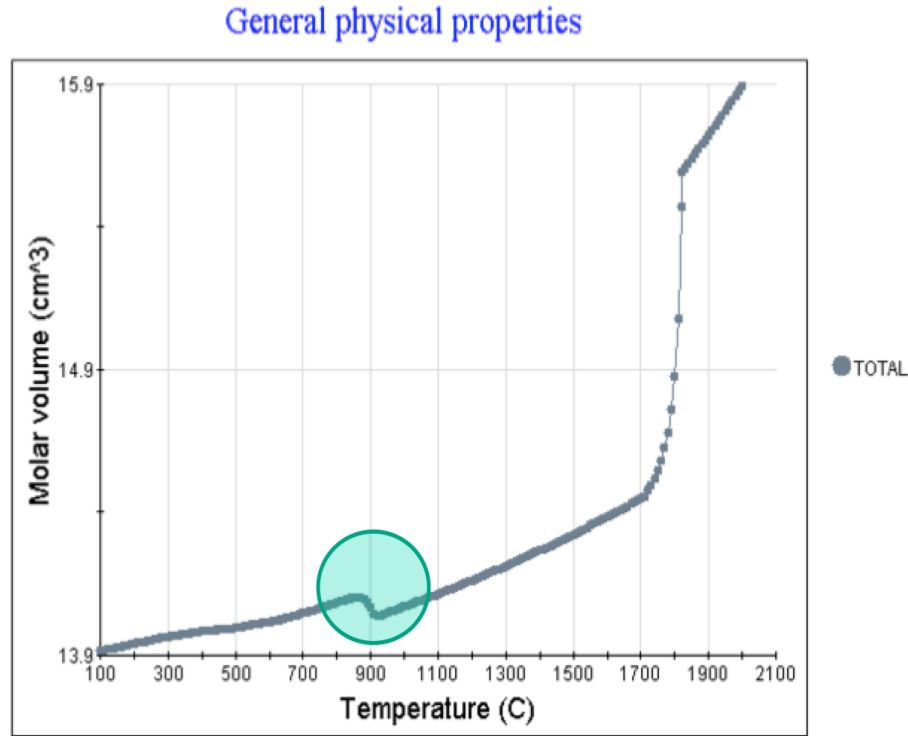

Figure 9. Molar Volume of Zr-2 as a Function of Temperature.

(Composition in wt%: Zr: 98.23; Cr:0.1; Fe:0.1; Ni: 0.05; Sn: 1.4; O: 0.12)

Coatings Development of Fe-Cr-Al for Zirconium Alloys (Zr-2 and Zr-4)

The main objective here is to avoid the formation of brittle intermetallic sigma phase, or the (Fe, Al) intermetallic (Fe_3Al), which possess needle shapes and destroys strength and elongation. Initially, the analysis of the binary Fe-Cr phase diagram was carried out to establish the phase field of the sigma phase existence in the T-x space. Its appearance is associated with the spinodal decomposition in the solid phase. The phase exists at intermediate temperatures from 500 to 800°C. The addition of small amounts of aluminum shifts its location, so the next step constructed a number of iso-thermal cross-sections for the Fe-Cr-Al ternary phase diagram at T = 1123K, 973K, 873K, 823K, 773K, 673K, respectively. The binary phase diagram for Fe-Cr is shown in Figure 10. The sigma phase forms between 500 to 800°C, so the operating temperature should be either below 500°C or above 800°C, respectively. Sputtering temperature

for Fe-Cr-Al has been obtained for binary (Fe-Cr) and ternary (Fe-Cr-Al) coatings based on the construction of the corresponding phase diagrams, as shown in Figure 11. The sputtering should be conducted from the phase field free of sigma phase. As can be seen for ternary (Fe-Cr-Al), the sputtering temperature should be below 500°C or above 700°C, so the addition of aluminum brings down the temperature from 800°C to 700°C.
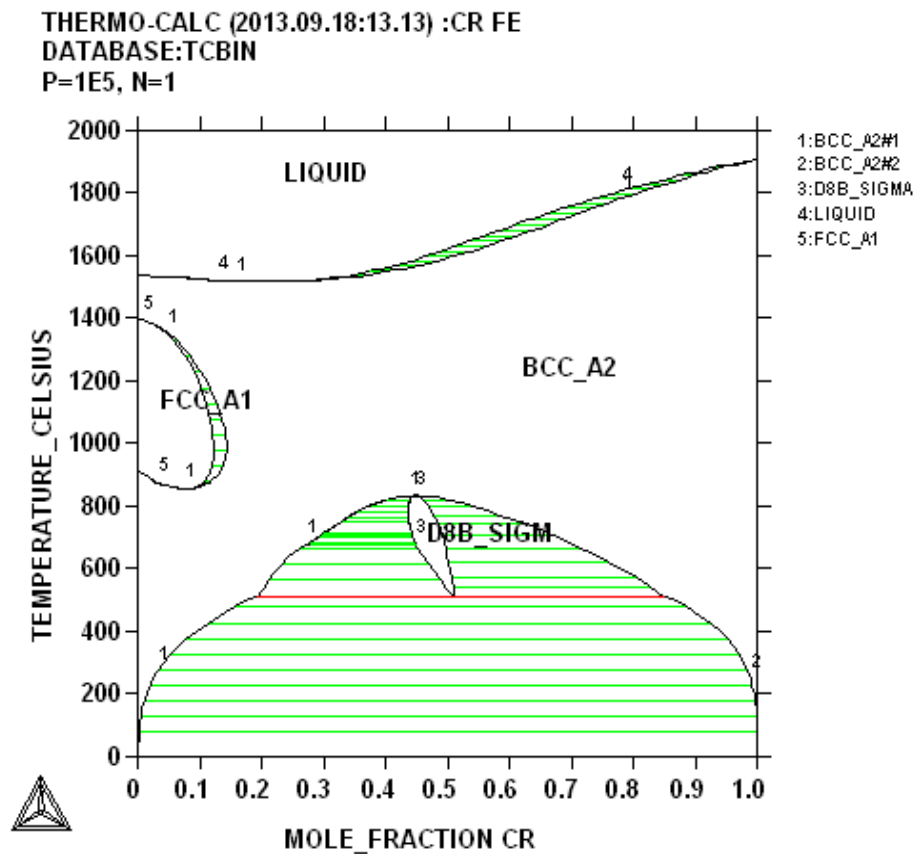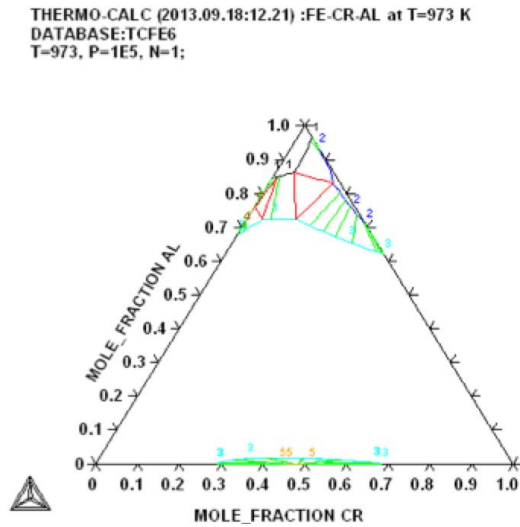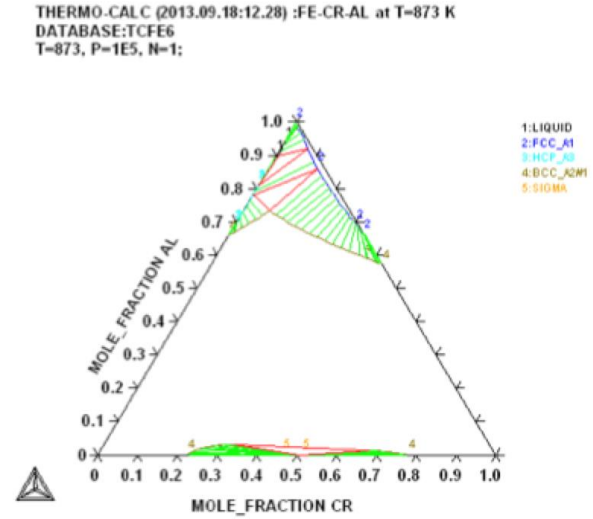

Figure 10. Binary Phase Diagram for Fe-Cr.

THERMO-CALC (2013.09.18:12.21) :FE-CR-AL at T=973 K
DATABASE:TCFE6
T=973, P=1E5, N=1;

1:LIQUID
2:FCC_A1
3:BCC_A2
4:HCP_A3
5:SIGMA

THERMO-CALC (2013.09.18:12.28) :FE-CR-AL at T=873 K
DATABASE:TCFE6
T=873, P=1E5, N=1;

1:LIQUID
2:FCC_A1
3:HCP_A3
4:BCC_A2#1
5:SIGMA
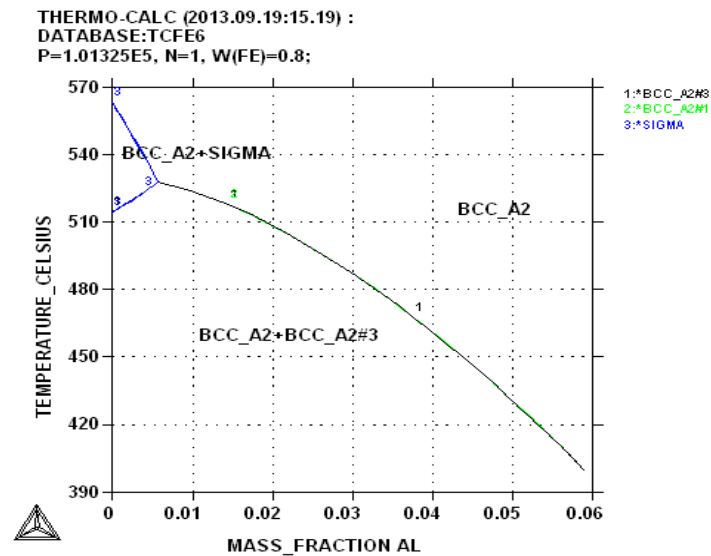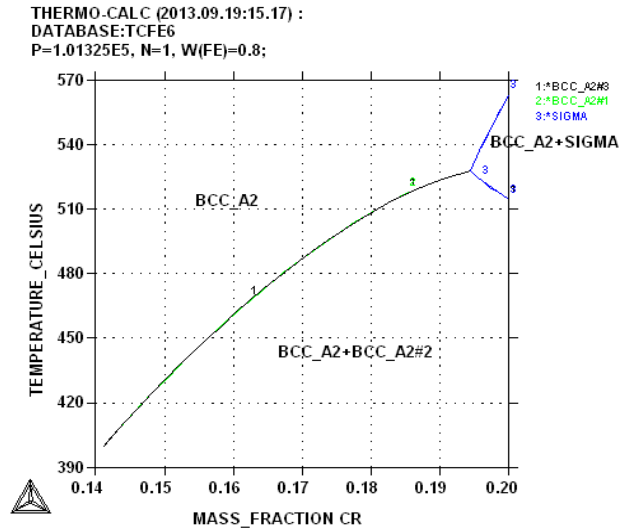
(a) 700°C   (b) 600°C

Figure 11. Selection of Sputtering Temperature for Fe-Cr-Al at different temperatures.

Fixing the value of Fe to 0.8 (mass fraction) requires about 0.05 (mass fraction) or 5% Al, in order to form Al_2O_3 on the surface to protect the coating, where as the Cr content, looking at the isopleth should be lower than 19%, to avoid sigma phase. Both mass fraction for Al and Cr is shown in Figure 12.

THERMO-CALC (2013.09.19:15.19) :
DATABASE:TCFE6
P=1.01325E5, N=1, W(FE)=0.8;

1:*BCC_A2#3
2:*BCC_A2#1
3:*SIGMA

(a) Mass Fraction for Aluminum

(a) Mass Fraction for Chromium

Figure 12. Mass Fraction for Aluminum and Chromium for Fe-Cr-Al.

Conclusions and Recommendations

Thermodynamic properties and phase equilibria was described for Zirconium, Zr-2, and Zr-4. Hydrogen uptake, facilitates oxidation of Zr. At equilibrium state, hydrogen solubility is same for all three alloys, but Zr-4 is better than Zr-2 in terms of less hydrogen uptake, so hydrogen uptake is not a thermodynamic controlled phenomenon but driven by kinetics. Zr is thermodynamically unstable to oxidation even at room temperature and the process of oxidation and hydrogen pick-up is controlled kinetically, which increases with increase in temperature. First, principles atomistic simulations were used to elucidate kinetic aspects of hydriding and role of sub-oxide Zr_3O emphasized in slowing down Zirconium hydriding process. Plastic deformation of Zr is unusual (i.e., at lower temperature ~300°C) takes place by twinning and at elevated temperature the mechanism changes to conventional crystallographic slip. Future work is under way for the development of temperature dependent creep evolution model for Zr, which will be implemented using MOOSE.

Sputtering temperature for coatings should be either below 500°C or above 700°C. The optimal composition of Fe-Cr-Al protective coating should be in the range from 80-18-2 to 80-14-6, preferably 80-15-5 wt.% of Fe, Cr, Al. The chemical composition of YSZ-doped ZRO_2 should be established based on matching thermo-physical properties of Zr-2 and Zr-4 and desired temperature of oxygen transport activation to get self-healing mechanism started. Beryllium additions (~1ppm to 5ppm Be) should be

explored during Zr alloy ingot casting. Thermal stability of clad with Be ancillary additions still needs studied.

References

1. Zuzek E., Abriata J.P., San Martin A., and Manchester F.D., H-Zr (Hydrogen-Zirconium), "Binary Alloy Phase Diagrams," II Ed., Ed. T.B. Massalski, Vol. 2, 1990, pp. 2078–2080.
2. Busby, Jeremy T., Ilevbare, Gabriel, Andresen, Peter L. (red./ed.) | Blomqvist, Jakob, Olofsson, Johan, Alvarez, Anna-Maria, and Bjerkén, Christina (2012) "Structure and Thermodynamical Properties of Zirconium hydrides from first-principle," (peer-review paper) pp. 671–679, John Wiley & Sons, ISBN 9781118456835.